ABSTRACT

Studies on New Approaches of Chiral Discrimination for Chiral Analysis
by Regression Modeling of Spectral Data

Selorm Kwame Modzabi, Ph.D.

Mentors: Kenneth W. Busch, Ph.D. and Marianna A. Busch, Ph.D.

Two new approaches of chiral discrimination for enantiomeric composition analysis using isotropic spectroscopic techniques and multivariate regression modeling were investigated. This is in view of the urgent need for rapid and improved strategies for chiral analysis due to the rising preference and demand for chiral drugs.

In the first approach, (*S*)-(+)-1,2-propanediol or the racemic mixture of 2-butanol was reacted with the enantiomers of amino acids or chiral pharmaceutical compounds to form covalent derivatives (diastereomers). To circumvent usually long and cumbersome separation processes required by some chiral analysis techniques, the isotropic UV or fluorescence spectra of solutions of the reaction matrix containing the derivatized enantiomers were subjected to partial least squares regression (PLSR) modeling. PLSR was used as a means of extracting latent or structured information from the spectral data, which might contain interference and/or redundant information from the reaction matrix. Evaluation of the above approach using a test set of samples gave results with root-mean-square errors (RMSEs) of 0.0012-0.042.

In the second approach, PLS-1 regression analysis were performed on the UV spectral data of samples containing different compositions of enantiomeric pairs, which were non-covalently discriminated *in situ* using a multi-functional chiral selected, (*S*)-(-)-1-phenylethylamine. Enantiomeric compositions of test samples of three amino acids and a carbohydrate determined using the second approach gave RMSEs of 0.006-0.025.

In view of the need for micro-scale techniques in analyses such as this, a capillary tube, with a total volume of 95 µL, was custom-designed in the cause of this research for the measurement of fluorescence emission spectra of micro volumes of samples. The custom-designed capillary tube, which has an internal diameter of 1 mm and requires not more than 25 µL of sample solution for spectral measurement, was found to result in higher fluorescence emission intensities than measured using a commercial 10-mm pathlength fluorometer cell. Results of quantitative studies performed using the custom-designed capillary micro cell for spectral measurement were significantly identical to the results of studies conducted using the commercial cell.

Studies on New Approaches of Chiral Discrimination for Chiral Analysis by Regression Modeling of Spectral Data

by

Selorm Kwame Modzabi, BSc. Chemistry

A Dissertation

Approved by the Department of Chemistry and Biochemistry

_____

David E. Pennington, Ph.D., Interim Chairperson

Submitted to the Graduate Faculty of
Baylor University in Partial Fulfillment of the
Requirements for the Degree
of
Doctor of Philosophy

Approved by the Dissertation Committee

_____

Kenneth W. Busch, Ph.D., Co-Chairperson

_____

Marianna A. Busch, Ph.D., Co-Chairperson

_____

Stephen L. Gipson, Ph.D.

_____

C. Kevin Chambliss, Ph.D.

_____

Carlos E. Manzanares, Ph.D.

_____

Rafer S. Lutz, Ph.D.

Accepted by the Graduate School
May 2009

_____

J. Larry Lyon, Ph.D., Dean

Page bearing signatures is kept on file in the Graduate School.

TABLE OF CONTENTS

List of Figures……..… vii

List of Tables……..……. xiv

Acknowledgments……..……. xvi

CHAPTER ONE– Introduction……..……. 1

Chirality……..……. 1

Enantiomers……..….... 9

Diastereomers……..…… 15

Importance of Chirality……...……. 16

Chiral Analysis……..….. 19

Spectral Data Analysis……..….. 43

Multivariate Regression Analysis in Chemistry……..….... 46

Previous Studies……..…..... 59

Rationale and Scope of Research……..….. 61

CHAPTER TWO – Non-Separative, Covalent, Chiral Discrimination……..... 65

Introduction……..….... 65

Background on the Analysis of Phenylalanine and Tyrosine Using (*S*)-(+)-1,2-propanediol……..…… 70

Background on the Analysis of Atenolol and Norephedrine Using (*S*)-(+)-1,2-propanediol……..… 73

Methodology……..……. 76

Materials……..….... 76

Preparation of NSCDS Samples of Phenylalanine and Tyrosine..… 77

Preparation of NSCCDS and Control Samples of Phenylalanine and Tyrosine..……..… 78

Preparation of Chiral-Selector-Free Phenylalanine Samples…..…… 79

Preparation of NSCCDS and Control Samples of Atenolol..…..…... 79

Instrumentation, Spectra Collection, and Data Analysis……..…….. 80

Results and Discussion……..……. 80

Analysis of NSCCDS Samples of Phenylalanine……..……. 80

Analysis of control Samples of Phenylalanine……..……. 88

Analysis of Chiral-Selector-Free Phenylalanine Samples..…..…….. 96

Analysis of NSCCDS Samples of Tyrosine……..……. 103

Analysis of Control Samples of Tyrosine……..…… 109

Analysis of NSCCDS and Control Samples of Atenolol……..…. 115

Analysis of NSCCDS Samples of Norephedrine……..…. 122

NSCCDS Compared to Our previous Non-Covalent Discrimination Studies…….…….…. 127

Conclusion…….…… 136

CHAPTER THREE– Capillary Tube Micro Fluorometer Cell for Steady-State Fluorescence Measurement……...……... 137

Introduction…….….. 137

The Custom-Designed Capillary Micro Fluorometer Cell…….…... 140

Spectral Measurement Test…….….. 142

Initial Spectral Test…….…... 142

UV Excitation Spectral Response……..…… 145

Test for Qualitative Analysis……..… 151

Test for Quantitative Analysis……..….. 158

Conclusion……..… 165

CHAPTER FOUR– Micro-scale Fluorescence Measurement and Analysis of Log-Converted Spectral Data in Chiral Analysis…….…. 166

Introduction…….….. 166

Methodology…….. 176

Materials……..... 176

Preparation of NSCCDS Samples of Phenylalanine Using the Racemate of 2-Butanol…….…. 176

Preparation of Recrystallized 2_Butanol Phenylalanine Ester Samples…..……..... 177

Preparation of β-cyclodextrin Samples of Phenylalanine..… 178

Preparation of Real-Life Situation Samples of Phenylalanine Using the Racemate of 2-Butanol…….….. 178

Spectral Data Collection, Treatment, and Analysis……..…. 179

Results and Discussion…….…. 180

The Custom-Designed Capillary Micro Cell Compared with the Commercial Cell and the Capillary Flow-Cell……..... 212

Conclusion…….…… 216

CHAPTER FIVE – (*S*)-(-)-1-phenylethylamine As a Chiral Selector for Non-Covalent Enantiomeric Composition Analysis…….….. 216

Introduction…….…….. 216

Methodology…….……. 220

Materials…….…….... 220

Instrumentation, Spectra Collection, and Spectral Data Analysis……..…. 221

Analysis of the Amino Acids: Preparation of Stock and Sample Solutions……..… 221

Analysis of Arabinose…….…. 222

Preparation of Stock and Sample Solutions…….... 224

Results and Discussion…….…. 225

Analysis of Tyrosine…….…. 225

Analysis of Phenylalanine…….…… 231

Analysis of Alanine…..…….…. 237

Analysis of Arabinose…….….. 241

Conclusion……..… 253

REFERENCES……..…. 255

LIST OF FIGURES

Figure		page
1.1	Enantiomers of 6,6′-dinitro-2,2′-diphenic acid…….….	6
1.2	Generic structure of ansa compounds…….……	7
1.3	A: Structure of a triortho-substituted triarylboron. B: Structure of hexahelicene……...…….……..	8
1.4	Enantiomers of 1-chloro-2,2-dimethylziridine…….…….	8
1.5	Structure of (S)-(-)-1-phenylethylamine showing the groups attached to the stereocenter prioritized by the CIP sequence rule……..…	10
1.6	Assignment of configurations to enantiomers of 6,6′-dinitro-2,2′-diphenic acid using Fischer projections……..…	12
1.7	Hypothetical normal and anomalous ORD curves…….…...	21
1.8	Hypothetical absorption, CD spectra, and ORD curves…….…...	23
1.9	Molecular orbital energy levels and possible electronic transitions……..….	34
1.10	Schematic of the Agilent 8453 UV-vis photodiode array Spectrophotometer……..…	39
1.11	Jablonski diagram showing photoluminescence processes following light absortion…….…..	41
1.12	Schematic of the FluoroMax-2 spectrofluorometer (Jobin Yvon SPEX Instruments, SA Inc.)……..…	43
1.13	Hypothetical data swarm plotted on an XYZ coordinate system showing three principal components……..…	49
1.14	Ideal plots of variance as a function of PC in PC-based multivariate regression analysis techniques…….....	51
1.17	Schematic of the two major phases in multivariate regression analysis……..	54

2.1 Structure of **1**: (*S*)-(+)-1,2-propanediol **2**: Phenylalanine. **3**: Tyrosine…….…. 71

2.2 Structure of 4-[2-hydroxy-3-isopropylaminopropoxy]-phenylacetamide (Atenolol)…….….. 74

2.3 Structure of Norephedrine (2-amino-1-phenyl-propan-1-ol)…….…… 76

2.4 UV absorption spectra of 4 mM (*S*)-(+)-1,2-propanediol esterified D-and L-phenylalanine stock solutions……..... 81

2.5 UV absorption spectra of fifteen sample solutions prepared using 4 mM (*S*)-(+)-1,2-propanediol esterified D-and L-phenylalanine stock solutions……..…... 83

2.6 Multivariate, PLS-1 regression, calibration model plots for NSCCDS calibration samples of phenylalanine…….……..…. 85

2.7 UV absorption spectra of 4 mM NSCCDS and control D-and L-phenylalanine stock solutions…….…... 90

2.8 Mean-centered UV absorption spectra of4 mM (*S*)-(+)-1,2-propanediol (PD) esterified and associated D-and L-phenylalanine stock solutions…….…….. 91

2.9 Original and mean-centered UV absorption spectra of thirteen sample solutions prepared using 4 mM (*S*)-(+)-1,2-propanediol associated D-and L-phenylalanine stock solutions…….……..... 92

2.10 PLS-1 regression, calibration model plots for control or PD associated phenylalanine calibration samples…….…….……. 93

2.11 UV absorption spectra of 4 mM (*S*)-(+)-1,2-propanediol esterified and chiral-selector-free D- phenylalanine stock solutions…… 98

2.12 Mean-centered UV absorption spectra of fourteen sample solutions prepared using 4 mM chiral-selector-free D-and L-phenylalanine stock solutions……..... 99

2.13 PLS-1 regression, calibration model plots for chiral-selector-free phenylalanine calibration samples……..…….. 101

2.14 UV absorption spectra of (*S*)-(+)-1,2-propanediol derivatized or esterified 4 mM stock solutions of D-and L-tyrosine……... 104

2.15 UV absorption spectra of twelve samples solutions prepared using 2.5 mM (*S*)-(+)-1,2-propanediol esterified D-and L-tyrosine stock solutions……..…. 106

2.16 PLS-1 regression calibration model plots for NSCCDS calibration samples of tyrosine……...…… 107

2.17 UV absorption spectra for the control and NSCCDS tyrosine samples made up of varying enantiomeric compositions of D- and L-tyrosine……..… 110

2.18 Mean-centered spectra of the UV absorption spectra shown in Figure 2.18 for the fourteen control samples of tyrosine…….…. 111

2.19 PLS-1 regression, calibration model plots for the control calibration samples of tyrosine……...…… 113

2.20 UV absorption spectra for the control Atenolol and Atenolol reacted with PD (NSCCDS Atenolol) stock solutions……...…….. 116

2.21 Mean-centered spectra of the UV absorption spectra for fourteen NSCCDS and control Atenolol samples.....…….. 117

2.22 PLS-1 regression calibration model plots for the NSCCDS Atenolol calibration samples…….……... 119

2.23 PLS-1 regression calibration model plots for the control calibration samples of Atenolol……... 120

2.24 Color changes occurring during the reaction of Norephedrine with (S)-(+)-1,2-propanediol in the presence of HCl..……..… 124

2.25 Original UV absorption spectra for sixteen Norephedrine sample solutions prepared using 2.5 mM stock solutions of…….……... 125

2.26 Summary of the root-mean-squares error of prediction figures of merit for chiral selectors and…….. 133

3.1 Custom-designed capillary micro-cell consisting of a 95-mm long capillary tube……...…… 140

3.2 A: Custom-designed micro-cell before filing. B: Sample solution filling by capillary action……...……. 141

3.3 Fluorescence emission spectrum for deionized water collected using the commercial cell…….…… 143

3.4 A: Ten spectral replicates of the fluorescence emission spectrum of 2 mM tyrosine solution collected using the capillary cell……... 145

3.5 A: The fluorescence emission spectra of the empty capillary tube used for the custom-designed capillary cell……..... 147

3.6 A: Rayleigh and Raman scattering signals for deionized water due to excitation at 257.5 and 350 nm……..…... 150

3.7 A: Fluorescence emission spectra for racemic2-butanol-HCl blank solution collected using the capillary cell…….…. 153

3.8 A: Fluorescence emission spectra for 3 mM phenylananine solution collected using the capillary cell…….…… 154

3.9 A: Blank-corrected fluorescence emission spectra for 3 mM phenylalanine solution…….…..... 156

3.10 A: Ten replicated fluorescence emission spectra for the 2 mM tyrosine solution recorded using the custom-designed capillary micro cell……...…….…. 159

3.11 Plots of the PLS-1 regression model developed for the quantitative analysis test on the capillary and commercial cells……...…….…. 162

3.12 Fluorescence emission spectra collection using the capillary tube custom-designed as micro fluorometer cell……..…... 164

4.1 A: Original crystal sample of D-phenylalanine
B: White gelatinous precipitate product formed…….…. 180

4.2 H1 NMR spectrum of the solid product formed by reacting the racemate of 2-butanol with D-phenylalanine…….….. 181

4.3 C-13 NMR spectrum of the solid product formed by reacting the racemate of 2-butanol with D-phenylalanine…….….. 182

4.4 A: Fluorescence emission spectra of 5 mM stock solutions of racemate 2-butanol esters of D- and L-phenylalanine and……..……. 186

4.5 A: Fluorescence emission spectra of thirty NSCCDS sample solutions
B: Fluorescence emission spectra of thirty RE sample..……. 189

4.6 A: Mean centered fluorescence emission spectra of the thirty NSCCDS samples…….…. 190

4.7 PLS-1 regression model plots for the NSCCDS calibration samples listed on page 192..…….…..….. 194

4.8 PLS-1 regression model plots for the RE calibration samples listed on page 192..…….…..….. 196

4.9 PLS-1 regression model plots for the β-CD samples listed on page 192..…….…..... 198

4.10 A: Log_{10}-converted fluorescence emission spectra for the thirty NSCCDS phenylalanine samples compared with the…….……..…... 202

4.11 PLS-1 regression model plots developed using log_{10}-converted spectral data of the NSCCDS phenylalanine samples…….…..….. 203

4.12 PLS-1 regression model plots developed using the log_{10} converted spectral data of the recrystallized phenylalanine ester samples…..……..…… 205

4.13 UV absorption spectra of ten real-life (RL) samples made up of different compositions of the enantiomers of phenylalanine…….….. 209

4.14 A: PLS-1 regression calibration plot developed from the spectral data of the ten phenylalanine samples prepared for real life situation analysis…….…….…. 210

5.1 Chemical structures of (*S*)-(-)-1-Phenylethylamine (S-PEA), Alanine (Ala), Phenylalanine (Phe), Tyrosine (Tyr), and Arabinose…….. 220

5.2 A: UV absorption spectra of 2.5 mM aqueous solutions of tyrosine and (S)-(-)-1-phenylethylamine……. 226

5.3 Mean-centered UV absorption spectra of eighteen tyrosine-S-PEA sample solutions made up of varying compositions…… 227

5.4 PLS1 regression modeling plots of randomly selected eight tyrosine-S-PEA calibration samples……... 228

5.5 UV absorption spectrum (pink) of a 4 mM solution made up of 1:9 mole fraction ratio of D- and L- phenylalanine…….…..... 232

5.6 Mean-centered UV absorption spectra of seventeen phenylalanine-S-PEA sample solutions (4 mM)…….…. 234

5.7 UV absorption spectra for four different solutions: S-PEA, enantiopure D-alanine…….…. 237

5.8 A: UV absorption spectra of seventeen 4 mM alanine-S-PEA sample solutions……... 239

5.9 UV absorption spectra recorded for solutions of D-and L-arabinose dissolved in S-PEA solution…….…... 242

5.10 UV absorption spectra of sample solutions made up of varying enantiomeric compositions of D- and L-arabinose…….…... 244

5.11 Mean-centered UV absorption spectra of sample solutions made up of varying enantiomeric compositions of D- and L-arabinose……..... 245

5.12 PLS-1 regression calibration model plots developed for 3 mM arabinose-S-PEA calibration samples…….…… 246

5.13 PLS-1 regression calibration model plots developed for 12 mM arabinose-S-PEA calibration samples…….….. 247

LIST OF TABLES

Table		page
1.1	Transitions of typical chromophores…….……..….	36
2.1	Regression plot statistics for calibrating and cross-validating 4 mM NSCCDS calibration samples of phenylalanine made up of……..…...	87
2.2	Actual and predicted mole fractions of D-phenylalanine in the 4 mM NSCCDS validation samples of phenylalanine……...…….....	88
2.3	Regression plot statistics for calibrating and cross-validating 4 mM NSCCDS and control calibration samples of Phe…….……..	95
2.4	Comparison of the predicted mole fractions of D-phenylalanine in the control and NSCCDS validation samples……	96
2.5	Regression plot statistics for calibrating and cross-validating 4 mM NSCCDS and chiral-selector-free calibration samples of Phe…..……..	102
2.6	Actual and predicted D-phenylalanine mole fractions for 4 mM chiral-selector-free validation samples…….…….	103
2.7	Regression plot statistics for calibration and cross-validation of 2.5 mM calibration sample solutions of tyrosine made up…….…...	108
2.8	Actual and predicted mole fractions of D-Tyr of the 2.5 mM NSCCDS validation samples of tyrosine……..…..	109
2.9.	Regression plot Statistics for calibrating and cross-validating 2.5 mM NSCCDS and control calibration samples of tyrosine…….…	114
2.10	Comparison of the predicted mole fractions of D-tyrosine in the control and NSCCDS validation samples tyrosine…….…...	115
2.11	Regression plot statistics for calibrating and cross-validating 2 mM NSCCDS and control calibration samples of Atenolol……..…..	122
2.12	Comparison of the predicted mole fractions of S-Atenolol in the in the NSCCDS and control samples of Atenolol…...…….….	123

2.13 Comparison of the actual and predicted mole fractions of *1R,2S*-Norephedrine in the NSCCDS validation samples……..…… 126

2.14 Summary of the results of the NSCCDS study compared with the results of our existing non-covalent discrimination strategies…….…... 129

4.1 Comparison of experimentally measured proton and C-13 chemical shifts of the recrystallized solid product…….….. 184

4.2 Plot characteristics of the cross-validated PLS-1 regression plots for the NSCCDS, RE, and β-CD calibration samples listed on page 192...….. 199

4.3 Comparison of predicted D-phenylalanine mole fractions of the NSCCDS, recrystallized ester (RE), and β-CD validation samples…….…. 200

4.4 Comparison of the cross-validation PLS-1 regression plot statistics computed for the original and $\log_{10}$ spectral data…….…. 206

4.5 Prediction results for $\log_{10}$ and original spectral data analyses of NSCCDS validation samples of phenylalanine…….…..... 207

4.6 Prediction results for $\log_{10}$ and original spectral data analyses for recrystalized ester (RE) validation samples…….… 208

4.7 Summary of the prediction results for the analysis of real-life situation samples of phenylalanine……..... 211

4.8 Comparison of the root-mean-squares error of prediction (RMSEP) figures of merit for the analysis of phenylalanine…….…… 213

.

5.1 Comparison of the actual and predicted D-tyrosine mole fractions of 2.5 mM tyrosine validation samples…….…..… 230

5.2 Comparison of the cross-validated PLS-1 regression plot statistics computed for the calibration samples of phenylalanine and tyrosine……..….. 235

5.3 Comparison of the actual and predicted D-Phe mole fractions of 4 mM phenylalanine validation samples…….….. 236

5.4 Comparison of the cross-validated PLS-1 regression plot statistics computed for the calibration samples of alanine, phenylalanine, and……..….. 240

5.5 Comparison of the actual and predicted D-alanine mole fractions of alanine-S-PEA validation samples……..... 241

5.6 Comparison of the cross-validated PLS-1 regression plot statistics computed for the calibration samples of arabinose, alanine……..……..... 250

5.7 Comparison of the mole fractions of L-arabinose predicted for 3 and 12 mM arabinose-S-PEA validation samples……..…… 251

5.8 Results for the enantiomeric composition analysis of selected sugars using metal-modified amino acid chiral selectors…….……. 252

ACKNOWLEDGMENTS

To God the immortal I say praise, glory, and honor to your name through the Lord Jesus Christ, the risen savior, for all you have done for me. For, it is by you God are all things made and made beautiful, and I believe as the Bible says there is nothing that mankind has that mankind has not received or been given. May it ever be that all that is in me praise and honor your holy name in the name of Jesus Christ. Amen!

I say a big thank you to my mother, Bertha A. Modzabi, for bringing me up the way she did. She has always been there for me– encouraging and supporting me with her prayers. Mom, your love and concern for me are priceless and I know you will still be there for me till the Lord calls you home. To my dad, Stephen K. Modzabi, who could not live long enough (Died 2000) to see the fruit of his investment in me, I say to your blessed memory, thanks for the discipline instilled in me, your watchful eyes, love and concern; certainly, you imparted my life positively.

To my sisters, Mabel, Annie, and Nancy, and brothers Cephas and Samuel, I want to express my sincere thanks and appreciation to each of you for the valuable contribution each of you made to my life; right from childhood to this day. I want to thank Mr Paragon Pomeyie (Annie's husband) and Mr. Samuel Attom for the help they were to me.

I thank Baylor University and sincerely appreciate the opportunity and financial support given me to pursue this Ph.D. program. I thank Dr. Manzanares, who was vital in my admission to Baylor, and Nancy Kallus and Dr. Garner for their help during the Fall 2008 and Spring 2009 semesters. I thank you Dr. Pennington for your concern.

My mentors, Drs. M. A. and K. W. Busch, I want to thank you for the enormous contribution you made to my academic life. I appreciate your positive criticisms and valuable advice that has brought me this far. I owe both of you a lot for this academic achievement. And for Dr. K. W. Busch, may you never lose your humorous and amicable way of handling issues for they go a long way that you may think. Go near Marianna and you will find out the nice person she is. I am glad I have you both as my mentors.

To each of the other members of my Ph.D. committee, Drs. Stephen L. Gipson, C. K. Chambliss, C. E. Manzanares, and Lutz S. Rafer, I want to thank you for making time out of your busy schedule anytime I called upon you. Thank you for reading through my dissertation, making the necessary corrections, and offering useful advice. I particularly appreciate your patience with me during the last hours of getting you copies of my dissertation.

I thank my pastor, Olutunde Odedeji, the wife, Kemi Odedeji for their support, encouragement and prayers since we met, and the Church, RCCG, Living Faith Chapel as a whole for being a spiritual rock to stand on during my schooling in Baylor.

To members of the Busch group known to me, Dennis, Sayo, Jemima, Chris, Jody, and Tricia, I thank you for the friendly atmosphere you provided and your help.

My thanks go to my friends and colleagues, Charles, Shadrack, James, Paxman, Anthony, Patience, Julius, Joyce, Esther, Yvonne, Dorcas, Rose, Hawa, Thiru, Nanda, Basu, Bikram, Lekh, Andy, and Song because knowing you mean a lot to me.

I am not able to include by name all other people, far and near, who contributed positively to this achievement but you are surely appreciated and will ever be.

CHAPTER ONE

Introduction

Chirality

Many objects in nature reveal the concept of chirality. A familiar example is our hands, which posses a mirror-image symmetry relationship.

Just as a pair of objects can portray an object-mirror image relationship, pairs of molecules, which are the building blocks of many objects seen around us, are known to be chiral or exhibit chirality. The terms chiral and chirality are reported to be first coined by a British physicist, Thomas (1824-1907), who was knighted in 1866 by Queen Victoria [1-5]. These terms are documented to have first appeared in the 1894 printed version of Thomson's famous 2nd Robert Boyle Lecture. According to Gal [1, 2], it is not known whether he actually used those terms in the lecture since there is no stenographic record of the lecture. Thomson, who is also known Lord Kelvin, described the concept of nonsuperposability seen in certain objects saying, "I call any geometrical figure or group of points, chiral, and say it has chirality, if its image in a plane mirror, ideally realized, cannot be brought to coincide with itself'' [1-3]. According to Cintas and Gal, the printed document also shows that Lord Kelvin, in addition, said "Two equal and similar right hands are homochirally similar or allochirally similar. These are also called enantiomorphs, after a usage introduced, I believe by German writers. Any chiral object and its image in a plane mirror are heterochirally similar." The reference to the Germans in Kelvin's statements suggests that the concept he was describing had already

been observed and made public by the Germans, who had a different name for it. The word chiral, used by Kelvin, is derived from the Greek word hand, *χειρ* [2, 3, 5]. The word enantiomorph, according to the literature, was first used by Carl Friedrich Naumann, a German crystallographer and mineralogist, in his *Elemente der theoretischen Krystallographie* (Elements of Theoretical Crystallography, referred to as *Elemnete*), published in 1856 [1]. Naumann proposed the word enantiomorphism (enantiomorphie in German) to denote absolute oppositeness for which no displacement can compensate. Naumann used this term to describe the phenomenon of handedness and non-superposability in hemihedral pentagondodecahedral crystal structures that he had encountered in his work. It is noted that long before Naumann, the phenomenon of handedness was first examined by Immanuel Kant (1724 - 1804), a German philosopher, who in referring to the two hands wrote, *"sie können nicht kongruieren"* meaning they are not congruent, and said such objects were incongruent counterparts [1,2, 6, 7]. Kant's 'incongruent counterpart', however, might have faded with time because it is not used in modern stereochemistry as a term for chirality. The subject of chirality in chemistry in particular can be associated with two French scientists, Jean-Baptisté Biot (1774 - 1862) and Louis Pasteur (1822 - 1895). Biot, Pasteur's mentor, in 1812, noted a correlation between optical rotation and crystal hemihedrism [2, 4, 8]. Specifically, Biot found out that a quartz plate, cut at right angles to its crystal axis, rotated the plane of vibration of linearly polarized light. According to the literature, Biot recognized this rotation to be an inherent property of the quartz crystal and used the terms dextro- and levorotatory in his description of this optical property of the crystals. About three years later he found that certain organic liquids and solutions of certain organic compounds including turpentine,

sugar, camphor, and tartaric acid were capable of rotating the plane of polarization of linearly polarized light, which he indicated seemed to be a property of individual molecules. Pasteur's contribution to the field of chirality in chemistry took place in 1848. He discovered that the sodium ammonium salt of tartaric acid occurs as a conglomerate of two non-superposable crystal forms [1, 2, 4, 5,]. Pasteur then performed the first resolution of chiral compounds by separating the salts, which are noted to be hemihedral and asymmetric, under a magnifying lens using a pair of tweezers. He, however, never coined a term to describe the geometrical relationship between the two forms of his crystals instead he described them as *isomères*, the French word for isomers, which was coined by the Swedish chemist Jönes Jakob Berzelius (1779 - 1848) in 1830 [1]. The word *isomères* (isomers) refers to molecules with the same molecular formula but different structural formulae. Further experiments carried out by Pasteur led him to discover that similar to his solid crystals, solutions prepared from equal amounts of his crystals rotated plane polarized light equally in opposite directions. The direction of rotation of the light by one of the salts was found to be in the same direction obtained for one form of natural tartaric acid. It was therefore assigned the same direction of rotation of plane polarized light already assigned to tartaric acid, which was positive (+) or clockwise. In another designation, such a notation is referred to as dextro (a prefix from the Latin word dexter meaning on the right side) or *d*. The solution of the other crystal, which was noted to rotate light in the anti-clockwise or negative direction, was denoted as (-) or levo (on the left side) or *l*. Based on the dextro and levo assignments, molecules exhibiting clockwise direction of rotation of plane polarized light are said to be dextrorotatory while molecules with an anti-clockwise rotation of plane polarized light

are levorotatory. Pasteur concluded on the basis of his experiments that the phenomenon of rotation of plane polarized light was due to what he termed *dissymétrie moléculaire,* which means molecular dissymmetry. He went further to postulate that his crystals must have an object-mirror image relationship and pictured them as nonsuperimposable helices or tetrahedral arrangement of atoms in the molecules of the crystals [2, 4, 5, 8]. Pasteur therefore became the first to describe the relationship between optical rotation, dissymmetry at the molecular level, and the nonsuperimposable relation between molecules with an object-mirror image relationship. According to the literature, Pasteur never used the word chiral in any of his descriptions [1]. However, he is by his contributions considered by many to be the founder of stereochemistry and molecular chirality [1, 2, 5, 8].

The next major breakthrough with vast application in modern stereochemistry occurred in 1874 when van 't Hoff, a Dutch physical and organic chemist and Le Bel, a French chemist, independently published their ideas on the tetrahedral arrangement of atoms in molecules [8, 9]. It is noted that van 't Hoff's approach was geared towards finding a model that could account for isomers known at that time while Le Bel's approach, which was more of Pasteur's approach, sought to find the relationship between molecular asymmetry and optical rotation. Generally, the property of rotation of plane polarized light is termed optical activity and molecules exhibiting this property are said to be optically active molecules.

In modern stereochemistry, molecules are described as chiral or achiral (no chirality) based on symmetry operations. According to symmetry operations, a molecule is achiral only and only if it has an axis of improper rotation; that is, an n-fold rotation

(360^o /n) followed by reflection in the plane perpendicular to the axis of rotation, which maps the molecule onto itself. Thus, any molecule lacking this axis is chiral or dissymmetric according to the older description. Chiral molecules, however, are not necessarily asymmetric because they can have an axis of symmetry of a kind [4]. Pasteur's pair of sodium ammonium salts of tartaric acid, which he found to exhibit opposite but equal optical activity, is described in modern stereochemistry as a pair of enantiomers. The term enantiomer, which gradually replaced the older terminology of enantiomorph, is derived from the Greek words *enantios* meaning opposite and *meros* meaning part. Enantiomers belong to a class of isomers known as stereoisomers, which are molecules with the same molecular and structural formulae but differ in the spatial arrangement of their atoms or group of atoms. According to Ramberg [7], Pasteur also found out that a solution made up of equal amounts of his salts had no effect on plane polarized light as Mischerlich had already shown. Such a mixture of enantiomers is referred to as a racemic mixture or a racemate.

Chirality is known to originate differently in different molecular systems. The most common of these is the type observed for a molecular system made up of a central atom to which are bonded four different atoms or groups represented as Cabcd [4, 5, 8]. As noted earlier, this system was proposed independently in 1874 by van't Hoff and Le Bel. According to them, the four different substituents (a,b,c and d) are arranged tetrahedrally around the central carbon atom. Van't Hoff, who worked with Kekule, specified that in a three-dimensional space, the four substituents linked to the carbon atom pointed to the corners of a regular tetrahedron, and that exactly two nonsuperposable forms or structures (enantiomers) were possible [4, 5, 8]. In modern

terms the central carbon in such a molecular system is referred to as the stereocenter or stereogenic atom; it is also called a chiral center. Based on later developments in stereochemistry, the number of stereoisomers possible for a molecule with *n* number of stereocenters is given by 2^n. Hence, a molecule with one stereocenter will have two (2^1) stereoisomers (enantiomers) and a molecule with two stereogenic centers will ideally have four isomers (2^2).

Another origin of chirality in molecules is the presence of what is referred to as a chiral axis [4]. Molecules with this origin of chirality do not have typical chiral centers as the Cabcd molecular system of chiral molecules mentioned above. In addition they have bonds with restricted rotation. Examples of compounds with axial chirality include allenes and ortho-substituted biphenyls. Figure 1.1 shows the structures of the enantiomers of an ortho-substituted biphenyl, 6 6′-dinitro-2 2′-diphenic acid; the chiral axis passes through the middle of the bond joining the phenyl groups. It can be seen from the structures that the arrangement the CO_2H and NO_2 groups on one of the phenyl

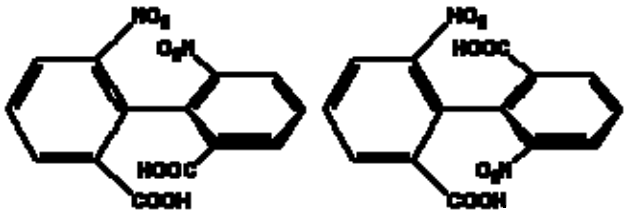

Figure 1.1. Enantiomers of 6 6′-dinitro-2 2′-diphenic acid

groups is opposite in the two structures. Apart from the possession of an axial chirality, some molecules are said to have an axial plane, which gives rise to their chirality [4]. An example of a class of compounds with chiral planes is the ansa (handle) compounds generically shown in Figure 1.2 below. The chiral plane defined, for example, for the

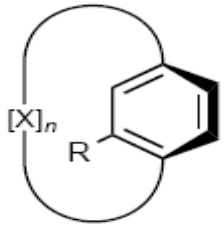

$X = CH_2$, $n \geq 6$

Figure 1.2. Generic structure of ansa compounds

generic ansa compound structure in Figure 1.2 consists of the alicyclic ring constrained to lie over one of the faces of the arene. One enantiomer of such a compound will have its chiral plane over one face of the arene while the chiral plane of the other enantiomer will lie over the opposite face of the arene. In these compounds, the chiral plane should usually contain as many of the atoms of the molecules as possible but with at least one out of plane atom or group for the molecule to be chiral. In addition, an important condition for chirality in these compounds requires the alicyclic ring (ansa: handle) to restrict, for example, the aromatic ring from swiveling through. Spiranes, which are nonplanar organic compounds, are known to exhibit chirality by virtue of their nonplanar structure [4]. Similar to the compounds with axial and planar chirality, spiranes may not have stereocenters. An example of a chiral spirane is spiro[2,2]pentane [4]. Other forms or origins of chirality are realized in compounds with propeller and helical structures [4]. For the propeller-structured compounds, all the groups representing the blades in one enantiomer must be twisted in the same sense but opposite to those of the other enantiomer. For helical structures, a trace of the helix from one end to the other would lead the tracer moving along the axis drawn through the helix in a clockwise direction for one enantiomer and the anti-clockwise direction for the other enantiomer. Examples of propeller and helical chirality are revealed respectively by the three-bladed tri-ortho-

substituted triarylboron and hexahelicene shown in Figure 1.3 A and B respectively; the substituents in the triarylboron are represented with the letters a, b, and c. In addition to the above-mentioned forms or origins of chirality encountered in chiral molecules,

A

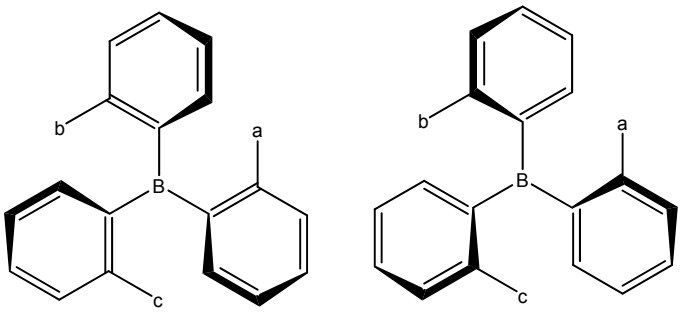

B

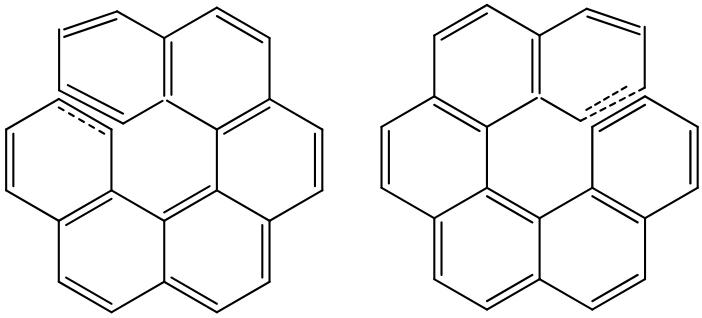

Figure 1.3. A: Structure of the enantiomers of a tri-ortho-substituted triarylboron. B: Structure of the enantiomers of hexahelicene

nitrogen compounds in which the nitrogen atom is part of a structure that restricts inversion at the nitrogen atom could lead to chirality in such compounds. An example of this is 1-chloro-2, 2-dimethylaziridine shown in Figure 1.4.

Figure 1.4. Enantiomers of 1-chloro-2,2-dimethylziridine

Enantiomers

Nomenclature of enantiomers. In addition to the dextro or positive sign (+) and levo or negative sign (-) notation used to denote the direction of optical rotation of enantiomers, optically active compounds are designated using descriptors to specify their spatial arrangement or configuration. Prior to 1951 [4], chemists were limited in assigning absolute configurations to chiral compounds due to lack of the necessary technology. Thus, relative configurations were assigned to chiral compounds by correlating their optical activities with that of other chiral compounds, for example, (+)- or (-)-glyceraldehyde ($HOCH_2CHOHCHO$). The situation, however, changed by 1951 with the development of the anomalous X-ray scattering technique, which is capable of determining the absolute configuration of chiral compounds. The specification of the absolute configuration of an optically active compound involves assigning to the compound descriptors that specify, according to a set of rules, the three dimensional structure of the compound. The most common or universally used system of descriptors for the specification of the absolute configuration of optically active compounds was developed by Chan, Ingold and Prelog (CIP). The CIP system uses the italicized forms of the letters R and S (*R* and *S*) to specify the absolute configuration of optically active compounds with stereocenters according to a set of rules. This set of rules, which can be found in many advanced-level organic texts, including several undergraduate organic textbooks, are used to assign priority to the four atoms or groups linked to the stereocenter in the order, for example, *A*>*B*>*C*>*D*. According to this order, the atom or group assigned the letter *A* has the highest priority and *D* the lowest. A model made of the compound with the assigned priorities is then required to be viewed from the side

directly opposite to the atom or group with the lowest priority (priority *D* atom or group). In this view, the rest of the three atoms or groups (*A*, *B*, and *C*) will present a tripodal array before the viewer. If the tripodal array in the sequence *A*→*B*→*C* is traced in a clockwise direction, the optically-active compound is assigned the descriptor *R* or *rectus*, meaning right in Latin. If the sequence, on the other hand, is traced in an anti-clockwise direction, the compound is assigned the descriptor *S* or *sinister*, meaning left in Latin. All optically active molecules having one or more stereocenters can be described by either an *R* or *S* descriptor(s) or some combinations of both for molecules with more that one stereocenter. To specify the absolute configurations of chiral compounds with chiral centers, the appropriate descriptor(s) is used in their chemical names. For example, the name (*S*)-(-)-1-phenylethylamine of a chiral compound shown in Figure 1.5 below indicates that: (1) the first carbon atom in the parent or longest hydrocarbon chain is the stereocenter (carbon atom with asterisk) of the compound, (2) the sequence of the priority of the tripodal groups, *A* (NH_2)→*B* (C_6H_5)→*C* (CH_3) are traceable only in the anti-clockwise direction, and (3) the compound rotates plane polarized light in the anti-clockwise direction as indicated by the negative sign.

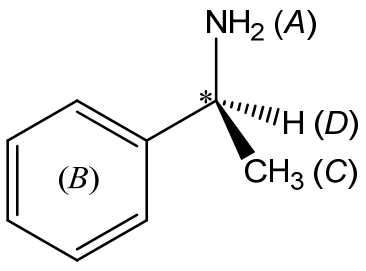

Figure 1.5. Structure of (*S*)-(-)-(1)-phenylethylamine showing the priority of groups attached to the stereocenter (in asterix) according to the CIP sequence rule.

As noted earlier, other forms of chirality are found in molecules in addition to the possession of a stereocenter. As such, other descriptors are used to specify the configuration of optically active molecules that do not have chiral centers. A set of descriptors, a*R* and a*S,* closely related to the CIP descriptors described above are used for the specification of the configuration of molecules with axial chirality. Similar to the CIP system, four groups, for example, the two pairs of groups of the ortho-substituted biphenyl shown in Figure 1.1 are required for the specification of the configuration molecules with axial chirality. Where more than two pairs of such groups are present, those closest to the center of the chiral axis are given priority. The groups are prioritized beginning with any pair of the four groups using, for example, the letters a and b for the first pair of groups and the letters c and d for the second pair according the CIP priority sequence rules; the priorities of the atoms or groups for the second pair is made without regard for that of the first pair [4]. Using the biphenyl in Figure 1.1 as an example, the prioritized groups are presented as Fischer projections shown in Figure 1.6 with the groups having priorities a and b on a vertical line and c and d on a horizontal line. The direction of the sequence a→b or b→c or c→d is then traced. If the direction of the sequence is clockwise as shown in the left Fischer projection then the configuration of the molecule is a*R*. On the other hand, an anti-clockwise direction signifies an a*S* configuration as shown in the right Fischer projection in Figure 1.6. The a*R* and a*S* configuration designations equally apply to spiranes. Other forms of descriptors, *M* and *P*, are also used particularly for optically active helical molecules. For this notation, if a trace of the helix along the axis drawn through the center of the helix describes a clockwise direction, the helix is assigned the descriptor *M*. If the helix is traced in the

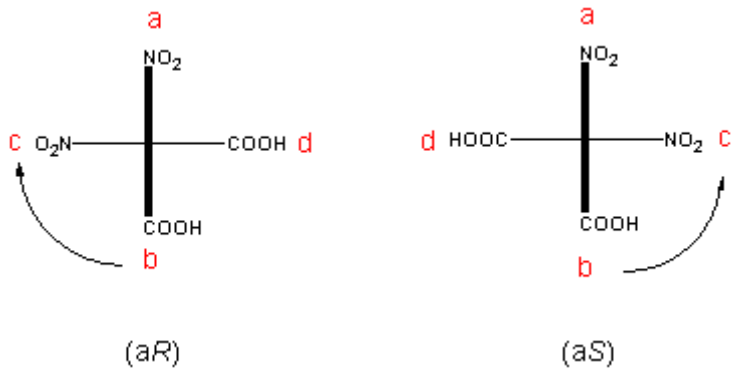

Figure 1.6. Fischer projections of CIP prioritized groups for the assignment of configuration to the enantiomers of 6,6`-dinitro-2,2`-diphenic acid having axial chirality

anti-clockwise direction then it has a *P* configuration. It should be noted that the use of these descriptors has no correlation with the direction of optical activity of the enantiomer. Readers interested in further discussion on this subject can find useful information in several advanced texts on stereochemistry including reference 4.

Properties of enantiomers. As mentioned earlier, enantiomers of compounds are pairs of molecules having equal but opposite optical activity. Enantiomers have a universal property, which is the nonsuperposability of the structure of one enantiomer of a pair on the structure of the other. Except for the rotation of plane polarized light, the enantiomeric pairs are said to have identical physical properties like density, boiling and melting point, solubility, dipole moment and refractive index [4, 5]. Likewise, they are said to exhibit identical chemical properties toward achiral molecules but tend to differ when they react with the same enantiomer molecule of an appropriate compound [4, 5] or are in a chiral environment.

Enantiomeric pairs of certain compounds are known to differ from each other in their response to certain isotropic spectroscopic techniques. For example, Eliel et al. [4, 10] found out in their study that while the IR spectra of the phthalates of (+)-, (-)-, and

racemic mixture of p-ethylphenylmethylcarbinol revealed identical spectra in chloroform solution, the mull spectra were different. This difference in spectra could be due to differences in hydrogen bonding in the different states of the molecules. Research conducted in our laboratory clearly showed that significant differences do exist between the UV spectra of the pure or solution forms of the enantiomeric pairs of several chiral compounds including limonene, 1,2-propanediol, and *N*-benzyl-α-methylbenzylamine [11, 12]. These spectroscopic differences indicate that though enantiomeric pairs may be identical in most of their physical properties, the stereochemical difference between a pair of enantiomers can manifest itself in their response to isotropic (non-polarized) light. As such, enantiomeric pairs could be studied using isotropic spectroscopy techniques. As mentioned earlier, a mixture of equal amounts of a pair of enantiomers forms a racemate or racemic mixture. Unlike enantiomeric pairs, racemic mixtures generally have zero optical activity or may exhibit optical rotation based on temperature, wavelength and solvent. Racemates could differ significantly in their properties (density, boiling point, melting point, solubility, etc.) relative to either member of the pair. Studies have shown that isotropic IR and electronic spectra of racemates differ more from those of the constituent enantiomers than the corresponding spectra for one of the constituent enantiomers compared to the other [4, 10, 13]. However, it is noted that these differences are not expected when conglomerates are formed [4].

In addition to having racemates, a pair of enantiomers can occur or be mixed in an unequal proportion to form what is referred to as an enantiomeric excess (ee). According to Eliel et al. [4], samples made up of different enantiomeric proportions (enantiomeric purity) ranging from the pure to the racemate will often differ in both their physical and

chemical properties. The enantiomeric excess, if the concentrations or moles of the individual enantiomers are known, is mathematically expressed as:

$$ee = \phi_1 - \phi_2 \qquad 1.1$$

where ϕ_1 and ϕ_2 are the mole fractions of the enantiomer such that ϕ_1 is greater than ϕ_2. In practice, the percent ee can be determined by dividing the specific optical rotation, $[\alpha_{F_{\phi 2}+F_{\phi 1}}]$, of the mixture by the specific rotation, $[\alpha_{F_{\phi 1}}]$,obtained for the enantiomer in excess as:

$$ee = ([\alpha_{\phi_1+\phi_2}]/[\alpha_{\phi_1}]) \times 100\% \qquad 1.2$$

The specific rotation, $[\alpha]$, is computed from the optical rotation, α (in degrees), using the equation:

$$[\alpha]_{\lambda}^{T} = \frac{100\alpha}{l \times c} \qquad 1.3$$

where T and λ are the temperature and the wavelength (usually the sodium D-line, 589 nm) respectively, l is the pathlength of the sample in dm and, c is the concentration expressed in grams per 100mL. It can be shown from equation 1.3 that the concentration, c, is directly proportional to the optical rotation, α. Consequently, if the concentrations or any other parameter directly proportional to the concentration can be determined accurately, the mole fractions of the enantiomers can be determined and the percent ee computed using equation 1.1 multiplied by 100. Specific rotation is known to depend, in addition to temperature and wavelength, on solvent (for solution samples) and sometimes concentration [4]. Thus the solvent and concentration must be specified (in parentheses) when the specific rotation of a solution sample is reported.

Diastereomers

Unlike enantiomers, some stereoisomeric pairs of molecules, which are optically active, have no object-mirror image relationship with each other. Such pairs of molecules are referred to as diastereomers or are said to form diastereomeric pairs. Diastereomers usually contain more than one chiral center resulting superimposable configurations or have substituents that give rise to different conformations (possession of chiral torsion axes) or a combination of both. In addition, diastereomerism can arise even though a compound may not possess a chiral center as in cis- and trans-1,3-dichlorocyclobutane and olefinic geometrical isomers. According to Eliel et al. [4], diastereomers differ in most, if not all, physical and chemical properties similar to constitutional isomers. They noted this to be due to a lack of isometry, in diastereomers. The term isometry, as used by Eliel et al., refers to the existence of identical distances between any pair of atoms found in any given pair of enantiomers. Closely related to diastereomers are meso stereoisomers. These molecules, unlike diastereomers, are not optically active even though they may have chiral centers. The optical inactivity of these molecules is usually due to the possession of plane of symmetry. Though diastereomers may occur naturally, they can be synthesized using chiral compounds as precursors. As such, enantiomers can be transformed covalently into completely new compounds with diastereomeric properties. In addition, diastereomeric properties can be induced in enantiomers through non-covalent intermolecular interactions leading to conformational changes; diastereomerism can arise from conformational changes according to Eliel et al. [4]. Diastereomeric transformation of enantiomers through covalent derivatization or

non-covalent complexation/association is of great importance because it allows for the discrimination of chiral compounds for chiral analysis. As such, isotropic spectroscopic techniques can be coupled with enantiomeric discrimination strategies for chiral analysis.

Importance of Chiral Molecules

The importance of chirality cannot be over-emphasized. This phenomenon pervades the whole universe. Almost all biological functions in living organisms involve the activities of chiral compounds. For example, it is documented that except for one, all the twenty naturally occurring amino acids that make up naturally occurring proteins are chiral and occur in the *l* form [4, 5, 14,]. Similarly, all naturally occurring sugars/carbohydrates, which are linked to many proteins and lipids involved in cell-cell recognition, and form part of the structural framework of RNA and DNA molecules, occur in the *d* form [4, 5, 14, 15]. The natural forms of these nucleic acids (RNA and DNA), which are related to gene expression and storage of genetic information, are known to be enantiomerically pure. Biological receptors responsible for distinguishing odor and taste in humans and animals work through chiral biodiscrimination. For example, Piutti (1886) [4] reported the isolation of dextrorotatory asparagine and noted it to have a sweet taste whereas the naturally occurring levorotatory counterpart is known to be tasteless– chiral receptors of the tongue were capable of discriminating the two enantiomers of asparagine. Another important biological function known to involve chiral interactions is enzymatic reaction or activity. Enzymes in their reactions are known to exhibit a high degree of specificity towards substrate molecules by reacting only with molecules of the correct stereochemistry in the presence of several other molecules. For example, the use of L-hexoses as sweeteners is based on the fact that

enzymes that are responsible for breaking down D-hexoses or sucrose are unable to metabolize L-hexoses [4, 16]. The above-mentioned and more of the chiral specific biological reactions are vital to survival.

The unfortunate and painful thalidomide incident in the 1960s is one reminder of the importance of chirality to pharmaceutical and allied industries. It turned out that the *S* enantiomer of thalidomide, which was administered in the racemic form (both in the *R* and *S* forms) to treat morning sickness in pregnant women is teratogenic. Consequently, many children born subsequent to the use of the drug had severe birth defects. After this painful episode, much attention was paid to studying the correlation between toxicological and pharmacological properties in relationship with chirality. Currently, the pharmaceutical and allied industries in major drug and chemical manufacturing nations are required to study the biological activities of each enantiomer of pharmaceutically potent compounds [4, 5, 17]. For example, the US Food and Drug Administration beginning in 1988 explicitly required the submission of detailed information on the enantiomers of chiral compounds in new drugs [4]. The current trend in drug policy is largely related to recent scientific and technological advancement, for example, in molecular biology and chemical analysis. With this advancement, it is now known with specifics that: (1) biological messenger molecules and cell receptor surfaces, which are the targets of many drugs, are chiral and (2) enantiomers of pharmaceutically important compounds could have different biological activities; one enantiomer could be active for a particular therapeutic application while the other may be inactive or toxic or have an entirely different therapeutic effect. It is, therefore, important that the biological activities of each of the enantiomers of a compound for drug application be thoroughly

known. In view of these possible different biological activities of the enantiomers of chiral compounds, single enantiomer drugs are preferred for other reasons such as (1) reduction in metabolic load on the body, (2) simplification of pharmacokinetics, and (3) more homogeneous response to treatment [18]. Pharmaceutical and allied industries worldwide are progressively making a switch from the manufacturing of racemic drugs to single-enantiomer drugs [19, 20]. According to the author of an article published in *Chemical and Engineering News*, the sale of chiral drugs for the first time reached $ 100 billion in 1999 with single-enantiomer drugs reaching $115 billion, up by 16 % from $ 99 billion in 1998 [19]. In Japan, single-enantiomer drugs have received four times as much approval as racemic drugs by the Japanese government in the early 2000s [20]. Figures for worldwide development and approval of single-enantiomer drugs show that the market share for single-enantiomer drugs increased from 27 % in 1996 to 39 % in 2002 [20]. This worldwide preference for chiral drugs and particularly single-enantiomer drugs undoubtedly underscores the importance of the phenomenon of chirality. In consonance with the high demand for chiral drugs is the need for new designs and methods of synthesis for the production of chiral drugs. The synthesis technique currently used for the production of single-enantiomer drugs is asymmetric synthesis, which has three major approaches: chiral pool synthesis, asymmetric induction synthesis, and asymmetric catalysis synthesis. However, non-asymmetric synthetic approaches followed by the use of separation techniques for the resolution and isolation of enantiomers from racemic mixtures are still in practice.

In addition to the pharmaceutical industry, the issue of chirality is important to the agrochemical and fragrance industries as well. The agrochemical industry, for example,

is faced not only with the challenge of developing and producing target-specific chiral chemicals for pest and weed control, but also the aftermath environmental impact of the application of these chemicals. Similar to the possibility of enantiomers exhibiting different therapeutic effects, the stimulation of olfactory glands are known to be chiral specific. The *R* enantiomer of limonene, for example has an orange odor while the *S* enantiomer has the odor of lemon. As such, the fragrance industry, like pharmaceutical industry, is faced with a similar task of development, synthesis, and analysis of chiral chemicals as the.

With the need for new designs and synthesis techniques for chiral compounds comes the demand for simple, efficient, robust, and rapid analytical techniques for catalyst evaluation in asymmetric synthesis, and enantiomeric purity assessment for quality control and combinatorial libraries. Consequently, chiral analysis techniques are high on the agenda of pharmaceutical and other companies involved in the development, production, testing, and selling of chiral chemicals. Several methods, both qualitative and quantitative, are available for chiral analysis. However, the current demands in the field of chirality are such that improved strategies are required.

Chiral Analysis

Generally, methods for analyzing chiral molecules can be classified into two categories: (1) chiroptical methods, which involve measuring spectral responses following the interaction of chiral molecules with polarized light and (2) methods that depend on transforming chiral molecules into diastereomers using covalent or non-covalent strategies prior to instrumental analysis. The chiroptical methods can be used for both qualitative and quantitative studies. The second category of methods, which are

usually combined with non-chiroptical or isotropic detection techniques, are normally used for quantitative analysis though they are capable of being employed for qualitative purposes as well.

The chiroptical methods employed for chiral analysis include: (1) polarimetry, (2) optical rotatory dispersion (ORD), (3) circular dichroism (CD), (4) vibrational circular dichroism (VCD), and (5) Raman optical activity (ROA) [4, 21].

Polarimetry, which is the oldest of all the chiroptical methods, measures at a single-wavelength (usually the sodium D-line, 589 nm) the rotation of plane polarized light by an optically sample. The property of optical rotation is said to be based on the phenomenon of circular birefringence, which is related to the refractive index of the sample [4]. Optical rotation in polarimetry is, thus, affected by the type of solvent used, the wavelength of the plane polarized light, and temperature. In practice, wavelengths used for polarimetric measurements are those at which the sample does not absorb. For a given pair of enantiomers, if the optical rotation measured in degrees of, for example, the *R* enantiomer is positive, the optical rotation of the *S* enantiomer will be negative.

Optical rotatory dispersion (ORD) is similar to the polarimetric technique in that it involves the measurement of the optical rotation caused by an optically active sample. However, the optical rotation in ORD is measured as a function of wavelength and it is known to arise as a result of the variation with wavelength of the indices of refraction of left-and right-circularly polarized light. ORD curves measured in the region of the absorption band of optically substances reveal what is know as anomalous dispersion. Anomalous ORD arises as a result of the difference in absorption of the left- and right-circularly polarized light, which in turn, leads to changes in the direction of rotation

(usually reversed) of the polarized light that passed through the sample. An anomalous ORD plot of ellipticity as a function of wavelength reveals a maximum and a minimum or an S-shaped curve with an inflexion point, which may or not coincide with the absorption maximum of the samples. A normal ORD curve, on the other hand, reveals what is known as a plain curve. Figure 1.7 shows a hypothetical plot of an anomalous ORD curve together with normal positive and negative ORD plain curves. Usually, ORD

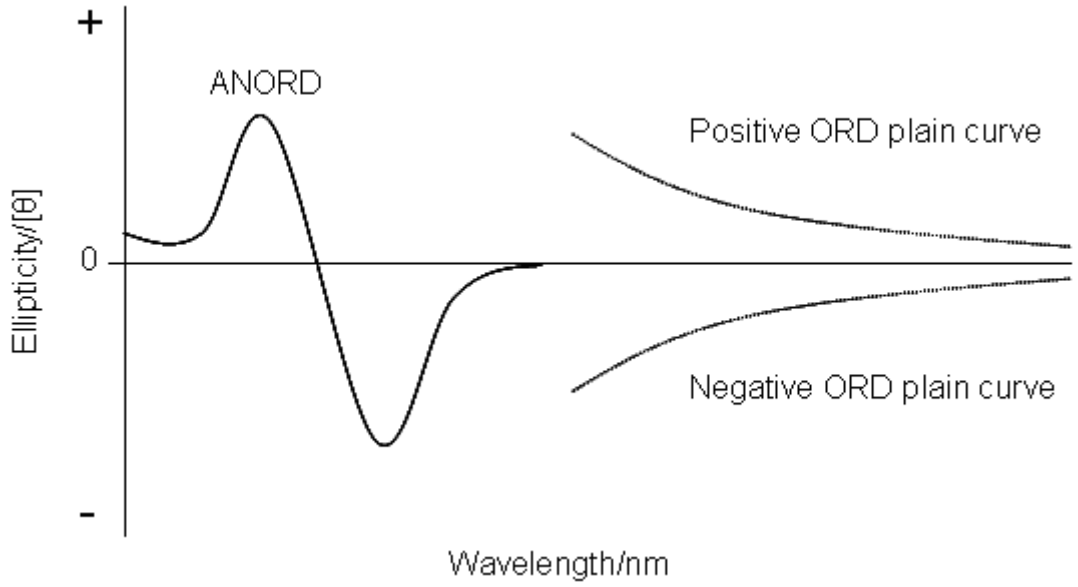

Figure 1.7. Hypothetical normal and anomalous ORD curves. ANORD: Anomalous ORD

measurements are performed in the UV-vis region because the ORD effect increases as the wavelength decreases. ORD can be measured in terms of ellipticity or the degree of rotation of the linearly polarized light transmitted through the optically active sample. The ellipticity, measured in radians, is due the superposition of the electric vectors with different amplitudes of the left- and right-circularly polarized components of the linearly polarized lights; the difference in amplitude of the electric vectors of the left- and right-circular polarized components of the plain polarized light is due to the differential

absorption by the optically active sample. Similar to polarimetric measurements, the ORD measurements of a given pair of enantiomers will have opposite signs. Circular dichroism, which is simply a measure of the change in absorbance, is due to the tendency of optically active substances to absorb left- and right-circularly polarized lights to different extents. Circular dichroism, therefore, is closely related to anomalous ORD, which is a measure the rotation of polarized light in the region of the absorption band of an optically active sample. Similar to ORD, the CD of optically active sample is measured in the UV-vis region. The CD phenomenon, which is due to differential absorption of left- and right-circularly polarized light, together with the change in the direction of rotation observed with anomalous ORD in the absorption band region of an optically active sample, is referred to as the Cotton-effect. The Cotton-effect can be positive or negative. The effect is said to be positive if the ORD maximum occurs at a longer wavelength than the absorption maximum of the optically active sample, while a negative Cotton-effect is said to result if the maximum occurs at a shorter wavelength.

Figure 1.8, hypothetically, shows how an ORD curve is related to the CD spectrum of an optically active sample and the two types of Cotton-effect mentioned above. CD spectra can be presented either as a plot of ellipticity as a function of wavelength or change in absorbance as a function of wavelength. Similar to polarimetric and ORD measurements, the circular dichroism spectra recorded for a pair of enantiomers, will have opposite signs. The difference in absorbance, ΔA, between the absorbance, A_L, of the left-polarized light and that of the right-polarized light, A_R, can be related to the difference in molar absorptivity, $\Delta\varepsilon$, using the Beer-Lambert's Law as

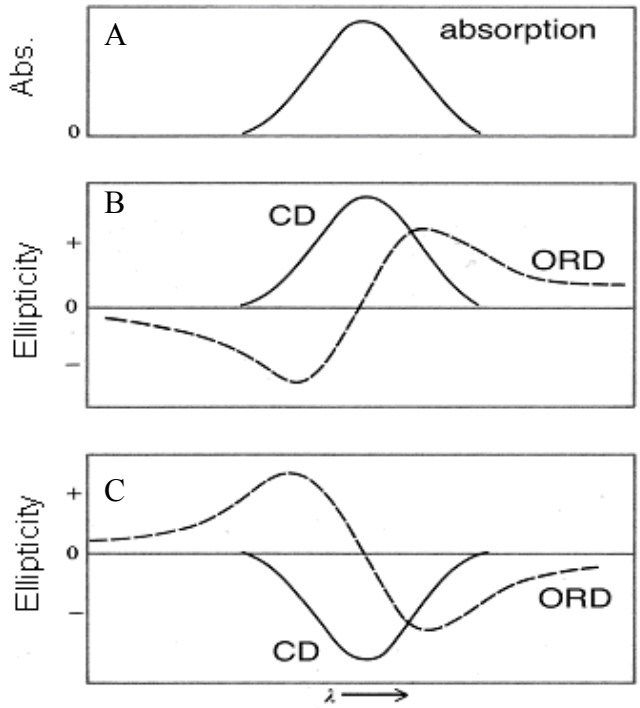

Figure 1.8. Hypothetical absorption, CD spectra, and ORD curves. A: An absorption band. B: CD and ORD spectra showing a positive Cotton-effect. C: CD and ORD spectra showing a negative Cotton-effect. Abs: Absorbance.

$$A_L - A_R = \varepsilon_L - \varepsilon_R(cl) \qquad 1.5$$

where ε_L and ε_R are the molar absorptivities of the optically active sample for the left- and right-circularly polarized light respectively, c is the concentration in mol L^{-1}, and l the pathlength in cm of the optically active sample. Equation 1.5 can be written in the form

$$\Delta A = \Delta \varepsilon c l \,. \qquad 1.6$$

As shown, CD measurement complies with the Beer-Lambert Law. As such, the CD technique, similar to the polarimetric and ORD techniques, can be used for quantitative analysis of chiral samples [22, 23]. However, among these three chiroptical techniques, the CD technique is preferred for quantitative analysis because it is more sensitive than the other two techniques for the determination of enantiomeric purity, particularly for samples with small angles of rotation.

Vibrational circular dichroism (VCD) is a technique that measures the difference in absorption between left- and right-circularly polarized infrared radiation. As such, it is an extension of circular dichroism into the infrared region to allow the probing of bond vibrations instead of just specific chromophores. The complementary technique, Raman optical activity (ROA), measures the difference in intensity of scattered left- and right-circularly polarized light produced by an optically active sample. Unlike the previous chiroptical techniques mentioned, VCD and ROA techniques provide more detailed information on functional groups and/or structure of the optically active molecule. The two techniques, thus, are used when detailed qualitative information is required [4, 24]. In addition, VCD and ROA spectral data can be used in quantum mechanical computations to determine the absolute configurations of small optically active molecules [25]. Similar to the regular IR technique, VCD, at present, is not suitable for the analysis optically active molecules in aqueous solutions. ROA, on the other hand, has been used to successfully analyze biomolecules in aqueous solutions [26]. Recent publications on the use of VCD and ROA for the determination of enantiomeric purity show VCD gives results within a limit of accuracy of 3 %, while results with the ROA are within a limit of accuracy of 0.1 % [26, 27]

The second category of methods, as noted earlier, requires the conversion of enantiomers into diastereomers either by covalent derivatization or by some non-covalent association (specific complex formation or some other intermolecular interaction). In these methods, the enantiomers are converted into diastereomers using another chiral substance in the enantiopure form (homochiral substance). The enantiopure or homochiral substance in this case is referred to as a chiral selector or chiral auxiliary

agent. It can also be called a chiral discriminating agent. The fundamental principle of analysis for these non-chiroptical methods is based on the fact that diastereomers, formed from a pair of enantiomers, become two different stereoisomers (see example 1 and 2 bellow); the enantiomers lose their object-mirror image property and acquire different

Example 1

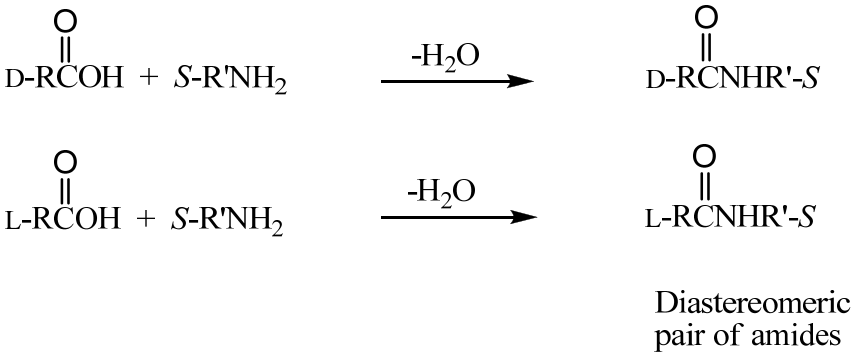

R contains the chiral center: D or L or *S*

Example 2

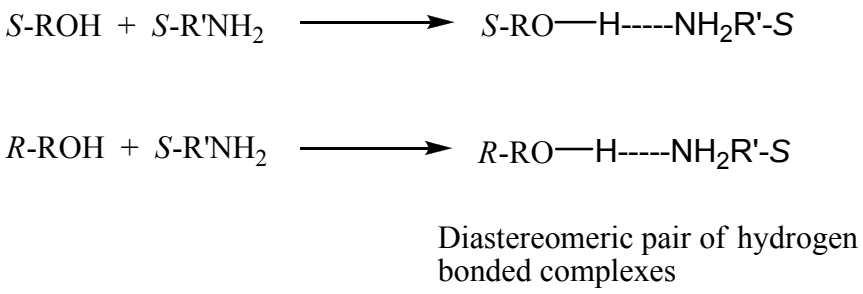

R contains the chiral center: *R* or *S*

physical and chemical properties. The pair of diastereomers formed could behave as constitutional isomers [4]. As such, diastereomeric pairs are relatively easier to identify or distinguish and separate than the enantiomeric pairs from which they were formed. The examples above illustrate the formation of a pair of covalent and non-covalent

diastereomers from two pairs of enantiomers. The first example shows the formation of a pair of amides (covalent diastereomers) from the D and L enantiomers of a chiral carboxylic acid using the *S* form of a chiral amine. The second example shows the formation of a pair of diastereomeric hydrogen bonded complexes between the *S* and *R* enantiomers of a chiral alcohol and the *S* form of a chiral amine. The amide products as well as the hydrogen bonded complexes shown in the examples are diastereomeric because of the presence of the same chiral center in both compounds.

Traditionally, non-chiroptical methods used for chiral analysis include NMR, chromatography, and electrophoresis. The use of NMR without a chiral auxiliary will require that the chiral compound should have an active nucleus or group of nuclei, whose signal differs significantly for the two enantiomers of the compound. This hardly occurs because the nuclei of pure enantiomers relax at significantly the same rate. To overcome this difficulty, cross-polarization and magic angle spinning NMR techniques were developed for both qualitative and quantitative analysis of chiral compounds [4]. However, these techniques could be used for only solid-state NMR measurements. With the strategy of converting enantiomers into diastereomers, chiral compounds could be analyzed both in the solid-state and in solution using regular NMR instruments. Diastereomerization of enantiomers for NMR analysis is carried out through either the use of covalent chiral derivatizing agents or the use of chiral shift reagents or solvents (for non-covalent diastereomerization) [4, 21, 28-30]. A typical example of a covalent derivatization agent used for NMR chiral analysis is the Mosher's reagent (α-methoxy-α-trifluoromethyl phenylacetic acid) while Europium tris [3(heptafluoropropylhydroxy-methylene)-(+)-camphorate] and 2,2,2-trifluoro-1-(anthryl)-ethanol are used as a chiral

shift reagent and chiral solvent, respectively. With the use of covalent chiral derivatization agents, non-NMR active chiral molecules can be derivatized with specific NMR active nuclei like the CF_3 group in the Mosher's reagent for analysis.

Chromatographic techniques are the most common techniques employed in chiral analysis. These techniques, which include both GC and HPLC, are used for both qualitative and quantitative chiral analyses. Chromatography is quite a powerful and versatile tool for analysis such as this because it can be coupled with a variety of sensitive detection systems as well as other analytical techniques. Chromatographic methods, therefore, are known for their sensitivity and accuracy if not for speed, simplicity, and low expense [4, 28]. Irrespective of the specific technique, GC or HPLC or other, chromatographic techniques for chiral analysis will require a chiral stationary phase or a chiral mobile phase if the enantiomers are not derivatized. In the case where neither a chiral stationary or mobile phase is employed, the enantiomers being analyzed are derivatized using a suitable chiral selector or derivatization agent prior to the analysis [4, 31, 32]. All chromatographic techniques for chiral analysis, therefore, depend on the involvement of stable or transient diastereomeric species, which as a result of their different solubility or stability or adsorption properties, allow for separation. Types of chiral stationary phases used in chromatographic techniques for chiral analysis include amides, carbohydrates (e.g., native and modified cyclodextrins), crown ethers, metal chelates, and proteins. Organic solvents, including chloroform, containing chiral mobile phase additives such as 2,2,2-trifluoro-1-(anthryl)-ethanol are used as chiral mobile phases for chiral analysis. Unlike HPLC, GC analysis requires that the chiral analyte be

volatile and thermally stable. While GC may continue to be used in this field of analysis, its application has been superseded by HPLC in recent times [4].

Capillary electrophoresis (CE), which is based on the original principle of electrophoresis discovered by F. F. Reuss in 1807 [33], is now a well-known technique employed mostly in biochemical or biological analysis. Capillary electrophoresis has gained a considerably vast application in chiral analysis for about a decade now [34]. This is not surprising since chirality is an important subject in biochemical and biological studies. Generally, electrophoresis, and for that matter CE analysis, is based on the differences in mobility of charged analytes through an electrolyte system under the influence of a strong electric field. For chiral analysis, CE techniques, similar to chromatographic techniques, are based on the formation of stable (covalent) or transient (non-covalent) diastereomeric species. Differences in the physicochemical properties of the diastereomers allow for the difference in mobility, which is determined by both electroosmosis and electrophoretic transport under the influence of the applied electric field. Chiral analysis using CE techniques can be performed directly or indirectly. The direct analysis involves analyzing, for example, a pair of enantiomers in their original form (no prior formation of diastereomers) by adding a chiral auxiliary agent to the electrolyte system (buffer). The interaction between the chiral analyte and the chiral auxiliary agent, which in this approach is non-covalent, leads to the formation of transient diastereomers. The indirect approach, on the other hand, requires the formation of diastereomers of the enantiomers prior to the separation. The indirect analysis, therefore, can be performed in a non-chiral electrolyte environment. Several CE techniques are available for application in chiral analysis. However, capillary isotachophoresis and

capillary zone electrophoresis (CZE) are the most systematically researched CE techniques for chiral analysis [35]. According to Vespalec et al. [34], CZE, due to its simplicity, has now become the electrophoretic technique of choice for chiral separations. It is noted that resolutions above 5 are common and values as high as 20 have been achieved, resulting in enantiomeric impurity detections below 0.1 % [35]. Compared to other methods, capillary electrophoresis is economical because it requires small samples and limited reagent. It is, however, not necessarily the fastest and the least cumbersome. Though both CE and chromatography techniques have certain things in common, CE is distinguished from chromatography in that an electric field must be applied. In addition, there is no mobile phase *per se* in CE techniques. CZE, in particular, is a free solution technique, which does not involve a stationary phase for separation. Other CE techniques, for example, gel capillary electrophoresis and those that employ capillary walls coated with chiral auxiliary agents are much more closely related to chromatography. Though electrophoresis, and for that matter CE, require generally that analytes must be charged species, neutral chiral molecules can also be analyzed by the formation of micelles using surfactant carriers [4, 34]. Because the basic interactions between chiral analytes and selectors are the same for both CE and chromatography, chiral selectors used in chromatographic separations are equally effective for analysis in chiral CE. Analyte detection in CE is usually accomplished using fluorescence and diode-array UV detectors. An extensive review on capillary electrophoresis in chiral analysis, including several of the chiral selectors used in chiral CE analysis, is published by Vespalec et al. [34]. More information on CE for chiral analysis can be found in this review publication.

In the early stages (1970s) of application for chiral analysis, mass spectrometric (MS) techniques were based on the differential volatility of isotopicaly labeled enantiomers. The separation of the chiral compound was manifested in the relative abundance of the molecular ions as function of time. In those early stages, molecular ions were generated using the electron impact (EI) and chemical ionization (CI) techniques [4, 36]. Since those early stages, significant improvement and refinement have been made in the use of MS for chiral analysis. To date, MS techniques used for chiral analysis can be classified into four major classes: (1) Host-guest diastereomeric adduct formation, (2) ion/molecule reaction diastereomeric adduct formation, (3) collision-induced dissociation, and (4) kinetic reaction method. All these four classes of MS techniques for chiral analysis require the use of chiral auxiliaries. Common chiral auxiliary agents employed in the first two methods include cyclodextrins and crown ethers while metal-coordinated chiral auxiliaries are used in the third and fourth techniques. It is noted that each of the above-mentioned technique can be used for recognition or identification as well as quantification studies [21, 37]. To quantify samples, calibration involving standards with known enantiomeric excess is required. Recent enantiomeric excess analysis using MS reported errors less than 2 % [21, 37].

Isotropic spectroscopic techniques are gradually gaining ground in their application in chiral analysis. This is because, generally, spectroscopic techniques are: (1) faster, (2) relatively simple yet capable of being made sophisticated in function, (3) more versatile, (4) sensitive and reliable, and (5) capable of providing detailed chemical information. It is, therefore, not surprising that more often than not other analytical techniques are coupled with spectroscopic detectors for detailed chemical information.

Isotropic spectroscopic techniques like regular UV and fluorescence spectroscopy are of interest, particularly for quantitative purposes, because they are simple, fast, sensitive, and can be used to analyze samples in a variety of solvents. Our research group has over the years employed these two spectroscopic techniques in research in quantitative chiral analysis. The focus of our research in chiral analysis includes method development. This involves investigating known chiral selectors for isotropic spectroscopic enantiomeric discrimination and designing new discrimination strategies and simple high throughput techniques.

UV and fluorescence spectroscopy, like other spectroscopic technique, is based on the principles of the interaction of matter with electromagnetic radiation. Electromagnetic radiation (ER) is made up of electric and magnetic fields oscillating at right angles to each other. ER can also be treated as particles or photons. ER cover a range of wavelengths from radio waves (~ 10^{6}-1 m) through microwaves (~ 1-10^{-1} m), infrared radiation (~ 10^{-2}-10^{-6} m), visible radiation (~10^{-2}-10^{-6} m), ultraviolet radiation (~ 10^{-7}-10^{-9} m), X-rays (~ 10^{-9}-10^{-13} m) to gamma rays (from 10^{-13} m and above) [38]. It should also be noted that no clear-cut boundaries exist between the various radiations constituting the electromagnetic spectrum. Unlike other forms of waves, electromagnetic waves can travel through a vacuum. The energy, E (in Joules, J), of a photon of a given electromagnetic radiation is related to its frequency, v (in Hertz, Hz), by the equation:

$$E = hv \qquad 1.7$$

where h is Plank's constant. The frequency, v, is related to the speed of light, c, in a vacuum by the equation:

$$c = \lambda v \qquad 1.8$$

where λ is the wavelength (usually in nanometers, nm). The interaction of molecules with electromagnetic radiation leads to characteristic responses or outcomes based on the energy or frequency of the radiation. For example, the interaction of molecules with gamma and X-rays, which are high energy radiations, results in changes in nuclear configurations and electron transitions between an inner and a higher energy shell. Spectroscopic techniques requiring such high energies include Auger electron spectroscopy and X-ray photoelectron spectroscopy. The result of electron transitions caused by the interaction of molecules with UV-vis radiations forms the basis UV-vis absorption spectroscopy. Unlike the X-ray and UV radiations, infrared and microwave radiations are of lower energies than the electronic energies of atoms or molecules. As such, infrared radiations are capable of inducing ground state molecular vibrations while microwaves can cause rotational motions in molecules. Radio waves, which are capable of inducing spin transitions in appropriate nuclei, form the basis of nuclear magnetic resonance spectroscopic techniques. It should be noted that molecular interactions with higher energy radiations could result in effects that are associated with lower energy radiation. For example, electronic transitions in molecules caused by UV absorption are accompanied by both vibrational and rotational motions (important in the gas phase) and infrared irradiation can produce rotational motions in the gas phase in addition to ground state molecular vibrations. The different regions of the electromagnetic radiation, as outlined above, thus provide different chemical information on substances: X-ray for crystal structure among others, UV-vis for electronic transitions in chromophores, infrared for bond vibrations and functional groups, and radio waves for molecular structure of molecules containing appropriate nuclei.

As mentioned earlier, isotropic UV-vis and fluorescence spectroscopy, which are the main non-chiroptical techniques employed by our research group for chiral analysis, usually employ radiation sources ranging from 190-800 nm. In certain instruments, however, the wavelength region is extended into part of the NIR region. For example the UV-vis instrument used (Agilent 8453 photo diode-array spectrophotometer) for our studies has a radiation source that ranges from 190 to 1100 nm Irradiation of molecules with UV-vis light, as mentioned above, results in electronic transitions from the ground state to higher energy states known as excited states. Because electronic energy levels in molecules are quantized, the energy of the radiation must be equal to the difference in energy between the higher electronic energy state and the ground state electronic energy for electronic transitions to occur. These transitions usually occur from the highest occupied molecular orbital (HOMO) to the lowest unoccupied molecular orbital (LUMO). Generally, molecules are made up of three types of molecular orbitals– the sigma, pi and nonbonding molecular orbitals. The sigma and pi orbitals have associated unoccupied higher-energy molecular orbitals (anti-bonding orbitals) with specific energies. In organometallic compounds, another type of molecular orbital, the d-orbital, may be present; these molecular orbitals have ground and higher energy states similar to sigma and pi molecular orbitals. In most molecules, sigma orbitals are the lowest-energy occupied molecular orbitals with pi molecular orbitals at a higher energy level and the nonbonding orbitals at still a higher energy level. Figure 1.9 shows in a simplified form the relative energy levels of molecular orbitals and the possible electronic transitions that can occur due to absorption of UV-vis light. The figure shows that the transition energy, for example, between the nonbonding orbital, n, and the anti-bonding pi orbital, π, is

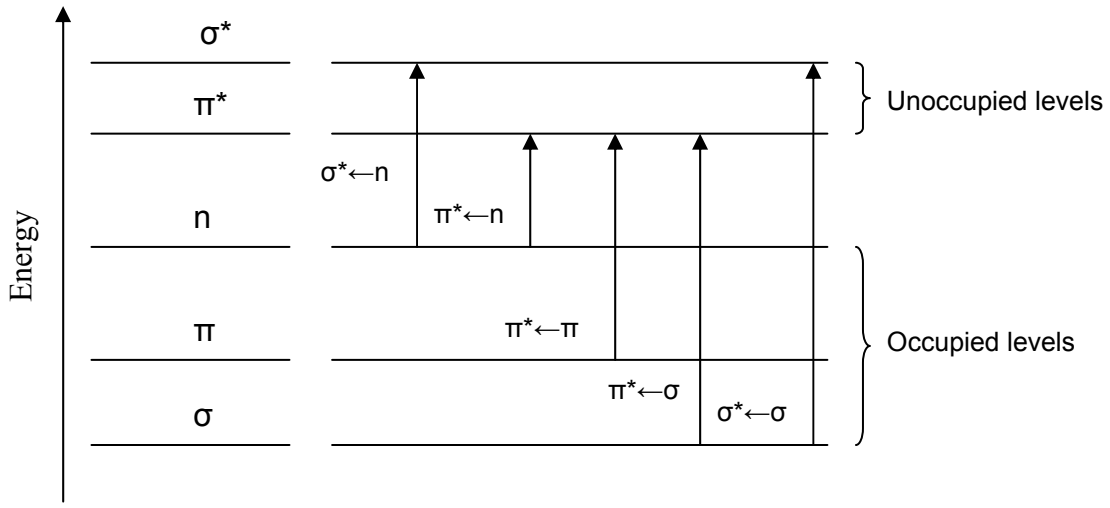

Figure 1.9. Molecular orbital energy levels and possible electronic transitions

lower than that between the pi bonding orbital and the anti-bonding pi orbital, π*.

It is, however, known that not all transitions that might appear feasible actually occur. For example, the π*←n transition is symmetry forbidden. While forbidden transition signals may not be observed for some molecules, they tend to show up with reduced intensity for others. With the quantization of electronic energy, it will be expected that signals for UV absorption should appear as sharp lines or narrow bands. None of these is observed in practice because molecules, unlike atoms, have vibrational as well as rotational (important only in the gas phase) motions, which are not frozen even at absolute zero but perturbed by the absorbed UV-vis radiation. Thus, the molecule is promoted from its ground state vibrational and rotational energy levels to the excited vibrational and rotational levels associated with the excited electronic state. Unlike electronic states, the energy differences between vibrational or rotational states in molecules are small. In addition, several of them are present for a given electronic state. Consequently, continuous UV-vis radiation passing through a sample of molecules is absorbed over a broad wavelength range and the ensuing signal appears as a broad band.

The UV absorption spectrum, thus, is an electron-vibronic spectrum. The association of vibrational excitation with electronic excitation allows the UV-vis absorption spectrum of a molecule to contain some information about the structure of the molecule. This is important for our chiral analysis, which involves the transformation of enantiomeric pairs into either covalent or non-covalent diastereomeric pairs. This is because, while the electron transition energies of the diastereomeric pairs may not differ significantly from each other, vibrational transitions should differ because of a lack of isometry in their structures. It is, thus, possible for us to probe the difference between diastereomerized enantiomers using isotropic UV-vis spectroscopy.

The electrons responsible for UV-vis absorption are part of bonds formed by a group of atoms. As such, the properties of the electrons are influenced by the nuclei of the atoms forming those bonds. The entire system of atoms and bonds responsible for a given transition in the UV-vis region is referred to as a chromophore. Table 1.1 shows typical chromophores found in organic molecules, their associated electronic transitions, wavelengths of maximum absorption (λ_{max}), and molar absorptivities (ε) [39]. The absorption bands of chromophores are affected by conjugation– a system of bonds in which at least a pair of double bonds alternated by a single bond. Conjugation leads to delocalization of electrons, which tends to lower the energy of transition and increase the density of electrons involved in the absorption. These changes result in absorption at longer wavelengths and/or increase in absorbance. Absorption to a longer wavelength is referred to as a bathochromic shift or red shift and an increase in absorption is termed a hyperchromic effect. In addition to conjugation, the absorption band of original chromophores can be modified by electron donating or withdrawing groups, which are

Table 1.1. Transitions of typical chromophores

Chromophore	Example of organic molecule	Solvent	Electronic transition	λ_{max} (nm)	ε_{max} (m^2 mol^{-1})
-C=C-	Pentene	Hexane	$\pi^* \leftarrow \pi$	190	1000
-C=O	Propanone	Hexane	$\pi^* \leftarrow \pi$	188	90
			$\pi^* \leftarrow n$	279	1.5
C_6H_6	Benzene	Hexane	$\pi^* \leftarrow \pi$	184	6000
				203	740
				255	20
-C=C-C=C-	Buta-1,3-diene	Hexane	$\pi^* \leftarrow \pi$	217	2100
-N=O	Nitromethane	Hexane	$\pi^* \leftarrow n$	278	1.7

collectively referred to as auxochromes. Electron donating auxochromes produce bathochromic and/or hyperchromic effects, while electron withdrawing auxochromes cause shift in absorption to shorter wavelengths and/or a decrease in absorbance. A shift in absorption to a shorter wavelength is known as a blue shift or hypsochromic effect and a decrease in absorbance is referred to as a hypochromic effect. Furthermore, solvents may produce significant changes including band broadening in the absorption bands of chromophores. Generally, polar solvents tend to be more effective in modifying absorption bands of chromophores than non-polar solvents. In addition to the effect of solvent molecules on chromophores, the presence of other chemical species, which can form hydrogen and ionic bonds or undergo intermolecular interactions, including dipole moment interactions with chromophores, can significantly modify the absorption bands of chromophores. Usually, the effect of auxochromes, solvent molecules, and other solutes in solutions are particularly significant if these species are directly associated with the chromophore system of the absorbing molecule. The further these species are from

the chromophore, the weaker their effect on the absorption band of the absorbing molecule. The effect of auxochromes and solutes in solutions of chromophores play vital roles in our isotropic spectroscopic methods of chiral analysis. This is because the diastereomeric effect induce in enantiomers through either covalent derivatization (employed is in this present research) or non-covalent association (e.g., inclusion or non-inclusion complex formation) are analytically useful only if the effect is reflected in the spectra. Consequently, our discrimination strategies are designed to induce changes in the chromophores of the chiral analytes and/or the chiral selectors.

As shown in Table 1.1, the extent of UV-vis light absorption and the wavelength region of absorption are characteristic of the chromophore involved. It is known that the amount of light absorbed scales directly with the number of the absorbing molecules. In addition, the amount of light absorbed by a sample is known to be independent of the intensity of the light. The first observation was verified by Wilhelm Beer (German astronomer; 1797-1850) and the second by Johanna Heinrich Lambert (German mathematician; 1728-1777). These two observations were put together to derive the Beer-Lambert Law, which is mathematically given by the equation:

$$A = \log_{10} \frac{I_0}{I} = \varepsilon c l \qquad 1.9$$

where A is the absorbance, I_0 and I are the incident and transmitted radiations respectively, ε the molar absorptivity coefficient in L mol^{-1} cm^{-1}, c the concentration in mol L^{-1}, and l the pathlength in cm. The ratio of the incident light to the transmitted light is equal to the inverse of the transmittance, T. Equation 1.9 above allows for the quantitative analysis of UV-vis active analytes. However, only certain electronic transitions associated with certain chromophores are accessible by ordinary UV-vis

instruments and useful for quantitative analysis. For example, σ*←σ transition can be induced in all organic molecules. These may occur either in the vacuum ultraviolet region (~ 170-10 nm) or close to the lower wavelength region of the far UV range (180-200 nm). Signals in the vacuum ultraviolet region require special instrumentation while those occurring in the far UV region, 180-200 nm, are usually not useful because they are interfered with by solvent absorption and are not particularly sensitive.

Modern regular or isotropic UV-vis spectroscopy instruments are quite simple. Figure 1.10 shows a schematic based on a modern Agilent 8453 isotropic UV-vis spectrophotometer used for spectra collection in the present research. Usually, the isotropic UV-vis light in a modern UV-vis instrument such as the Agilent spectrophotometer is generated using a deuterium and tungsten lamp. Light from these two sources are collimated using a collimating lens through a shutter system consisting of an optical on/of switch and a filter. The filter is used to reduce stray light in the UV range. The isotropic UV-vis light passes through the sample, which can be contained, depending on the need, in a quartz or ordinary glass cuvette. The transmitted light is collimated through a slit into a high resolution polychromator, which disperses the transmitted light onto a 1024-element diode-array detector made up of silicon photodiodes. Charge deposited on reversed-biased photodiodes is discharged when the dispersed transmitted light falls on the photodiode. The amount of current required to recharge a given photodiode is proportional to the intensity of transmitted light of a particular wavelength that impinged on the photodiode in question, since the photodiode

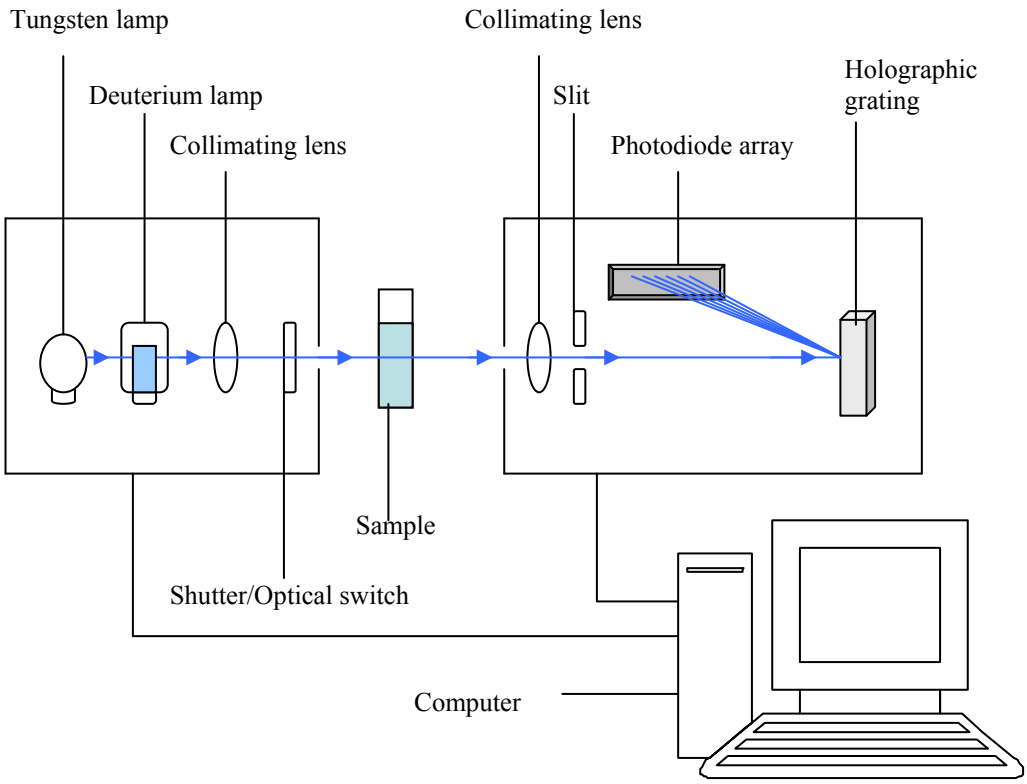

Figure 1.10. Schematic of the Agilent 8453, UV-vis, photodiode array spectrophotometer

was last interrogated. The optical configuration of the Agilent instrument is a single-beam configuration. Some spectrophotometers are based on a double-beam configuration in which the source light is split into a reference beam and a sample beam. The array of photodiodes used as a detector in the Agilent spectrophotometer can record absorbances over a range of wavelengths simultaneously. In addition, recording absorbance does not require scanning, hence no moving parts. As such, the spectrophotometer does not suffer from instrument variation errors associated with the use of moving parts in instruments. Elimination of such sources of error is important for our analysis because differences between the isotropic spectra of the diastereomers formed by our discrimination strategies are usually small.

As mentioned earlier, our techniques for chiral analysis techniques involve the use of isotropic fluorescence spectroscopy in addition to isotropic UV-vis spectroscopy. Fluorescence spectroscopy is similar to UV-vis absorption spectroscopy because it requires the same chromophores as UV-vis spectroscopy. Fluorescence emission is a consequence of absorption of UV light of usually higher intensity than used for UV spectroscopy. Figure 1.11 shows the light absorption and electron transition processes, which give rise to the fluorescence and other photoluminescence processes. This energy level diagram is referred to as a Jablonski diagram. As shown in the diagram, a molecule in its ground state (S_0), usually the singlet state, can be promoted to any of the excited singlet states (S_1or S_2) with the molecule being able to occupy any of the vibrational levels of the excited states. Molecules in an excited vibrational state can undergo vibrational relaxation from higher vibrational levels due to molecular collision to the lowest vibrational level of the first excited state, S_1. The extra vibrational energy is lost in the form of heat, which leads to a minuscule increase in temperature of the substance. Vibrational relaxation is an effective process and occurs within a shorter time (~ 10^{-12} s or less) than the average lifetime of an excited electronic state [39]. De-excitation from the lowest vibrational level of the first excited singlet state to any of the vibrational levels of the ground singlet state results in emission of light of a longer wavelength than the absorbed wavelength. This emission process, which occurs on a timescale of about 10^{-8} s is referred to as fluorescence emission. Molecules may also undergo intersystem crossing where the molecule may change from the singlet state to the triplet state (unpaired or parallel spin). De-excitation from the triplet excited state to the ground state leads to phosphorescence emission (10^{-4}-10 s or more). Other non-radiative processes

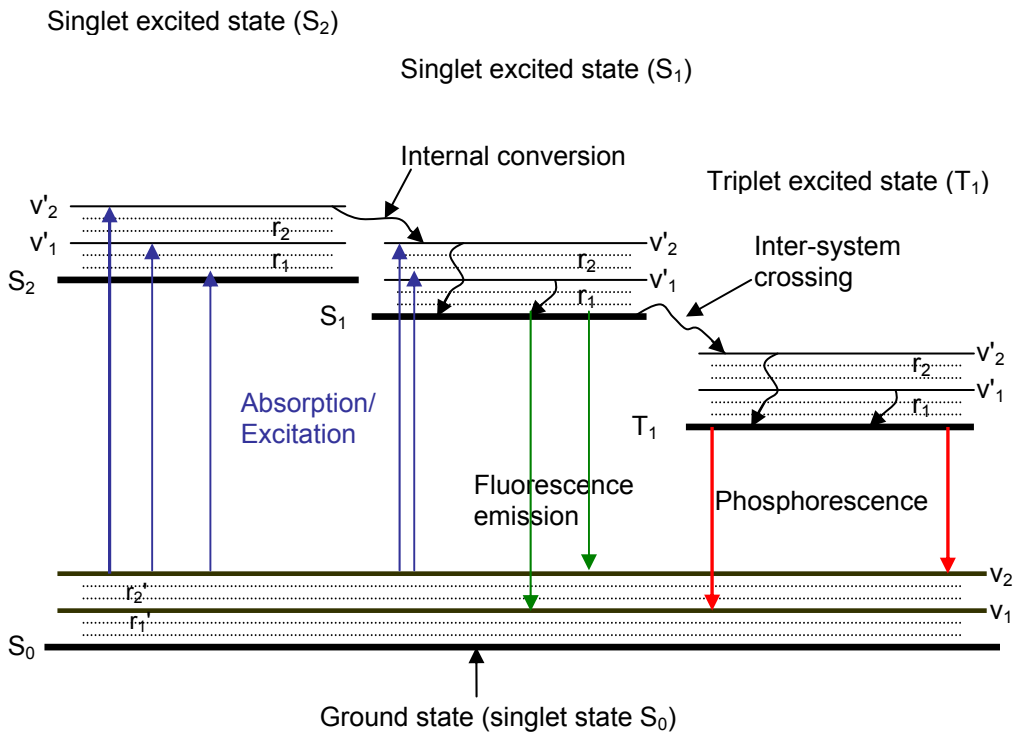

Figure 1.11. Jablonski diagram showing photoluminescence processes following light absorption. v : Vibrational level. r: Rotational level

including internal and external conversion can take place during molecular excitation. Fluorescence emission is affected by the same factors mentioned above, which affect the absorption spectra of chromophores. In addition, molecular rigidity, solvent molecules, and the presence of bulky molecules in solution can result in fluorescence quenching (reduction in fluorescence intensity).

The use of fluorescence spectral data for quantitative analysis is based on a linear equation derived from Beer's Law. The equation is given by the expression:

$$F = 2.3K'P_0\varepsilon cl \qquad 1.10$$

where F is the fluorescence intensity, K' is the a constant dependent on the quantum efficiency of the fluorescence process, P_0 is the incident beam power, ε is the molar

absorptivity in L mol^{-1} cm^{-1} of the fluorescing molecule, and *c* and *l* are the concentration (mol L^{-1}) and pathlength (cm) of the sample respectively. Equation 1.10 is derived based on the condition or requirement that the absorbance of the analytical solution is weak. As such, fluorescence spectroscopy is more sensitive than UV-vis spectroscopy. This is useful because it allows, for example, the analysis of chiral samples at much lower concentrations than possible with most chiroptical techniques including polarimetry. Similar to UV-vis instrumentation, spectrofluorometers or fluorometers are quite simple. They require a UV light source for excitation, an excitation monochromator or filter, an emission monochromator or filter, and a sample and reference photomultiplier for detection.

Figure 1.12 shows the schematic for the spectrofluorometer (FluoroMax-2, Jobin Yvon SPEX Instrument, S.A Inc.) used in the present research for the collection of fluorescence emission spectral data. The schematic in Figure 1.12 generally applies to most spectrofluorometers. Unlike UV-vis spectrophotometers, the fluorescence emission signal is collected at right angles to the excitation beam. Fluorescence emission signals, similar to UV-vis signals contain some amount of information on the structure of the fluorescing molecules. This is because, the fluorescence emission signal, as mentioned and shown in the Jablonski diagram above, is related to the vibrational states of the fluorescing molecule. Isotropic fluorescence spectroscopy, thus, can be used to probe spectral differences between diastereomers formed from enantiomers for the purpose of enantiomeric composition analysis.

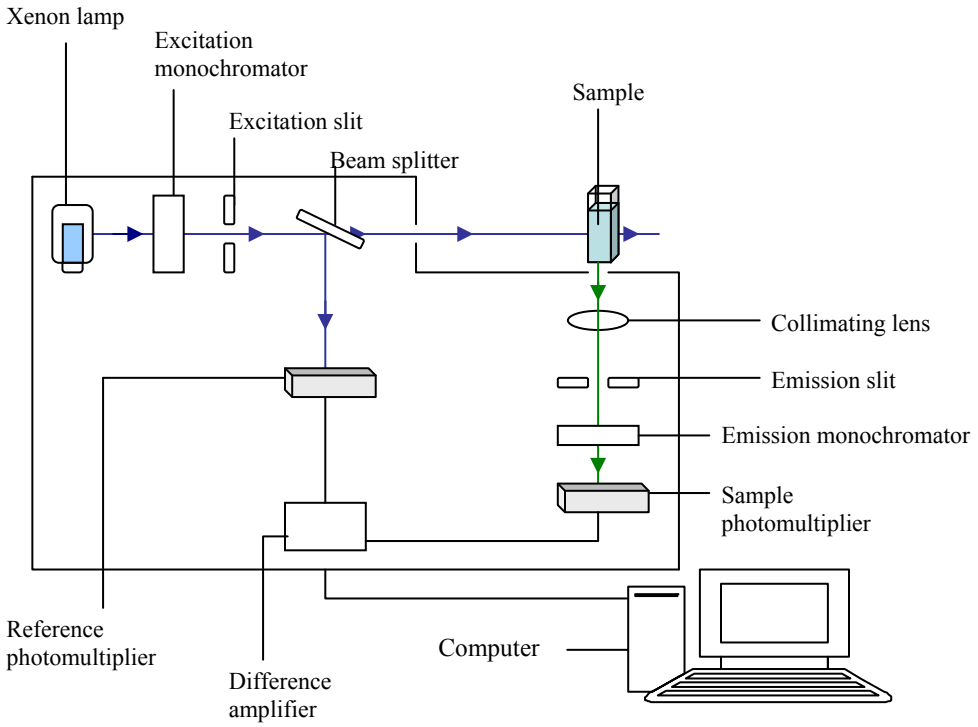

Figure 1.12. Schematic of the FluoroMax-2, Jobin Yvon SPEX Instrument, S.A Inc.

Spectral Data Analysis

Generally, spectral data may be analyzed for either qualitative or quantitative purposes. Qualitative analysis of data may be for the purpose of identification, differentiation, following a reaction, and characterization while the basic purpose for analyzing data quantitatively is to determine how much of a given component is available in a sample of interest. While the analytical chemist may be interested and involved in analyzing data for both qualitative and quantitative reasons, the organic chemist and researchers in biological chemistry may be mostly concerned with analyzing data for qualitative purposes. Whichever the case might be, there is one central reason for analyzing spectral data of samples: to obtain chemical information. This may be used for quality control, drug development, diagnosis, decision and policy making, and more. As

such, spectral data analysis is a vital aspect of any analytical science. To the analytical chemist, data analysis becomes almost unavoidable.

Usually, quantitative analysis of spectral data, which are collected for samples/matrices containing single analytes or for the purpose of determining a single analyte are, traditionally, performed using a univariate regression model. Such a model is based on a mathematical expression, which shows a linear relationship between an independent variable, *x,* and a dependent variable, *y*. Such a relationship can be expressed in a simplified form as:

$$y = a \pm bx \qquad 1.11$$

where *a* and *b* are coefficients representing the intercept (baseline offset/background in e.g., spectral data) and slope (related e.g., to absorptivity) of the curve showing the linear relationship between the independent variable *x* and the dependent variable *y*. For spectral data, the variable *x* may represent a spectral property, for example, absorbance or emission while *y* may represent, say, the concentration of the analyte. Because data will always consist of some level of error, *e*, usually random error, a linear model must take into account the error part of the data. A typical univariate linear model taking the error in the data into account will, thus, be of the form:

$$y = a \pm bx + e \qquad 1.13$$

For a univariate linear model to be useful for quantitative analysis, the spectral property measured must scale directly with the amount of the analyte. As such, spectroscopic analytical techniques that comply with the Beer-Lambert law or for which a linear relationship can be defined between a measured spectral property and amount/concentration of analyte, can be used for quantitative analysis. Because UV-vis

absorption and fluorescence emission intensity comply with the Beer-Lambert law or scale directly with concentration, most quantitative analytical techniques depend on the measurement of these two spectral properties for quantitative analysis.

For univariate determination of the unknown concentration of a UV-vis or fluorescence active analyte, the absorbances or fluorescence emission intensities of standard solutions of the pure form of the analyte are measured. The absorbance or emission is usually measured at the wavelength of maximum absorption or emission. In this case, care must be taken not to use concentrations that exceed the linear range of the Beer-Lambert law. A calibration curve of the standards is then prepared by plotting concentration (y-axis) as a function of absorbance or fluorescence emission (x-axis). The absorbance or fluorescence emission of the unknown, measured under the same conditions as the standards, is then traced horizontally from the absorbance axis (y-axis) of the calibration plot until it crosses the calibration curve. A straight vertical line is then drawn from where the horizontal line crosses the calibration curve to the concentration axis (x-axis). The value of the concentration at the point where the vertical line crosses the concentration axis is the concentration of the unknown. Otherwise the concentration of the unknown can be determined using the equation of the calibration line, which relates absorbance or emission to concentration through the intercept and slope of the calibration line. In cases where other components in a sample are suspected or observed to contribute to the absorption or emission of the analytes, the standard addition method is used to overcome errors that might result because of the matrix [40].

However, the situation regarding multicomponent analysis in the determination of enantiomeric compositions of chiral analytes is not as simple due to the following

reasons: (1) spectral differences among sample solutions made up of identical total concentrations but varying enantiomeric compositions are quite small, (2) the spectral differences do not necessarily occur uniformly at a single wavelength, and (3) information in one wavelength or a region of wavelengths may be complementary. In situations of this kind, the use of univariate regression modeling is hardly an option. Consequently, multivariate regression modeling tools are required.

Multivariate Regression Analysis in Chemistry

Multivariate regression analysis is traditionally a statistical tool used for data analysis in which a dependent variable depends on several independent variables. Its introduction into chemistry was basically for the purpose of acquiring maximum chemical information from chemical data. In the late 1960s and early 1970s, automated data collection and computation in chemistry were made relatively easier as a result of the technological advancement of that period [41]– the computer. One of the rippling effects of this is that it became possible to collect larger volumes of chemical data than before. This in turn, created a challenge for chemists, who were faced with analyzing larger volumes of chemical data than before. During this same era, improved mainframe computers with statistical software packages were becoming increasingly available. These factors, in addition to a change in attitude in the statistics and analytical chemistry communities, according to Brown [41], led to the development of a chemical sub-field now called chemometrics. Chemometrics is defined in several ways in the literature [41-43]. Each definition, however, clearly indicates that chemometrics involves the application of statistical and mathematical methods in chemistry. According to the International Chemometric Society (ICS), chemometrics is the science of relating

measurements made on a chemical system or process to the state of the system via application of mathematical or statistical methods [44]. Though chemometrics began as a sub-field of chemistry in the late 1960s and early 1970s, its practice dates as far back as 1908 [41]. Since the 1970s, chemometrics evolved as it should to include, currently, several areas of application such as experiment design, pattern recognition, and signal processing in chemistry and related fields.

Multivariate statistical tools employed in chemistry come in various forms. The most common of these tools used for chemical data analysis include multiple linear regression (MLR), principal component regression (PCR) and partial least squares regression (PLSR). Unlike univariate regression modeling where, for example, absorbance at a single wavelength is related to analyte concentration by a linear model of the form shown by equation 1.12, multivariate linear regression modules for spectral data analysis are formulated using more than one wavelength. The equation for a multivariate linear regression, taking error (e) in the data into consideration, will have a form that can be general written as:

$$y = a \pm \Sigma b_i x_i + e \qquad 1.13$$

where the dependent or response variable, y, (e.g., concentration) is related to a weighted linear combination of all the independent variables, x_i (e.g. absorbances at given wavelengths). The weighting, b_i, is the partial regression coefficient indicating the rate of change of the response variable, y, as a function of the predictor variable, x, at the ith level.

The MLR technique is designed to use a selection of variables (at least as many as there are chemical components) for the model based on the level of significance of the

variable. The level of significance of the variable is determined by the probability to enter and leave, that is, how statistically significant the regression term of the variable is [45]. Because of the large volume of data, models for multivariate regression analysis are computed as matrices and/or vectors. For example, in an MLR analysis, the predictor variable, *X*, (absorbance at different wavelengths) is a data matrix of the form *n x k* (*n* is the number of rows and *k* the number of columns) while the variable to be predicted or response variable, **y**, (e.g., enantiomeric composition) is an *n x 1* vector. The matrix equation showing the regression of **y** on **X** can be written in the form [21]:

$$\mathbf{y} = \mathbf{Xb} \qquad 1.14$$

where **b** is the regression vector, which can be determined by multiplying equation 1.14 by the transpose matrix, $\mathbf{X}^T$, as:

$$\mathbf{X}^T\mathbf{y} = \mathbf{X}^T\mathbf{Xb} \qquad 1.15$$

$$\mathbf{b} = (\mathbf{X}^T\mathbf{X})^{-1}\mathbf{X}^T\mathbf{y} \qquad 1.16$$

Thus, with the spectral and concentration data of a set of calibration samples, the actual vector, **b**, can be computed. This can then be used together with the **X**-spectral data of an unknown sample to predict the response variable vector, **y** (concentrations or enantiomeric compositions).

As noted earlier, the MLR technique uses a selection of variables for model computation. Though this approach has the advantage of making the model simple, the technique has several disadvantages [45]: (1) because of the use of selected variables, MLR is unable to account for unusual samples; (2) the benefit of multivariate signal averaging is significantly reduced; (3) the model is unable to account for colinearity,

resulting in poor predictability [46, 47]. Thus, the MLR technique is not usually used in the analysis of complex spectroscopic data.

PCR, similar to PLSR, is able to deal with colinearity in spectral data because it is based on the technique of using an orthogonal set of factors called principal components (PCs) to represent the variation present in a large set of data. The concept of principal components is can be illustrated using a set hypothetical data. Consider, for example, a set of hypothetical data for which three variables were measured. This data set, with a variable space of three can be projected as a swarm of data points on an XYZ coordinate system (three independent variables) as shown in Figure 1.13. The idea of the principal

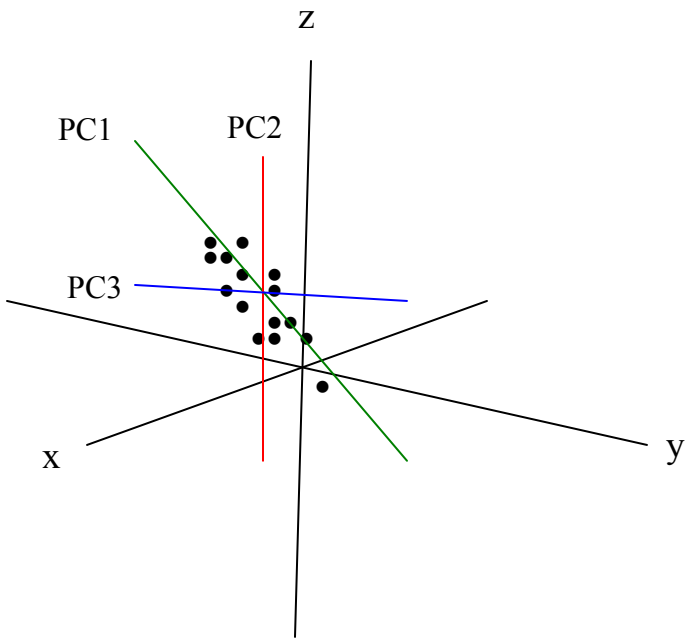

Figure 1.13. Hypothetical data swarm plotted on an XYZ coordinate system showing three PCs. The three principal components (PC1, PC2, and PC3) represent orthogonal spaces of maximum variation in the data.

component is synonymous with defining new orthogonal vectors within the data swarm to represent regions of variation in the data points. Thus, the first principal component, PC1, of the data swarm, as shown in Figure 1.13, is a line drawn through the swarm with the direction of the direction of the maximum variance. PC2, as shown in the figure, is a

vector orthogonal to PC1, which defines the maximum possible variation in the swarm orthogonal to the vector defined by PC1. Subsequent PCs are defined to capture the successively smaller variation in the data. Usually, the variation captured by the PCs decreases as the number of PCs increase. Thus, PC1 should capture most of the variation in the data followed by PC2 and so on. The PCs shown in Figure 1.13 have actually defined a new orthogonal coordinate system on which the data can be projected. As such, each data point has a new set of coordinates defined by the PCs. These new coordinates defined by the PCs are referred to as scores. Because the PCs, as shown in Figure 1.13 represent maximum variation in the data, they are variance-scaled eigenvectors [21]. Each PC can be defined in terms of the contributions of the original variables of the data to it. These contributions are referred to as loadings [22, 46] and the higher the loading, the more important the variable is to the PC in question. For a given data set, there is a maximum number of PCs to be computed, which is equal to the smaller of the number of variables or n-1 samples (n is total number of samples)[21, 45]. Up to this point, it can be deduced from the discussion on the computation of PC that two goals– elimination of colinearity and reduction in dimensionality of data– are achieved through principal component computation. Colinearity, which is correlation within measurements of the same variable, for example, x-variables (independent variables), is eliminated because the new coordinate system defined for the data points by the PCs are orthogonal (mathematically independent). The dimensionality of the data is reduced because the size of the data to be used for the PC based multivariate model is determined by the number of PCs, which cannot be more than the smaller of the number of variables or n-1 samples. Although as many as the smaller of the number variables or n-1 samples

of PCs can be computed, not all of them relate to the structured information in a given data set. This is because, ideally, as the number of PCs increases, the less the variance explained by successive PCs become less and more noise is incorporated in the model. A graphical illustration of this situation showing the plot of unexplained variance or explained variance as a function of the number of PCs may look like Figure 1.14A or B. The variance curves in Figure 1.14A and B show that the use of PC3 and PC4 may contribute noise to the model because compared to PC1 and PC2, they explain less of the variation in the data. These two PCs might therefore not be necessary and their removal from a model computed with the four PCs will result in further reduction of the variable space of the data. In addition, the elimination of such PCs should lead to a better model.

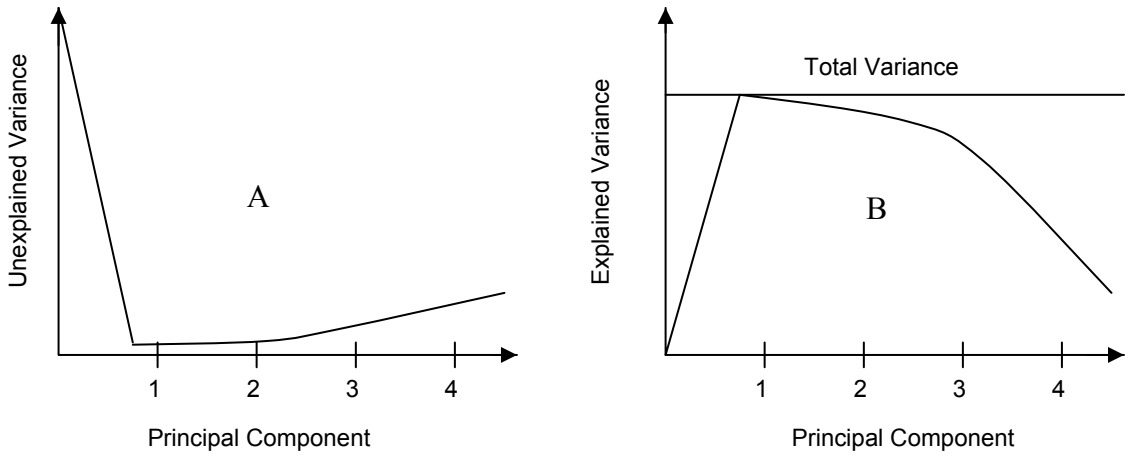

Figure 1.14. Ideal plots of variance in data as a function principal component. A: Unexplained variance increasing with increasing number of PCs. B: Explained variance decreasing as the number of PCs increase

For PCR analysis, the scores matrix denoted **T** is used in the matrix equation (**y** = **Xb** equation 1.14) shown for MLR technique. Thus, the matrix equation for the PCR model is of the form [21]:

$$\mathbf{y} = \mathbf{Tb} \qquad 1.17$$

Using data for a set of calibration samples where, for example, the concentrations of the samples are known, the regression coefficient vector, **b**, can be computed by multiplying equation 1.17 by the transpose, $\mathbf{T}^T$, of the scores matrix and solving for **b** as:

$$\mathbf{T}^T\mathbf{y} = \mathbf{T}^T\mathbf{T}\mathbf{b} \qquad 1.18$$

$$\mathbf{b} = (\mathbf{T}^T\mathbf{T})^{-1}\mathbf{T}^T\mathbf{y} \qquad 1.19$$

Though PCR analysis is capable of eliminating colinearity and reducing the dimensionality of a data set as explained above, it is limited because its application involves the use of only the data on the independent variable (**X**-data) for PC computation. This is problematic because the variation in the **X**-data, which was used to compute the scores matrix, **T**, for the prediction of the **y** (e.g., concentrations) vector, may not correlate entirely with **y**. In addition, it is possible that the variance in the **X**-data that is related to **y** is just a portion of the entire variation in the **X**-data [45]. Consequently, PCR may fail in finding relevant linear combinations of variables for modeling **y**. To overcome the limitation of PCR technique, the partial least squares regression (PLSR) technique is used.

The PLSR technique was developed and popularized in analytical science particularly by Wold [47]. With the PLSR algorithm, the limitation mentioned for the PCR technique is circumvented by using the covariance of the **X**-data (spectral data) with the **y**-data (e.g., concentrations) in conjunction with the **X**-data to compute the scores matrix for the model [45]. Once the PLSR scores matrix is obtained, the vector, **b**, can be found as shown above using the **y**-data of the calibration samples. This makes the PLSR technique particularly powerful for multivariate calibration and prediction of spectral data because: (1) as noted, it takes into account both the concentration (*y*) and the spectral

variables (x-variables), (2) it minimizes the dimensionality in data and focuses on variables that are relevant to the calibration model [45-48]. Two variants of the PLSR technique can be identified: PLS-1 (or PLS1) and PLS-2 (or PLS2). PLS-1 is used when only one type of dependent variable (y-variable) is to be determined while PLS-2 is used when more than one dependent variables is to be determined simultaneously. However, it is possible to use PLS-1 to determine each dependent variable individually in the case where more than one dependent variable is of interest. For detailed mathematical derivations and discussion on the subject of multivariate regression analysis, the reader is referred to more extensive materials [21, 45-48].

Generally, multivariate regression analysis of spectral data is performed in two phases: the calibration phase and the prediction phase. The goal in the calibration phase is to develop a model that relates two sets of data, **X** and **y**, where **X** is the matrix of the independent x-variables (spectral data), and **y** is a vector of the dependent y-variables (concentrations). This is schematically shown in Figure 1.15A. In the second phase (Figure 1.15B), which is the prediction phase, the model developed from the calibration data is used in conjunction with the measured independent x-variable data of the unknown to predict the dependent y-variables of the unknown.

Though highly sophisticated statistical packages are available for multivariate data analysis, these software packages are yet to be designed to automatically identify and model specific spectral band regions containing structured information only. Because structured information in spectra may be contained only in certain spectral band regions, calibration models will have to be optimized. While model optimization can be achieved using certain manual tools provided by the software, this could become a

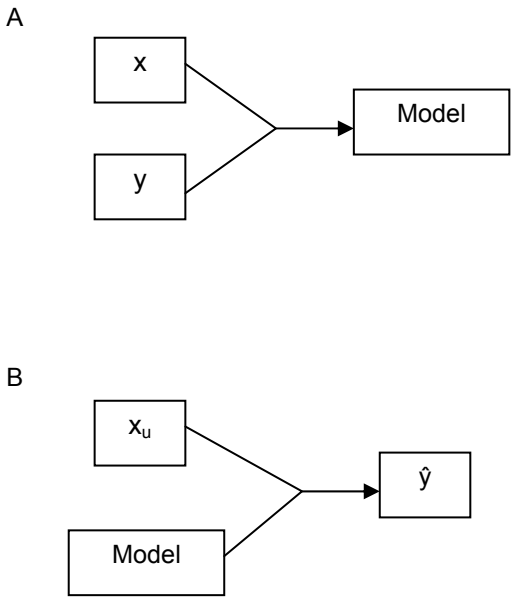

Figure 1.15. Schematic of the two major phases in multivariate regression analysis of spectral data. A: Calibration phase– model development using known x- and y-variables. B: Prediction phase– calibration model used in conjunction with measured x-variables (x_u) of unknown to predict unknown y-variables ($\hat{y}$).

laborious and time-consuming task. As such, spectral data could be subjected to simple data manipulation techniques such as spectral mean centering prior to modeling in order to visually identify spectral band regions, which show variation among samples. Spectral mean centering is performed by summing up the spectral responses measured, for example, absorbances or emission intensities wavelength by wavelength for all the samples. The sum of the spectral responses is then divided by the total number of samples to obtain the mean spectral response. This mean is then subtracted from the spectral response of each sample to obtain the mean centered spectrum of each sample. Spectral mean centering is particularly useful for prior selection of spectral band or wavelength regions to be used for modeling when differences in original spectra of samples can hardly be seen. The spectral mean centering approach for selecting spectral

band regions for modeling is employed in the analysis of spectral data in this research to facilitate model optimization.

Several commercially available multivariate statistical packages including MATLAB and the Unscrambler can be used to perform multivariate regression analysis of spectral data. The Unscrambler statistical package, which is designed by CAMO Software, AS, is employed for PLS-1 regression analysis of spectral data collected for the chiral analysis studies reported here. A typical Unscrambler PLS-1 regression model is associated with four plots: the scores plot, regression coefficient plot, residual variance or explained variance plot, and the predicted versus measured plot.

The Unscrambler scores plot is usually presented as a plot of the second PC (y-axis) versus the first PC (x-axis). The plot reveals relationships among samples and patterns in the sample. Samples close to each other in the plot indicate similarity, for example, in spectra captured by the two PCs. Thus, the further apart a pair of samples is the more different they are. In addition, the scores plot will reveal unusual samples or outliers and show groups in a set of samples. Furthermore, it shows the percentage of the variation explained by the first and second PCs. The software shows the scores plot in terms of the two PCs because these PCs usually capture substantially more of the variation in a given data set than any subsequent PCs. The Unscrambler usually shows below the scores plot the percentages of the variation in the x- and y-data explained by the first two PCs.

The regression coefficient (rc) plot is constructed as a plot of the regression coefficients of the independent or predictor variables as a function of wavelength. It summarizes the relationship between the predictor variable (spectral data) and the

response variable (concentration) for the number of PCs used in the model. The regression coefficient associated with a given predictor variable (x-variable) may have a positive or negative sign. Regression coefficient curves, thus, may be positive or negative or have both positive and negative values. A positive regression coefficient curve shows that the response variables (y-variables) change in the same direction as the predictor variables (x-variables). A negative rc curve, on the other hand, shows that the response variables change in an opposite direction to the predictor variable. An rc curve showing both positive and negative values indicates that the response variables show both forms of variation with the predictor variables. Regression coefficients can be presented as raw or weighted values. Raw rc values indicate nothing more than the relationship between the response and the predictor variables. Weighted regression coefficients, on the other hand, reveal the importance of the predictor variables.

The residual variance plot, which is constructed as a plot of the residual variances of the PCs used to develop the model versus the PCs, is a measure of the unexplained part of the information associated with a PC for a given set of data. For a given PC, the smaller the residual variance is, the smaller the unexplained part of the information captured by the PC is. Residual variance can be computed for the y- or x-variable. It can also be expressed as a percentage in which case it is referred to as explained residual variance. A given PC may have a small residual variance or a high explained residual variance but the information associated with the PC may not be important for the model. Thus, the residual variance plot or explained variance plot may show PCs with low residual variances or high explained residual variances but are not included in the model.

The Unscrambler regression plot is a plot of the predicted values for the response variable versus its measured or known values. This plot, which summarizes the results of the other plots, reveals three regression lines– the line for the linear model (ideal situation), the fitted calibration line, and the cross-validation line. The line for the model passes through the origin of the plot or has an offset of zero with a slope of 1. For data showing high or strong correlation between predictor and response variables, both the fitted calibration and cross-validation lines are hardly distinguishable from the regression line of the linear model. In addition to the regression lines or curves, the plot reveals plot statistics for the calibration and cross-validation curves or lines. The plot statistics consist of the slope, offset, correlation coefficient, root-mean-squares error of prediction or calibration, and standard error (standard deviation of residuals associated with PCs). The plot statistics of calibration curves or lines usually approximate those of the model but do not always reflect the actual correlation between predictor and response variables because they are fitted. The extent of correlation between predictor and response variables are better verified by cross-validating the samples used in developing a calibration model. To cross-validate a set of samples, a calibration model is developed using all but one of the samples. The left-out sample is then predicted with the developed calibration model. The process is repeated on all the other samples in the set. A plot of the predicted versus actual or known values of the samples constitutes a cross-validation regression line or curve. Usually, cross-validation regression lines having slopes and correlation coefficients higher than 0.98 and root-mean-square errors of prediction of not more than 0.05 result in quite good predictions of similar future samples, giving root-mean-square errors of prediction not more than 0.05.

As explained earlier, regression models may require optimization to make them representative and improve their predictive ability. PLS-1 regression models developed using spectral data collected for samples in this research were optimized prior to sample prediction by: (1) spectra mean centering used for the selection of spectra band regions revealing spectral variation among samples as noted and (2) cross-validation of calibration samples used in developing models. Based on this, cross-validated PLS-1 models, whose slopes and correlation coefficients were greater than 0.98, and root-mean-squares errors of prediction less than 5 % were used for sample prediction. The enantiomeric compositions of the calibration samples used to develop the PLS-1 regression calibration models were entirely different from those of the samples predicted. The root-mean-squares error (RMSE) mentioned above is a frequently-used measure of the difference between the value of a quantity or parameter predicted by a model or an estimator and the actual or known value of the quantity or parameter predicted or estimated. It is a measure of accuracy and therefore employed as a figure of merit for evaluation or comparison. The RMSE is expressed in the same units as the quantity being predicted or estimated. The acceptable limit of this error depends on the discipline and the quantity or parameter being studied. Generally, however, the smaller the value of the RMSE is, the higher the accuracy of the results. In many applications, including principal component analysis and partial least squares regression, where it is not always easy to analyze the degrees of freedom [45, 47], RMSE is computed using the expression:

$$RMSE = \sqrt{\sum_{i=1}^{n} (y_i - \hat{y}_i)^2 / n} \qquad 1.20$$

where y and $\hat{y}$, respectively, are the actual or known and predicted values of the ith sample and n is the number of samples modeled. Because RMSE is a measure of

accuracy and used for evaluation or comparison, it is used in enantiomeric composition analysis to evaluate or compare techniques or various chiral selectors employed in the same analytical technique.

Previous Studies

As a result of the need for improved strategies for the assessment of enantiomeric purity, for example, for catalyst evaluation in asymmetric synthesis, to meet standards or requirements set by governmental agencies for pharmaceutical industry, and to meet the need of large combinatorial libraries required in drug development, the demand for rapid, reliable, and robust analytical methods for chiral analysis is on the increase. In this regard, spectroscopic methods, according to Finn [28], are most suitable. Recently, our research group (The Busch Group, Center for Analytical Spectroscopy, Baylor University) developed a nontraditional strategy for the determining enantiomeric composition of chiral analytes. The strategy is based on: (1) the use of isotropic spectroscopic techniques (e.g., ordinary UV or fluorescence spectroscopy), (2) the induction of diastereomeric behavior in enantiomers, and (3) multivariate regression modeling of spectral data. This strategy, irrespective of the means for diastereomeric property induction and the isotropic spectroscopic technique employed, is referred to as chiral analysis by regression modeling of spectral data abbreviated CARMSD. In its initial stages, CARMSD studies were performed using isotropic NIR spectroscopy with native cyclodextrins as chiral auxiliaries for inducing diastereomeric spectral properties in enantiomers [21]. The results of the studies were rather disappointing due to several reasons, including solubility limitations of native cyclodextrins in water, which are noted in an account on these studies [21]. However, the poor results of the NIR studies led to

the use of ordinary UV-vis spectroscopy in combination with the native cyclodextrins, which turned out to be successful. The chiral auxiliary agent, cyclodextrins (CDs), employed in these studies are truncated-cone or barrel-shaped macrocyclic homochiral sugar molecules that function as ideal inclusion complexing agents for solubilising lipophilic guest analytes in aqueous media [4, 21, 49-54]. In the CARMSD studies, CDs are used to discriminate enantiomeric pairs through the formation of transient, non-covalent inclusion complexes. This interaction transforms appropriate enantiomeric pairs into transient diastereomeric pairs with different spectral properties. The initial studies using UV-vis spectroscopy showed that the spectra of sample solutions of different enantiomeric compositions of an appropriate chiral analyte dissolved in a stock solution of cyclodextrin of a given concentration, varied with the enantiomeric compositions. On the basis of this, it was possible to design multivariate regression models from the spectral data of calibration samples. These models were used to successfully predict the enantiomeric composition of independently prepared validation samples [21]. The studies since then have progressed passed the use of native cyclodextrins to include modified cyclodextrins, surfactants, and simple sugars [11, 21, 55]. In addition, CARMSD studies have been extended to include fluorescence spectroscopy. The use of fluorescence spectroscopy has significantly increased the sensitivity of the technique. This allows appropriate samples to be analyzed at significantly lower concentration levels [55]. To date different classes of chiral analytes including amino acids and several pharmaceuticals have been successfully analyzed using the CARMSD technique [56-61]. Presently, the CARMSD technique is used by others [62, 63]. As a matter of fact, the level of accuracy achieved using the CSRMSD technique is comparable to most

traditional techniques employed for enantiomeric composition analysis. Compared to existing chromatographic and NMR chiral techniques, CARMSD is simpler, faster, and significantly more cost effective. As such, the CARMSD technique has a great potential for routine and high throughput application than existing chromatographic and NMR techniques. Automation of the CARMSD technique will greatly enhance its industrial application.

Rationale and Scope of Present Research

Just as the demand for improved strategies for assessing enantiomeric purity has been on the rise in recent times, so has our research group continued in its efforts to improve and broaden the application of the CARMSD technique for enantiomeric composition analysis. We deduced over the years from our CARMSD studies that the extent of discrimination of pairs of enantiomers, through the formation of diastereomers, is vital for the effectiveness of the CARMSD technique. This is because the difference in the isotropic spectra, for example, of a pair of enantiomers complexed with cyclodextrin, depends on how different the complexes are. We have noticed that generally, the more significant the difference between the spectra of the discriminated pair of enantiomers is, the better the model and predictions made using the model. Based on this, we used a different approach to discriminate enantiomeric pairs in the present research with the aim of enhancing the difference between enantiomeric pairs. The different approach employed in the present research involves converting enantiomeric pairs to covalently formed diastereomers. As different covalent compounds, the chemical and physical properties (including spectral properties) of the diastereomers are expected to be significantly different. This should result in optimum differences in spectral property

because, in principle, the two diastereomers represents two distinct stereoisomers. As such, the covalent discrimination approach should lead to a better model and prediction result. In addition to the covalent derivatization, a novel approach involving subjecting samples of the covalent diastereomers to isotropic spectral analysis without prior separation of the diastereomers from the reaction medium is employed. This is unlike the chromatographic or electrophoretic techniques involving covalently derivatized enantiomers, which require separation prior to detection. Analysis of the isotropic spectral data containing spectral information on both the covalent diastereomers and the rest of the reaction medium should not adversely affect the effectiveness of the method. This is because partial least squares regression, which is employed for the spectral data analysis, is capable of extracting structured information in data sets such as this that might contain interference and redundant information. The present strategy of covalently derivatizing enantiomers and recording the spectral data of the entire reaction medium containing the diastereomers (not separated) is termed a non-separative, covalent, chiral discrimination strategy (NSCCDS).

We also postulated on the basis of our previous results that for non-covalent approaches of inducing diastereomeric behavior in enantiomers, stereocenter-containing chiral selectors that can give rise to interactions at chiral centers or within a bond length of chiral centers with chiral analytes, should enhance enantiomeric discrimination. This is because such interactions are more likely to reflect the stereochemical differences between a pair of enantiomers than interactions at points remote from chiral centers. In addition, in non-covalent chiral discrimination, both the chances and effectiveness of chiral selector-chiral analyte interaction can be enhanced with the use of a chiral selector

that has different functional groups, for example, hydroxyl, amino, and phenyl functional groups. Furthermore, it is possible that such a multifunctional chiral selector would be able to discriminate different classes of chiral molecules. The present research was thus designed to investigate these new approaches of enhancing chiral discrimination for the determination of enantiomeric composition by regression modeling of spectral data.

The second chapter of this dissertation describes the application of the covalent discrimination approach using (*S*)-(+)-1,2-propanediol as the chiral selector for covalent derivatization. In this covalent derivatization, (*S*)-(+)-1,2-propanediol was reacted with selected amino acids using the Fischer esterification reaction. In a similar study, proton and C-13 NMR spectra recorded for the recrystallized product of the reaction of 2-butanol with an amino acid, phenylalanine, showed that the Fischer esterification reaction adapted for our analysis leads to ester formation. Results for the NMR studies are discussed in Chapter 4. For the analyses in Chapter 2, separate stock solutions of the covalently derivatized enantiomeric pairs were prepared. For each enantiomer, the entire reaction medium was used to prepare the stock solution. Samples for analysis were then prepared by mixing different compositions of the separate stock solutions. The third chapter covers a study on a capillary tube (internal diameter of 1 mm) custom-designed for use as a micro flurometer cell. The performance of the capillary cell, which requires only 25 μL of sample solution for fluorescence emission measurement, is compared with that of a commercial fluorometer cell. The cell was designed and investigated because of the need for microanalytical techniques for routine and high throughput applications in chiral analysis. Chapter 4 describes another study on the application of the covalent discrimination approach using the racemic mixture of 2-butanol as the covalent

derivatization agent instead of (*S*)-(+)-1,2-propanediol. In addition, the chapter discusses the results of an NMR study that showed that the Fischer esterification approach employed by us for covalent derivatization of amino acids, leads to ester formation. Furthermore, analysis using β-cyclodextrin as a chiral selector is compared to the covalent approach. The result of the investigation of modeling $\log_{10}$-converted spectral data is also described in Chapter 4. The final analysis described in Chapter 4 is on a real-life application of the covalent approach. In this real-life application, different compositions of the enantiomers of phenylalanine were weighed into different vials and mixed together to simulate samples for real-life analysis. Identical amounts of the racemic mixture of 2-butanol acidified with HCl were then added to each sample and heated together. The samples were allowed to cool, quantitatively transferred into identical but separate volumetric flasks, and diluted to the mark. The spectra of the samples were then collected and subjected to PLS-1 regression analysis. Chapter 5 covers a study carried out using a multifunctional chiral selector, (*S*)-(-)-1-phenylethylamine, whose point of interaction with appropriate chiral analytes is a bond length from its chiral center. The use of (*S*)-(-)-1-phenylethylamine was to verify our postulate that chiral discriminations based on non-covalent interactions can be enhanced with the use of a multifunctional chiral selector, whose point of interaction with the chiral analyte is at the chiral center or a bond length from the chiral center.

CHAPTER TWO

Non-Separative, Covalent, Chiral Discrimination Strategy

Introduction

Over the years, our research group, as noted in chapter one, focused on developing improved strategies involving chiral selectors that depend on non-covalent interactions for enantiomeric excess (ee) or enantiomeric composition (ec) analysis. This is basically because available techniques requiring the formation of covalent derivatives of enantiomers for ee or ec analysis are usually time-consuming, cumbersome, and expensive [4, 21, 28, 56]. These covalent derivatization techniques, however, yield quite accurate results. This is because, fundamentally, they involve analyzing covalently formed diastereomeric pairs, which have different chemical and physical properties. By virtue of being diastereomers, these pairs of compounds have no mirror image optical properties unlike their corresponding enantiomeric pairs.

Although several strategies or techniques are available for ee or ec analysis, there is still room for improved strategies to cater for the growing demands in the field of chiral analysis as mentioned in the previous chapter. Our research group has been working consistently over the years to contribute to meeting this growing demand for new analytical strategies for chiral analysis. Recently, we developed a new chiral discrimination strategy for application in chiral analysis by regression modeling of spectral data (CARMSD). With the new strategy, as noted in Chapter 1, covalently derivatized enantiomers are analyzed without being separated from the reaction medium

prior to the instrumental analysis. The new approach is thus referred to as non-separative, covalent, chiral discrimination strategy (NSCCDS). This strategy combines the sensitivity and broad-base application covalent derivatization of enantiomers for chiral analysis with the robust, fast, simple, and inexpensive attributes of our existing strategies [11, 21, 55, 56]. Specifically, the new approach involves reacting covalently, a chiral selector with an appropriate chiral analyte in the presence necessary reagents under the required reaction conditions in a suitable vessel. The entire reaction medium including the derivatized chiral analyte is then diluted using a suitable solvent to an appropriate concentration for spectral analysis. For calibration purposes, for example, in enantiomeric composition determination, different compositions of the enantiomers of the chiral compound to be analyzed will be required. Equal amounts of reagent solution containing the chiral selector will then be added to the different compositions of the enantiomers and reacted under the appropriate conditions. At the end of the reaction, the reaction media containing the derivatized enantiomers are quantitatively transferred into separate volumetric flasks of identical volume and diluted to the marks using a suitable solvent. Spectral data of these samples are then collected to develop a calibration model. The calibration model is then used in conjunction with the spectral data of unknowns prepared under the same conditions as the calibration samples to determine the enantiomeric compositions of the unknowns. This strategy can be combined with any spectroscopic technique suitable for quantitative analysis. UV-vis and fluorescence spectroscopy can be employed for analyses involving UV active chiral analytes or chiral selectors. For non-UV active chiral analytes or chiral selectors, IR or Raman techniques can be used. This technique is expected to result in optimum discrimination of

enantiomers because the enantiomers are subjected to competition, which will be influence by kinetic and/or thermodynamic factors in favor of one of the enantiomers. This is because pairs of enantiomers are known to react differently with other chiral compounds. Differences in spectra from sample to sample will be due to the derivatized enantiomers in the sample matrix since all samples will contain identical amounts of reagents to begin with. As such, the compositions of enantiomers can be determined without separating the derivatized enantiomers. In addition, the use of PLS-1 regression analysis will allow spectral information related to the enantiomers to be modeled by virtue of principal component computation. The elimination of separation or isolation processes in our new discrimination strategy distinguishes it from the existing chromatographic, electrophoretic, and NMR techniques employed in analyses such as this [4, 21]. In addition, the new strategy is different from chiroptical techniques because it does not require the use of polarized light. Generally, the new strategy should lend itself to any covalent reaction that can take place between a given chiral selector and a given pair of enantiomers. Our interest, however, is in simple, one-step, chemical reactions requiring simple experimental conditions as well as apparatus. Most covalent reactions can be carried out in this manner. As such, the technique should have a broad-base application.

This chapter describes the enantiomeric composition analyses of phenylalanine, tyrosine, and two pharmaceutical compounds, Atenolol and Norephedrine, using our new strategy, NSCCDS. In these analyses, (*S*)-(+)-1,2-propanediol (PD), which is a dialcohol, was used as the chiral selector for covalent derivatization of the enantiomers of the above chiral analytes. In order to verify the basis of the strategy, that is, covalent derivatization

of a pair of enantiomers will result in differences in the isotropic spectra of the enantiomers, the enantiomeric pairs of the above-mentioned chiral compounds were derivatized separately using (*S*)-(+)-1,2-propanediol (PD). Separate stock solutions of the derivatized enantiomers were then prepared for each pair of enantiomers of a given chiral compound. The stock solution of each derivatized enantiomer was prepared without separating the derivatized enantiomer from the reaction medium, that is, the entire reaction medium containing the derivatized eanatiomer was diluted to prepare the stock solution. The spectra of the stock solutions of the enantiomeric pair of each of the chiral compounds were than recorded for evidence of the discrimination. To demonstrate that enantiomeric compositions of the chiral analytes can be assessed as noted for the strategy, that is, without separating the derivatized enantiomers from the reaction medium, different compositions of the stock solutions were mixed. The spectra of these solutions containing different amounts of the derivatized enantiomers and other components that might be present in the reaction medium were then collected. The spectral data obtained were subjected to PLS-1 regression analysis for enantiomeric composition determination. It is recognized that these analyses differ from real-life analyses even though tailored on the basis of our new strategy and thus identical in principle. In a real-life situation, the strategy is expected to be used in analyzing a pair of enantiomers occurring together as one sample and not separate entities combined on purpose. As such, application of the strategy for a real-life analysis situation was investigated in a different study. This is described in a later chapter (Chapter 4). Though these analyses, which are discussed later in this chapter, were performed differently from what is expected in a real-life situation, their design served a number of purposes: (1) to show that covalent derivatization results

in differences in spectra of enantiomeric pairs and (2) to demonstrate that enantiomeric compositions of covalently derivatized enantiomers can be assessed without separating the derivatives from the reaction medium. As outlined above, the two goals were to be achieved using one set of sample preparation. This is important in view of the fact that we intend to carry out this study at the possible minimum cost. In addition, the analyses in this chapter were so designed to allow us to perform control analyses by which it can be shown systematically that covalent derivatization plays a vital role in the analyses. Chromatographic techniques that depend on derivatizing enantiomers for enantiomeric purity assessment, usually involve long separation stages requiring significant amounts of solvents. None of these is required for our new strategy, NSCCDS. In this regard, our new strategy, non-separative, covalent, chiral discrimination strategy is faster, simpler, and less expensive.

The use of chiral solvents or chiral selectors for direct enantiomeric purity assessment (non-covalent approach) is a well-known chiral discrimination strategy employed in some chromatographic and NMR techniques [4, 21, 64, 65]. This suggests that it might be possible to carry out the analyses in this study successfully without having to transform the enantiomeric pairs into covalent derivatives (diastereomers). As such, control experiments or analyses were performed to verify the effect of converting the enantiomers into covalent derivatives of diastereomers. Samples for the control analyses contained the chiral analytes, the chiral selector, and any reagent used in the covalent dirivatization. These control samples were not subjected to the conditions of the covalent derivatization. Thus, the control samples were analyzed in the unreacted form. In addition, sample solutions, containing only phenylalanine (no chiral selector or

reagent) in varying enantiomeric compositions, were analyzed. These chiral selector- and reagent-free samples were prepared at the same concentration level as the NSCCDS and control sample solutions of phenylalanine.

In this study, samples prepared using our new strategy, NSCCDS, are referred to as NSCCDS samples while those for the control analysis are referred to as control samples of the analyte in question.

Background on the Analysis of Phenylalanine (Phe) and Tyrosine (Tyr) using (*S*)-(+)-1,2-*propanediol (PD)*

Being organic acids (containing the carboxyl functional group), phenylalanine and tyrosine can react with (*S*)-(+)-1,2-propanediol (PD), which is a dialcohol, to form PD esters. Esterification of carboxylic acids using alcohols can be performed using a simple, single-step, synthesis approach known as the Fischer esterification named after the German chemist, Emil Fischer [66]. The reaction involves a nucleophilic substitution in which the OH group of a carboxylic acid is replaced by the alkoxide group (OR) of an alcohol. This reaction, which is catalyzed by a mineral acid, is an equilibrium reaction and results in the formation water. Fischer esterification is usually performed under reflux and works well with primary and secondary alcohols. The use of tertiary alcohols results in the formation of alkenes through elimination. Equation 2.1 below shows the schematic of the Fischer esterification reaction between the carboxylic acid functional group (COOH) and the OH alcohol functional group. Being an equilibrium reaction, the

$$RCOOH + R'OH + H^+ + \text{heat} = RCOOR' + H_2O \qquad 2.1$$

amount of ester formed is controlled by Le Chatelier's principle. Removing water from the reaction system or using an excess amount of alcohol will shift the equilibrium to the

side of the ester (RCOOR). The latter approach, which is easier to accomplish, is usually used as a means of driving the reaction to completion. The structure of (*S*)-(+)-1,2-propanediol, shown together with those of phenylalanine and tyrosine in Figure 2.2, reveals PD is both a primary and a secondary alcohol. Consequently, (*S*)-(+)-1,2-propanediol can, form a mono or diester or a mixture of both when reacted with a carboxylic acid. However, the terminal OH of PD is less hindered than the OH on the stereogenic carbon. As such, it is possible that formation of the monoester using the terminal OH would be favored over the other. The formation of an ester bond using the terminal OH will locate the Phe or Tyr molecule two bonds away from the stereogenic center of PD. On the other hand, a bond formed using the OH attached to the stereogenic

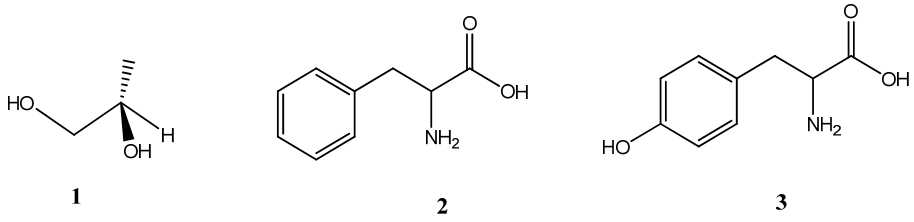

1 **2** **3**

Figure 2.1. **1**: (*S*)-(+)-1,2-propanediol (chiral selector). **2**: Phenylalanine. **3**: Tyrosine.

carbon will locate the amino acids within a bond length from the stereogenic center of PD. Generally, neither the type of ester (mono or di) nor the point of linkage of the amino acids will compromise the diastereomeric relationship between the ester pairs that might be formed with these amino acids. The type of ester formed should, therefore, not preclude chiral discrimination. Reaction Scheme I shows the two types of monoester that can possibly be formed, for example, with phenylalanine using the terminal OH and the OH attached to the stereocenter of (*S*)-(+)-1,2-propanediol (structure 4 and 5

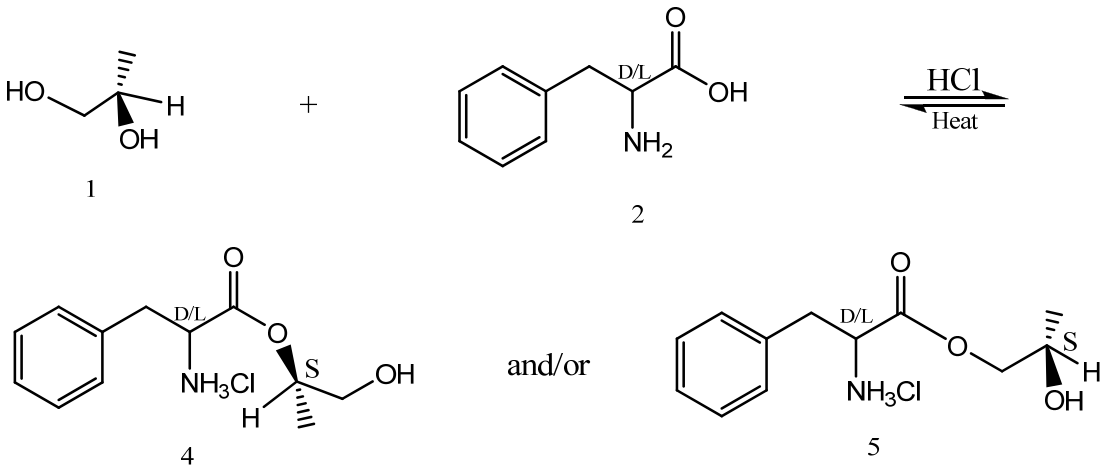

Scheme I. Reaction schematic showing the formation of monoester hydrochlorides of phenylalanine using the terminal OH or the OH attached to the stereogenic center of (*S*)-(+)-1,2-propanediol.

respectively). Comparison of structure 4 and 5 shows that the stereocenters in the monoester for the OH attached to the stereocenter of PD are closer to each other than they are in the monoester for the terminal OH. As such, any chiral discrimination effect that depend on chiral center proximity, should be enhanced in pairs diastereomeric monoesters formed using the OH attached to the stereocenter of (*S*)-(+)-1,2-propanediol. Reaction Scheme II shows the formation of the diester (structure 6). This reaction might be less favorable because it will involve bulkier and sterically more hindered molecules. However, the expected sterically hindered diester, in principle, should be less liable to racemization through inversion of configuration. Its formation might, therefore, enhance discrimination of the enantiomers of the amino acids. The use of (*S*)-(+)-1,2-propanediol as a chiral selector thus appears to have some characteristics that might be useful for chiral discrimination for the purpose of enantiomeric composition analysis.

Unlike our existing cyclodextrin guest-host complex strategies, which are efficient for chiral analytes with sizes appropriate for inclusion in the cavity of the

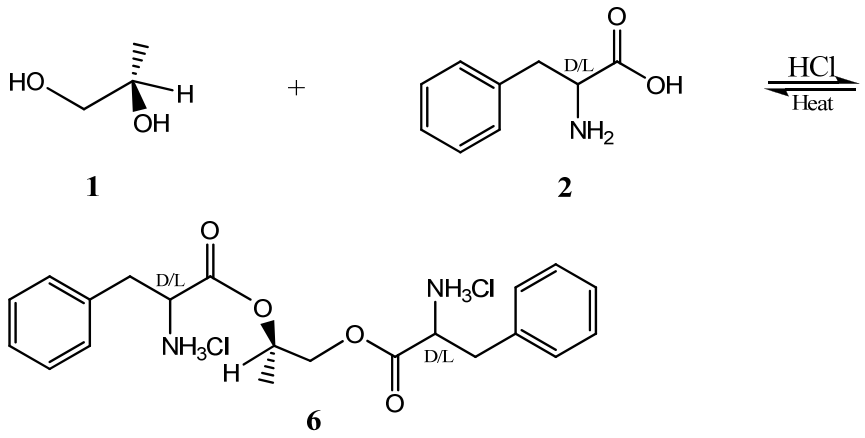

Scheme II. Reaction schematic showing phenylalanine diester hydrochloride formation by the reaction of phenylalanine with both OH groups of (*S*)-(+)-1,2-propanediol. Structure **1** and **2** (see Scheme I). **6**: Phenylalanine hydrochloride 1,2-propyl diester

cylodextrins, our new NSCCDS is applicable to molecules of any size provided they have the right functional groups to react covalently. In addition, our new strategy is less limited by the type of solvent that can be used in the analysis because covalent reactions can be performed in a variety of solvents. Furthermore, this new strategy is less restricted in terms of the concentration of analytes and chiral selectors that can be used [11, 21, 55, 56]. This is because samples can be analyzed at any concentration that is not less than the quantitation limit of the analyte and outside the linear range of the probe technique. As such, isotropic IR techniques can be combined with this strategy for enantiomeric purity assessment. Thus, our new covalent, chiral discrimination strategy combined with isotropic spectroscopic techniques, has several advantages over its chromatographic and NMR counterparts.

Background on the Analysis of Atenolol and Norephedrine using (*S*)-(+)-1,2-propanediol

Atenolol, chemically known as 4-[2-hydroxy-3-isopropylaminopropoxy] phenylacetamide, is an FDA approved prescription drug. Atenolol is a hydroxyl propyl

amine, which contains also an amide and a phenyl functional group. This drug, whose structure is shown in Figure 2.2, belongs to a class of pharmaceuticals known as beta-blockers (β-blocker), which are used for treating cardiovascular diseases among others [67, 68]. Compared to other β-blockers, Atenolol is reported to cause fewer side effects of depression, nightmares, and bronchospastic reactions [67].

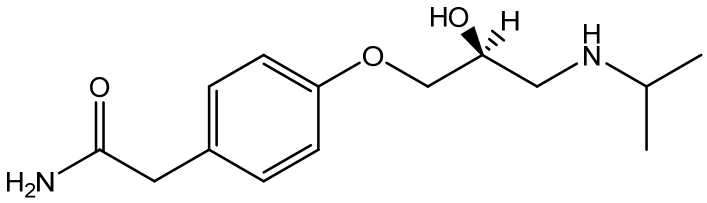

7

Figure 2.2. Structure of 4-[2-hydroxy-3-isopropylaminopropoxy] phenylacetamide (Atenolol)

Current resolution and enantiomeric composition analysis of this compound involves the use of chromatographic, electrophoretic, NMR and mass spectrometric techniques [67, 68]. Bhushan et al. [67] reported the reverse-phase TLC and LC analysis of Atenolol derivatized with Marfey's reagent (1-fluoro-2,4-dinitrophenyl-5-L-alanine amide). Marfey's reagent was introduced in 1984 by Marfey for indirect LC resolution of amino acids [67]. This reagent is known to react stoichiometrically with α-amino groups of D- and L-amino acids without racemization in about an hour at a temperature of 40 ^{o}C. The diastereomers formed are reported to have large differences in their retention factors and are easily separated on non-chiral columns in LC. Up to date, however, no technique has been found in the literature, which uses (*S*)-(+)-1,2-propanediol as a chiral selector for enantiomeric composition analysis of Atenolol. Unlike phenylalanine and tyrosine, Atenolol has no carboxyl functional group to react directly with (*S*)-(+)-1,2-

propanediol to form an ester. In addition, alcohols are not known to react directly with amines or amides according to the Fischer esterification reaction scheme. However, amides are known to undergo acid hydrolysis on heating to form the corresponding carboxylic acid and the ammonium ion of the corresponding amine according to reaction equation 2.2 below [69].

$$RCONHR' + H^+ + H_2O + \text{heat} = RCOOH + {}^+NH_3R' \qquad 2.2$$

In the presence of an alcohol and a proton from a mineral acid, the carboxylic acid formed can react with the alcohol to for an ester as shown earlier in equation 2.1. Hypothetically, therefore, it is possible that the reaction of Atenolol with (*S*)-(+)-1,2-propanediol in the presence of HCl will lead to the formation of an ester of Atenolol; the reaction of PD with the enantiomers of Atenonlol might form a diastereomeric ester pair of Atenonol.

Norephedrine, which is also known as phenylpropanolamine, was added to the list of analytes after the analysis of Atenolol turned out to be successful. Norephedrine, which is known to act on the sympathetic nervous system, is used as a pharmaceutically active ingredient in cough and cold medicines [70]. Norephedrine, unlike Atenolol, contains only a hydroxyl and an amine functional group as shown in Figure 2.3. Similar to the situation with Atenolol, no literature is found that reveals the possible product that could be formed when excess PD is heated together with Norephedrine in the presence of HCl. However, hypothetically, heating Norephedrine in the presence of HCl, could possibly lead to the formation of a carbocation through the elimination of water as a result of the protonation of the OH group attached to the chiral carbon in Norephedrine (see Figure 2.3). The carbocation is likely to be stable because it can be resonance

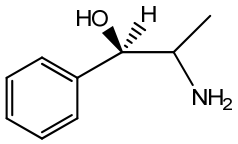

8

Figure 2.3. Structure of 2-amino-1-phenyl-propan-1-ol (Norephedrine)

stabilized by the phenyl group. Subsequent nucleophilic attack on the carbocation by a PD molecule could possibly lead to the formation of an ether, that is, substituting the OH group of Norephedrine with the alkoxide group of PD.

The literature shows that amide and amine functional groups can be converted to *N*-monoalkyl amides and alkylated amines, respectively, using alcohols. However, these reactions are usually performed using metallic catalysts under severe reaction conditions of pressure and temperature [71-73]. Although some of these reactions are shown to result in high yields (≥ 96 %), they are short of the objectives for developing the NSCCDS for enantiomeric composition analysis. This is because the reactions are complex, multi-step, time-consuming, and expensive– a simple and fast reaction scheme is desirable. As such, even though our proposed reaction scheme lacks documentation and we could not predict the products of the reactions, the two pharmaceutical compounds were subjected to the NSCCDS analysis using (*S*)-(+)-1,2-propanediol in the presence of HCl.

Methodology

Materials

Enantiopure phenylalanine (D and L: ≥ 99%), tyrosine (D and L: 99%), 4-[2-hydroxy-3-isopropylaminopropoxy] phenylacetamide (*R/S*-Atenolol: 99%), (*1R,2S*) and

(*1S,2R*)-phenylpropanolamine (*1R,2S*/*1S,2R*-Norephedrine: 99 %) and (*S*)-(+)-1,2-propanediol (≥ 99 %), were purchased from Aldrich Chemical Company, Inc. and used as received. ACS grade (12.01 M) concentrated hydrochloric acid was used as the catalyst for the Fischer esterification scheme.

Preparation of NSCCDS Samples of Phenylalanine and Tyrosine

A mass of 0.1652 g of enantiopure D- or L-phenylalanine was carefully weighed into a 24-mL glass vial. (*S*)-(+)-1,2-propanediol (440 µL) and 70 µL of concentrated HCl were then added. This was then heated in a water bath at 80 ^{o}C for an hour while stirring. The preparation was allowed to cool to room temperature and transferred quantitatively into a 250-mL volumetric flask. The solution was then made up to the mark with deionized water to obtain a 4 mM stock solution of D- or L-phenylalanine. It should be noted that the (*S*)-(+)-1,2-propanediol derivatized phenylalanine was not separated prior to preparing the analytical stock solution– the entire reaction medium at the end of the derivatization reaction was used in preparing the analytical stock solution. This constitutes the non-separative, covalent, chiral discrimination strategy. The derivatized D- and L-phenylalanine stock solutions were then used to prepare fifteen sample solutions for analysis by mixing pre-determined volumes of the stock solutions using a 1000 µL eppendorf pipet. For each sample solution the exact composition in terms of weight of the derivatized D- or L-phenylalanine stock solution was determine by weighing on an analytical balance (METTLER AE200) during the mixing. The mole fraction of D- or L-phenylalanine for each sample solution was computed using the weight composition instead of the pre-determined volume compositions of the samples. No attempt was made at varying the samples at a regular mole fraction interval.

The stock and samples solutions for tyrosine were prepared according to the procedure outlined for phenylalanine. A concentration of 2.5 mM instead of 4 mM was used for tyrosine because it has a higher molar absorptivity coefficient than phenylalanine. Twelve sample solutions were prepared for analysis by mixing predetermined volumes of the D- and L-tyrosine stock solutions using a 1000 μL eppendorf pipet as usual. The enantiomeric compositions in mole fractions, of the sample solutions, were computed using the pre-determined volumes of the PD derivatized or esterified D- and L-tyrosine stock solutions constituting the sample solutions.

Preparation of Control Samples of Phenylalanine and Tyrosine

Weights of the D and L enantiomers of phenylalanine and tyrosine, identical to the weights used in preparing the stock solution for the NSCCDS analyses, were carefully weighed into sample vials. Carefully measured amounts of (*S*)-(+)-1,2-propanediol and HCl, identical to amounts used in preparing the NSCCDS phenylalanine and tyrosine stock solutions, were added and dissolved with out heating with some amount of deionized water. The dissolved samples were quantitatively transferred from the samples vials into volumetric separate volumetric flasks and diluted to the marks with deionized water. Separate sets of sample solutions of phenylalanine and tyrosine were prepared for analysis by mixing known weights of the corresponding D and L enantiomer stock solutions as usual. It should be noted that the esterification step, which requires heating the enantiomers together with (*S*)-(+)-1,2-propanediol in the presence of HCl, was omitted in the preparation these control stock solutions.

Preparation of Chiral-Selector-Free Phenylalanine Samples

Analytical stock solutions of enantiopure D- and L-phenylalanine were prepared with amounts of D- and L-phenylalanine identical to the amounts used for the NSCCDS and control stock solutions above. Unlike the control samples, these solutions were prepared without the (*S*)-(+)-1,2-propanediol chiral selector. In addition, the solutions were prepared without heating. Sample solutions for analysis were prepared by mixing known weights of the enantiopure D- and L-phenylalanine stock solutions as before. The purpose for analyzing these samples without the chiral selector is to verify the need for a chiral selector in analyses such as these at low concentration levels (e.g., 4 mM).

Preparation NSCCDS and Control Samples of Atenolol

Stock and samples solutions for NSCCDS analysis of Atenolol were prepared according to the procedure outlined for phenylalanine above. The stock solutions were prepared at a 2 mM concentration level. This required a mass of 0.0267 g of *R*- or *S*-Atenolol. A volume of 450 μL of (*S*)-(+)-1,2-propanediol and 50 μL of HCl were added to the *R*- or *S*-Atenolol weighed out into a glass vial and heated in a water bath at 80 ^{o}C for one hour. After the heating and cooling processes, the entire reaction medium was quantitatively transferred into a 50-mL volumetric flask and diluted to the mark. Fourteen sample solutions were prepared for analysis by mixing known weights of the *R*- and *S*-Atenolol stock solutions. The enantiomeric compositions in terms of mole fraction of the sample solutions were computed using the weight compositions of the stock solutions of *R*- and *S*-Atenolol making up the sample solutions prepared for analysis. Stock and sample solutions for control analysis were prepared in the same way as those for the NSCCDS analysis except for the omission of the heating process.

Instrumentation, Spectra Collection and Data Analysis

An Agilent 8453, photodiode array, UV-vis spectrophotometer, equipped with a low pressure deuterium lamp (190-800 nm) and a low-noise tungsten lamp (370-1100 nm) for UV-vis and NIR irradiation of samples, was used to record the UV-vis spectra of all the samples. The instrument has a wavelength range of 190-1100 nm. A black-wall, 10 mm pathlength, quartz sample cell, with a 2.5 mm wide window, was used as the UV-vis sample cell for spectra recording. Before collecting the spectrum of each sample solution, the UV-vis spectrum of deionized water, used as blank, was recorded. On measuring the spectrum of a sample solution after the blank, the instrument software (Agilent ChemStation A.08x) automatically computes and displays the blank-corrected UV-vis spectrum of the sample solution. The blank-corrected UV-vis spectral data, as well as the enantiomeric composition data of the samples, were then subjected to multivariate, PLS-1, regression analyses using the Unscrambler™ statistical package, version 9.7 (CAMO, Inc., Woodbridge, NJ). The data analyses were performed following the procedure described in Chapter 1– spectral mean centering, wavelength selection, full-cross-validated calibration model development, and test sample prediction.

Results and Discussion

Analysis of NSCCDS Samples of Phenylalanine

Figure 2.4A shows the UV absorption spectra from 222 to 322 nm of the 4 mM stock solutions of the (*S*)-(+)-1,2-propanediol derivatized D- and L-phenylalanine. Figure 2.4B is the mean-centered UV absorption spectra of the stock solutions. Figure 2.4A clearly shows the usual absorption peak of phenylalanine, which has a maximum at 257

nm. Unlike Figure 2.4A, the mean-centered spectra in Figure 2.4B clearly reveals that the stock solutions have different UV absorbances, with the derivatized L-phenylalanine showing higher absorbance between 228 and 278 nm. The difference, for example, in absorbance between the two solutions at 259 nm is 0.01 absorbance units (AU). This difference is twice the magnitude of the instrument error in absorbance (± 0.005 AU). This indicates the recording of an actual difference in absorbance between the two solutions. As noted in Chapter 1, an NMR study discussed later in Chapter 4 shows that an HCl catalyzed reaction of 2-butanol with phenylalanine under heat leads to ester formation. Based on this, the difference in absorbance between the stock solutions should be due to the formation of diastereomeric esters of phenylalanine by the esterification of the enantiomers of phenylalanine with (*S*)-(+)-1,2-propanediol (PD).

The UV absorption spectra from 230 to 271 nm of the fifteen sample solutions, made up of different enantiomeric compositions, of the PD derivatized D- and L-phenylalanine are shown in Figure 2.5A. The mean centered UV absorption spectra, which are labeled in terms of the mole fractions of the D-phenylalanine enantiomer are shown in Figure 2.4B. Like all other spectra labeled in this chapter using mole fractions, the mole fractions shown in Figure 2.4B are corrected to two decimal places (2 dp). Similar to the stock solutions, the mean-centered spectra in Figure 2.5B, shows differences in absorbance of the fifteen samples solutions. Since these sample solutions have identical total phenylalanine concentrations, the differences revealed in Figure 2.5B can only be due to the variation in enantiomeric composition of the samples. This, in turn, can arise only because the spectral property of the PD esterified D-phenylalanine is different from that of the PD esterified L-phenylalanine enantiomer. This reinforces the

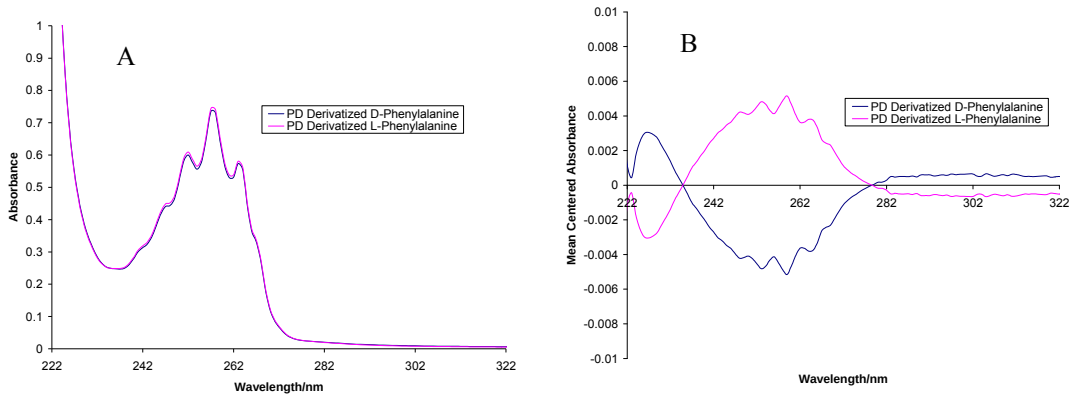

Figure 2.4. A: UV absorption spectra of 4 mM PD esterified D-and L-phenylalanine stock solutions. B: The mean-centered spectra of A. Note the difference in absorbance between the two solutions in B. The difference in absorbance, 0.01 AU, at 259 nm is greater than the instrument error of ± 0.005 AU.

statement made about the mean-centered spectra (see Figure 2.4B) of the stock solutions that covalent diastereomers (ester pair) of phenylalanine were formed as a result of the esterification reaction. The mean centered spectra in Figure 2.5B reveals a typical situation in analyses such as this where variations in spectra of samples tend to occur less uniformly and in different wavelength regions. Situations of this kind, undoubtedly, require multivariate regression analysis for the extraction of latent structured information. The usefulness of a chiral discrimination strategy for enantiomeric composition analysis lies in how well the differences in a probed property of samples discriminated using the strategy, correlate with the enantiomeric compositions of the samples. As, such the spectral data for the phenylalanine samples, discriminated using our new covalent strategy, NSCCDS, was subjected to multivariate, PLS-1 regression modeling. Seven calibration samples, with D-phenylalanine mole fractions of 0.0496, 0.151, 0.250, 0.300, 0.501, 0.733, and 0.950, were randomly selected from the fifteen samples prepared to develop a PLS-1 calibration model.

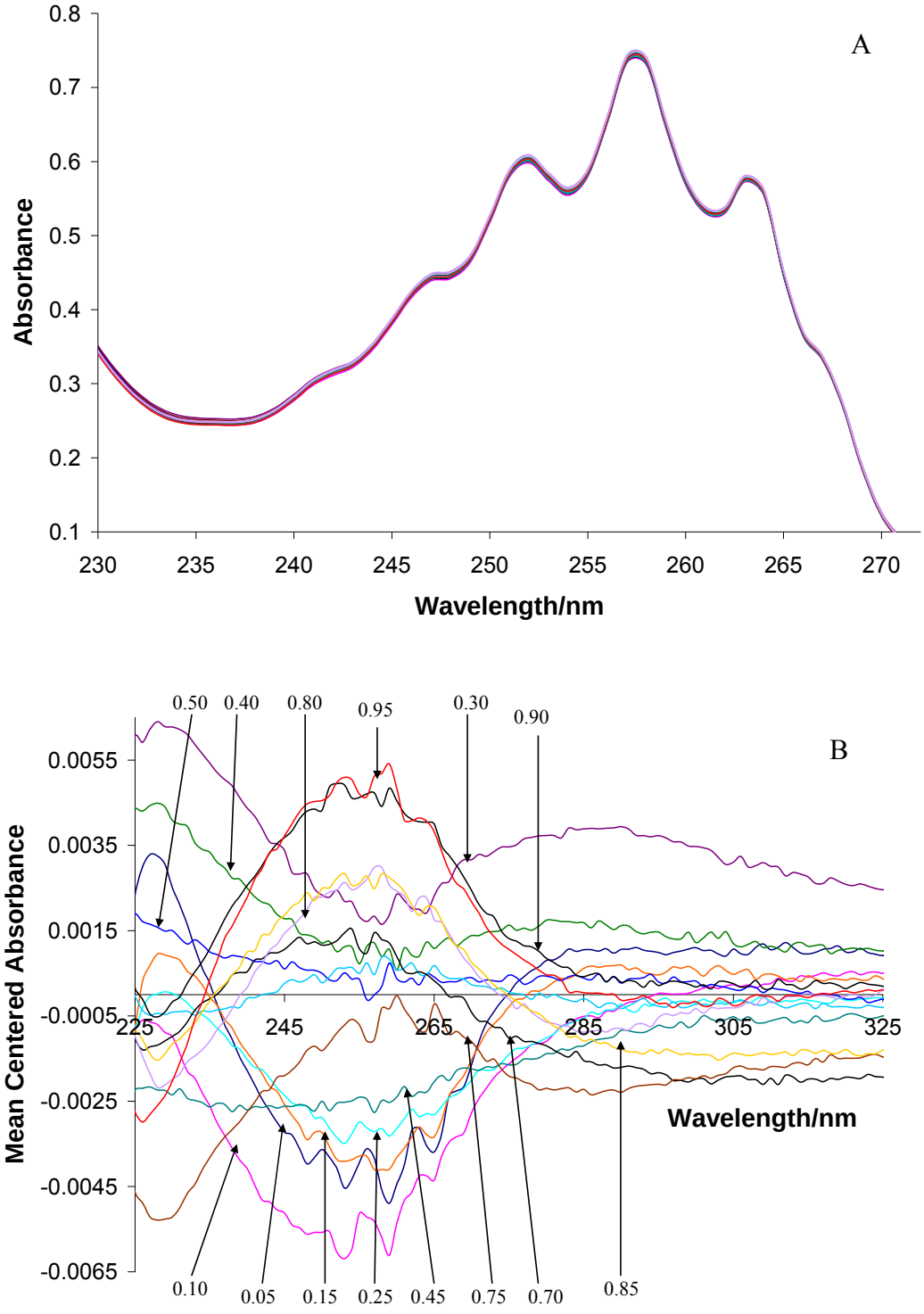

Figure 2.5. A: UV absorption spectra of fifteen sample solutions prepared using 4 mM PD esterified D-and L-phenylalanine stock solutions The samples solutions were made up of different enantiomeric compositions but identical total phenylalanine concentrations. B: The mean-centered spectra of A labeled in terms of the mole fractions (to two decimal places) of the D-phenylalanine enantiomer.

Figure 2.6A, B, C, and D show the multivariate, PLS-1 regression, calibration model plots developed using the above calibration samples. Figure 2.6A is the scores plot, 2.6B is the regression coefficient as a function of wavelength plot, 2.6C is the explained variance as a function of principal component plot and 2.6D is the predicted (y-axis) versus known (x-axis) calibration sample mole fraction plot. Chapter 1 can be referred to for what each of these plots stand for. In this discussion, the plots are interpreted relevant to the data analyzed. The scores plot in Figure 2.6A, which is constructed using the first PC as the x-axis and the second PC as the y-axis, shows a pattern that reveals the compositions of the calibration samples in terms of the D-phenylalanine mole fraction in an increasing order from left to right. Figure 2.6B, which is the regression coefficient plot, shows the modeled wavelength region, 230-567 nm, and relationship between the spectral data (x-variables) and the enantiomeric composition (y-variables) of the samples. The positive part (above zero) of the curve shows that the regression coefficients of the x-variables in the region are positive. This indicates that the y-variables vary in the same direction with the x-variables in that wavelength region. The opposite interpretation holds for the negative part (below zero) of the regression curve. The regression coefficient with the highest positive value is associated with the260 nm wavelength and the regression coefficient with the highest negative value is recorded at 240 nm; the enantiomeric compositions change most with spectral data associated with these wavelengths. Part of the curve shows some noise (400-567) but an attempt to model a narrower wavelength region, 230-400 nm, resulted in a model with a lower figure of merit (higher RMSE of cross-validation). This indicates that though the wavelength region from 400 to 567 nm reveals some noise, some amount of relevant

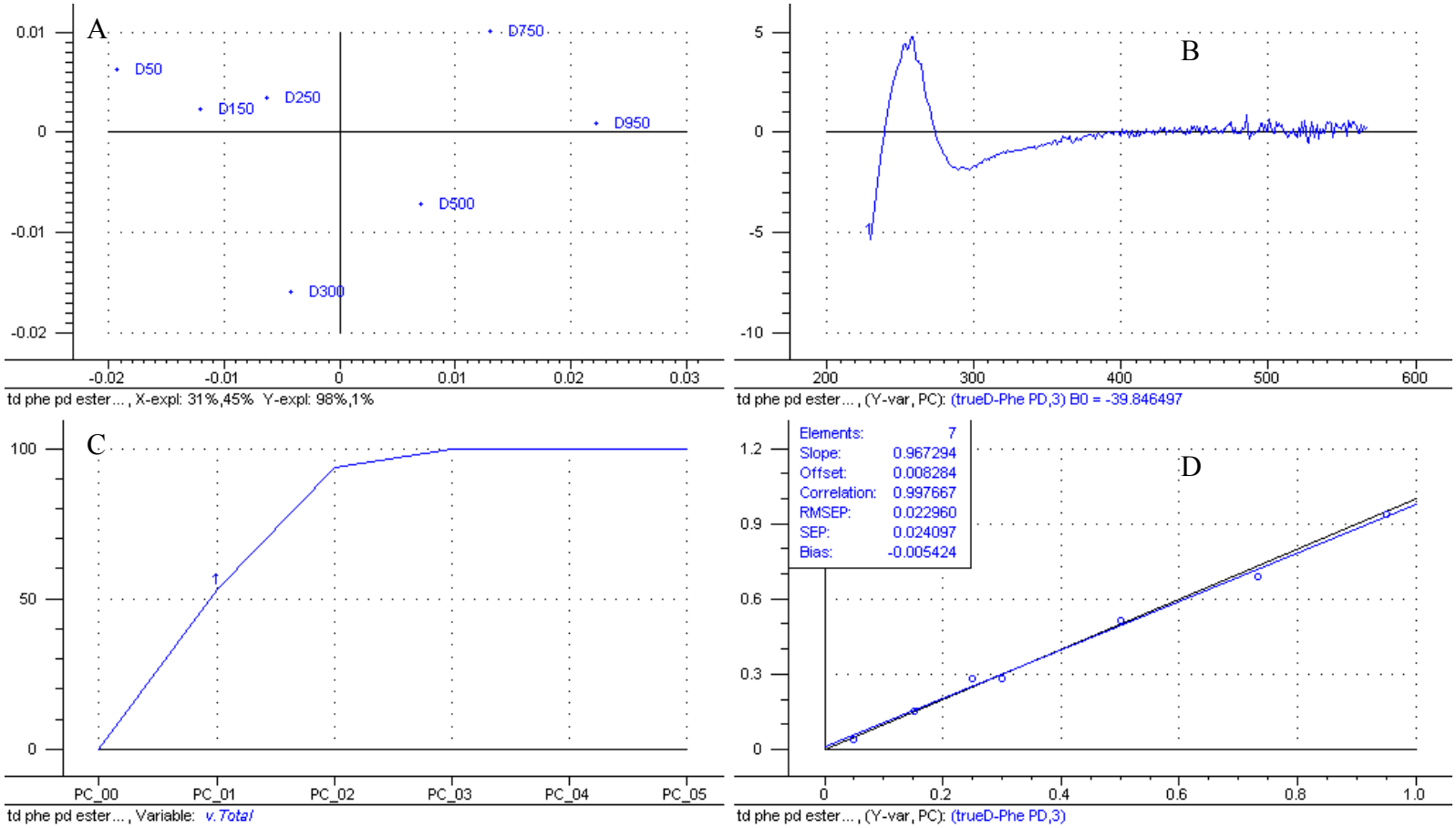

Figure 2.6. Plots of PLS-1 regression calibration model developed using the UV absorption spectral data and known enantiomeric compositions of NSCCDS calibration samples of phenylalanine. A: scores plot, B: regression coefficient as a function of wavelength plot, C: percent explained variance as a function of principal component plot, and D: calibration and cross-validation regression lines for the fitted (black) and predicted (blue) mole fractions, respectively, versus the known mole fractions of calibration samples. The model required three PCs (see below plot B or D).

information is resident in that region of the spectra. Such situations are encountered. The explained variance plot in Figure 2.6C reveals that five PCs were computed in developing the calibration model. The percent explained variances of these PCs are 53.34, 93.67, 99.59, 99.59, and 99 59 %. However, only three PCs were needed in describing the relationship between the spectral data and the enantiomeric compositions. Of the selected three PCs, the first PC explained 31 % of the variation in x-data (spectral data) and 98 % of the variation y-data (enantiomeric composition, ec). The second PC explained 45 and 1 % of the variation in the x- and y-data respectively. Thus, the two PCs explained 76 % of the variation in the x-data and 99 % of the variation in the y-data. The explained variations are displayed below the scores plot (Figure 2.6A). Based on the Unscrambler software, if the sum of the variation in the x- or y-data explained by the first two PCs is 70 % of more, then the model explains a significant portion of the information in the data and the relationship between the predictor (x) and response (y) variables can be reported with a high degree of certainty. Figure 2.6D shows two regression lines– the fitted calibration model line shown in black and the cross-validation regression line shown in blue. The plot statistics (slope, offset, correlation coefficient, root-mean-squares error, and standard error) for these two regression lines are compared in Table 2.1. The table shows that the plot statistics for the cross-validation, which reveals the actual relationship between the spectral data and enantiomeric composition of the calibration samples, are not significantly different from those for the calibration line (best-fit). For example, the slope and correlation coefficient for the cross-validation are 0.967 and 0.998 respectively. These are significantly identical to those computed for the calibration, both of which have the value 0.999. The values of the cross-validation plot

statistics in Table 2.1, therefore, indicate clearly that the UV absorption spectra of the calibration samples correlate well with their enantiomeric composition as portrayed by the first two PCs.

Table 2.2 compares the result of the prediction of the mole fractions of independent test/validation samples, predicted using the calibration model, with the

Table 2.1. Regression Plot Statistics for Calibrating and Cross-Validating 4 mM calibration samples made up of varying compositions of (*S*)-(+)-1,2-propanediol esterified D- and L-phenylalanine (NSCCDS analysis).

Regression Plot Statistic (RPS)	RPS value for Calibration	RPS value for Cross-Validation
Slope	0.999	0.967
Offset	0.000428	0.00828
Coefficient of Correlation	0.999	0.998
Root-Mean-Square Error	0.00966 (≈ 1 %)	0.0229 (≈ 2.3 %)
Standard Error (standard deviation of residuals)	0.0104 (≈ 1 %)	0.0241 (≈ 2.4 %)

actual or known mole fractions. NR in Table 2.2 stands for a mole fraction that could not be computed because the weight of the solution of the derivatized Phe enantiomer in question was mistakenly not recorded during the sample preparation. Clearly, Table 2.2 shows that the predicted mole fractions of the test samples closely match the actual mole fraction. The highest absolute deviation recorded is0.026. The root-mean-square error of prediction (RMSEP), which is the average error of deviation for the predicted value from the actual or known value, is 0.014. As noted in Chapter 1, the RMSE is a figure of merit, which can be used in evaluating techniques. The RMSEP value of 0.014 computed for this analysis indicates quite a high merit because it shows quite a low level of deviation from the actual enantiomeric compositions of the test or validation samples.

Table 2.2. Actual and predicted D-Phe mole fractions of 4 mM validation samples containing varying compositions of D- and L-phenylalanine esterified with (*S*)-(+)-1,2-propanediol (NSCCDS analysis)

Actual D-Phe ø[a]	Predicted D-Phe ø	Absolute error of Prediction	Actual L-Phe ø	Predicted L-Phe ø	Absolute error of Prediction
0.103	0.0848	-0.0182	0.897	0.915	0.018
0.400	0.407	0.007	0.600	0.593	-0.007
0.451	0.425	-0.026	0.549	0.575	0.026
0.597	0.596	-0.001	0.403	0.404	-0.001
NR[b]	0.773	-	NR	0.227	-
0.801	0.801	0.0	0.199	0.208	0.009
0.851	0.859	0.008	0.149	0.141	-0.008
NR	0.877	-	NR	0.123	-
RMSEP[c]		0.014			0.014

[a] Mole fraction, [b] Not recorded, [c] Root-mean-square error of prediction

Thus, the NSCCDS is quite effective for the assessment of the enantiomeric composition of phenylalanine at a concentration level of 4 mM. In addition, the results shows that with our new strategy, analysis of future samples, similar to those analyzed in this study, could be within an error margin of ± 0.014 mole fraction units.

Analysis of Control Samples of Phenylalanine

Control samples of phenylalanine were prepared as described above to evaluate the effect of the covalent derivatization discrimination. As noted above, covalent derivatization or formation of covalent diastereomers, which is the heart of our new discrimination strategy, might not be necessary because chiral solvents are used successfully in non-covalent resolution of enantiomers in some chromatographic and NMR chiral analysis techniques. The samples for this control analysis are referred to here as control or (*S*)-(+)-1,2-propanediol (PD) associated phenylalanine samples.

Figure 2.7 shows the UV absorption spectra from 222 to 322 nm for the 4 mM PD derivatized and PD associated D- and L-phenylalanine stock solutions. The spectra for the NSCCDS D- and L-phenylalanine stock solutions are shown in pink and blue colors respectively. The corresponding spectra for the control or PD associated stock solutions are shown in green and brown. Figure 2.7 shows the usual absorption band of phenylalanine with a maximum at 257 nm. The figure reveals significant differences between the two sets of phenylalanine solutions– the PD derivatizes phenylalanine solutions have higher UV absorption coefficients in the spectral regions from about 224 to 244 nm and 270 to 302 nm than the PD associated phenylalanine (control) stock solutions. A careful examination of the two sets of spectra in the wavelength region, 224-235 nm, reveals a bathochromic shift in the spectra for the NSCCDS stock solutions relative to those for the control stock solutions.

Figure 2.8 shows the mean-centered UV absorption spectra from 222 to 322 nm for the 4 mM NSCCDS and control D and L-phenylalanine (control) stock solutions. The spectrum for the PD esterified D-phenylalanine is in blue, that of the esterified L-phenylalanine in pink and the spectra for the PD associated D- and L-phenylalanine enantiomers are shown in green and brown colors respectively. Figure 2.8 reveals additional significant differences between the two sets of phenylalanine solutions. The figure shows that the spectra for the control or PD associated phenylalanine solutions cross at 234 and 283 nm while those for the NSCCDS solutions cross at 235 and 279 nm. This spectral crossing at difference wavelengths clearly reveals the relative shift in absorption wavelength of these two sets of phenylalanine solutions. Figure 2.8 also shows that the UV absorption of the NSCCDS prepared D-phenylalanine solution,

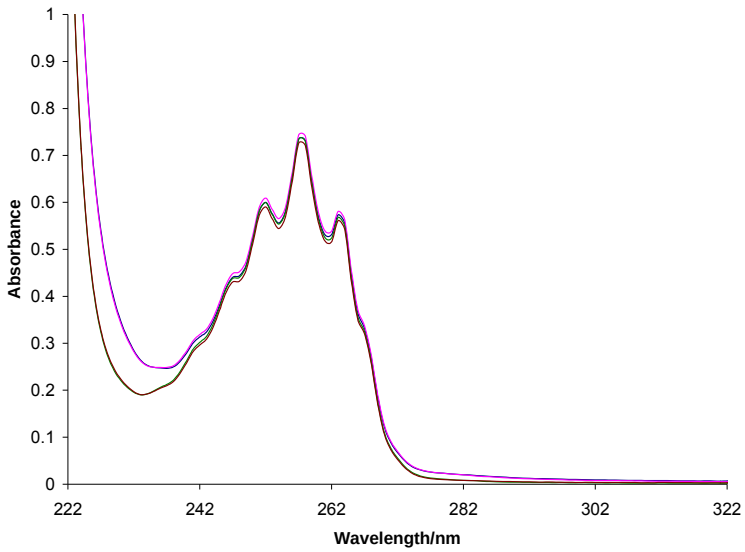

Figure 2.7. UV absorption spectra of 4 mM NSCCDS and PD associated or control (not heated) D-and L-phenylalanine stock solutions. Blue spectrum: NSCCDS D-phenylalanine. Pink spectrum: NSCCDS L-phenylalanine. Green spectrum: Control D-phenylalanine. Brown spectrum Control L-phenylalanine.

between 235 and 285 nm, is higher than that of the L-phenylalanine solution. The control or PD associated phenylalanine solutions, on the other hand, reveal the exact opposite effect. The differences in spectra revealed in Figure 2.7 and 2.8 clearly shows that the NSCCDS phenylalanine (esterified phenylalanine) stock solutions are different from the control or PD associated phenylalanine stock solutions.

Figure 2.9A and B, respectively, are the original and mean-centered UV absorption spectra (230-290 and 227-307nm respectively) for thirteen control phenylalanine sample solutions prepared using the 4 mM control D-and L-phenylalanine stock solutions. Figure 2.9A clearly shows the usual absorption band of phenylalanine, which has a maximum at 257 nm. Unlike Figure 2.9A, the mean-centered spectra in Figure 2.9B, which are labeled in terms of the mole fractions (to two decimal places) of the D-phenylalanine enantiomer, shows that there are quite significant differences in the spectra of the control sample solutions.

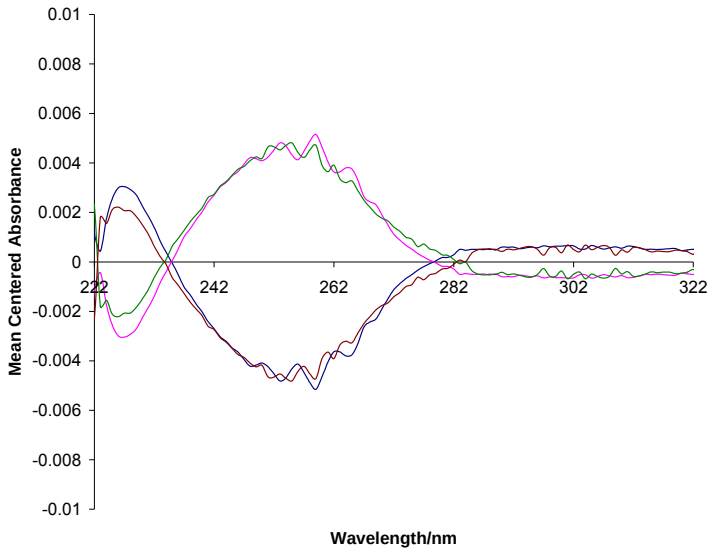

Figure 2.8. Mean-centered UV absorption spectra of 4 mM (*S*)-(+)-1,2-propanediol (PD) esterified and associated or control (not heated) D-and L-phenylalanine stock solutions. Blue spectrum: PD esterified D-phenylalanine. Pink spectrum: PD esterified L-phenylalanine. Green spectrum: PD associated D-phenylalanine (control solution). Brown spectrum PD associated L-phenylalanine (control solution).

Figure 2.10A, B, C, and D show the plots for the PLS-1 regression calibration model developed to verify the correlation of the spectral differences shown in Figure 2.9B with the compositions of the samples. The plots were developed using the spectral data and enantiomeric compositions of six randomly selected control calibration samples with D-phenylalanine mole fractions of: 0.151, 0.399, 0.500, 0.801, 0.897, and 0.950. Figure 2.10A is the scores plot constructed with the second PC as the y-axis and first PC as the x-axis. Figure 2.10B is the regression coefficient as a function of wavelength plot, 2.10C is the percent explained variance as versus of PC plot, and 2.10D is the calibration model (black line) and cross-validation (blue line) regression lines plot (predicted versus known mole fraction plot). Figure 2.10A and C, respectively, show that the scores and percent explained variance plots of the control calibration samples of phenylalanine are not significantly different from those of the NSCCDS phenylalanine calibration samples.

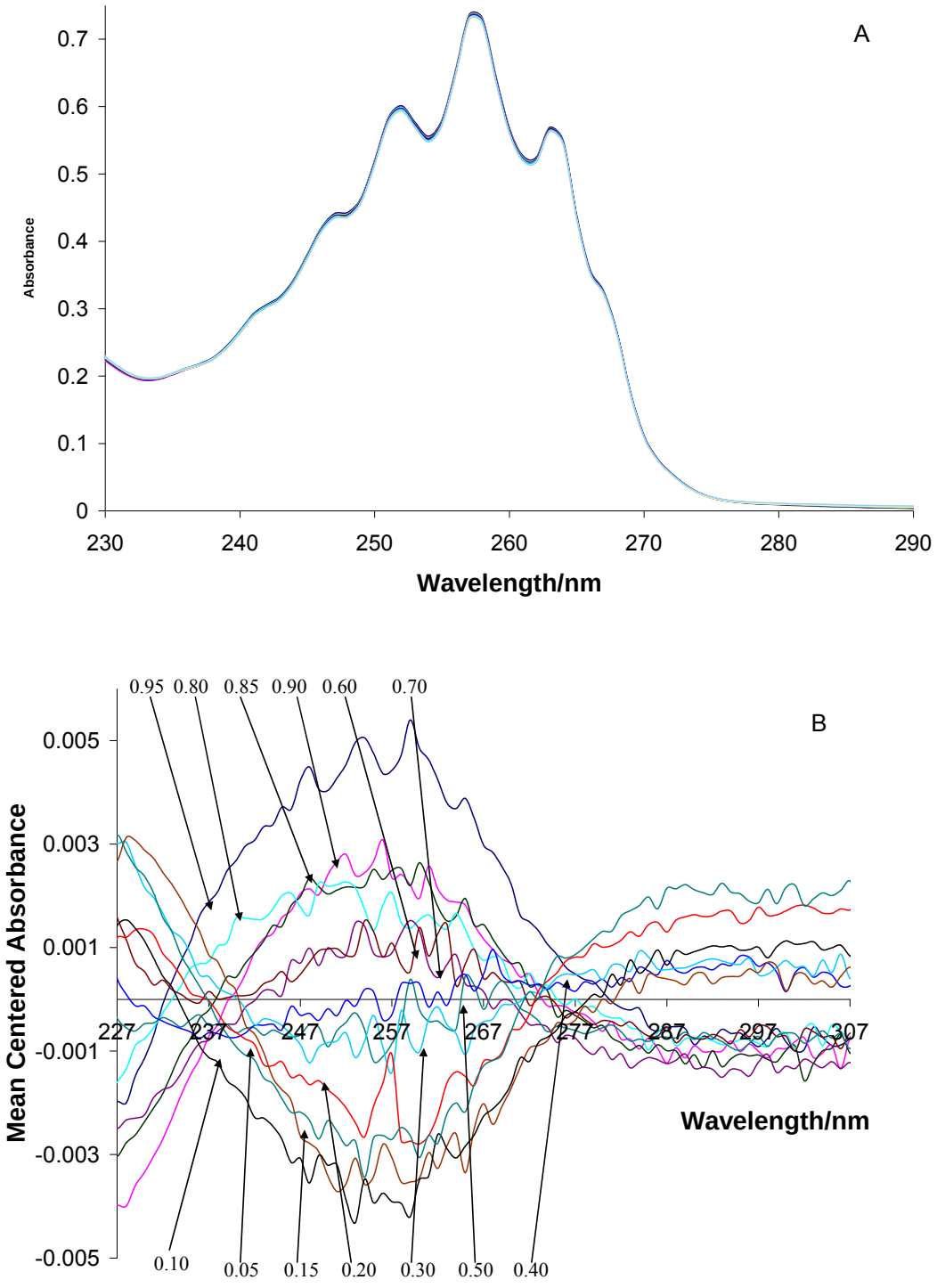

Figure 2.9. Original and mean-centered UV absorption spectra of thirteen sample solutions prepared using 4 mM PD associated or control (not heated) D-and L-phenylalanine stock solutions: A is original UV absorption spectra and B is mean centered UV absorption spectra. The samples were made up of different enantiomeric compositions but identical total phenylalanine concentrations. The mean centered spectra are labeled in terms of the mole fractions (to two decimal places) of the D-phenylalanine enantiomer.

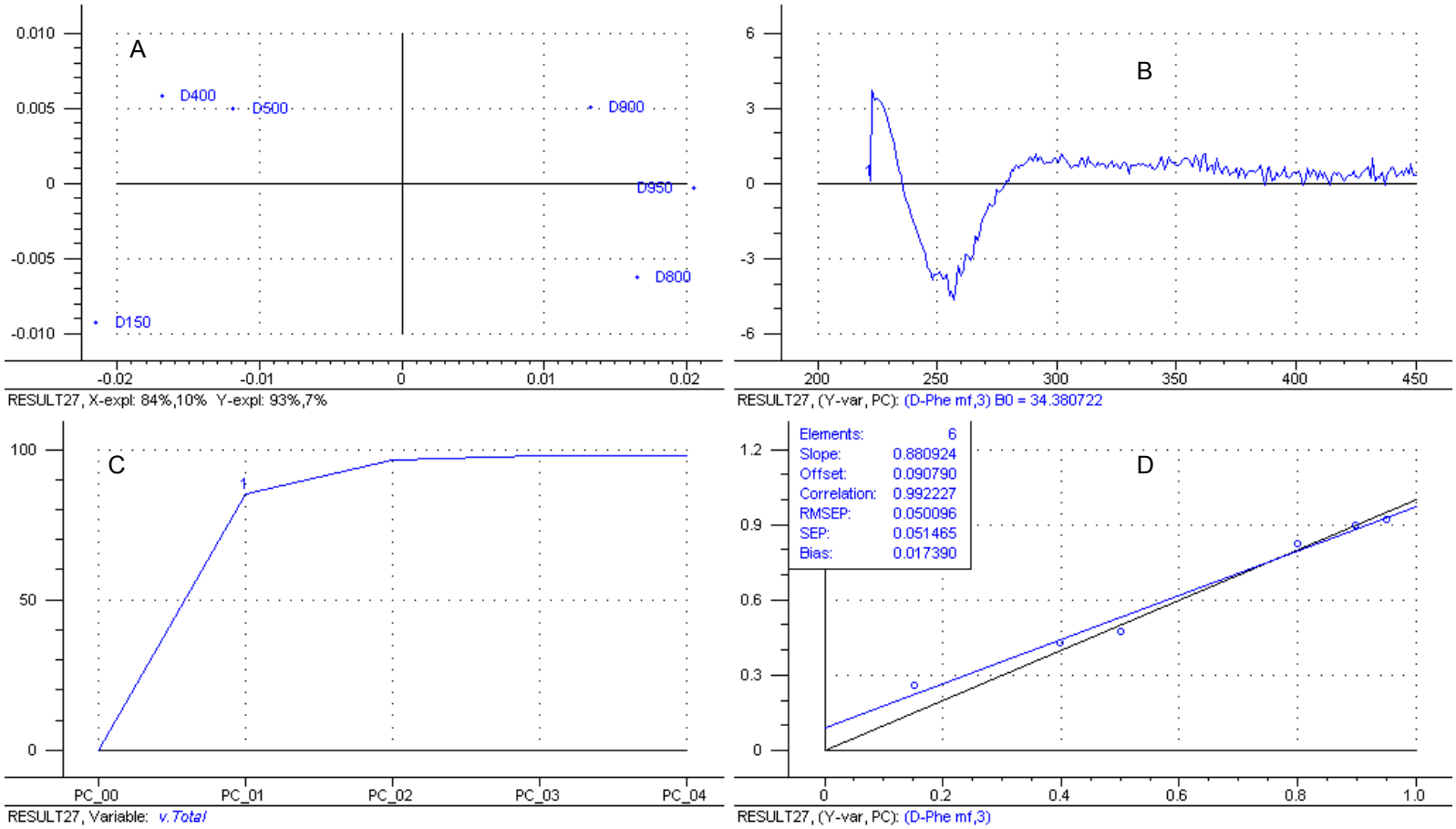

Figure 2.10. Plots of PLS-1 regression calibration model developed using the UV absorption spectral data and known enantiomeric compositions of the control or PD-associated calibration samples (not heated) of phenylalanine. A: scores plot, B: regression coefficient as a function of wavelength plot, C: percent explained variance as a function of principal component plot, and D: calibration and cross-validation regression lines for the fitted (black) and predicted (blue) mole fractions, respectively, versus the known mole fractions of calibration samples. The model required three PCs (see below plot B or D).

However, the regression coefficient plot in Figure 2.10B indicates that a shorter wavelength range was required for modeling (222-450 nm) the control calibration samples compared to the corresponding NSCCDS samples (235-567 nm). In addition, Figure 2.10D shows that the cross-validation regression line (blue) for the control samples of phenylalanine differs from that for the corresponding NSCCDS calibration samples. The differences between the two regression lines, in terms of the cross-validation plot statistics, are shown in Table 2.3. The table also shows the plot statistics of the fitted calibration lines for the two sets of calibration samples. It is clear from the table that the regression plot statistics of calibration for the control and NSCCDS samples are not significantly different from each other. This is not surprising because the calibration plots are fitted as mentioned earlier. As such, calibration regression lines, usually, havegood regression plot statistics. However, the cross-validation plot statistics for the control calibration samples differ from the plot statistics of the fitted calibration line. On the other hand, the cross-validation plot statistics for the NSCCDS samples compare quite favorably with the plot statistics of the fitted calibration plot. Generally, the closer the values of the plot statistics for the cross-validation regression line are to those of the fitted calibration line, the better the correlation between the predictor (spectral data) and the response variable (enantiomeric composition). Thus, the plot statistics in Table 2.3 indicate a slightly higher degree of correlation in the data for the NSCCDS phenylalanine samples than the control phenylalanine samples. This is in spite of the fact that the first two PCs for the control samples explained 94 and 100 % of the variation in the x- and y-data respectively, compared 76 and 99 % for the NSCCDS calibration samples.

Table 2.3. Regression Plot Statistics for Calibrating and Cross-Validating 4 mM NSCCDS and control calibration samples made up of varying compositions of D- and L-phenylalanine.

Regression Plot Statistic (RPS)	RPS value for NSCCDSS[a] Calibration	RPS value for Control Samples Calibration	RPS value for NSCCDSS Cross-Validation	RPS value for Control Samples Cross-Validation
Slope	0.999	0.999	0.967	0.881
Offset	0.000428	0.0003	0.00828	0.0908
Corr[b]. Coefficient	0.999	0.999	0.998	0.992
RMSE[c]	0.00966	0.006	0.0229	0.0500
SE[d] (SDR)[e]	0.0104	0.007	0.0241	0.0501

[a] Non-separative, covalent, chiral discrimination samples, [b] Correlation, [c] Root-mean-square error, [d] Standard error, [e] Standard deviation of residuals

Table 2.4 compares the absolute errors of prediction computed for the mole fractions of nine control validation samples with those computed for the mole fractions of the NSCCDS validation samples. The magnitudes of the absolute errors of prediction for

Table 2.4. Comparison of the predicted D-phenylalanine (Phe) mole fractions in the control and NSCCDS validation samples of phenylalanine made up of varying enantiomeric compositions of D- and L-Phe.

Actual D-Phe ø[a] for Control Sample	Predicted D-Phe ø for Control Sample	Absolute error for D-Phe ø Prediction	Actual D-Phe ø for NSCCDS[b] Sample	Predicted D-Phe ø for NSCCDS Sample	Absolute error for D-Pheø Prediction
0.0499	0.0160	-0.0339	0.103	0.0848	-0.0182
0.102	0.124	0.022	0.400	0.407	0.007
0.200	0.227	0.027	0.451	0.425	-0.026
0.299	0.259	-0.04	0.597	0.596	-0.001
0.601	0.576	-0.025	NR	0.773	
0.700	0.701	0.001	0.801	0.801	0.0
0.855	0.846	-0.009	0.851	0.859	0.008
			NR[b]	0.877	
RMSEP[c]		0.026			0.014

[a] Mole fraction, [b] Non-separative, covalent chiral discrimination strategy, [c] Root-mean-square error of prediction

the control samples compared to those for the NSCCDS samples (see Table 2.2) show that generally, PD is less effective for the analysis of phenylalanine when used as a non-covalent chiral selector. The root-mean-square error of prediction computed for the analysis of the control samples is 0.026. This error is about twice the prediction error of 0.014 computed for the NSCCDS samples. Though the results of these two analyses appear to suggest that (S)-(+)-1,2-propanediol (PD) is more effective as covalent chiral selector, the results also indicate that PD can be used for non-covalent discrimination analysis. This is because of the low RMSEP, 0.026, computed for the analysis.

Analysis of Chiral-Selector-Free Phenylalanine Samples

We have found out in our research on chiral analysis over the years that the isotropic UV-vis spectral signatures of the enantiomeric pairs of certain chiral liquids vary significantly [11, 12]. Such samples have been analyzed without a chiral selector. In addition, it was possible to analyze these liquids and other solid chiral compounds at elevated concentrations ($\geq$ 15 mM) without the use of a chiral selector. At such high concentrations, however, most chiral compound will not dissolve in water, which is a preferred solvent for analyses such this. For example, phenylglycine and tyrosine, which must be heated to dissolve in water at concentration levels greater than 4 mM, tend to precipitate with time on cooling. As such, chiral compounds behaving similarly to phenylglycine and tyrosines cannot be analyzed effectively without a chiral selector. In addition, it is important and desirable to be able to assess enantiomeric purity at low concentration levels because the concentrations of chiral active pharmaceutical ingredients (API) in most therapeutic drugs are low. Examples of such drugs include Boniva (API: 2.5mg), Detrol (API: 1, 2 ,and 4 mg), and Singulair (API: 4, 5, and 10 mg).

It is, therefore, important that chiral analysis techniques being developed for analyzing such categories of compounds should be capable of doing so effectively at low concentration levels. Our new strategy must thus be tested against the possibility of assessing enantiomeric purity of chiral compounds at the concentration levels, for example, at which phenylalanine was analyzed using the NSCCDS approach without a chiral selector.

Figure 2.11 shows the UV absorption spectrum (blue spectrum) from 222 to 322 nm of a 4 mM stock solution containing only enantiopure D-phenylalanine. The figure also shows the spectrum (pink spectrum) of the 4 mM D-phenylalanine stock solution prepared using the NSCCDS approach. It is obvious from the figure that the spectrum for the chiral-selector-free or pure D- phenylalanine is different from the spectrum recorded for the NSCCDS D- phenylalanine stock solution. The difference shown in Figure 2.11 between the NSCCDS and pure D- phenylalanine stock solutions is similar to that recorded between the control and NSCCDS phenylalanine stock solutions shown in Figure 2.7. In fact, the spectra of the control and pure phenylalanine stock solutions have similar signatures. Figure 2.11 reveals that the NSCCDS D-phenylalanine solution has a higher UV absorption from about 227 to 244 nm and 272 to 302 nm than the pure D-phenylalanine solution. In addition, the NSCCDS D- phenylalanine stock solution shows a bathochromic shift relative to the enantiopure D- phenylalanine solution in the spectral region from 222 to 242 nm. These spectral differences confirm that phenylalanine is transformed into a derivative of PD, whose spectral signature differs significantly from pure phenylalanine.

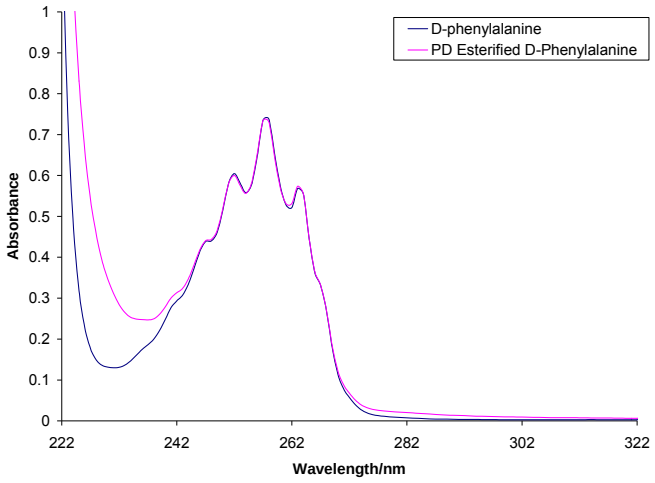

Figure 2.11. UV absorption spectra of 4 mM (*S*)-(+)-1,2-propanediol (PD) esterified and chiral-selector-free (enantiopure) D- phenylalanine stock solutions. Blue spectrum: enantiopure D-phenylalanine. Pink spectrum: PD esterified D-phenylalanine (NSCCDS sample)

Figure 2.12 shows the mean-centered spectra from 222 to 224 nm for fourteen sample solutions, which were prepared by mixing know weights of the 4 mM chiral-selector-free or pure D- and L-phenylalanine stock solutions. The mean-centered spectra for the pure phenylalanine samples are clearly different from the mean-centered spectra recorded for the NSCCDS and control phenylalanine samples (see Figure 2.5 and 2.9). These differences recorded for the mean-centered spectra of these three sets of phenylalanine samples reflect the effect of the (*S*)-(+)-1,2-propanediol chiral selector on the spectral property phenylalanine. Figure 2.12 shows that there is some variation in UV absorption of the pure phenylalanine sample solutions. To determine whether the variation in spectra of the pure phenylalanine samples correlate with the enantiomeric compositions of the samples, the original spectral data of the pure phenylalanine samples were subjected to PLS-1 regression modeling.

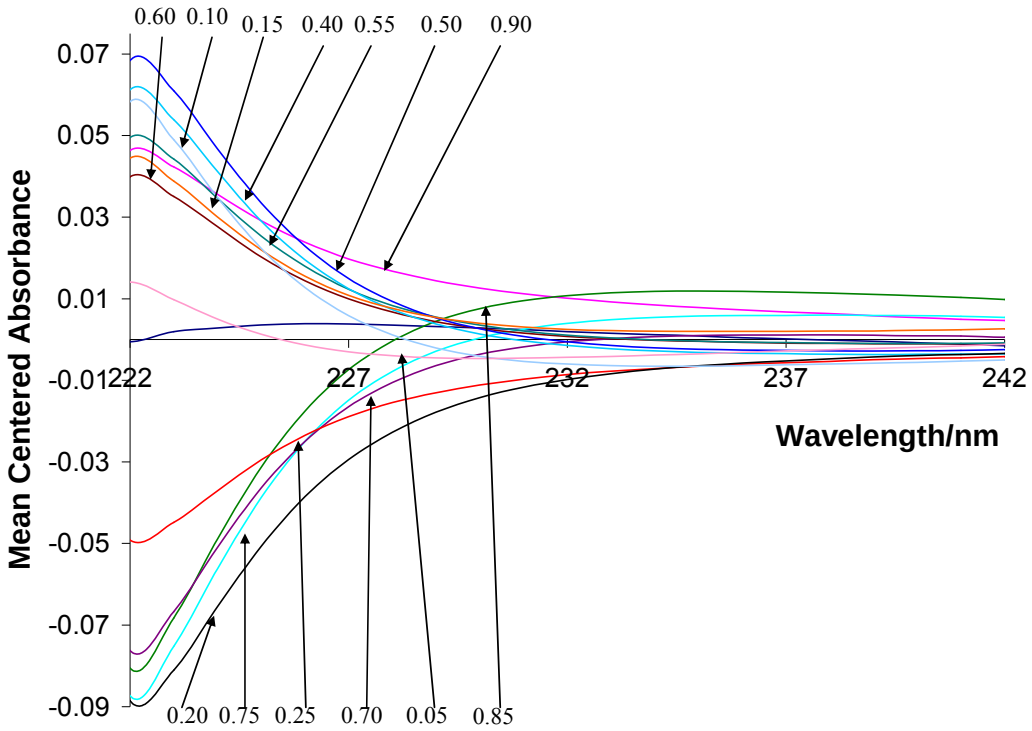

Figure 2.12. Mean-centered UV absorption spectra of fourteen chiral-selector-free sample solutions made up of different enantiomeric compositions 4 mM enantiopure D-and L-phenylalanine. The spectra are labeled in terms of the mole fractions (to two decimal places) of the D-phenylalanine enantiomer.

Figure 2.13A, B, C, and D show the PLS-1 regression model plots developed using the spectral data of seven samples. The seven samples were randomly selected from the fourteen samples prepared for analysis. Figure 2.13A is the scores plot. Apart from the mismatch of sample D150 the scores plot shows that the first two PCs describe the samples in terms of the D-phenylalanine compositions in an increasing order of the mole fraction of D-phenylalanine from left to right. Unlike the NSCCDS samples, the regression coefficient curve shown in Figure 2.13B for the pure phenylalanine samples has only a positive phase. This indicates that the enantiomeric compositions of the pure phenylalanine calibration samples change in the same direction as the spectral data in the modeled wavelength region. Figure 2.13C, which is the explained variance versus PC

plot, shows that five PCs were computed to explain the variation in the data. that the variation in the spectral data poorly explains the variation in the composition of the samples. The explained variances, from the first through to the fifth PC are 50, 70.47, 19.82, 45.22, and 45.51 %. For this data set, the first two PCs explained 99 of the variation in spectral data and 72 % of the variation in the enantiomeric composition. However, only the first PC was necessary in developing the model. Figure 2.13D shows the calibration and cross- validation regression lines for the pure phenylalanine (chiral-selector-free Phe) samples. It is clear from the figure that the cross-validation regression line (blue) deviates significantly from the fitted calibration line (black line). The plot statistics associated with the two regressions lines are compared in Table 2.5 with those of the previously discussed NSCCDS phenylalanine samples. The plot statistics reported in Table 2.5 for the pure phenylalanine samples clearly indicate poor correlation in data unlike those for the NSCCDS phenylalanine samples. For example, values for the slope and correlation coefficient of both the fitted calibration and cross-validation lines are significantly lower than the minimum acceptable value of 0.9, which is required for a meaningful regression of the sample composition (response variable) on the spectral data (predictor variable) to attained. The root-mean-squares errors and standard deviation of the residuals (standard error) are quite high. An attempt made at predicting a set of validation samples using the calibration model (Figure 2.13D) for the pure phenylalanine samples resulted in poor predictions. The predictions are shown in Table 2.6 in comparison with the actual mole fractions of the validation samples. From the table, except for two samples with actual D-phenylalanine mole fractions of 0.899 and 0.249, the deviations or errors in the predicted mole fractions of the rest of the samples are

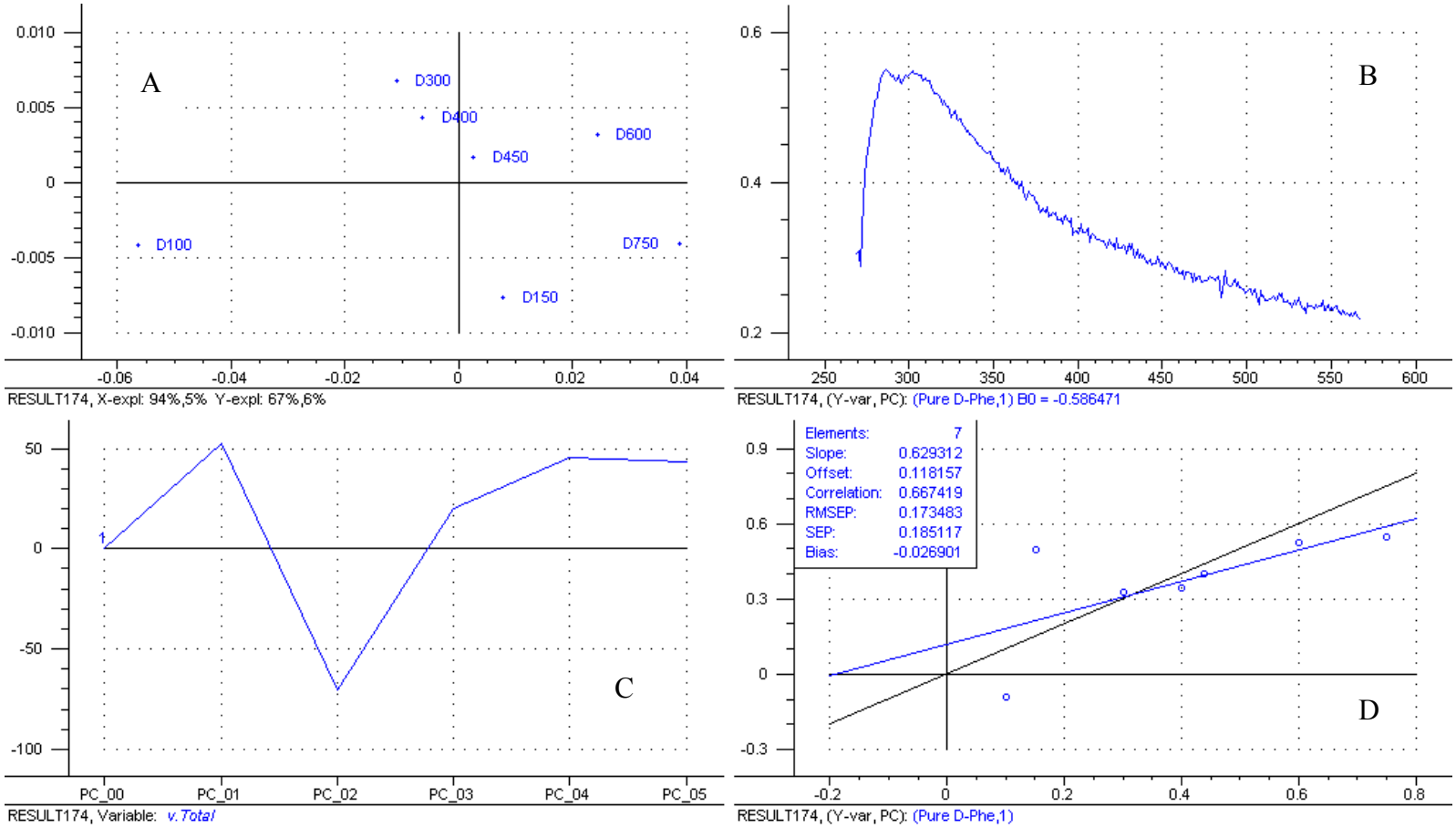

Figure 2.13. Plots of PLS-1 regression calibration model developed using the UV absorption spectral data and known enantiomeric compositions of chiral-selector-free phenylalanine calibration samples. A: scores plot, B: regression coefficient as a function of wavelength plot, C: percent explained variance as a function of principal component plot, and D: calibration and cross-validation regression lines for the fitted (black) and predicted (blue) mole fractions, respectively, versus the known mole fractions of calibration samples. The model required only one PC (see below plot B or D).

Table 2.5. Regression Plot Statistics for Calibrating and Cross-Validating 4 mM NSCCDS and chiral-selector-free calibration samples of Phe made up of varying compositions of D- and L-phenylalanine

Regression Plot Statistic (RPS)	RPS value for NSCCDSS[a] Calibration	RPS value for EPS[b] Calibration	RPS value for NSCCDSS Cross-Validation	RPS value for EPS Cross-Validation
Slope	0.999	0.668	0.967	0.629
Offset	0.000428	0.130	0.00828	0.118
Corr[c]. Coefficient	0.999	0.817	0.998	0.667
RMSE[d]	0.00966	0.124	0.0229	0.173
SE[e] (SDR)[f]	0.0104	0.134	0.0241	0.185

[a] Non-separative, covalent, discrimination strategy samples, [b] Enantiopure sample, [c] Correlation, [d] Root-mean-square error, [e] Standard error, [f] Standard deviation of residuals

unusually high. For example, the validation sample with an actual D-phenylalanine mole fraction of 0.851 has an absolute error as high as -0.256. The root-mean-square error of prediction computed for the analysis is 0.16. This is about 11.4 times the error computed for the NSCCDS analysis of phenylalanine. The prediction results for the pure phenylalanine samples indicate that the variations observed in the spectra of the pure phenylalanine samples were not caused by the differences in enantiomeric compositions of the samples. The observed variations could be due to instrument variation. Should this be the case, it will imply that differences in spectra caused by instrument variation in analyses such as this cannot result in meaningful correlation of spectral data with samples composition. In other words the correlation between spectral data and enantiomeric composition observed in the analysis of the NSCCDS and control phenylalanine samples are due to actual discrimination effects of the (*S*)-(+)-1,2-propanediol chiral selector. The experimentation with the pure phenylalanine samples undoubtedly show that a chiral selector is needed at a concentration level of 4 mM for assessing the enantiomeric purity

Table 2.6. Actual and predicted D-phenylalanine mole fractions for 4 mM validation samples containing varying compositions of chiral-selector-free (enantiopure samples) D- and L-phenylalanine

Actual ø[a] for Enantiopure D-Phe	Predicted ø[a] for Enantiopure D-Phe	Absolute error of Prediction
0.951	0.737	0.214
0.899	0.866	0.033
0.851	1.107	-0.256
0.801	0.884	-0.083
0.501	0.614	-0.113
0.249	0.240	0.009
0.0497	0.287	-0.2373
Root-Mean-Squares Error of Prediction		0.16

[a] Mole fraction

of phenylalanine. Generally, the analysis suggests that except for the enantiomers of neat chiral liquid compounds, whose isotropic spectral signatures differ significantly, a chiral selector may be required in assessing enantiomeric composition of chiral compounds in solution at low concentration levels.

Analysis of NSCCDS Samples of Tyrosine

Figure 2.14A and B contain the original UV absorption spectra and the mean-centered spectra, respectively, from 235 to 349 nm of the 2.5 mM NSCCDS D- and L-tyrosine stock solutions. Figure 2.14A shows the usual tyrosine absorption band in aqueous solution with a maximum at 274 nm. The absorption band is due to the $A_{1g} \leftarrow B_{2u}$ forbidden л*← л transition of the phenolic group of tyrosine. Similar to phenylalanine, the mean-centered spectra in Figure 2.14B clearly shows that the tyrosine stock solutions differ in their spectral properties: PD derivatized L-tyrosine absorbs more

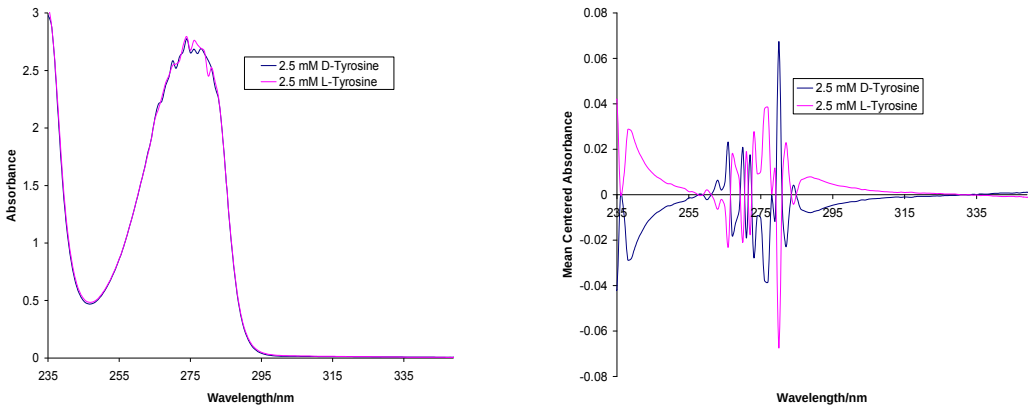

Figure 2.14. A: UV absorption spectra for PD derivatized or esterified 4 mM stock solutions of D-and L-tyrosine. B: Mean-centered spectra of A. Note the difference in absorbance between PD esterified D- and L-Tyr in B. The difference in absorbance, 0.056, at 239 nm is greater than the instrument error, ± 0.005.

UV light than the D-tyrosine counterpart between 236 and 258 nm, and 285 and 330 nm. The difference in absorbance between these stock solutions at 239 nm is 0.056 AU and at 289 nm a difference of 0.014 AU is recorded. These differences cannot be due to instrument errors because both are more than twice the instrument error in absorbance, which is ± 0.005. Thus, actual spectral differences were recorded.

Figure 2.15A and B show the original UV absorption spectra (247-321 nm) and the mean-centered UV absorption spectra (286-236 nm) for the twelve sample solutions prepared using the 2.5 mM NSCCDS tyrosine stock solutions. Similar to the stock solutions (Figure 2.14), the mean-centered spectra clearly depict spectral differences among the samples. As noted for phenylalanine, these differences in absorbance should be due to the formation of a diastereomeric ester pair of tyrosine as a result of the esterification of tyrosine using (*S*)-(+)-1,2-propanediol in the presence of HCl. Being diastereomers, the D- and L-tyrosine should be different in their spectral properties, hence the differences in absorbance recorded.

Figure 2.16A, B, C, and D show the plots for the PLS-1 regression calibration model developed to investigate the correlation of the spectral differences shown by the mean-centered spectra for the NSCCDS tyrosine samples solutions. Six calibration samples, with D-tyrosine mole fractions of 0.250, 0.400, 0.450, 0.500, 0.600, and 0.700, were randomly selected from the twelve samples prepared to develop the calibration model. The plot in Figure 2.16A is the scores plot, 2.16B the regression coefficients as a function of wavelength plot, 2.16C the percent explained variances versus PC plot, and 2.16D the regression line plot (plot of predicted verses known mole fractions of the calibration samples). The scores and regression coefficient plots reveal features about the spectral and enantiomeric composition data of the tyrosine samples that are significantly identical to that discussed previously for the NSCCDS phenylalanine samples. The explanations given for the phenylalanine samples, thus, hold here as well. However, different wavelength regions were required in modeling the two samples: 289-349 nm for tyrosine and 230-567 nm for phenylalanine. This is not surprising because the two molecules are different with different UV absorption properties. As such, the (*S*)-(+)-1,2-propanediol derivatives of these two compounds should have different spectral properties. The percent explained variance plot for the NSCCDS tyrosine samples, in Figure 2.16C, reveals four PCs with percent variances of 34.23, 96.77, 98.28, and 98.57 %. However, only three PCs were adequate for the model. Of these, the first two PCs together explained 98 % of the variation in the spectral data and 99 % of the variation in the sample composition. These percentages indicate that a significant amount of information in the data is accounted for by the model. As such, the relationship between the spectral data and sample composition can be reported with a high degree of certainty.

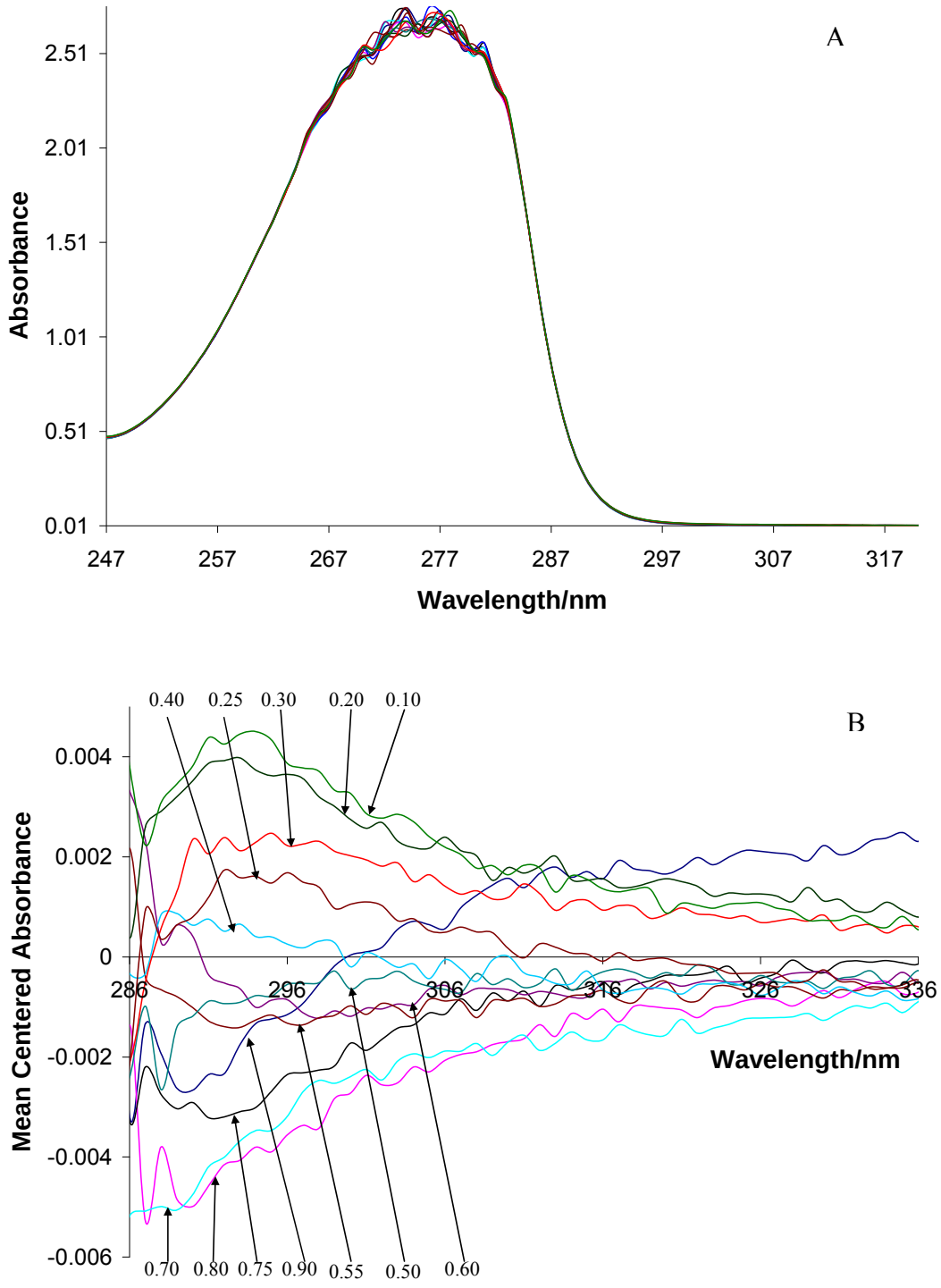

Figure 2.15. A: UV absorption spectra of twelve sample solutions prepared using 2.5 mM PD esterified D- and L-tyrosine stock solutions. B: Mean-centered spectra of A. The samples solutions are made up of different enantiomeric compositions but identical total tyrosine concentrations. The mean centered spectra are labeled in terms of the mole fractions (to two decimal places) of the D-tyrosine enantiomer.

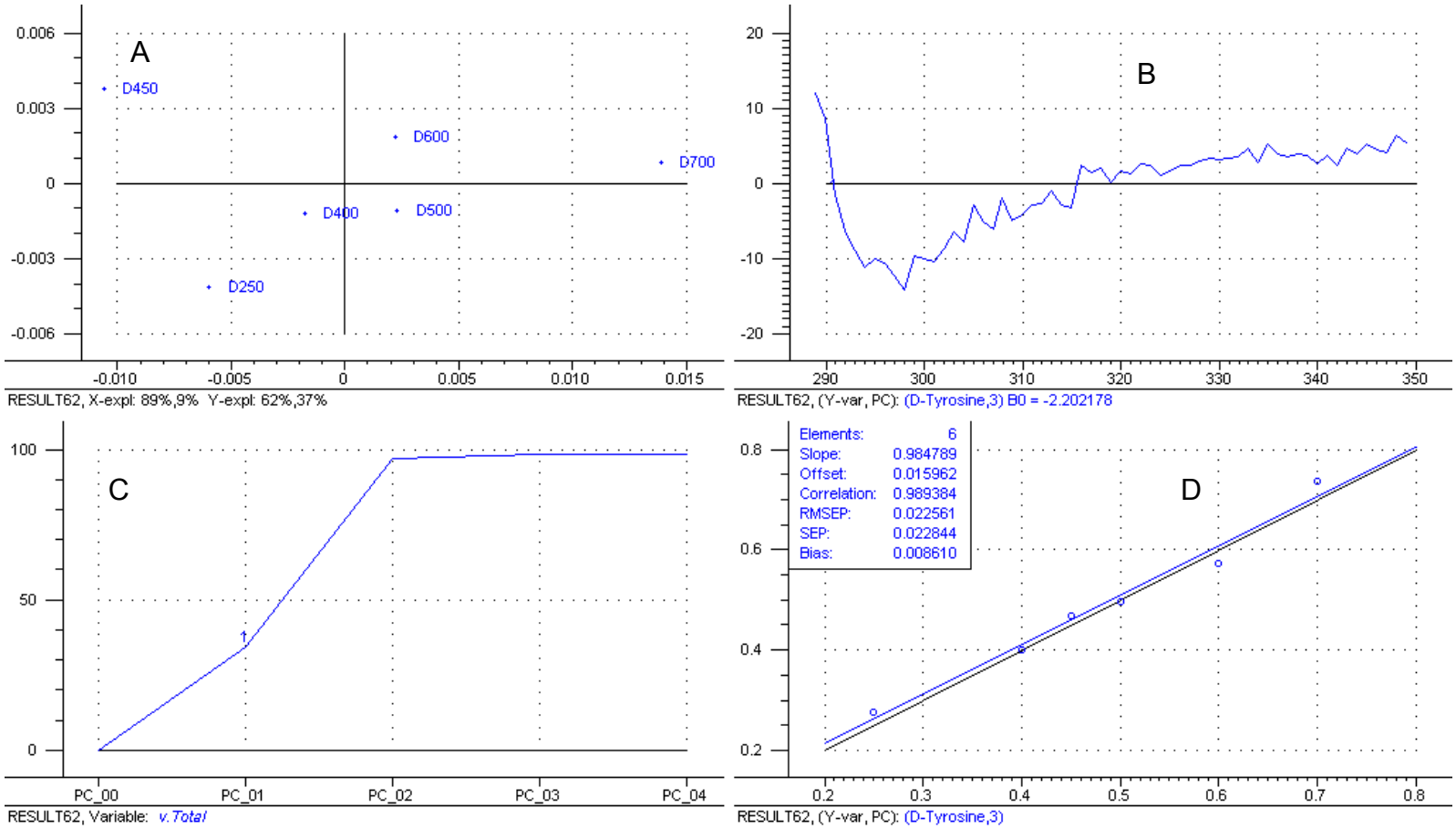

Figure 2.16. Plots of PLS-1 regression calibration model developed using the UV absorption spectral data and known enantiomeric compositions of NSCCDS calibration samples (heated) of tyrosine. A: scores plot, B: regression coefficient as a function of wavelength plot, C: percent explained variance as a function of principal component plot, and D: calibration and cross-validation regression lines for the fitted (black) and predicted (blue) mole fractions, respectively, versus the known mole fractions of calibration samples. The model required three PCs (see below plot B or D).

Table 2.7 shows the plot statistics for the fitted calibration (black line) and cross-validation (blue line) regression lines shown in Figure 2.16D for the NSCCDS tyrosine calibration samples. The offset, root-mean-squares error, and standard error for the cross-validation regression line of the NSCCDS tyrosine samples differ from the corresponding values computed for the fitted calibration line. However, values for the slope and correlation coefficient compare favorably with those for the fitted calibration

Table 2.7. Regression Plot Statistics for the Calibration and Cross-Validation of 2.5 mM calibration sample solutions of tyrosine made up of varying enantiomeric compositions of (*S*)-(+)-1,2-propanediol (PD) esterified D- and L-tyrosine (NSCCDS analysis).

Regression Plot Statistics (RPS)	RPS value for Calibration	RPS value for Cross-Validation
Slope	0.998	0.985
Offset	0.000755	0.0160
Coefficient of Correlation	0.999	0.989
Root-Mean-Squares Error	0.0057	0.023
Standard Error (standard deviation of residuals)	0.0062	0.023

line. Except for the offset, the cross-validation plot statistics for the NSCCDS tyrosine calibration samples are significantly different from the cross-validation plot statistics of the NSCCDS phenylalanine calibration samples reported in Table 2.1.

Table 2.8 shows the mole fractions predicted for the rest of the six NSCCDS tyrosine samples used as validation samples. The table also shows the actual mole fractions of these validation samples. Compared to predictions for the NSCCDS phenylalanine samples (see Table 2.2), slightly higher deviations/errors are associated with most of the predicted NSCDS tyrosine smples. The root-mean-square error of prediction (RMSEP) computed for the analysis is 0.030. Though higher than the RMSEP

computed for the NSCCDS phenylalanine samples, the analysis still indicates effective discrimination of tyrosine using (*S*)-(+)-1,2-propanediol. This is because the 0.03 root-mean-square error is within the error margin usually reported for existing chromatographic and NMR techniques employed in analyses such as this [21].

Table 2.8. Actual and predicted D-Tyr mole fractions of 2.5 mM validation samples of tyrosine esterified with PD (NSCCDS analysis). The samples contain varying enantiomeric compositions of D- and L-Tyr.

Actual ø[a] for D-Tyr	Predicted ø for D-Tyr	Absolute error of Prediction	Actual ø for L-Tyr	Predicted ø for L-Tyr	Absolute error of Prediction
0.800	0.794	0.006	0.200	0.206	-0.006
0.750	0.737	0.013	0.250	0.263	-0.013
0.550	0.581	-0.031	0.450	0.419	0.031
0.300	0.248	0.052	0.700	0.752	-0.052
0.200	0.166	0.034	0.800	0.834	-0.034
0.100	0.0766	0.0234	0.900	0.923	-0.023
RMSEP[b]		0.030			0.030

[a] Mole fraction, [b] Root-mean-square of prediction

Analysis of Control Samples of Tyrosine

Similar to phenylalanine, control samples of tyrosine were analyzed. The set of spectra labeled A, in Figure 2.17, are the UV absorption spectra from 235 to 335 nm of the fourteen 2.5 mM control sample solutions of tyrosine. These control tyrosine solutions contain identical amounts of (*S*)-(+)-1,2-propanediol and HCl as the previously discussed NSCCDS tyrosine samples. As in the case of phenylalanine, heating was avoided during the preparation of the tyrosine stock solutions from which the control tyrosine samples were prepared. The spectra reveal the usual absorption band of

tyrosine, which has a maximum at 274 nm. Figure 2.17 also shows a second set of spectra labeled B, which belongs to the twelve NSCCDS tyrosine samples discussed previously. The figure clearly shows a significant difference in UV absorption property

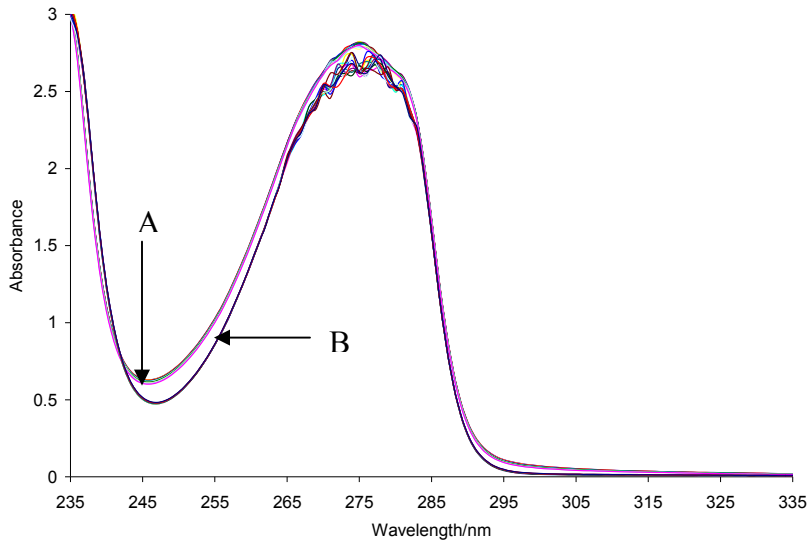

Figure 2.17. UV absorption spectra for two different sets of tyrosine samples made up of varying enantiomeric compositions of D- and L-tyrosine. Spectra set A is for the fourteen control samples (no heating).and spectra set B is for the twelve samples prepared using the NSCCDS approach (heating).

of the two sets of tyrosine samples. Unlike phenylalanine, (see Figure 2.4), the absorbances of the control samples of tyrosine turned out to be higher than the absorbances of the NSCCDS tyrosine samples. This can be seen in the spectral regions from 244 to 282 nm and 290 to 325 nm. This difference in spectral response of the NSCCDS phenylalanine and tyrosine solutions reveals that the chiral selector, (*S*)-(+)-1,2-propandiol, has different spectral effects on this two chiral analytes.

Figure 2.18 shows the mean-centered UV absorption spectra from 285 to 435 nm for the fourteen control samples of tyrosine. The figure clearly reveals differences in absorbance among the individual control sample solutions of tyrosine. This is a clear

indication of the formation of diastereomeric species of tyrosine in solution through a non-covalent interaction of the D- and L-tyrosine enantiomers with (*S*)-(+)-1,2-

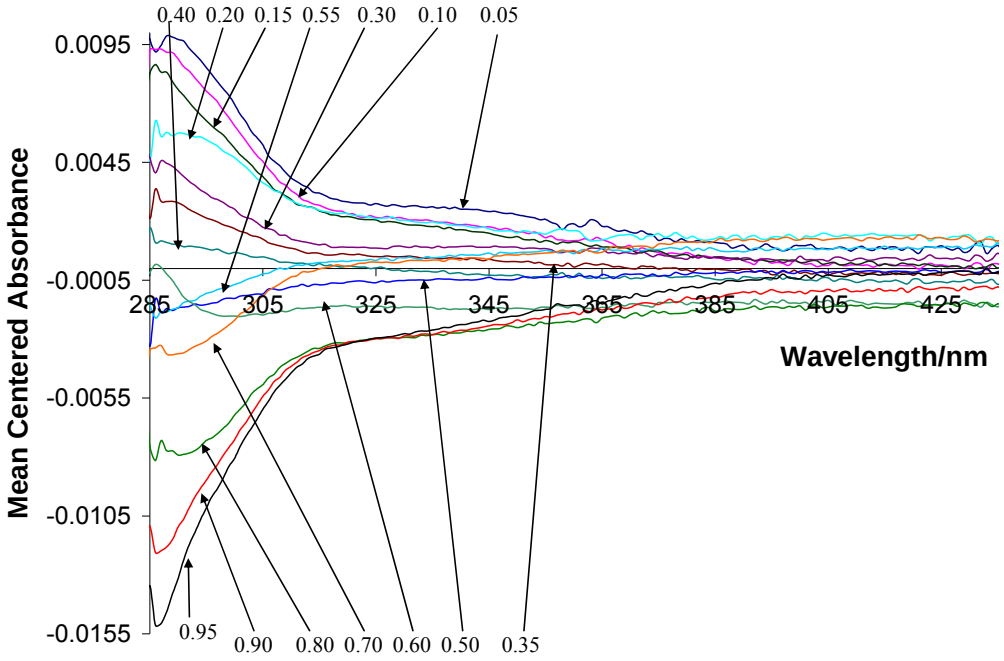

Figure 2.18. Mean-centered spectra of the UV absorption spectra shown in Figure 2.17A for the fourteen control samples (not heated) of tyrosine. The spectra are labeled in terms of the mole fractions (to two decimal places) of the D-tyrosine enantiomer.

propandiol. Unlike the enantiomers, the non-covalent tyrosine-PD diastereomers are two different compounds with different properties, hence the spectral difference recorded for the control tyrosine sample solutions.

Figure 2.19A, B, C, and D show the PLS-1 regression calibration model plots for six control sample randomly selected from the fourteen prepared for analysis. The six calibration samples consist of D-tyrosine mole fractions of: 0.0492, 0.199, 0.299, 0.504, 0.800, and 0.950. Figure 2.19A is the scores plot, which is constructed as a plot of the second PC verses the first PC. Figure 2.19B is the regression coefficient as a function of

wavelength plot, 2.19C the percent explained variance versus PC plot, and 2.19D the calibration and cross-validation regression lines plot. The scores plot in Figure 2.19A reveals a pattern in the control samples that is similar to that for the NSCCDS tyrosine samples. However, the regression coefficient plot in Figure 2.19B shows that the relevant spectral information in the spectral data for the control samples of tyrosine, is resident in a longer wavelength region than identified for the NSCCDS tyrosine samples (see Figure 2.16B). The explained variance plot in Figure 2.19C shows that four PCs were computed with percent variances of not less than 99.58 %. The first PC explained 98 and 100 % of the variation in the spectral data and enantiomeric composition respectively while the second PC explained 2% of the variation in the spectral data and 0 % of the variation in enantiomeric composition. Because the variation explained by the second PC is insignificant, the first PC, which explained almost the entire variation in the data, was adequate for the model. Thus, the model was developed based on one PC. Similar to the scores plot, the regression line plot in Figure 2.19D shows that the fitted calibration and cross-validation regression lines for the control samples of tyrosine are not significantly different from the lines obtained for the NSCCDS tyrosine samples.

Table 2.9 shows the plot statistics for the calibration and cross-validation regression lines of the two sets of tyrosine calibration samples (control and NSCCDS). The table shows that both the calibration and cross-validation plot statistics of the two sets of calibration samples of tyrosine compare favorably with each other.

Table 2.10 compares the absolute errors of prediction computed for the mole fractions of a set of NSCCDS and control validation samples of tyrosine. The result forthe NSCCDS samples is the same result reported earlier in Table 2.8; they are repeated

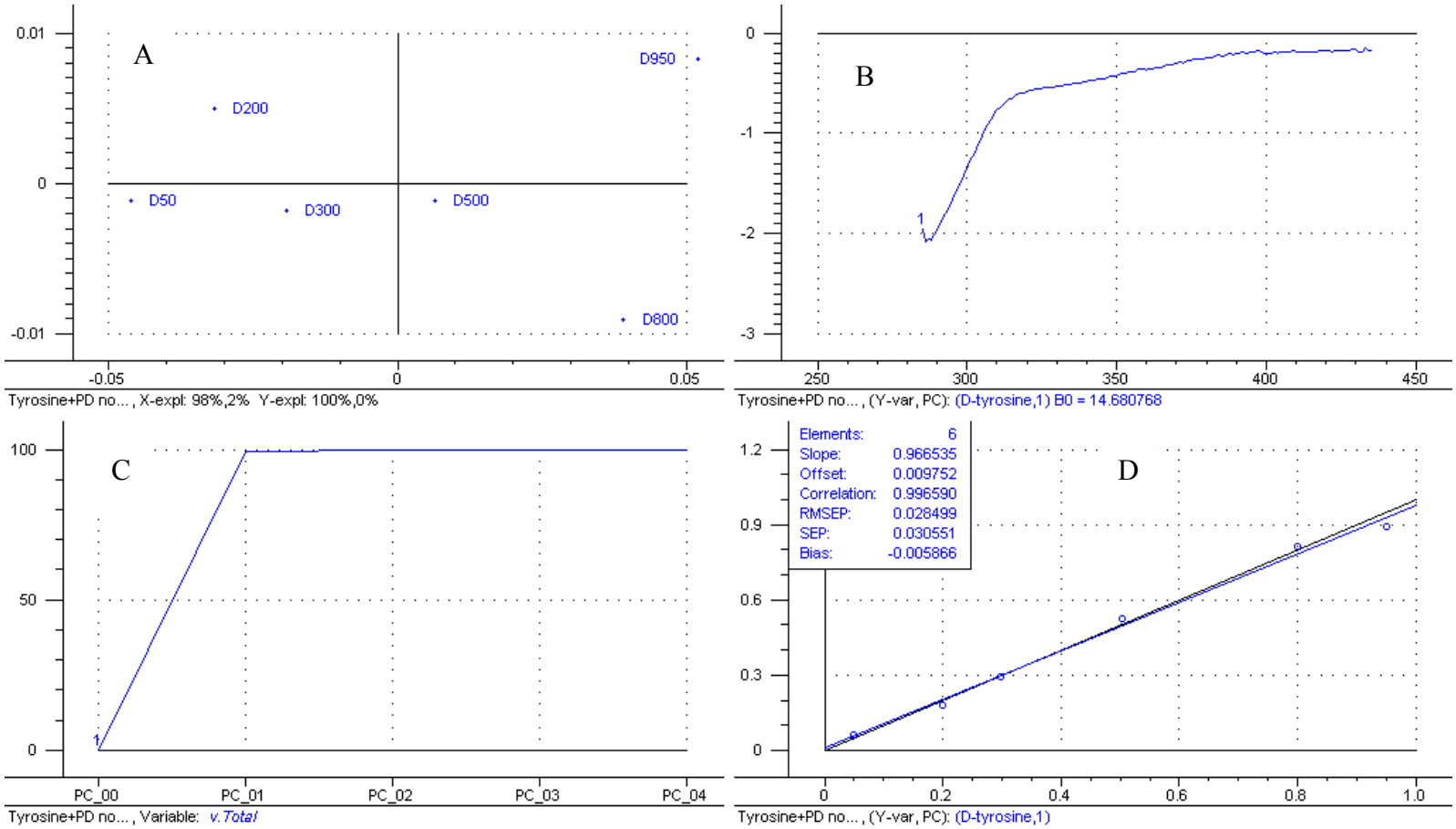

Figure 2.19. Plots of PLS-1 regression calibration model developed using the UV absorption spectral data and known enantiomeric compositions of control calibration samples of tyrosine. A: scores plot, B: regression coefficient as a function of wavelength plot, C: percent explained variance as a function of principal component plot, and D: calibration and cross-validation regression lines for the fitted (black) and predicted (blue) mole fractions, respectively, versus the known mole fractions of calibration samples. The model required only one PC (see below plot B or D).

Table 2.9. Regression Plot Statistics for Calibrating and Cross-Validating 2.5 mM NSCCDS and control calibration samples of tyrosine

Regression Plot Statistic (RPS)	RPS value for NSCCDSS[a] Calibration	RPS value for Control Samples Calibration	RPS value for NSCCDSS Cross-Validation	RPS value for Control Samples Cross-Validation
Slope	0.998	0.998	0.985	0.967
Offset	0.000755	0.00102	0.016	0.00975
Corr[b]. Coefficient	0.999	0.999	0.989	0.997
RMSE[c]	0.0057	0.015	0.023	0.028
SE[d] (SDR)[e]	0.0062	0.016	0.023	0.031

[a] Non-separative, covalent, chiral discrimination strategy samples, [b] Correlation, [c] Root-mean-squares error, [d] Standard error, [e] Standard deviation of residuals

here in Table 2.10 for the purpose of comparison. It is obvious from the table that except for the NSCCDS sample with D-tyrosine mole fraction of 0.300, the absolute errors computed for both sets of validation samples are, generally, quite low. However, most of the predictions for the control analysis are slightly better than the predictions for the

Table 2.10. Comparison of the predicted mole fractions of D-tyrosine (Tyr) in the 2.5 mM NSCCDS and control validation samples of tyrosine made up of varying enantiomeric compositions of D- and L-Tyr.

Actual D-Tyr ø[a] for NSCCDS[b] Sample	Predicted D-Tyr ø for NSCCDS Sample	Absolute error for NSCCDS Sample	Actual D-Tyr ø for Control Sample	Predicted D-Tyr ø for Control Sample	Absolute error for Control Sample
0.800	0.794	0.006	0.100	0.109	0.009
0.750	0.737	0.013	0.150	0.153	0.003
0.550	0.581	-0.031	0.344	0.357	0.013
0.300	0.248	0.052	0.400	0.427	0.027
0.200	0.166	0.034	0.599	0.568	-0.031
0.100	0.0766	0.0234	0.898	0.884	-0.014
RMSEP[c]		0.030			0.019

[a] Mole fraction, [b] Non-separative, covalent, chiral discrimination strategy, [c] Root-mean-square error of prediction

NSCCDS analysis. The root-mean-squares error of prediction computed for the control analysis is 0.019 and that for the NSCCD analysis is 0.03. In the case of phenylalanine, root-mean-square errors of prediction of 0.014 and 0.026 were computed for the NSCCDS and control analysis respectively. These prediction errors show that the non-covalent discrimination, which is responsible for the control analyses, is comparable to the covalent discrimination approach, NSCCDS, for the analysis of the two amino acids.

Analysis of NSCCDS and Control Samples of Atenolol

Figure 2.20 shows the UV absorption spectra from 235 to 335 nm for the 2 mM control stock solution of *R*-Atenolol and the 2 mM stock solution of *R*-Atenolol prepared by reaction the enantiomers of Atenolol with PD in the presence of HCl (NSCCDS solution). Figure 2.20 clearly shows that the NSCCDS and control solutions of *R*-Atenolol are spectrally different. The spectral effect of reacting PD with Atenolol, as shown in Figure 2.20, is similar to the spectral effect recorded for reacting phenylalanine with PD (compare with Figure 2.7): *R*-Atenolol reacted with PD has higher UV absorbance in certain wavelength regions (243 to 280 nm and 290 to 300 nm) than the corresponding control solution (no heating). It was noticed during the sample preparation, that the reaction of Atenolol with (*S*)-(+)-1,2-propanediol in the presence of HCl, resulted in the formation of a light brown liquid product from an initially colorless liquid. This change in color, coupled with the difference in absorbance recorded between the two stock solutions of *R*-Atenolol (NSCCDS and control stock solutions) shown in Figure 2.20, indicate that a transformation of a sort did occur. The transformation could

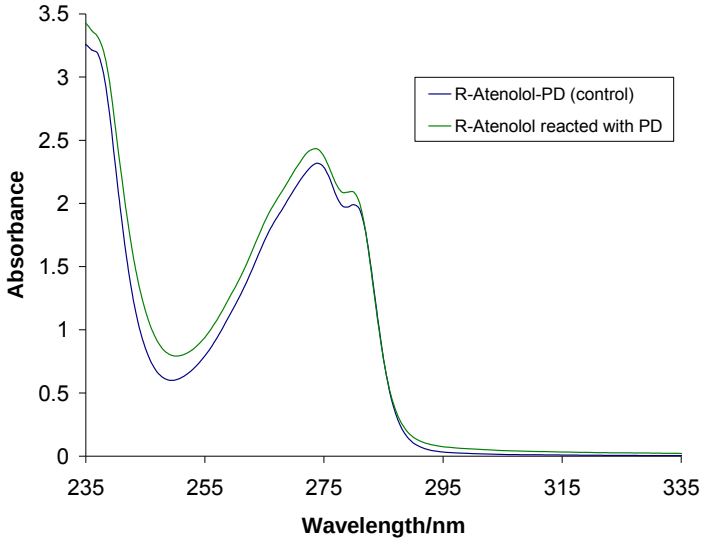

Figure 2.20. UV absorption spectra for 2 mM control stock solution of *R*-Atenolol (blue spectrum).and 2 mM stock solution of *R*-Atenolol prepared by reaction *R*-Atenolol with PD (NSCCDS Atenolol).

possibly be the formation of an ester of Atenolol as explained earlier. However, this cannot be substantiated because we do not have experimental evidence.

Figure 2.21A and B show the mean-centered UV absorption spectra for fourteen samples each of the NSCCDS and control Atenolol samples, respectively. Both mean-centered spectra, which are labeled in terms of the mole fractions of the *R*-Atenolol enantiomer, reveal variations among the samples. However, the spectra are significantly different. This reveals the difference in effect of the covalent and non-covalent discrimination approaches on Atenolol. To determine how the different spectral effects reflect the discrimination of the enantiomers of Atenolol, the spectral data for the two sets of Atenolol samples were subjected to PLS-1 regression analysis.

Figure 2.22A, B, C, and D show the multivariate, PLS-1 regression, calibration model plots for seven NSCCDS calibration samples of Atenolol, which were randomly selected from the fourteen samples prepared. The calibration samples consist of *S*-

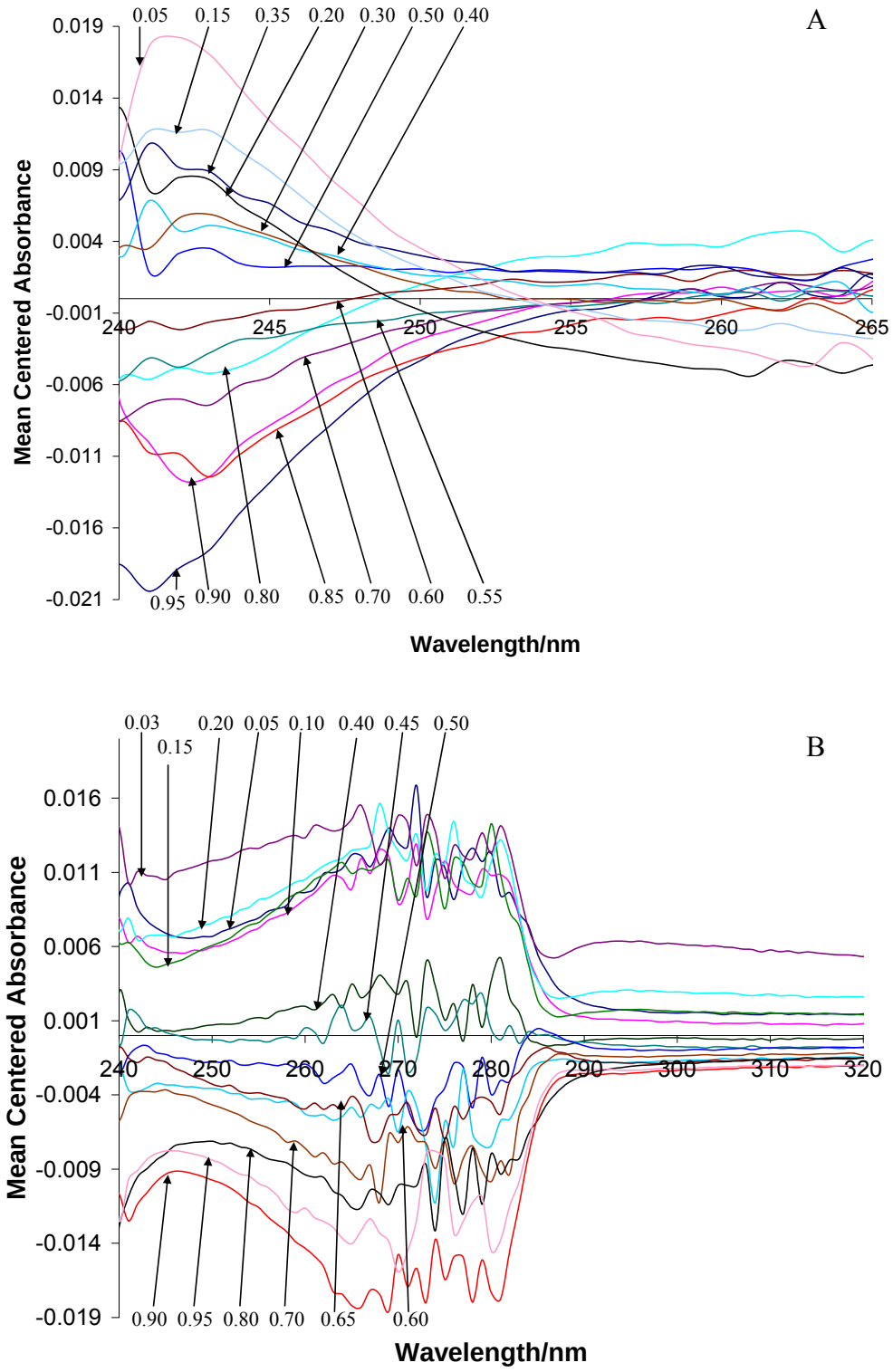

Figure 2.21. Mean centered spectra of the UV absorption spectra for the two sets of fourteen Atenolol samples. A: Mean-centered spectra for the NSCCDS Atenolol samples (heated). B: Mean-centered spectra for the control Atenolol samples (not heated). The spectra are labeled in terms of the mole fractions (two decimal places) of the *R*-Atenolol enantiomer.

Atenolol mole fractions of: 0.0493, 0.148, 0.299, 0.398, 0.499, 0.712, and 0.951. Figure 2.22A is the scores plot, 2.22B is the regression coefficient as a function of wavelength plot, 2.22C is the percent explained variation versus PC plot, and 2.22D is the fitted and predicted (by cross-validation) versus actual mole fraction regression lines (black and blue respectively) plot.

The PLS-1 regression calibration model plots developed using the data on the control samples (not heated) used for calibration are shown in Figure 2.23A, B, C, and D. Figure 2.23A is the scores plot, 2.23B is the regression coefficient as a function of wavelength plot, 2.23C is the percent explained variation versus PC plot, and 2.24D is the fitted and predicted (by cross-validation) versus actual mole fraction regression lines (black and blue respectively) plot. The calibration model for the control analysis was developed from the spectral data of six instead of seven randomly selected control samples. This is because one sample was identified as an outlier. The six calibration samples consist of *S*-Atenolol mole fractions of: 0.0495, 0.200, 0.349, 0.501, 0.551, and 0.899. The scores plots, Figure 2.22B and 2.23B, for the two sets of Atenolol samples (NSCCDS and control samples) are similar; show increasing order from left to right of *S*-Atenolol composition. Similarly, the regression coefficient plots (see Figure 2.22B and 2.23B) show that the same spectral band region is required in developing models for the two sets of calibration samples. However, all of the regression coefficients computed for the control samples, unlike the NSCCDS samples, are positive. This indicates that the sample compositions change in the same direction with the spectral data. The percent variances versus PC plots (see Figure 2.22C and 2.23C) are also similar. The average percent variance for the PCs of the NSCCDS model is 96.63 % and that for the PCs of

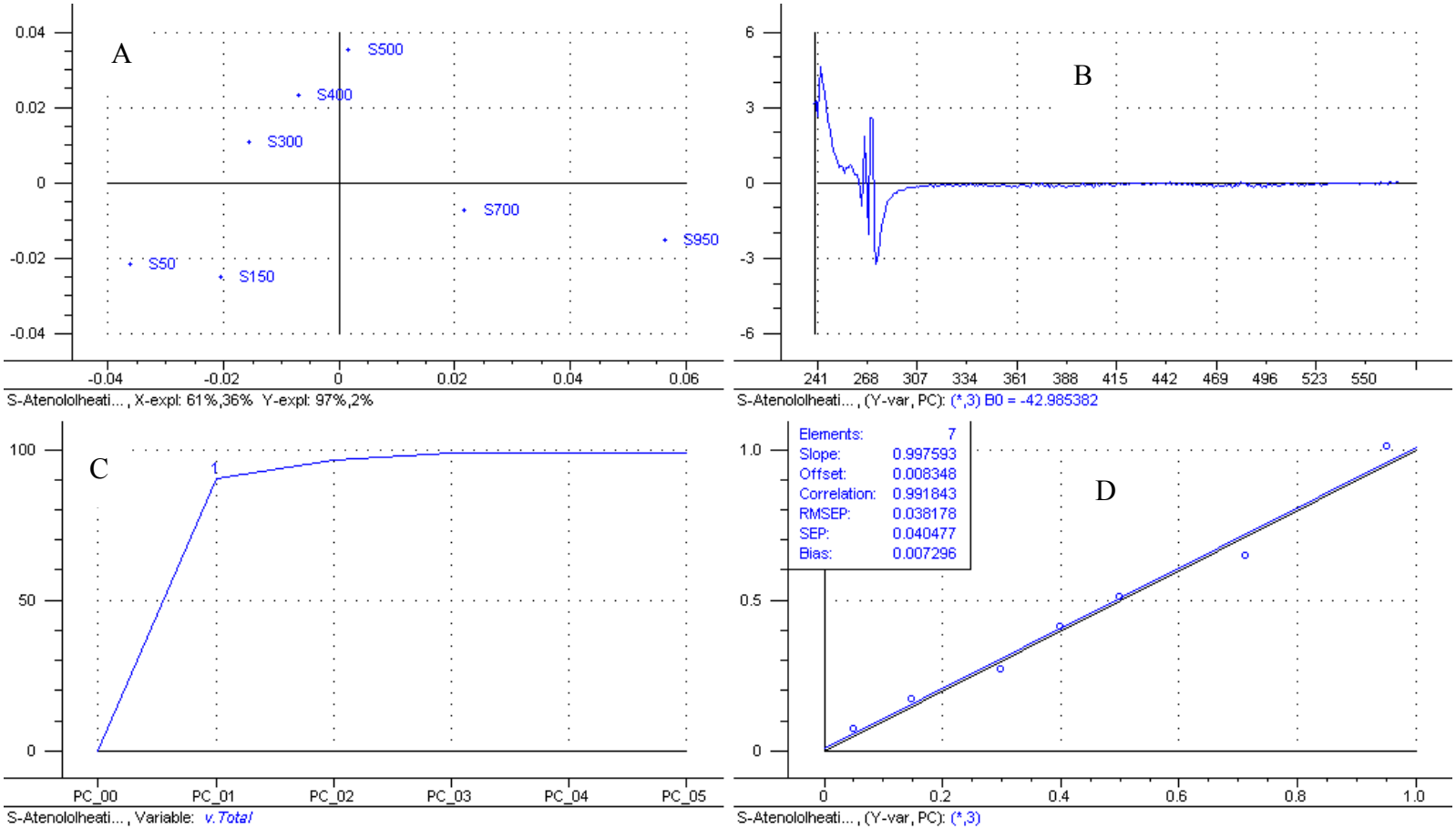

Figure 2.22. Plots of PLS-1 regression calibration model developed using the UV absorption spectral data and known enantiomeric compositions of NSCCDS calibration samples (heated) of Atenolol. A: scores plot, B: regression coefficient as a function of wavelength plot, C: percent explained variance as a function of principal component plot, and D: calibration and cross-validation regression lines for the fitted (black) and predicted (blue) mole fractions, respectively, versus the known mole fractions of calibration samples. The model required three PCs (see below plot B or D).

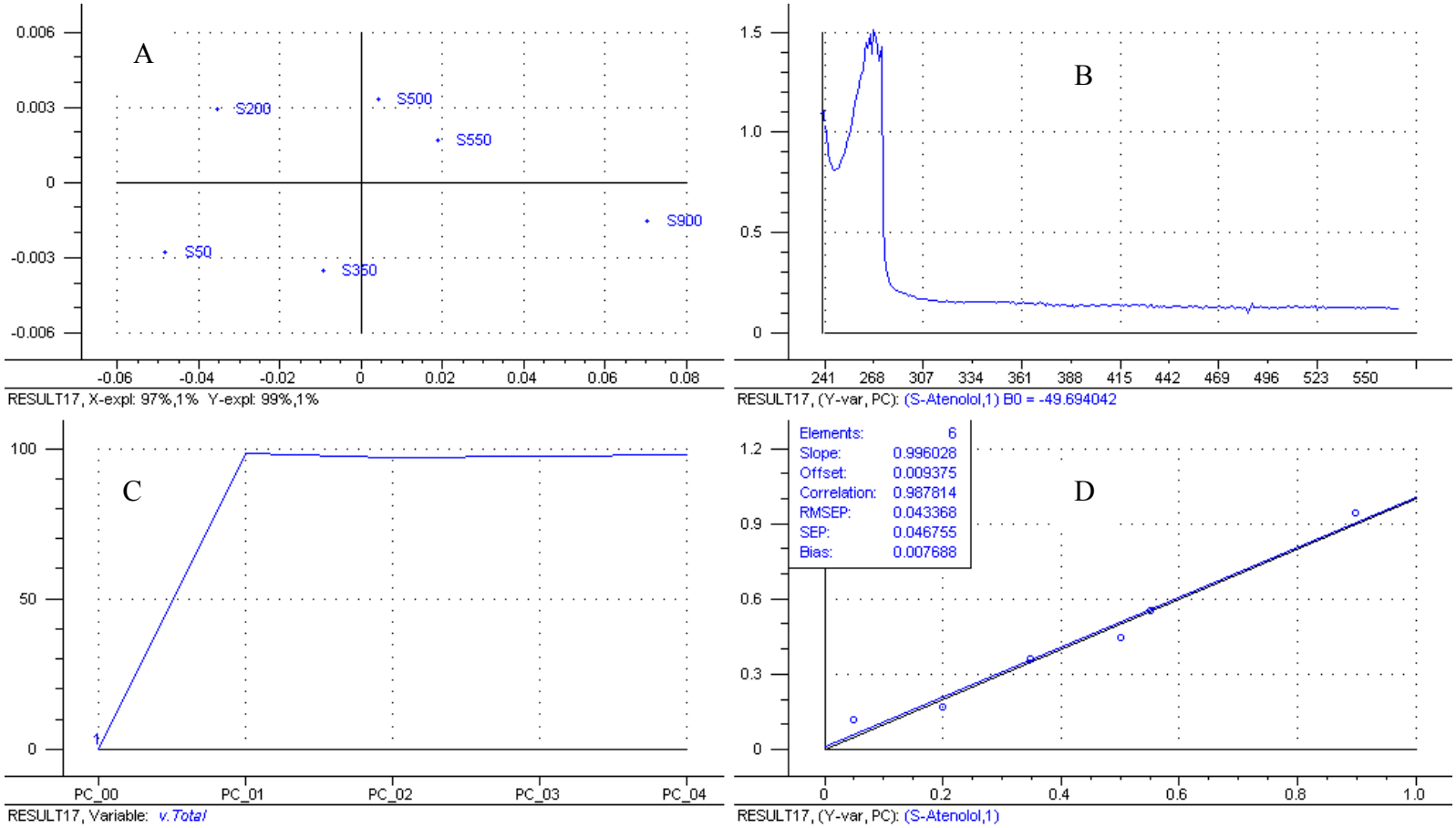

Figure 2.23. Plots of PLS-1 regression calibration model developed using the UV absorption spectral data and known enantiomeric compositions of control calibration samples of Atenolol (not heated). A: scores plot, B: regression coefficient as a function of wavelength plot, C: percent explained variance versus principal component plot, and D: calibration and cross-validation regression lines for the fitted (black) and predicted (blue) mole fractions, respectively, versus the known mole fractions of the calibration samples. The model required only one PC (see below plot B or D).

the control model is 97.68 %. Three PCs were needed for the NSCCDS model, the first two of which explained 97 % (61 plus 31 %) of the variation in spectral data and 99 % (97 plus 2 %) of the variation in enantiomeric composition. On the other hand, only one PC was required for the model developed using data on the control samples. This model explained 97 and 99 % of the variation in the spectral data and enantiomeric composition respectively. The plot statistics computed for the fitted calibration and cross-validation regression lines shown in Figure 2.22D and 2.23D, respectively, for the NSCCDS and control samples are reported in Table 2.11. Though most of the values of the plot statistics shown in Table 2.11 compare favorably, the root-mean-square and standard errors for these two sets of samples differ: data for the control calibration samples are associated with higher errors than the data on the NSCCDS calibration samples.

Table 2.12 compares the results of predicting the rest of the fourteen NSCCDS and control samples of Atenolol used as validation samples. These two sets of validation samples were predicted using the corresponding calibration models, whose plots are shown in Figure 2.22 and 2.23, respectively. It is obvious from the table that the absolute errors computed for predicting the NSCCDS samples, compared to those computed for the control samples, are smaller. For example, an absolute error as high as -0.492, was computed for the control sample with *S*-Atenolol mole fraction of 0.701. The highest absolute error of prediction computed for the NSCCDS samples is 0.072. The root-mean-square error of prediction (RMSEP) computed for the control analysis of Atenolol is 0.21. This error is five times higher than the RMSEP of 0.042 computed for the NSCCDS analysis. With 97 and 99 % of the variation in the spectral data and enantiomeric composition explained by the PC used for the model developed for the

Table 2.11. Regression Plot Statistics for Calibrating and Cross-Validating 2mM NSCCDS and control calibration samples of Atenolol.

Regression Plot Statistic (RPS)	RPS value for NSCCDSS[a] Calibration	RPS value for Control Samples Calibration	RPS value for NSCCDSS Cross-Validation	RPS value for Control Samples Cross-Validation
Slope	0.999	0.989	0.998	0.996
Offset	0.00537	0.00451	0.00835	0.00938
Corr[b]. Coefficient	0.999	0.995	0.992	0.988
RMSE[c]	0.010	0.028	0.038	0.043
SE[d] (SDR[e])	0.011	0.031	0.040	0.047

[a] Non-separative, covalent, chiral discrimination strategy sample, [b] Correlation, [c] Root-mean-square error, [d] Standard error, [e] Standard deviation of residuals

control analysis, a strong correlation in data, leading to low prediction errors would be expected. The high prediction errors computed for the control samples indicates that the spectral information associated with the calibration samples is not representative of the entire set of samples prepared for analysis. This could possibly be due to unstable and non-specific diastereomeric interactions between Atenolol and the (*S*)-(+)-1,2-propanediol chiral selector. The results for the control analysis of Atenolol is an example of a situation in which non-covalent discrimination strategies may fail because of the inability to form specific and stable non-covalent diastereomeric complexes. Our new covalent discrimination approach or strategy should be less prone to such weaknesses because it depends on the formation covalent compounds, which are relatively more stable.

Analysis of NSCCDS Samples of Norephedrine

As noted earlier, the reaction of Atenolol with PD in the presence of HCl led to the formation of a light brown liquid product with color. During the reaction of

Table 2.12. Comparison of the predicted mole fractions of *S*-Atenolol in the 2 mM NSCCDS and control validation samples of Atenolol made up of varying enantiomeric compositions of *R*- and *S*-Atenolol.

Actual ø[a] of *S*-Atenolol (NSCCDSS[b])	Predicted ø of *S*-Atenolol (NSCCDSS)	Absolute error of Prediction (NSCCDSS)	Actual ø of *S*-Atenolol (Control Sample)	Predicted ø of *S*-Atenolol (Control Sample)	Absolute error of Prediction (Control Sample)
0.101	0.116	-0.015	0.950	1.011	-0.061
0.198	0.270	-0.072	0.850	0.944	-0.094
0.451	0.419	0.032	0.800	1.026	-0.226
0.601	0.617	-0.016	0.701	1.193	-0.492
0.650	0.695	-0.045	0.601	0.634	-0.033
0.801	0.743	0.058	0.400	0.356	0.044
0.850	0.832	0.018	0.300	0.282	0.018
RMSEP[c]	0.042			0.21	

[a] Mole fraction, [b] Non-separative, covalent, chiral discrimination strategy sample, [c] Root-mean-square error of prediction

Norephedrine with the PD chiral selector, changes in color were carefully monitored over the one-hour heating process. It was observed after heating for more than three minutes at 80 ^{o}C that the samples began to develop a similar brownish coloration. Figure 2.24A and B show the colors of the solutions formed on heating Norephedrine and (*S*)-(+)-1,2-propanediol together in the presence of HCl. Figure 2.24A shows the colorless clear solutions of the two enantiomers of Norephedrine three minutes into the heating process. Figure 2.24B reveals the clear light brown liquid product obtained at the end of the one hour heating process. The color change observed in this reaction is comparable to that observed during the reaction of Atenolol with the PD chiral selector. This observation suggests that similar to the situation with Atenolol, some sort of transformation took place. As explained in the case Atenolol, we are unable to tell the type of product formed by the reaction of Norephedrine with PD because no experiments were performed to determine the products of the reaction. However, subjecting the spectral data of samples

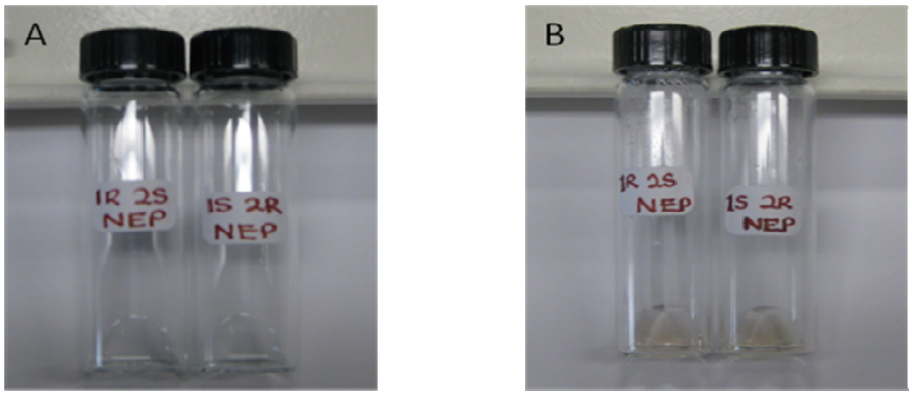

Figure 2.24. Color changes occurring during the reaction of Norephedrine with (S)-(+)-1,2-propanediol in the presence of HCl. Both compounds were heated together in the presence of HCl at 80 °C. A: color of the liquid product formed after three minutes of heating. B: color of the liquid product formed at the end of the heating process (one hour).

of the above reaction to PLS-1 regression modeling for enantiomeric composition analysis, should reveal if diastereomeric products ensued. Thus, the light brown liquids shown in Figure 2.24B were used to prepare samples, the UV spectra data of which were subjected to PLS-1 regression analysis.

Figure 2.25A shows the UV absorption spectra (225-268 nm) for sixteen samples solutions prepared using 2.5 mM stock solutions of *1R,2S*- and *1S,2R*-Norephedrine reacted with PD in the presence of HCl. The Figure 2.5 reveals that there are differences in the absorbances of the spectra of the samples. The mean centered spectra of the UV absorption spectra shown in Figure 2.5A are presented in Figure 2.5B to clearly show the differences in the spectra. The spectra are labeled in terms of mole fractions (two decimal places) of the *1S,2R*-Norephedrine enantiomer. Typical of spectra collected in these analyses, Figure 2.5B shows that the spectra for the Norephedrine samples do not vary regularly in a given wavelength region. To develop a calibration model for the analysis, a random selection, as usual, of calibration samples was performed. The mole fractions of the calibration samples in terms of the *1R,2S*-Norephedrine enantiomer

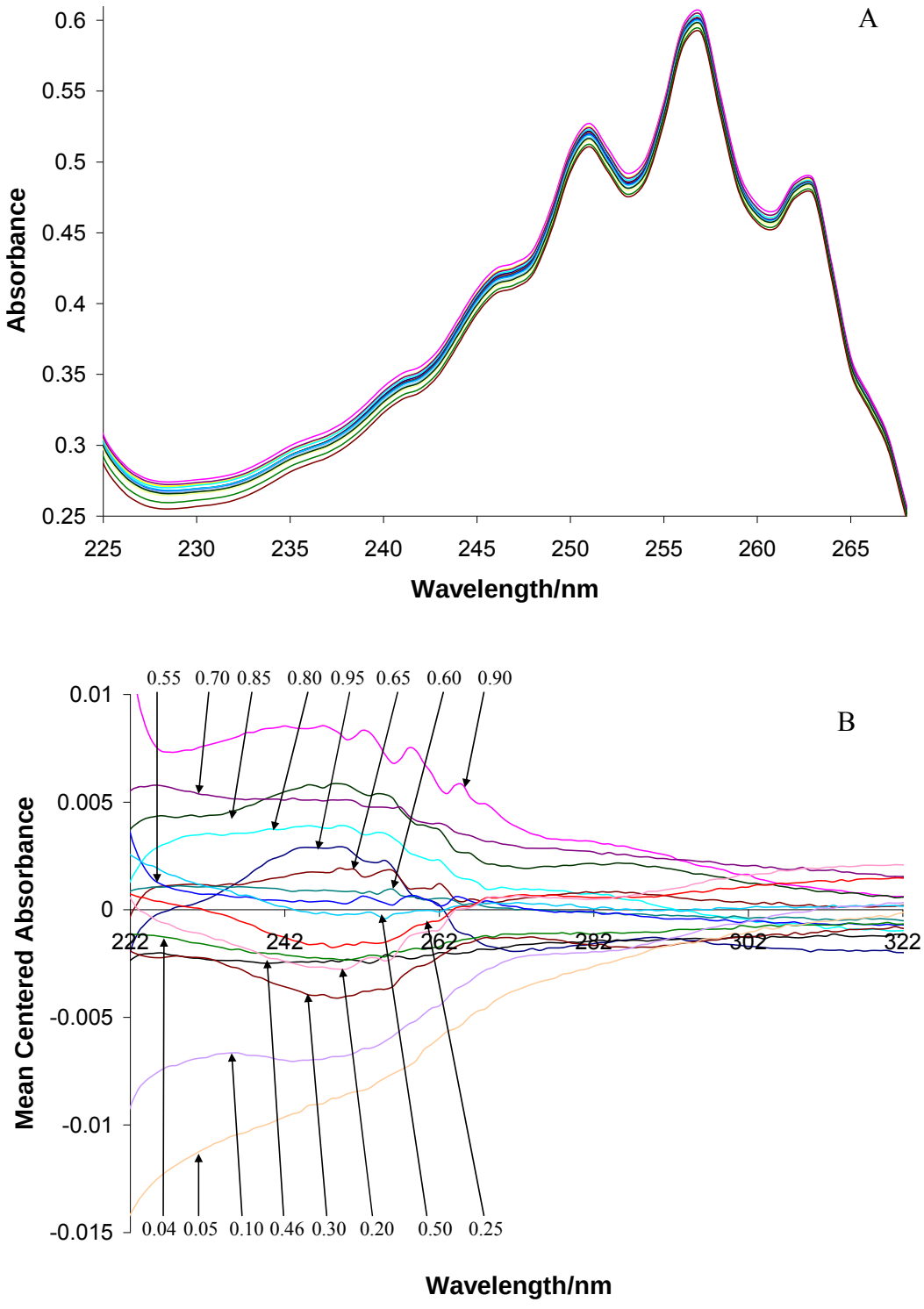

Figure 2.25. A: original UV absorption spectra of sixteen Norephedrine sample solutions prepared using 2.5 mM stock solutions of 1R,2S- and 1S,2R-Norephedrine reacted with PD (NSCCDS analysis) The samples are made up of varying enantiomeric compositions but identical total Norephedrine concentrations. B: mean centered spectra of the UV absorption spectra shown in A. The mean centered spectra are labeled in terms of the mole fractions (two decimal places) of the *1R,2S*-Norephedrine enantiomer

are0.101, 0.149, 0.399, 0.451, 0.501, 0.599, 0.701, and 0.949. The calibration model developed was then used to predict the rest of the samples used as test or validation samples.

Table 2.13 compares the results of the predicted *1R,2S*-Norephedrine enantiomer mole fractions with the actual mole fractions of the validation. Except for the

Table 2.13. Comparison of the actual and predicted mole fractions of *1R,2S*-Norephedrine in the NSCCDS validation samples of Norephedrine

Actual mole fraction of *1R,2S*-Norephedrin	Predicted mole fraction of *1R,2S*-Norephedrin	Absolute Error of prediction
0.0493	0.127	0.0777
0.200	0.216	0.016
0.301	0.283	-0.018
0.348	0.357	0.009
0.540	0.549	0.009
0.799	0.75	-0.049
0.898	0.882	-0.016
Root-mean-squares error of prediction		0.037

sample with *1R,2S*-Norephedrin enantiomer mole fraction of 0.0493, the absolute errors computed for the predicted mole fractions show that the samples were predicted with quite a high level of accuracy. The root-mean- square error of prediction computed for the analysis is 0.037, which is slightly lower than the 0.042 root-mean-squares error computed for the analysis of Atenolol. These errors indicate a similar level of performance of the covalent discrimination strategy in the analyses of these pharmaceuticals using (*S*)-(+)-1,2-propanediol as a chiral selector. The correlation of the spectral data of the samples of Atenolol and Norephedrine, prepared by reacting these

drugs with PD in the presence of HCl, with enantiomeric composition clearly indicates that the reactions resulted in a discrimination effect. Unlike these samples, samples for the control analysis of Atenolol, where no heat was applied to chemically react Atenolol with PD, resulted in a root-mean-square error as high as 0.21. As such, the NSCCDS approach employed in analyzing these pharmaceuticals has a discriminatory impact.

NSCCDS Compared to Our Previous Non-Covalent Discrimination Studies

This section compares our new non-separative, covalent, chiral discrimination strategy in which PD is used as a covalent chiral discriminator with a selected number of our existing non-covalent chiral discrimination strategies as well as the present non-covalent PD discrimination strategy (referred to herein as control analysis).

Noted in Chapter 1, the root-mean-square error (RMSE) is a frequently-used measure of the difference between the value of a quantity or parameter predicted by a model or an estimator and the actual or known value of the quantity or parameter predicted or estimated. It is a measure of accuracy and therefore employed as a figure of merit for evaluation or comparison. The RMSE is expressed in the same units as the quantity being predicted or estimated. In analyses such as this, the root-mean-square error of prediction, as it is usually referred to, is used to evaluate or compare techniques or various chiral selectors employed in the same analytical technique. The acceptable limit for this error depends on the discipline and the quantity or parameter being studied. Generally, however, the smaller the value of the RMSE is, the higher the accuracy of the results. The method or technique used to obtain such results will thus be considered to have a high RMSE figure of merit. In our chiral analysis by regression modeling of spectral data (CARMSD) technique, differences in spectral data of samples, made up of

varying enantiomeric compositions, are correlated with the enantiomeric compositions of the samples. The strength or extent of the correlation depends on how unique the spectra of the individual samples are, which in turn, depends on the effectiveness of the chiral selector and the discrimination strategy. Our prediction results, therefore, depend on the chiral selector and the discrimination strategy. Consequently, the RMSEP computed in our analyses is a direct evaluator of the chiral selector and the discrimination strategy employed.

Table 2.14 compares our new covalent discrimination strategy, NSCCDS, in which (*S*)-(+)-1,2-propanediol was used as a chiral selector, with a selected number of our previous chiral selectors and the discrimination strategies employed. The studies are compared in terms of the concentration levels at which the analyses were preformed and the root-mean-square errors of prediction computed for the analyses. In order to have a leveled ground for comparison, only studies in which a given chiral selector was used to analyze at two amino acids or two pharmaceutical molecules, comparable to those analyzed in the present study, were considered. In addition, only studies performed using UV spectroscopy as used in the present study were selected for comparison. Based on these criteria, previous UV-vis studies involving β-cyclodextrin and carboxymethyl-γ-cyclodextrin (CM-γ-CD) as chiral selectors were chosen. In these studies, both chiral selectors were used as transient, non- covalent, inclusion complex forming chiral selectors. β-Cyclodextrin was used in different studies to analyze four amino acids: aspartic acid, phenylglycine, phenylalanine, and tyrosine. Carboxymethyl-γ-cyclodextrin, on the other hand, was used to analyze two pharmaceuticals, Ephedrine and Norephedrine. The information presented on β-Cyclodextrin in Table 2.14 was taken

Table 2.14. Summary of the results for the NSCCDS study compared with the results for our existing non-covalent discrimination strategies used in the analysis of selected amino acids and pharmaceutical molecules

Discrimination Strategy	Chiral Selector	Chiral Analyte and Concentration (mM)	RMSEP
CED[a]	(*S*)-(+)-1,2-propanediol	Phenylalanine: 4	0.014
		Tyrosine: 2.5	0.030
		Atenolol: 2.5	0.042
		Norephedrine: 2.5	0.037
Non-CED	(*S*)-(+)-1,2-propanediol	Phenylalanine: 4	0.026
		Tyrosine: 2.5	0.019
		Atenolol: 2.5	0.21
	β-Cyclodextrin	Aspartic Acid: 30	0.11
		Phenylalanine: VSC[b]	0.053
		Phenylglycine: 15	0.027
		Tyrosine: 15	0.015
	Carboxymethyl-γ-Cyclodextrin	Ephedrine: 15	0.044
		Norephedrine: 7.5	0.086

[a] Covalent enantiomeric discrimination, [b] Varying sample concentration: 6.011, 6.744, 7.507, 8.233, and 9.129 mM.

from reference 55 and 56 while that on carboxymethyl-γ-cyclodextrin was taken from reference 55. The root-mean-square errors of prediction for the analyses involving these two chiral selectors were computed using the prediction results from the references.

It is clear, with reference to Table 2.14 that relatively high concentrations of analytes were required in the analyses involving the two cyclodextrins. For example, aspartic acid was analyzed at a concentration of 30 mM, which is 7.5 times higher than

the highest concentration of 4 mM employed in the analysis of phenylalanine in this present study. These high concentrations are typical of the transient, non-covalent, inclusion complex forming strategies combined with isotropic UV-vis spectroscopy by our group for chiral analysis. One factor that could possibly explain the need for such high concentrations is the nature of the non-covalent interactions responsible for the chiral discrimination. It is reported that native cyclodextrins and the carboxymethyl derivatives have hydrophobic cavities [4, 21, 34, 51], which allow easy displacement of water molecules from the cavity by hydrophobic molecules. The cavity of these cyclic glucose oligosaccharides are known to be lined up with ether-like anomeric oxygen atoms, C3, and C5 hydrogen atoms which participate in inclusion complex formation through hydrogen bonding, dipole moment, and van der Waals interactions with appropriate guest molecules. It is possible that the effectiveness of these intermolecular interactions could be influenced by how close these molecules can get to each other in solution. For example, appropriately small amounts of most hydrophobic organic liquids (e.g., toluene, benzene, etc.) will dissolve in an appropriate amount of water. This is because the molecules of these organics will be effectively dispersed in the water through intermolecular association with the water molecules. At such low concentration levels, the association of water molecules with the organic molecules becomes more effective than the organic molecule-organic molecule association. However, as the number of the organic molecules is increased in the same amount of water, the organic molecule-organic molecule association becomes more effective than the association of the organic molecules with water molecules. The organic liquid will eventually begin to separate out of solution to form its own phase. As such, concentration can influence the effectiveness

of intermolecular association in solution. It is therefore possible that the higher the concentration of cyclodextrin and the chiral analyte, the more effective the intermolecular association hence the formation of non-covalent diastereomers. Our new covalent discrimination strategy, on the other hand, is less affected by this concentration phenomenon because once the enantiomer is covalently derivatized, the covalent molecule formed inherently acquires diastereomeric properties relative to its counterpart. However, an appropriate concentration of the covalently derivatized enantiomer is needed for spectroscopic analysis. This is because the covalently acquired diastereomeric spectral property must be made sensitive to the spectroscopic probe technique. The relatively low analyte concentration required for our present covalent discrimination strategy, highlights one advantage the present strategy has over the existing non-covalent discrimination strategies. This is because smaller amounts of samples can be analyzed thereby reducing the cost of analysis. It is worth pointing out however, that high concentration is not a necessary condition for effective enantiomeric discrimination in non-covalent discrimination strategies. This is because chiral selectors could form, for example, effective or strong hydrogen bonds with appropriate chiral analytes that could lead to significant changes in spectra. Under such conditions, high concentrations may not be necessary so long as the analysis is performed at a concentration at which the spectroscopic probe technique is sensitive enough. A typical example in this present study is the successful analysis of tyrosine at 2.5 mM using (*S*)-(+)-1,2-propanediol as a non-covalent chiral selector (control analysis of tyrosine). The RMSEP computed for this non-covalent PD analysis of tyrosine is only 0.019. This shows that while concentration may be an important factor in non-covalent discrimination strategies, the

effectiveness of non-covalent discrimination strategies also depend on the analyte in question. As shown earlier, the analysis of Atenolol using (*S*)-(+)-1,2-propanediol in a non-covalent discrimination approach (control analysis of Atenolol) resulted in an RMSEP that is as high as 0.21. The high RMSEP indicates an ineffective discrimination, which may be because the concentration used was not high enough or because of the nature of Atenolol or both. However, when the same (*S*)-(+)-1,2-propanediol was used to analyze Atenolol according to our new covalent discrimination strategy, NSCCDS, at the same concentration, an RMSEP of 0.042 was computed. This is a significant improvement showing how the change in discrimination strategy is able to overcome the problem of ineffective chiral discrimination due to either the effect of concentration or type of chiral analyte or both.

Figure 2.26 shows the bar plots for the root-mean-square errors of prediction computed for the various studies involving the three chiral selectors: PD, β-CD, and CM-γ-CD. For each chiral selector and strategy, the lowest RMSE value (LREV), the highest RMSE value (HREV), and the range of the RMSE values (RER) for the analysis of at least two chiral compounds in each class of amino acids and pharmaceuticals, are plotted. The range of the RMSE is computed by subtracting the LREV from the HREV.

For the analyses of the amino acids, Figure 2.26 shows that the LREVs computed for the use of PD for the present covalent discrimination (green bar, 0.014) and non-covalent discrimination (purple bar, 0.019) studies, are comparable to the LREV computed for β-cyclodextrin in a previous non-covalent discrimination (yellow bar, 0.015) study. In terms of the highest RMSE error values (HREV), however, β-CD has a significantly high value (yellow bar, 0.11). The HREVs for the use of PD for the

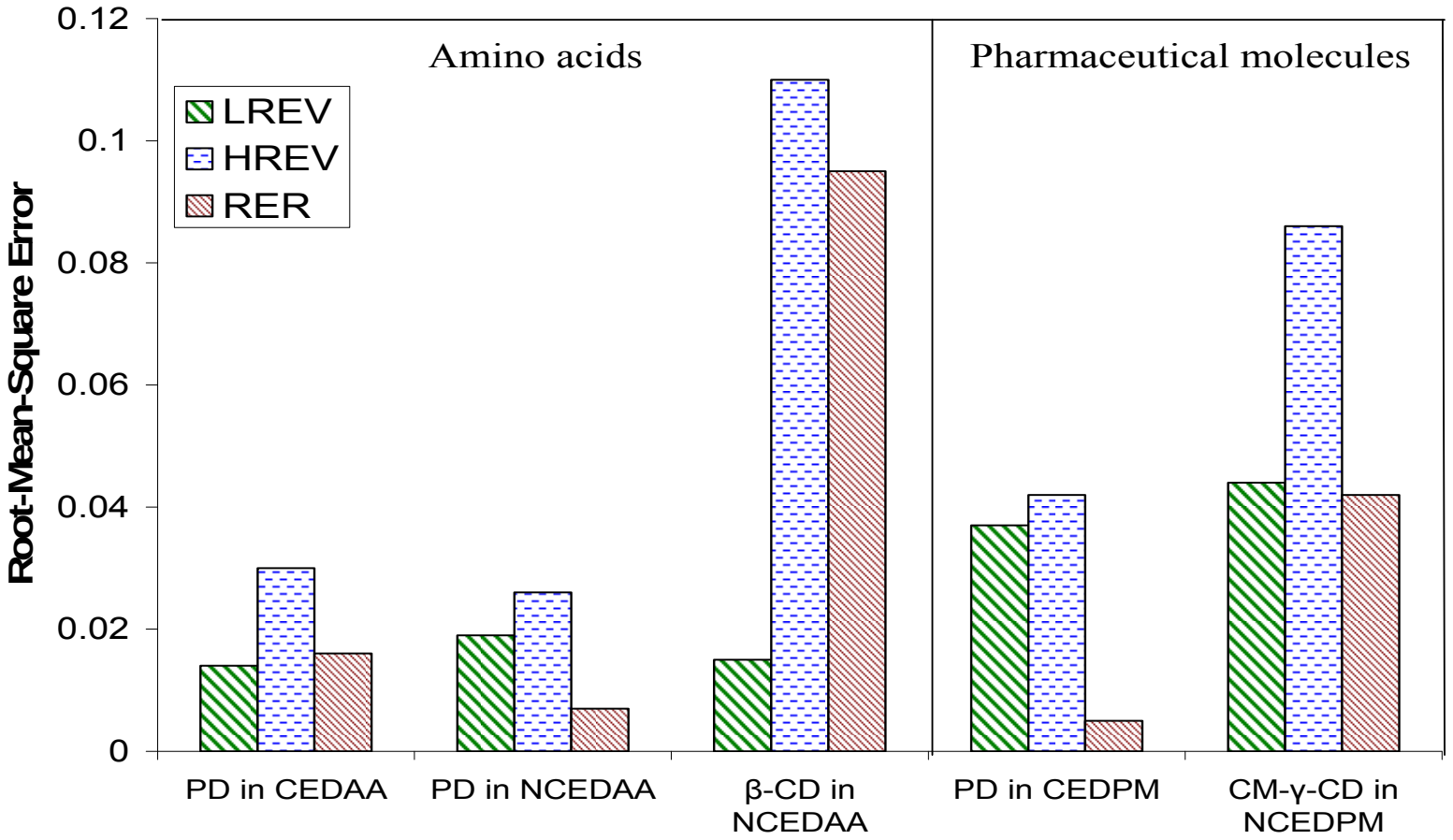

Figure 2.26. Comparison of the root-mean-square error of prediction figures of merit for chiral selectors and their discrimination approaches used in the analyses of selected amino acids and pharmaceuticals reported in Table 2.14. LREV: lowest root-mean-square error value. HREV: highest root-mean-square error value. RER: root-mean-square error range. PD: (*S*)-(+)-1,2-propanediol. β-CD: β-Cyclodextrin. CM-γ-CD: Carboxymethyl-γ-cyclodextrin. CEDAA: covalent enantiomeric discrimination of amino acids. NCEDAA: non-covalent enantiomeric discrimination of amino acids. CEDPM: covalent enantiomeric discrimination of pharmaceutical molecules. NCEDPM: Non-covalent enantiomeric discrimination of pharmaceutical molecules.

present covalent (NSCCDS studies) and non-covalent discrimination studies (control studies) are quite low: 0.03 and 0.026 respectively. The RER computed for β-CD used in previous non-covalent discrimination studies 0.095. This is significantly higher than the RERs, 0.016 and 0.007, computed for PD used in the present study for covalent non covalent discriminations, respectively. The root-mean-square error range (RER) can be used to measure not the effectiveness but the consistency of a chiral selector in its use for the analyses of a given class of chiral compounds. The smaller the RER value of a chiral selector is for a given class of analytes, the more consistent the chiral selector is for the analysis of compounds in the given class and vice versa. In this regard, PD is more consistent in its use for the analysis of the selected amino acids than β-CD because its RERs are smaller than the RER computed for β-CD used in analyzing the selected amino acids. In other words, the effectiveness of the discrimination by β-CD depends on the amino acid being analyzed than the effectiveness of the discrimination by PD employed in both the covalent non-covalent discrimination studies. Reference to Table 2.14 for the analyses of phenylalanine and tyrosine, for example, shows this to be the case. The dependency of the discrimination effect of cyclodextrins on the analyte is explained by the effectiveness of the formation of inclusion complexes, which depend on the size of the analyte relative to the cyclodextrin cavity.

With regard to the pharmaceuticals, Figure 2.26 shows that the HREV and RER computed for PD (brown bars, 0.042 and 0.005 respectively) are significantly lower than those computed for carboxymethyl-γ-cyclodextrin (CM-γ-CD) (pink bars, 0.086 and 0.042 respectively). The HREVs and RERs for PD and CM-γ-CD reveal a trend that is identical to that observed for the analyses of the amino acids using PD and β-CD. As

such, CM-γ-CD used for the non-covalent analysis of the pharmaceuticals, compares in the same way to PD used for the covalent studies of the pharmaceuticals as β-CD compares to PD for the analysis of the amino acids.

Apart from β-CD and CM-γ-CD, our group employed other chiral selectors for non-covalent discrimination studies with UV-vis, which do not fall completely under the criteria used in comparing the present PD studies with those of β-CD and CM-γ-CD. These other previous studies involved the use of mixed cyclodextrins, surfactants plus cyclodextrins, and simple sugars as chiral selectors for enantiomeric composition determination [55, 56]. The chiral compounds studied include amino acids and pharmaceuticals. These chiral compounds were analyzed at concentration levels that ranged from 3.75 to 15 mM and the root-mean-square errors of prediction computed range from 0.018 to 0.11. Similar to β-CD and CM-γ-CD, the non-covalent discrimination analyses involving these other chiral selectors show that the effectiveness of the analyses depends on the chiral analyte– a limitation that our newly developed covalent discrimination strategy, NSCCDS, is intended to overcome. As demonstrated with the analyses of phenylalanine, tyrosine, Atenolol, and Norephedrine, which yielded RMSEP values that range from 0.014 to 0.042, our new covalent discrimination strategy, NSCCDS, appears not to be analyte dependent. Consequently, in situations where our non-covalent discrimination approaches may be the cheapest and/or simplest but not necessary the most effective, our new covalent discrimination approach could be a suitable alternative.

Conclusion

Although our existing non-covalent discrimination approaches may be less cumbersome because they do not require, for example, heating, our newly developed covalent discrimination strategy, is undoubtedly more effective. The new covalent strategy appears in this study to overcome the limitations of concentration and dependency of effectiveness of chiral discrimination on type of analyte that we sometimes encounter in our non-covalent discrimination approaches. The successful analysis of the pharmaceuticals suggests that with PLS-1 regression modeling, useful information on chiral discrimination can be obtained in analyses such as this with little or no prior knowledge about the products of the reaction employed.

In general, the successful analysis of all the selected chiral analytes using our newly developed covalent discrimination approach shows that the approach can be used to effectively analyze chiral compounds similar to those studied.

Finally, with the availability of several simple covalent reactions for the conversion of enantiomeric pairs to pairs of diastereomers, our newly developed non-separative, covalent, chiral discrimination strategy, combined with PLS-1 regression modeling of spectral data, could be useful for industrial application.

CHAPTER THREE

Capillary Tube Micro Fluorometer Cell for Steady-State Fluorescence Measurement

Introduction

This chapter describes a study carried out on a capillary tube custom-designed for the measurement of steady-state fluorescence emission. This study is an alternative approach to a previous attempt made by our research group to develop a flow injection system for enantiomeric composition analysis [55]. As in the case of the previous study, the goal of this present study is to develop a high throughput microanalytical technique that can be employed in enantiomeric composition analysis.

Since the introduction, microanalytical techniques have attracted a lot of interest in chemical analysis [74]. Today, several microanalytical techniques including selected-area X-ray photoelectron spectroscopy, capillary electrophoresis, and capillary chromatographic techniques can be identified [75-82]. Mocroanalytical techniques have made possible measurement of micro-size amounts of samples, carrying out micro-scale separation and purification processes, and (3) performing micro-scale analyses of samples. Microanalytical techniques have become important because of the need to obtain detailed and specific chemical information, cut down on material usage, reduce waste, shorten analysis time, and in general, cut down the cost of analyzing samples.

Worldwide sales of chiral drugs in single-enantiomer forms continue to grow as a result of increased knowledge about the possible differential pharmacological effects of enantiomers and the benefits of single-enantiomer drugs [83, 84]. Consequently,

documentation on drug stereochemistry and the differential biological effects of enantiomers have become important issues for the pharmaceutical industry and regulatory authorities [83, 84. In addition, there is the demand for the determination of enantiomeric purity in combinatorial libraries for drug development [21]. The demand for chiral analysis techniques to cater for the needs of the chiral drug industry has therefore grown over the years. Of particular interest will be micro-scale techniques that are robust, simple, efficient, and cost effective for high-throughput applications. According to Finn, spectroscopic methods are the most promising for the rapid determination of the enantiomeric content of organic molecules [28]. Such methods will be useful, for example, in catalyst evaluation in asymmetric synthesis, chiral drug quality control, analysis of both chiral drugs and chiral biological molecules in biological samples for medical diagnosis, and finding new and better therapeutic chiral drugs [21]. Up to date, several techniques have been developed for rapid measurement of enantiomeric excess [28, 85-88]. Some of these methods include enzymatic and reaction microarrays techniques, which are designed for micro-scale applications [86, 87]. One of the recent advances in the developments of a micro-scale instrument for chiral analysis is the successful miniaturization of the polarimeter by Bobbitt and Yeung [21, 89]. The instrument consists of a 1 μL flow cell with a 1 cm pathlengh interfaced with a liquid chromatographic system. Its complicated optical design is noted to have the capability of detecting optical activity as low as 15 μdeg for 11 ng of fructose. It was, however noted that the high instrument cost and optical complexity limited the use of this instrument and the technique involved for high-throughput micro-scale applications [21]. Following this, a variety of improved polarimetric techniques coupled with chromatographic systems

were developed [21]. However, these instruments and the employed techniques, similar to that of Bobbitt and Yeung, were noted to be either too expensive or complicated and could, therefore, not be used for high-throughput chiral analysis [28]. As such, there is the need for inexpensive and efficient microanalytical techniques for routine and high throughput chiral analysis in industry as well as research.

Our research group, previously, developed a flow injection system interfaced with a Jobin Yvon-SPEX Fluoro Max-2 spectrofluorometer for fluorescence emission measurement in isotropic studies of enantiomeric composition analysis [55]. The instrumentation involved the use of a quartz capillary tube with an internal diameter of 0.2 cm as a flow cell for fluorescence emission measurement. Though sample detection with the system was generally possible, its application for enantiomeric composition analysis failed to yield the desired results.

Chapter two described the successful analysis of samples prepared using our new covalent discrimination strategy by multivariate PLS-1 regression modeling of the ordinary UV-vis spectral data of the samples. The UV-vis spectral data collection required the measurement of not less than 600 μL (0.6 mL) amounts of the samples. This volume of sample is extremely large compared to the sample size required, for example, in micro-scale capillary liquid chromatographic (LC) and electrophoretic analytical techniques [77, 79, 80], which are limited when it comes to routine and high-throughput applications. The present study is, therefore, aimed at employing a micro sample cell requiring significantly reduced sample volume, among other things, for spectral measurement in analyses such as this.

Noted earlier, the present micro-scale fluorescence measurement is a modification of our previous flow injection system in which a quartz capillary cell was employed as a flow cell. In this present study, a capillary tube was custom-designed and used as a micro sample cell for steady-state fluorescence emission measurements without a flow system. This approach is similar to the use of a regular fluorometer cell for steady-state fluorescence emission measurement of fixed volumes of sample solutions. As will be noted in the next section, the use of this cell involves simple steps that will allow its usage for routine and high throughput analyses in industry and research.

The Custom-Designed Capillary Micro Fluorometer Cell

Figure 3.1A shows our custom-designed capillary micro sample cell, which is compared with a commercial, 10 mm pathlength, micro fluorometer quartz cell shown in Figure 3.1B. Our custom-designed micro-cell is made up of a 95 mm long quartz capillary tube with an internal diameter of 1 mm. The 1 mm internal diameter represents the longest possible pathlength of the cell. The tube is fitted with a ferrule at one end. A

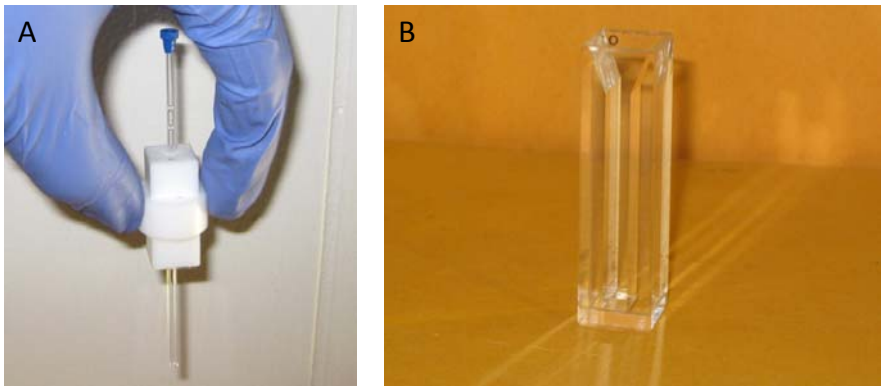

Figure 3.1 A: Custom-designed capillary micro-cell consisting of a 95 mm long capillary tube, a Teflon holder and a ferrule at one end. B: Commercial, 10 mm pathlength, micro fluorometer quartz cell. The commercial cell requires a sample volume of 1400 μL.

Teflon material, which is carefully molded to fit into the sample holder of the spectrofluorometer, functions as a holder for the capillary tube inserted perfectly in the middle of the Teflon holder. The Teflon holder allows easy handling and ensures that the capillary tube is positioned in the path of the excitation light. The cell has a number of attractive features. Firstly, the ferrule attached to one end of the cell allows, for example, water to be pushed through the tube for easy cleaning. The ferrule, also, serves as a suitable point for passing nitrogen gas through the tube for drying. Secondly, the cell has a small total volume of 75 µL, which allows for quick cleaning and drying. Thirdly, only the volume of the capillary below the Teflon holder, as shown in Figure 3.1A, needs to be filled with sample solution for measurement. This part of the cell requires only 25 µL of sample solution compared with 1400 µL sample solution required by the commercial micro-cell. In addition, filling the custom-designed micro-cell with sample solution does

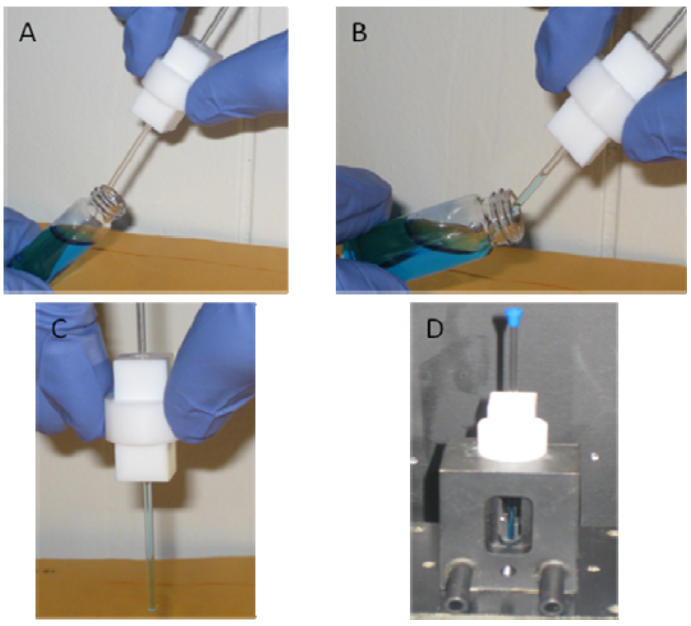

Figure 3.2 A: Custom-designed micro-cell before filing. B: Sample solution filling by capillary action. C: Sample solution holding by capillary action. D: Cell position during measurement.

not require any kind of pipet. Sample solutions are admitted into the cell by capillary action. The same force of action holds the sample solution vertically in the capillary tube when it is placed in the sample cell holder of the spectrofluorometer. Figure 3.2A, B, C, and D portray the stages involved in sample measurement using the capillary cell. Figure 3.2A shows the capillary cell before filling, 3.2B during sample solution filling by capillary action, Figure 3.2C sample solution holding by capillary action, and Figure 3.2D the cell position in the spectrofluorometer during spectral measurement.

Spectral Measurement Ttest

Initial spectral test. The performance of our custom-designed micro-cell, as a fluorescence cell, was initially verified in comparison with the commercial fluorescence micro-cell shown in Figure 3.1B. This was done by using it to record the emission spectra of deionized water and a solution of 2 mM tyrosine. The deionized water was excited at 274 nm even though water is usually excited at 350 nm for instrument calibration purposes in fluorescence spectroscopy. Usually, most fluorescence active molecules are excited at wavelengths lower than 350 nm, which will require that in order for our custom-designed capillary cell to be useful, it should allow for sample excitation in the far and mid UV regions. As such, the deionized water was excited through the capillary cell at the excitation wavelength for tyrosine to reveal, if any, possible interference.

Figure 3.3 shows the fluorescence emission for the deionized water from 282-500 nm recorded using our custom-designed capillary cell and the commercial fluorometer cell at 2 or 5 nm emission slit widths. Spectrum A is the emission spectrum of the

deionized water recorded using the commercial (10 mm pathlength) cell with the instrument emission slit width set at 5 nm. Spectrum B in the same figure is the emission spectrum of the deionized water recorded using our custom- designed capillary cell with the instrument emission slit width set at 2 nm and spectrum C the emission spectrum of

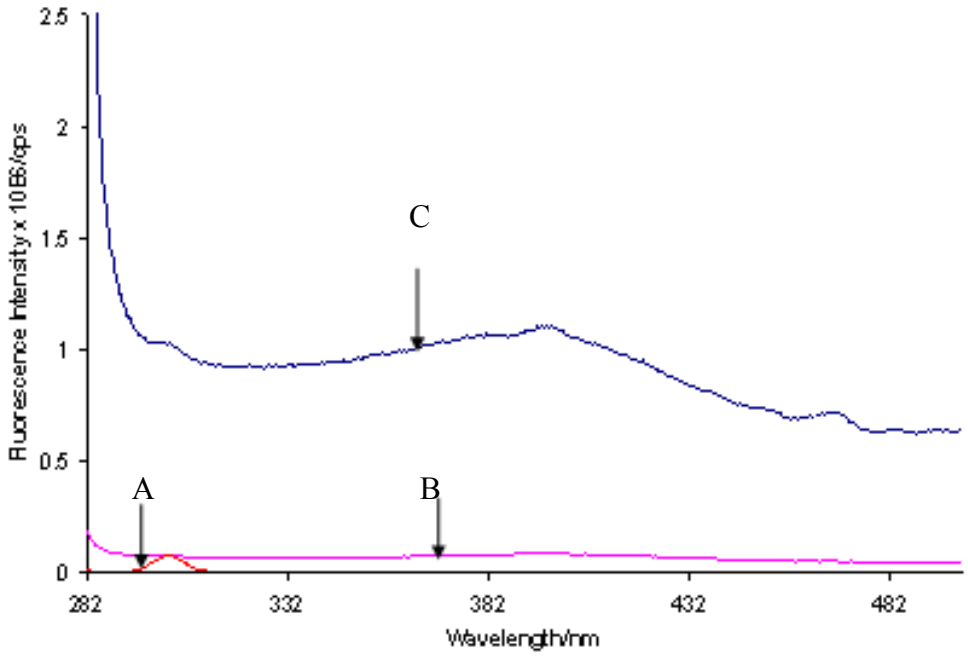

Figure 3.3 A: Fluorescence emission spectrum for deionized water collected using the commercial cell at an emission slit width of 5 nm, B and C: Fluorescence emission spectrum for the same deionized water recorded using our custom-designed capillary cell at emission slit widths of 2 and 5 nm, respectively.

the same water recorded using the capillary cell but at an emission slit width of 5 nm. Spectrum C, in Figure 3.3, shows an unusually intense and broad emission peak over the entire wavelength scanned (282-500 nm). The peak of the emission is centered on 397 nm with shoulders at 301 and 470 nm. This is in sharp contrast with spectrum A recorded with the commercial cell. Spectrum A reveals only the peak at 301 nm, which is by far, of significantly lower emission intensity. Contrary also to spectrum C, the emission intensity of spectrum B, which was recorded using the same capillary cell but at

an emission slit width of 2 nm, is similar to that for spectrum A recorded using the commercial cell. The emission, however, covers the entire wavelength region scanned as recorded for at the 5 nm slit width. These results show that the capillary tube fluoresces and possibly scatters light strongly in contrast with the commercial cell. Spectrum B, compared with C, indicates that the intensity of the emission and possibly scattered light of the capillary tube can be controlled by manipulating the instrument emission slit. As such, the spectral measurement test using the 2 mM tyrosine solution was performed with the instrument emission slit width set at 2 nm. However, the spectra collected with the commercial cell for comparison were recorded at an emission slit width of 5 nm. This is because the use of narrower slit widths resulted in noisy spectra.

The set of spectra (282 to 500 nm) labeled A, in Figure 3.4, are ten replicated fluorescence emission spectra of the 2 mM tyrosine solution recorded using the capillary cell. The set of spectra labeled B, in the same Figure 3.4, are eight fluorescence emission spectra of the same tyrosine solution recorded over the same wavelength range as A using the commercial cell. The solution was excited at 274 nm in both cases. The spectra were collected after an instrument warm up time of thirty minutes. Two obvious deductions can be made from Figure 3.4. Firstly, the usual fluorescence emission peak maximum of tyrosine is identically recorded in both sets of spectra. This indicates that there is no compromise on essential spectral features in the use of our custom-designed capillary micro-cell compared with the 10 mm commercial cell. Secondly, spectral fluctuation is similar in the use of both cells. These obvious deductions indicate that our custom-designed capillary cell compares favorably with the 10 mm commercial cell in terms of spectral recording. However, the intensities of the spectra recorded using the capillary

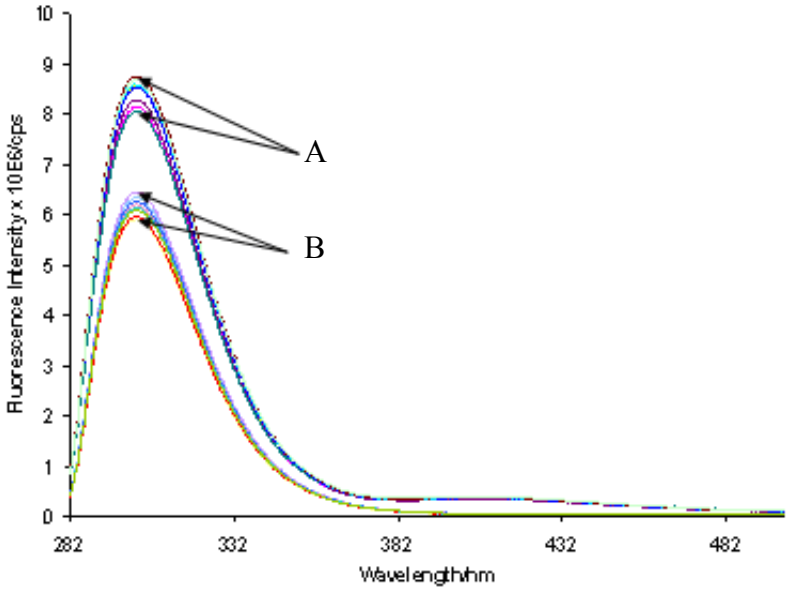

Figure 3.4. A: Ten spectral replicate of the fluorescence emission spectrum of 2 mM tyrosine solution collected using the capillary cell, B: Eight spectral replicates of the fluorescence emission spectrum of the same 2 mM tyrosine solution collected using the 10 mm commercial cell.

cell are higher than those recorded using the commercial cell. This could mean higher sensitivity in fluorescence detection with the use of our capillary cell. Spectra set A in Figure 3.4 reveals a low and broad intensity peak centered on 397 nm in the spectra collected using the capillary cell. No such peak is recorded in the use of the commercial cell.

UV excitation spectral response. The broad peak revealed by the spectra for the 2 mM tyrosine solution collected using the custom-designed capillary cell appear to be characteristic of the capillary tube. This is because it is present in the fluorescence emission spectrum for deionized water (see Figure 3.3C) recorded using the capillary cell at the 5 nm emission slit width. Consequently, two experiments were designed to investigate the response of the custom-designed capillary cell to UV excitation. The first experiment was to measure the UV excitation spectral response of the empty capillary

cell at a higher excitation frequency in comparison with that of the empty commercial cell and the detector signal recorded at the same excitation wavelength. To do this, the cells were excited at 257.5 nm and the emissions scanned from 274-450 nm. The detector signal was recorded over the same wavelength range with the excitation light turned on at 257.5 nm without any cell in the cell compartment.

Figure 3.5A shows the UV excitation spectral response for the empty capillary cell recorded with the instrument emission slit width set at 3 or 5 nm. Figure 3.5B shows the spectral response of the empty commercial cell and the detector signal. The signals in Figure 3.5B were recorded with the width of the spectrofluorometer emission slit set at 5 nm. It is obvious from Figure 3.5A that the capillary tube used for our micro-cell fluoresces strongly over the entire wavelength scanned. This is in contrast with the commercial micro fluorometer quartz cell, whose signal is just about twice the detector signal. The intense and broad fluorescence emission recorded for the capillary tube suggests that the quartz material from which the capillary tube is made might be contaminated with strong fluorescence or UV active materials. It is also possible that the emission signal observed for the capillary tube might be coupled with strong scattering of the excitation light.

Usually, scattering signals in fluorescence emission can be easily verified because scanning the fluorescence emission over wavelengths including the excitation wavelength should reveal a Rayleigh (excitation peak) peak. In addition, scattering signals in emission spectra are easily identified due to the fact that they are always red-shifted by a fixed frequency from the excitation wavelength irrespective of the excitation wavelength.

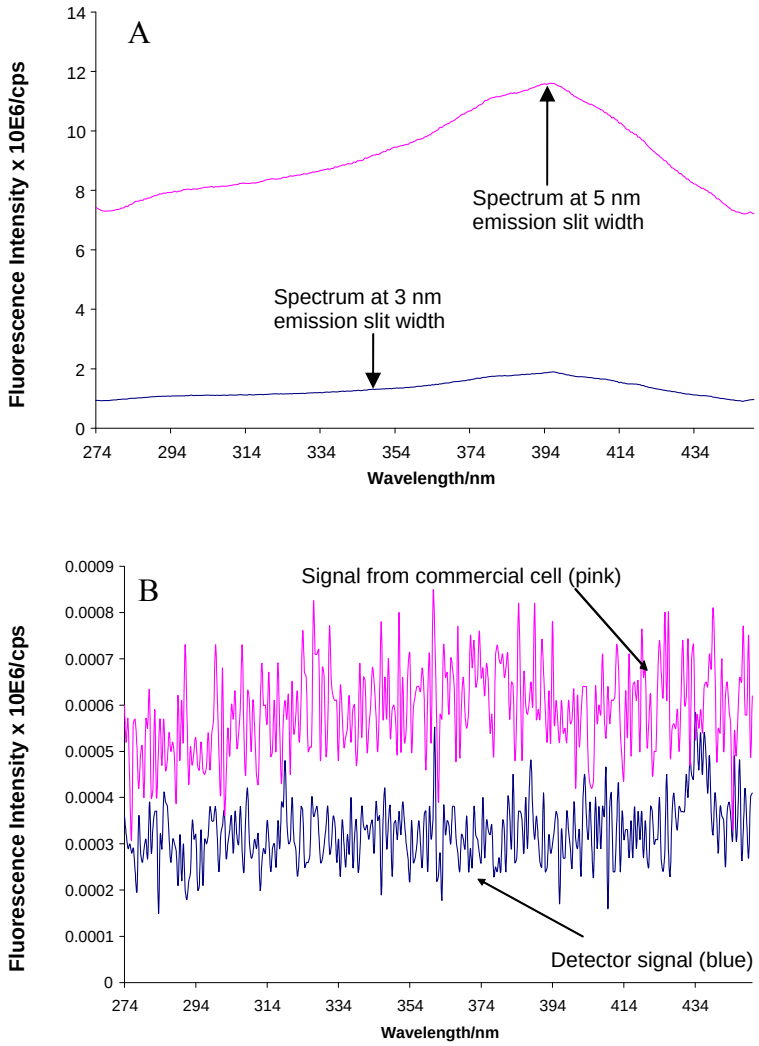

Figure 3.5 A: The fluorescence emission spectra of the empty capillary tube used for the custom-designed capillary cell. The spectra were recorded with the instrument emission slit set at 3 or 5 nm, B: Signal recorded for the empty commercial cell (pink) and the detector signal (blue).

Moreover, unlike fluorescence emission peaks, they usually appear as narrow bands. In view of the ease of verifying scattering in fluorescence emission measurement, the second experiment was designed to determine whether the capillary tube scatters and absorbs UV light as suspected. For this determination the empty capillary cell was excited at two wavelengths, 257.5 and 350 nm. The spectral responses at these wavelengths were compared with those of deionized water excited through the

commercial cell at the same wavelengths. Scattering signals in fluorescence emission spectra of a sample can be confirmed by changing the excitation wavelength. This is because changing the excitation wavelength would cause the position of the Raman band to change correspondingly. For example, the emission spectrum of water exhibits a Raman band at 397 ± 1 nm when excited at 350 nm. Changing the excitation wavelength to 257.5 nm will cause the position of the Raman band to be shifted to 282 ± 1 nm, which is the same frequency from 257.5nm as 397 ± 1 nm is from 350 nm. As such, the presence of an excitation peak and a scattering signal in the emission spectra of the empty capillary cell excited, for example, at 257.5 nm, can be confirmed by excitation at 350 nm (hence the excitation at two wavelengths). Though the Raman band positions might differ, collection of the emission spectra of water at the two excitation wavelengths (257.5 and 350 nm) was to confirm by comparison, suspected light scattering behavior of the capillary tube.

Strong absorption of excitation light can be verified using the intensity of an excitation peak and its Raman band in the fluorescence emission spectra of an excited sample. This is because complete absence of an excitation peak in the emission spectrum of a sample, scanned over wavelengths including that of the excitation, will indicate complete absorption of the excitation wavelength by the sample. In addition, a significant reduction in intensity of the peak of a given excitation wavelength will be accompanied by a low intensity Raman band relative to the Raman band associated with an excitation wavelength at which lesser amount of the excitation light is absorbed. Consequently, exciting the capillary cell at 257.5 and 350 nm and collecting the emission

spectra over wavelengths including 257.5 and 350 nm, should reveal the possible light scattering effect and absorption suspected of the capillary tube.

Figure 3.6A shows the spectral responses from 230-800 nm of deionized water excited at 257.5 and 350 nm through the commercial cell. The spectra in Figure 3.6B are the fluorescence emission responses from 230-800 nm of the empty capillary cell excited at the same wavelengths as the deionized water. Figure 3.6A clearly reveals the Rayleigh scattered or excitation peaks for water at 257.5 and 350 nm, which are numbered 1 and 3 respectively. In addition, the figure clearly reveals the Raman band of water at 397 nm (peak 4) due to excitation at 350 nm and its first overtone at 794 nm (peak 8). The 794 nm overtone is truncated as result of limited instrument wavelength range. The first overtone of the excitation peak at 350 nm is recorded at 700 nm (peak 7). Figure 3.6A also shows the change in the position of the Raman band of water from 397 nm to 282 nm (peak 2) when the deionized water was excited at 257.5 nm instead of 350 nm. The first overtones of both the excitation at 257.5 nm and the Raman band at 282 nm are recorded at 515 nm (peak 5) and 564 nm (peak 6) respectively. The presence of the excitation peaks, the corresponding Raman bands and their shift in positions relative to the excitation peaks, clearly confirms the scattering effect of water.

Figure 3.6B, which shows the fluorescence emission spectral responses of the empty capillary cell, has rather unusual spectral features. Compared to the spectral response of water, the emission response of the capillary cell excited at 257.5 nm reveals strong absorption, labeled 1, of the excitation wavelength by the capillary tube. The first overtone of the 257.5 nm excitation light, labeled 5, is also strongly absorbed. These absorptions are accompanied by intense and broad fluorescence emissions covering

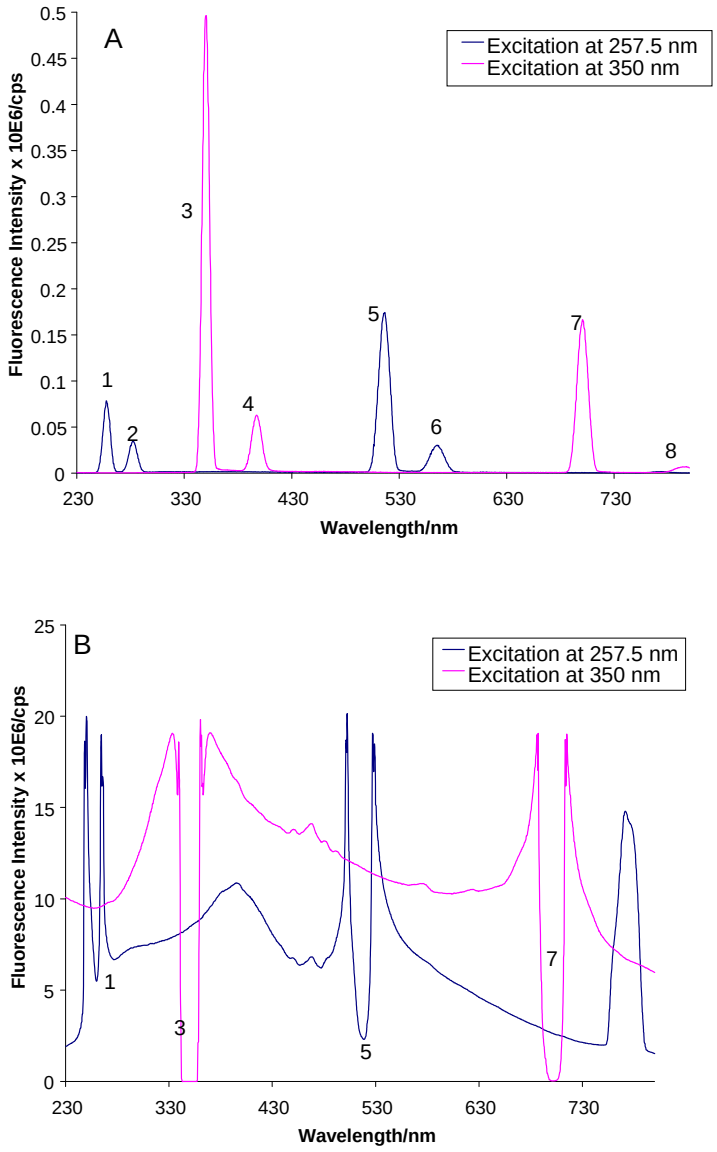

Figure 3.6 A: Rayleigh and Raman scattering signals for deionized water due to excitation at 257.5 and 350 nm. B: Fluorescence emission response of the empty capillary cell due to excitation at 257.5 and 350 nm.

almost the entire wavelength scanned. A distinct peak that appears to be a scattered signal is recorded at 779 nm. In addition, Figure 3.6B reveals an even stronger absorption effect by the capillary tube when it was excited at 350 nm– the excitation wavelength is completely absorbed in addition to its first overtone. The fluorescence

emission associated with the excitation at 350 nm is more intense than that for the 257.5 nm excitation. Unlike the emission spectrum recorded for the excitation at 257.5 nm, no scattering signal was recorded when the capillary cell was excited at 350 nm. This is probably because with excitation at a longer wavelength (350 nm) than 257.5 nm, the Raman scattering signal, if any, should occur at a longer wavelength than 779 nm. This signal, however, cannot be seen in the spectrum because of the limited instrument wavelength range. The UV excitation spectral response of the capillary tube undoubtedly indicates that the quartz material from which the capillary tube is made contains contaminants that absorb UV strongly and fluoresce intensely. High quality quartz material from which, for example, the commercial fluorometer cell is fabricated, should not absorb UV light in the mid or near UV region (~ 200-400 nm). This is confirmed by the excitation spectral response recorded for the empty commercial fluorometer quartz cell (see Figure 3.5B).

Test for qualitative analysis. The experiment on the UV excitation spectral response of the capillary cell revealed that the cell absorbs UV strongly at 257.5 and 350 nm and fluoresces intensely over almost the entire spectral region from 230 nm to 780 nm. This could possibly limit the use of the custom-designed capillary cell for fluorescence emission measurement as intended. It was therefore necessary to investigate the possibility of using the cell for measuring the fluorescence emission spectrum of a sample excited at a wavelength absorbed by the capillary tube. The aqueous solution of phenylalanine has a UV absorption maximum at 257 nm. Consequently, the fluorescence emission spectra of aqueous solutions of phenylalanine are usually collected by excitation at 257 nm. With the UV absorption of phenylalanine being identical to one of the UV

absorption wavelengths of the capillary tube, a qualitative analysis test was performed on the custom-designed capillary cell by using it to measure the fluorescence emission spectra of phenylalanine at different emission slit widths. To do this, a blank solution was first prepared by pipeting 400 μL of racemic 2-butanol and 200 μL of HCl into a 50-mL volumetric flask and diluting to the mark using deionized water. A mass of 0.0124 g of L-phenylalanine was then dissolved in some volume of the blank solution and quantitatively transferred into a 25-mL volumetric flask. This was diluted to the mark using the same blank solution to prepare a 3 mM phenylalanine solution. The fluorescence emission spectra of the butanol-HCl blank and 3 mM phenylalanine solutions were then recorded at selected emission slit widths. The solutions were excited at 257.5 nm and the emission scanned from 274 to 450 nm. In addition, the spectra of the same butanol-HCl blank and 3 mM phenylalanine solutions were collected using the commercial cell with the instrument emission slit width set at the same values used for the capillary cell measurements.

Figure 3.7A shows the fluorescence emission spectra of the blank solution recorded at 5, 3, 2, 1, and 0.5 nm emission slit widths using the capillary cell and Figure 3.7B the emission spectra of the same blank solution recorded over the same wavelength range using the commercial cell. The spectra in Figure 3.7A reveal the usual capillary cell peak centered on 397 nm and a second peak recorded at 284 nm. This second peak is probably due to 2-butanol emission. The spectra of the blank in Figure 3.7B, recorded using the commercial cell, reveal only the peak at 284 nm. Both Figure 3.7A and B show that the fluorescence emission intensity of the blank solution is a function of emission slit

width– decreasing with decreasing slit width. This is because the amount of light reaching the photomultiplier detector decreases with decreasing slit width.

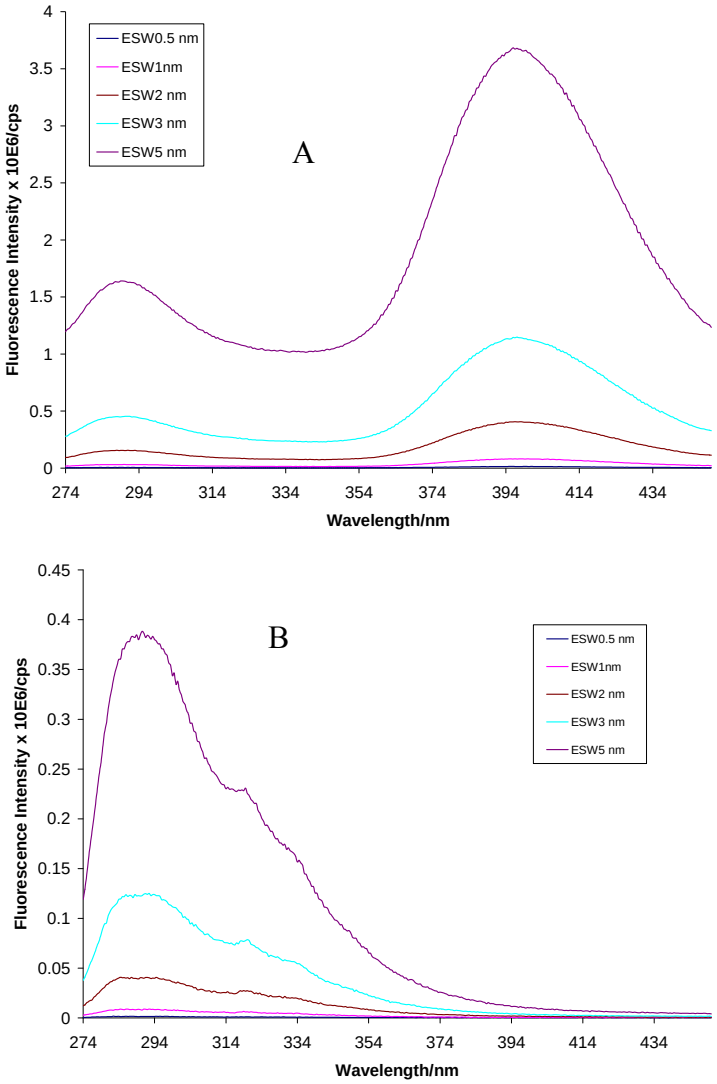

Figure 3.7 A: Fluorescence emission spectra for racemic 2-butanol-HCl blank solution collected using the capillary cell at different emission slit widths. B: Fluorescence emission spectra of the same blank solution collected using the commercial fluorometer cell at the same emission slit widths shown in A.

Figure 3.8A and B are the fluorescence emission spectra for the 3 mM phenylalanine solution recorded using the capillary and commercial cells respectively. These spectra were collected at the same emission slit widths as the blank solution. The

emission spectra for the phenylalanine solution in Figure 3.8A and B, compared to those for the blank in Figure 3.7 A and B, reveal that except for higher intensities, the spectra for the 3 mM phenylalanine solution are similar to those for the blank solution. Figure

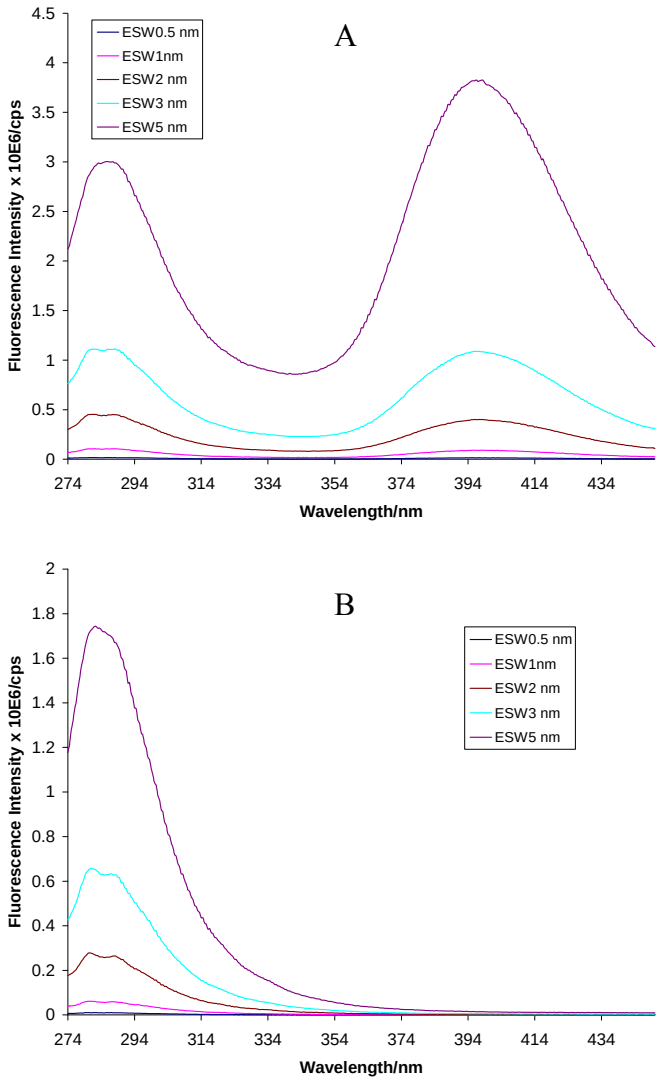

Figure 3.8 A: Fluorescence emission spectra for 3 mM phenylalanine solution collected using the capillary cell at different emission slit widths, B: Fluorescence emission spectra of the same phenylalanine solution collected using the commercial cell at the emission slit widths shown in A

3.8A shows that the emission spectra collected for the phenylalanine solution using the capillary cell differ significantly from the previously shown emission spectra for the 2

mM tyrosin solution (see Figure 3.4), which were collected using the same capillary cell. Comparison of the two figures show that the capillary peak at 397 nm is more prominent in the emission spectra for phenylalanine excited at 257.5 nm than tyrosine excited at 274 nm. This difference clearly indicates that the intensity and broadness of the characteristic 397 nm capillary peak depends on wavelength of excitation. This implies that, the capillary tube is contaminated with certain specific fluorescence active materials that are more sensitive to certain wavelengths of excitation than others.

To obtain the blank-corrected spectra for the 3 mM phenylalanine solution, the spectra for the butanol-HCl blank, recorded at different emission slit widths, were subtracted from the corresponding 3 mM phenylalanine spectra.

Figure 3.9A shows the blank-corrected spectra of the 3 mM phenylalanine solution obtained for the capillary cell at emission slit widths of 0.5, 1, 2, 3, and 5 nm. Figure 3.9B shows the blank-corrected spectra of the same 3 mM phenylalanine solution obtained for the commercial cell at the same emission slit widths used for the capillary cell. It is obvious from Figure 3.9A and B that the blank-corrected spectra obtained for both cells clearly reveal the usual phenylalanine emission band with a maximum at 282 nm. This emission band is due to the л* ← л transition of the phenyl group. It is a singlet-singlet emission band, which arises from the $^1A_{1g} \rightarrow {}^1B_{2u}$ symmetry forbidden absorption transition of the phenyl group of phenylalanine. In addition, the shapes of the phenylalanine emission peaks, compared for the same emission slit widths, are identical in the blank-corrected spectra for the two cells. This indicates that our custom-designed capillary micro-cell is comparable to the commercial cell. However, some unusual features are revealed in some of the blank-corrected spectra shown in Figure 3.9A for the

capillary cell. For example, the nature of the blank-corrected spectrum for the 5 nm slit width implies that the emission intensity of the blank solution, from about 323 to 373 nm, is higher than that of the 3 mM phenylalanine solution in the same spectral region. The peak shown from about 374 to 432 nm indicates the opposite. This unusual behavior

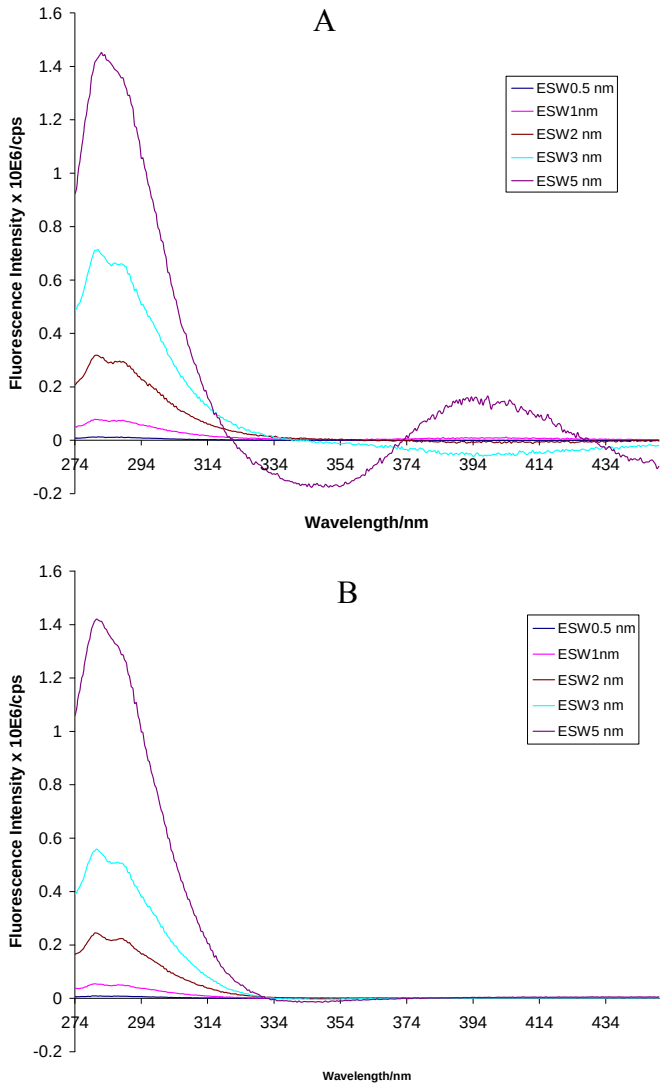

Figure 3.9 A: Blank-corrected fluorescence emission spectra for 3 mM phenylalanine solution obtained from spectra collected using the capillary cell at different emission slit widths. B: The blank corrected fluorescence emission spectra of the same phenylalanine solution obtained from spectra collected using the commercial cell at the same emission slit widths as in A.

could be due to changes in spectral property as a result of changes in solution environment: possibly changes in pH. This is because the pH of the blank solution, made up of 2- butanol and HCl, could be changed when phenylalanine is dissolved in it. This is because the amine group in phenylalanine is a weak base that can accept protons in solution. In addition, butanol could possibly form hydrogen bonds with phenylalanine in solution. As such, the intermolecular association, for example of butanol in the blank solution could be different from its intermolecular association in the phenylalanine solution. The spectral properties of butanol could therefore not be the same in both the blank and the phenylalanine solution. Figure 3.9B, which shows the blank-corrected spectra for the commercial cell, revealsthat the blank-corrected spectra obtained for spectra recorded at the 5 nm emission slit width, portrays a negative spectral deviation from about 334 to 364 nm. This is, however, significantly weaker than the deviation for the capillary cell measurement. While this effect may be associated with the solutions, the difference in the magnitudes of it for the two cells seems to suggest that differences in sensitivity of the cells might be important– determining the extent to which the effect is reflected in spectra. This is because the fluorescence emission spectra recorded using the two cells show that higher emission intensities were always recorded in the use of the capillary cell than the commercial cell. Though some of the blank-corrected spectra for the capillary cell are unusual, the blank-corrected spectra for the spectra collected at 0.5, 1, and 2 nm emission slit widths, except for the higher intensities, are identical in shape to those for the commercial cell at the same emission slit widths This implies that with the correct emission slit setting, our custom-designed micro-cell can be used to collect

spectra for qualitative analysis with identical spectral results as the 10 mm pathlength commercial cell. In addition, the higher emission intensities could improve sensitivity in the use of the capillary cell.

Test for quantitative analysis. This analysis test was performed on the capillary cell in comparison with the commercial cell to determine how the spectral characteristics of our custom-designed capillary cell might influence the results of our enantiomeric composition analyses. To do this, two new sets of replicated fluorescence emission spectra of the 2 mM tyrosine solution were recorded using both cells. The spectral data were subjected to multivariate PLS-1 regression analysis using the Unscrambler statistical package (The Unscrambler^{TM} version 9.7; CAMO, Inc., Oslo, Norway). This analysis test is important because our analytical technique for enantiomeric purity determination depends on the analysis of small spectral differences among samples using the multivariate PLS-1 regression modeling. Consequently, the spectra measurements should be devoid of any bias that may lead to misleading analysis results. For example, incremental or irregular variations in spectra measurement due to changing spectral property of a sample cell used for spectra collection will result in misleading analysis results. This test was thus designed to verify the spectral stability and the reproducibility of our custom-designed capillary cell during fluorescence emission spectra measurement.

Figure 3.10 shows the two new sets of replicated spectra for the 2 mM tyrosine. Spectra set A are the spectra recorded using our custom-designed capillary cell and spectra set B, those recorded using the commercial cell. Unlike the previous sets of spectra, these new sets of repeated spectra appear to fluctuate less in the peak region. This might be due to less instrument variation during spectra collection because a longer

instrument warm up time (1h) was allowed in this measurement than the previous measurement (30 min). The time allowed for the instrument to warm up could be important considering the fact that the Jobin Yvon FluoroMax-2 spectrofluorometer used for the spectra collection is quite old. Prior to modeling, each spectrum in each set of spectra was treated as the spectrum of a sample solution of tyrosine with a different concentration. As such, the first spectrum collected in each set was assigned

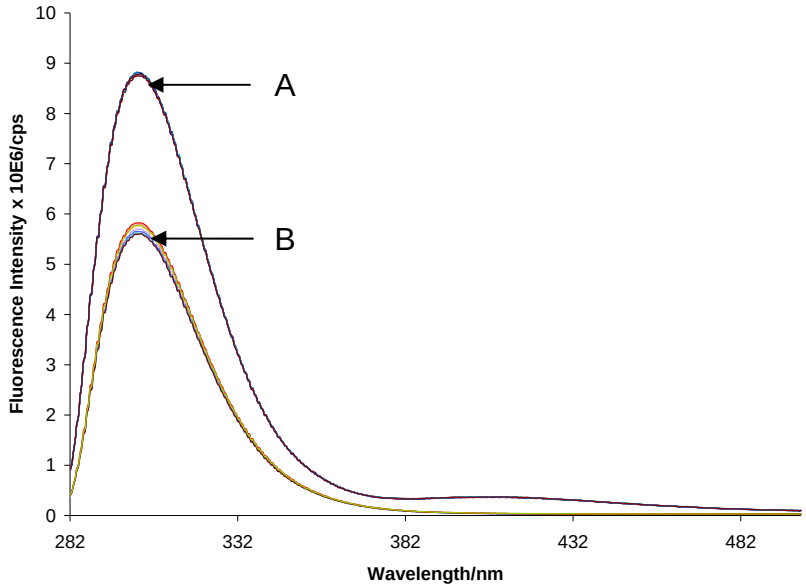

Figure 3.10 A: Ten replicated fluorescence emission spectra for the 2 mM tyrosine solution recorded using the custom-designed capillary micro cell. B: Nine replicated fluorescence spectra for the same tyrosine solution recorded using the 10 mm pathlength commercial micro-cell.

aconcentration value of 1, the second a concentration value of 2, and so on to correspond with the order in which the spectra were recorded. This spectral treatment could give rise to one of three possible regression lines: (1) a regression line showing strong correlation of the replicated spectral data with the order of spectra collection, (2) a regression line showing poor correlation (scattered points) of the replicated spectral data with the order of spectra collection, and (3) a flat regression line showing the replicated spectra are

identical (reproducible) with no correlation with the order of spectra collection. If the regression analysis results in the first possibility then an incremental spectral variation by the cell is verified. This behavior will be revealed by two plot statistics, slope and correlation coefficient, of the cross-validated PLS-1 regression line for the replicated spectral data. Under this condition, the plot statistics should have values not less than 0.9 – the minimum value set by the Unscrambler statistical package for a response variable to be considered to be meaningfully correlated with its predictor variable. The verification of such inherent spectral variation in the cell could create a misleading impression of good spectral data correlation with enantiomeric composition in actual experiments. Should the regression analysis result in the second possibility then an irregular spectral response of the cell is verified. Under this condition, the values of the regression plot statistics will be lower than the minimum value of 0.9. Such an inherent irregular spectral response by the cell will lead to high errors in analyses. The third possibility, a flat regression line, will portray a stable spectral response by the cell, which will signify high reproducibility of the cell during spectral measurement. Such response is desirable for quantitative analysis because it will eliminate bias in analysis results.

Figure 3.11A, B, C, and D are the PLS-1 regression model plots for the spectral data of the two sets of replicated spectra (see Figure 3.10) collected using the capillary and the commercial cells. Figure 3.11A is the scores plot constructed with the second principal component (PC) as the y-axis and the first principal component as the x-axis; the first and second PCs usually describe most of the variation in a set of data. The blue symbols in the left half of the scores plot represent the set of replicated spectra recorded for the commercial cell and the green symbols in the right half of the plot those recorded

for the custom-designed capillary micro-cell. The first and second PCs of the scores plot clearly describe the two sets of replicated spectral data as two distinct groups of samples. This description is in terms of intensity because the intensities of the spectral replicate for the tyrosine solution collected using the capillary are clearly different from the spectral replicate collected for the same solution using the commercial (see Figure 3.10). In addition, the two PCs used for the scores plot reveal the small differences among the individual spectra of the two sets of spectra (capillary and commercial cell spectra) collected for the tyrosine solution. Figure 3.11B shows the regression coefficient curve, which is a plot of regression coefficient as a function of wavelength. The curve assumes the general shape of the replicated spectra shown in Figure 3.10 and shows that all the regression coefficients associated with the mathematical model are positive (curve above the zero on the y-axis). Plot C in Figure 3.11 is the explained validation variance plot, which is a plot of percent explained variance versus principal component. Figure 3.11C shows that a total of eight PCs were computed. However, only one, the first PC, was needed for the model. This first PC explained 100 % of the variation in the spectral data and 1 % of the variation in order of spectral collection. With only 1 % of the variation in order of spectral collection explained, no significant information relevant to the linear model (PLS-1 model) is explained in the order of spectral collection by the first PC. Though the second PC explained 34 % of the variation in the order of spectral collection, the total variation explained by the two PCs, 35 %, is still significantly below the threshold for meaningfulness (70 % and above according to the Unscrambler statistical package). Plot D in Figure 3.11 is the regression line plot. In this case, it is the predicted order of spectra collection (predicted by cross-validation) versus the actual or known

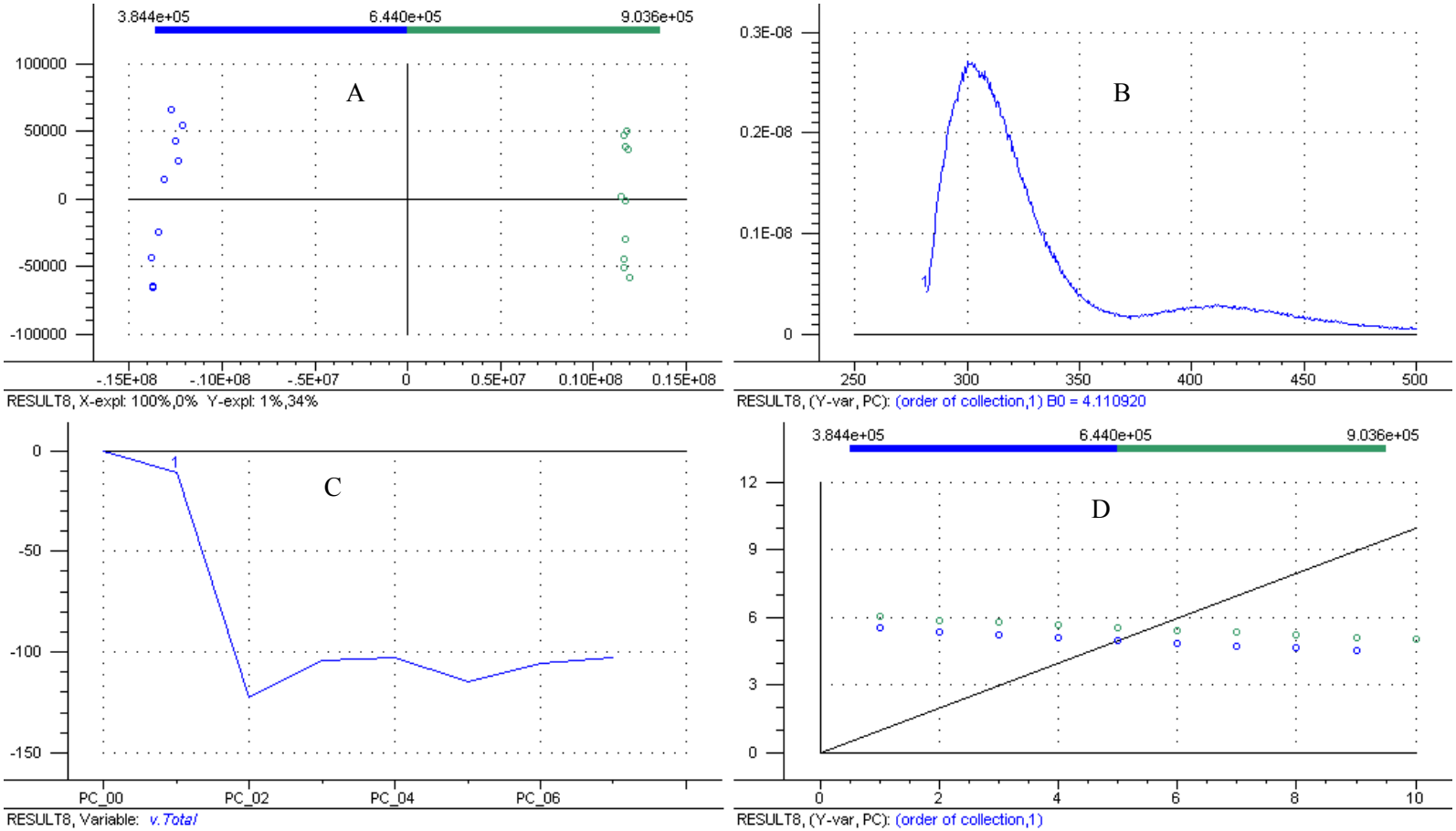

Figure 3.11 Plots of the PLS-1 regression model developed for the quantitative analysis test on the capillary and commercial cells. The plots were developed using the fluorescence emission spectral data and order of spectral collection of the two sets of replicated spectra collected for a 2 mM solution of tyrosine using the capillary and commercial cells. A: scores plot, B: regression coefficient as a function of wavelength plot, C: percent explained variance as a function of principal component plot, and D: predicted order of spectral collection for spectra collected using the capillary (green symbols) and commercial (blue symbols) cells, versus the actual order of spectral collection. The model required only one PC (see below plot B or D)

order of spectral collection. This plot shows that the replicated spectra, recorded using both the commercial and custom-designed capillary micro-cells, have no correlation with the order of spectra collection. This is because the regression lines described by the corresponding blue and green symbols for the two sets of replicated spectra are almost parallel to the horizontal axis of the plot. As such, the regression lines, undoubtedly, show that both cells do not have spectral properties that change incrementally or irregularly. This implies that the spectral response of our custom-designed capillary cell is constant for a given set of measurement conditions and comparable to the commercial fluorometer cell.

The comparable performance of the capillary cell, which has a pathlength of 1 mm, compared to the commercial cell, raises a question about the need for longer pathlength, 10 mm, usually used in fluorometer sample cells. This study, at this stage, is unable to provide an answer to the question and neither could it explain the higher emission intensities recorded in the use of the capillary cell. The fluorescence emission has quite a number of competing processes such as external conversion, internal conversion, and intersystem crossing among others such that one will expect a larger volume of sample and a considerably longer sample pathlength to observe fluorescence emission to an appreciable level. There should, therefore, be some unique property or the other of the cell which though not known at this stage accounts for its satisfactory performance. On the other hand, the condition required for establishing a linear relationship between fluorescence emission and sample concentration may provide an answer to why it was possible to use the cell for quantitative analysis (regression analysis) even though it has a pathlength of only 1 mm. The modified fluorescence

emission equation for quantitative analysis requires that the absorbance, A of the sample, given by

$$A = \varepsilon bc \text{ .....3.4}$$

where ε is the molar absorptivity (mol.$^{-1}$ L cm^{-1}) of the sample, b the pathlength (cm), and c the concentration (mol. L^{-1}), must be small (< 0.05). This is conventionally achieved via the concentration by using dilute solutions. However, the pathlength b, which can be changed, is directly proportional to the absorbance A. The shorter the pathlength is the lower the absorbance. As such, the shorter pathlength of the capillary cell might possibly be important in its use for the quantitative analysis test described earlier.

The picture in Figure 3.12 shows an experimenter about to collect the fluorescence emission spectrum of a sample using the custom-designed capillary cell.

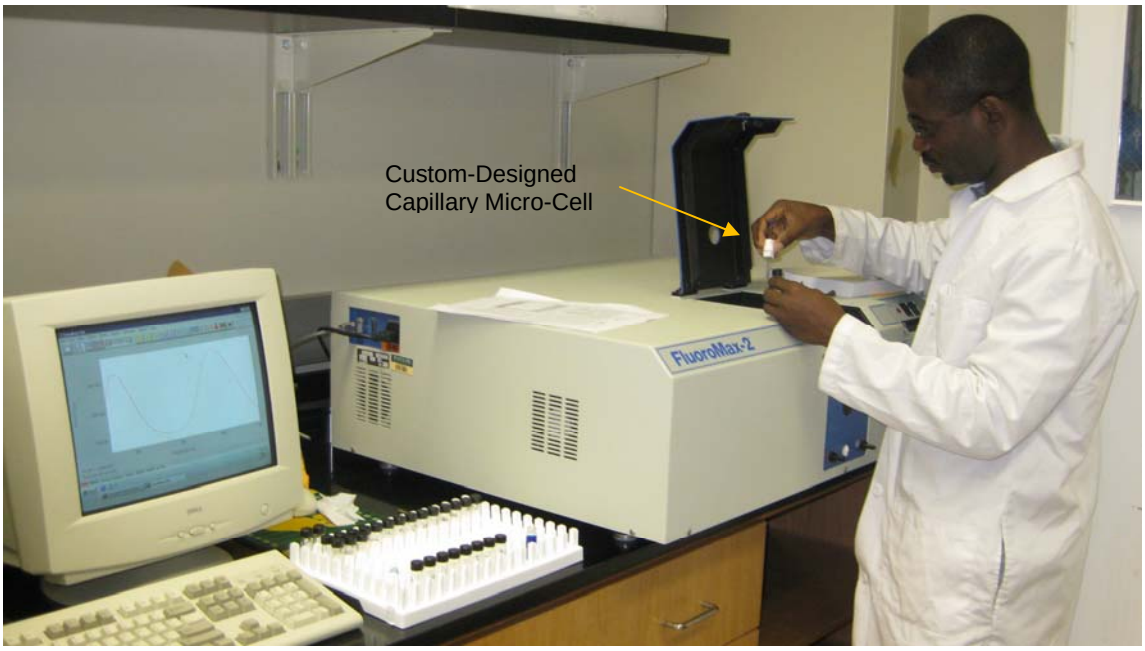

Figure 3.12. Fluorescence emission spectra collection using the capillary tube custom-designed as a micro fluorometer cell for fluorescence emission measurement of 25µL volumes of samples. The spectra were recorded with the Jobin Yvon FluoroMax-2 spectrofluorometer located in the Instrumental Analysis Laboratory of the Chemistry and Biochemistry Department, Baylor University.

Notable in the use of the capillary micro-cell is the shorter time it takes to go through the cycle of collecting the spectrum of a sample compared with the commercial cell; it took fifty-three minutes to collect single scan spectra of the thirty samples on the Fluoro Max-2 spectrofluorometer. Recording the spectra of the same number of samples under the same conditions on the same instrument, using the commercial cell, will take about one hour twenty-five minutes to complete– saving about 32 minutes of analysis time.

Conclusion

The results of the performance tests on the custom-designed capillary cell show that: (1) though the capillary tube absorbs UV light and fluoresces, its function as a sample cell, under the appropriate instrument setting, is comparable with that of the 10 mm pathlength fluorometer cell for qualitative analysis and (2) the capillary cell can be used for quantitative analysis on the basis of the regression analysis shown in Figure 3.8, and (3) with a required sample volume of 25 μL, compared to the 1400 μL of sample volume required for the commercial cell, fluorescence emission can be accurately measured on a micro-scale. This study has, therefore, identified three major advantages of the custom-designed capillary cell over the commercial cell are identifiable: (1) requirement of much smaller sample volume, 25 μL compared to 1400 μL for the commercial cell, for spectra measurement and (2) higher fluorescence emission intensity (higher sensitivity) , and (3) significant reduction in spectra collection time. As such, the custom-designed capillary micro-cell was used in place of the commercial 10-mm pathlength micro-cell for spectra collection in a study on phenylalanine, which is described in the next chapter.

CHAPTER FOUR

Micro-Scale Fluorescence Measurement, the Use of the Racemic Mixture of 2-Butanol as a Chiral Selector, and the Modeling of Log-Converted Spectral Data

Introduction

Chapter 2 described in detail our recent chiral discrimination strategy, NSCCDS, and its successful application in the analyses of four chiral compounds including phenylalanine. This chapter describes analyses performed using the racemate of 2-butanol (the use of the racemic mixture is discussed later) in place of (*S*)-(+)-1,2-propanediol as the chiral selector for the analysis of the same phenylalanine studied. The purpose for using a different chiral selector in analyzing the same chiral compound is to investigate the generality of our new strategy. Chapter 3 described the investigation of the spectral properties and performance of a capillary tube that was custom-designed by us for steady-state fluorescence emission measurement. The investigation showed that the performance of the custom-designed capillary cell is comparable to that of a standard fluorometer cell. To show that the custom-designed capillary cell can be used for actual experiments, it was employed in this study for the collection of the fluorescence emission spectra of all the samples analyzed. The capillary cell, as noted earlier, does not require more than 25 μL solution for fluorescence emission measurement. As such, we by this study demonstrate the use of a microanalytical measurement technique suitable for routine and high throughput chiral analysis. This is in view of the expensive nature of the chiral industry.

In this study, four different analyses of phenylalanine were performed. The first analysis follows the same approach described in Chapter 2 for the application of our new covalent discrimination strategy, NSCCDS. The second analysis was in two parts. The first part of the second analysis involved preparing, isolating, and recrystallizing the 2-butanol derivatized D- and L-phenylalanine. Part of the recrystallized product obtained for D-phenylalanine was used for NMR analysis. This was done to establish that the adapted esterification scheme leads to ester formation. In the second part of the second analysis, the recrystallized products of D- and L-phenylalanine were used for enantiomeric composition analysis. In the third analysis, β-cyclodextrin was used as a chiral selector for non-covalent chiral discrimination of phenylalanine at the same concentration used in the first analysis mentioned above. This will allow direct comparison of our new covalent discrimination strategy, NSCCDS, with the non-covalent discrimination strategy of β-cyclodextrin. The fourth analysis was performed to illustrate the application of our newly developed covalent strategy in real-life situations as mention in Chapter 1. To do this, different known compositions of the solid enantiomers of phenylalanine were weighed into different glass vials, that is, each sample is a mixture of the two enantiomers as will be found in real-life situations for analysis. Identical amounts of reagent solution (the racemate of 2-butanol plus HCl) were then added to the solid mixtures and heated together in a water bath for esterification. The samples were allowed to cool and quantitatively transferred with deionized water into volumetric flasks of identical volume. They were then diluted to the marks and subjected to spectral measurement. We refer to these samples as real-life (RL) samples in order to differentiate them from samples for the first analysis.

Data manipulation is important in analyses such this because application of the appropriate data treatment to raw data could maximize or enhance information extraction. On the other hand, data pre-treatment could lead to misleading or lose of information. The analysis of $\log_{10}$converted spectral data in this study is intended to: (1) find out if converting the usually wide range of spectra intensities recorded to $\log_{10}$ data to make them relatively more comparable will improve the results of the analysis and (2) to evaluate the possibility of introducing linearity in spectral band regions where spectra intensities might not vary linearly with sample composition. These measures were considered because it has been noticed by our group over the years that some of the obvious spectral variations recorded among samples do not necessarily lead to good correlation with sample composition. While such occurrences could be due to poor chiral discrimination, other factors could be responsible. An example of such a factor is non-linear scaling of spectra with sample concentration or enantiomeric composition in this case. Presently, the Unscrambler statistical package used in analyzing our data can only handle linear variations within a data set. As such, spectral data manipulation to introduce linearity in the data might enhance extraction of information and improve the result of the analysis.

The logarithmic scale, as noted in the paragraph above, is useful when there is a wide range of values of a given quantity that needs to be made comparable in order for the figures to be more meaningful. For example, pH is the negative log of the hydronium ion in solution. If the concentration of hydronium ion in solution should be used to compare solutions, an acidic solution of pH 2 will be said to have hydronium ion concentration of 0.01 M (10^{-2} M). A neutral solution (pH = 7) will be 0.0000001 M (10^{-7}

M) and a basic solution of pH 12 will be said to have a hydronium ion concentration of 0.000000000001 M (10^{-12} M). Unless the software used in a given analysis to compare values with magnitudes of this kind is specifically designed to handle such a wide range of values (10^{-2}-10^{-12} M), the hydronium concentration of the basic solution could be interpreted as noise relative to that of the acid. This will lead to loss of relevant information because the hydronium concentration of the basic solution is meaningful and important. Taking the negative log of this range converts it to pH 2-12. In this log-converted form, the hydronium ion concentration of the basic solution is unlikely to be ignored on the basis of its magnitude compared with the acidic solution. Instances of this nature, arising in the analysis of actual spectra could lead to loss of relevant information if variations in spectra of such magnitude are ignored. Log_{10} pre-treatment of spectra could therefore make a wide range of intensities recorded for modeling relatively more comparable and meaningful in our spectral data analysis. Furthermore, spectral intensities that might vary exponentially with sample concentration (enantiomeric composition in this case), at certain wavelengths, could be transformed to vary linearly with concentration (enantiomeric composition in this case) if $\log_{10}$ is taken of the intensities. If, for example, the fluorescence intensity of a given set of samples should vary exponentially with concentration in a given spectral region then such spectral region would obey the original fluorescence equation, written in Chapter 1 in the form

$$F = KP_0\left(1 - 10^{-\varepsilon bc}\right) \text{.....3.1}$$

where F is the total intensity of light emitted by the sample, K a constant that depends on the quantum efficiency of the fluorescence process, P_0 the power of the excitation beam, ε

the molar absorptivity (L mol^{-1} cm^{-1}), *b* the pathlength (cm) of the sample, and *c* the concentration (mol L^{-1}) of the sample. Taking $\log_{10}$ of equation 3.1 gives

$$\log_{10} F = \log_{10}(KP_0) - \left[\log_{10}(KP_0) + \log_{10} 10^{-\varepsilon bc}\right] \text{.....3.2}$$

Equation 3.2 can be reduced to

$$\log_{10} F = \varepsilon bc \text{ .....3.3}$$

Equation 3.3 shows a linear $\log_{10}$ relationship of the fluorescence emission intensity (*F*) with the concentration (*c*), which in this case corresponds to enantiomeric composition. Modifying the fluorescence spectral data according to equation 3.3 should, therefore, introduce a linear relationship between the fluorescence emission intensity and the concentration (enantiomeric composition in this case) in spectral regions where the two parameters relate exponentially. With this, spectral variations that might not fit the linear PLS-1 regression model but might contain important structured information could be taken advantage of in the PLS-1 regression modeling. This might improve the results of the analysis.

Based on the above two examples on the effect of the logarithm function, $\log_{10}$ spectral pre-treatment could be useful in chiral analysis by regression modeling of spectral data (CARMSD). Consequently, $\log_{10}$ converted spectral data of the samples in this study were subjected to the multivariate, PLS-1 regression modeling analysis in comparison with the regression modeling analysis of the original spectral data.

Conventionally, enantiomeric analysis using non-chiral techniques that depend on analyzing diastereomeric forms of enantiomers require resolution of enantiomeric pairs with homochiral chiral selectors. This is because when a pair of enantiomers of a compound reacts with a single enantiomer of another compound, they form a pair of

diastereomers, which are not mirror images of each other but rather different compounds. The diastereomers can be isolated together from the reaction mixture and analyzed using non-chiral chromatographic or NMR techniques as well as chiroptical techniques. Traditionally, racemates are not used for the resolution of enantiomers in these techniques. This is because the reaction of a pair of enantiomers with the racemate of a chiral compound should result in the formation products that are not simply a pair of diastereomers but a mixture of stereoisomers. The stereoisomers will relate with each other both as diastereomeric and enantiomeric pairs. Under this condition, the above mentioned non-chiral techniques are limited when it comes to analyzing the enantiomeric pair of the chiral analyte quantitatively. In addition, chiral techniques, including chiral chromatography, requiring some separation or the other of the derivatized products, may run into problems because a complex separation procedure will be required. As such, the use of chiral selectors in the racemate form is not a viable option in these techniques.

The choice to use the racemate of 2-butanol instead of one of its enantiomers in place of (*S*)-(+)-1,2-propanediol for chiral discrimination was motivated by two factors: its relatively low price and ready availability. Prior to the experiment, the possibility of the success of using the racemate of 2-butanol as a chiral selector in combination with non-chiroptical or isotropic fluorescence spectroscopy for the present study, was carefully examined. Reaction Scheme I shows that the Fischer esterification of D-phenylalanine with the racemate of 2-butanol (reaction A) could form a pair of diastereomeric ester hydrochlorides, which is enantiomeric to the pair of esters that could be formed with L-phenylalanine (reaction B). A test solution for analysis, prepared by

A

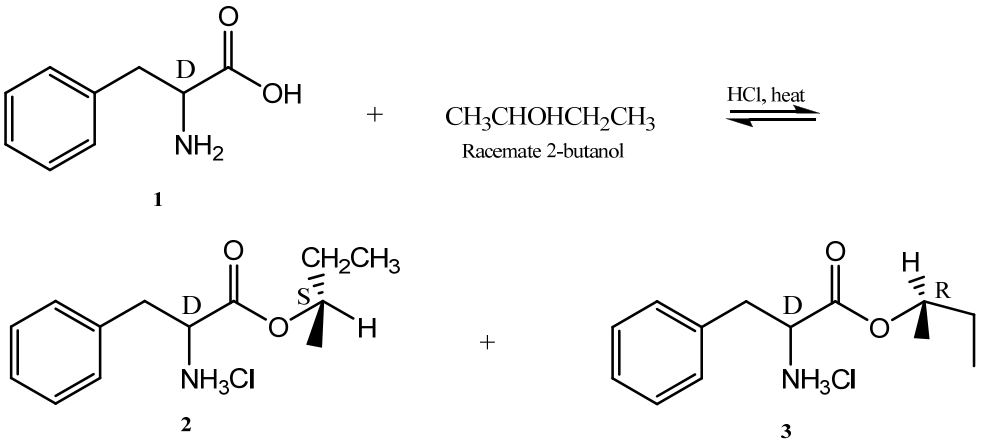

B

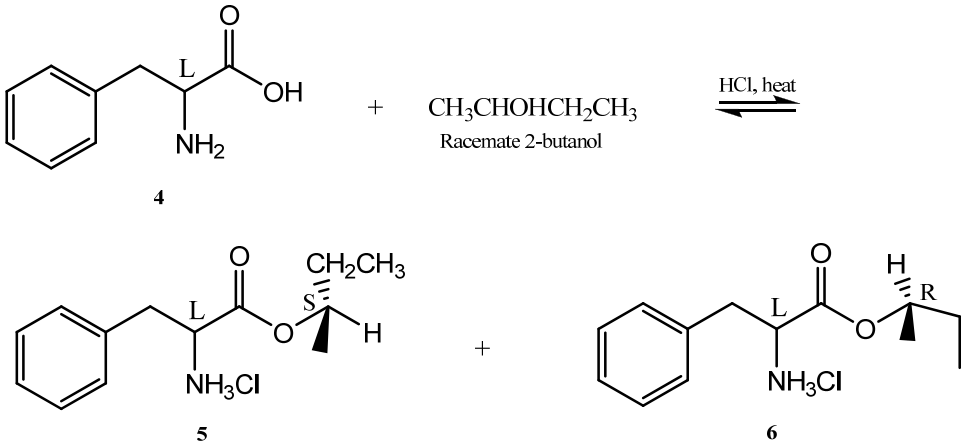

Scheme I. A and B show the formation of diastereomeric pairs of ester hydrochlorides by the reaction of D- and L-phenylalanine with the racemate of 2-butanol. **1**: D-phenylalanine. **2**: (*S*)-2-butyl D-phenylalanine ester hydrochloride. **3**: (*R*)-2-butyl D-phenylalanine ester hydrochloride. **4**: L-phenylalanine. **5**: (*S*)-2-butyl L-phenylalanine ester hydrochloride. **6**: (*R*)-2-butyl L-phenylalanine ester hydrochloride

mixing known amounts of the D- and L-phenylalanine ester solutions will thus contain four stereoisomers made up of two pairs of enantiomers. Based on this, one might conclude that the discrimination of D- and L-phenylalanine using the racemate of 2-butanol combined with non-chiroptical fluorescence spectroscopy should not lead to a

successful enantiomeric composition analysis of phenylalanine– the analysis has no sound basis for success. Such a conclusion may hold for the non-chiral NMR technique because for quantitative purposes, the use of NMR will require the resonance frequency of the diastereotopic nuclei in the derivatized enantiomers to be detected. The use of non-chiral NMR should result in the same signals for both of the diastereomeric pairs of say the D and L forms of the chiral analyte. This is because the diastereomeric pair, D*R* and D*S*, formed by the *R* and *S* forms of a chiral selector with the D form of a chiral analyte, is enantiomerically related to the diastereomeric pair, L*S* and L*R*, formed by the same *R* and *S* forms of the same chiral selector with the L form of the same chiral analyte. Thus, the use of a non-chiral NMR technique for the quantitative analysis of enantiomeric pairs, which are covalently resolved with the racemate of a chiral selector, will be ineffective. For chiral NMR techniques, a special chemical shift reagent capable of effectively discriminating the diastereomeric pair of say the D form of the chiral analyte from the diastereomeric pair of the L form in the sample will be required. On the other hand, our non-chiroptical or isotropic spectroscopic techniques have no limitation and do not require special reagents in analysis of samples with the above-mentioned unusual composition because they do not require separation and probe bulk spectral properties of samples. Consequently, any effect that can bring about differences in the spectral properties of the bulk of sample solutions is all that is needed to spectrally differentiate one sample from the other. If the effect scales directly with sample composition, it should be possible to use the isotropic spectral data of the samples for quantitative analysis of the samples. In the present case, for example, reaction Scheme I shows that four stereoisomers will be present in a sample made up of D- and L-

phenylalanine if the sample is reacted with the racemate of 2-butanol. The same situation is presented when separate solutions of D- and L-phenylalanine reacted with the racemate of 2-butanol are mixed to prepare test solutions as in the first analysis. In such a sample solution, the ester formed by the *S* form of 2-butanol with D-phenylalanine (D*S*) will be enantiomeric to the ester formed by the *R* form of 2-butanol with L-phenylalanine (L*R*). Similarly, the ester formed by the *S* form of 2-butanol with L-phenylalanine (L*S*) will be enantiomeric to the ester formed by the *R* form of 2-butanol with D-phenylalanine (D*R*) as portrayed by reaction Scheme I. The sample will thus, have two pairs of enantiomers or enantiomeric interactions: (1) D*S* and L*R* (molecules **2** and **6** in Scheme I) and (2) D*R* and L*S* (molecules **3** and **5** in Scheme I). Enantiomeric interaction, by convention, should not allow for spectral discrimination (the situation can be different at high concentrations as noted in Chapter 2 though) of samples of different enantiomeric compositions. However, the possible chiral interactions in such a sample are not limited to the above enantiomeric interactions only. Diastereomeric pairings or interactions are equally possible in the same sample: D*R* and D*S* (structure **2** and **3**), D*S* and L*S* (structure **2** and **5**), D*R* and L*R* (structure **3** and **6**), and L*R* and L*S* (structure **5** and **6**) constitute diastereomeric pairings or interactions in the sample. These diastereomeric pairings or interactions outweigh the enantiomeric pairings or interactions. Based on this, each test sample solution will have a net of diastereomeric pairing or interaction, which should vary according to sample composition. Consequently, the spectral properties of sample solutions made up of varying enantiomeric compositions should vary according to the diastereomeric excess pairing or interaction. In addition, being in the same solution, the spectral property of each individual species (D*R*, D*S*, L*R*, and L*S*) could be affected by

the possible complex chiral interactions in solution. This complex chiral interaction could impart a unique spectral property to the sample solution. This can as well result in spectral differences among samples made up of different compositions of these individual species (D*R*, D*S*, L*R*, and L*S*).

Furthermore, the *R* and *S* enantiomers of 2-butanol cannot react equally with the enantiomers of phenylalanine. This is because the members of a pair of enantiomers have the property of reacting differently with other chiral molecules. As such, the esters are not expected to be formed to the same extent; sample solutions prepared from D- and L-phenylalanine esterified with the racemate of 2-butanol should thus have net diastereomeric properties. Based on this, chromatographic techniques can be employed provided an effective separation can be achieved prior to analyte detection. Generally, chromatographic techniques, usually, take a long time and in this particular example a complex separation protocol, unlikely to be suitable for routine and high throughput analysis, may be required.

As explained above, the bulk properties of sample solutions made up of different compositions, for example, of the above-mentioned four hypothetical stereoisomers will vary as a result of either the effect of the excess diastereomeric interaction or complex chiral interaction or both. Thus, such samples can be spectrally differentiated using isotropic spectroscopic techniques (ordinary UV-vis and fluorescence spectroscopy), which are employed by us for chiral analysis. It is possible that the spectral differences will be small and occur at different spectral band regions but the use of multivariate regression techniques such as PLS-1 regression will allow such information in the spectral data to be assessed.

Based on the above careful examination of the implications of using the racemate of 2-butanol for chiral analysis, we came to the conclusion that it is possible to employ the racemic mixture of 2-butanol as a chiral selector in our new covalent discrimination strategy for the analysis of phenylalanine. Thus, the racemic mixture of 2-butanol is the chiral selector used in the analysis described in this chapter.

Methodology

Materials

Enantiopure Phenylalanine (D and L, ≥ 99 %), racemic mixture of 2-butanol (99 %), and homochiral β-cyclodextrin hydrate (β-CD) were purchased from Aldrich Chemical Company. ACS Grade concentrated hydrochloric acid (12.1 M) was used as the acid catalyst in the esterification reaction. All chemicals were used as received.

Preparation of NSCCDS Samples of Phenylalanine Using the Racemate of 2-Butanol

The NSCCDS samples of phenylalanine prepared using the racemic mixture of 2-butanol were the samples prepared for the first analysis of phenylalanine. The samples were prepared using the same procedure followed in preparing the NSCCDS samples in Chapter. For this analysis, however, 2 mL of the racemate of 2-butanol, 1mL of HCl, and 0.2065 g of enantiomerically pure D- or L-phenylalanine were used. The samples were heated at 75 ^{o}C to prepare the 2-butanol derivatized or esterified phenylalanine products. The derivatized D- and L-phenylalanine samples were used to prepare 5 mM stock solution, which were mixed to prepare thirty sample solutions made up of different enantiomeric compositions for analysis. The samples were varied at a regular mole fraction interval of 0.03.

Preparation of Recrystallized 2-Butanol Phenylalanine Ester Samples

To verify that esters were actually formed during the esterification reaction adapted for our new covalent discrimination strategy, enantiomerically pure D- or L-phenylalanine were reacted with the racemic mixture of 2-butanol as in the first analysis. This time however, the reaction products for the D- and L-phenylalanine enantiomers were not diluted to prepare stock solutions. Rather, 10 mL of the racemate of 2-butanol was added to the D- or L-Phenylalanine product and left overnight. White gelatinous precipitates were formed overnight. These precipitates were filtered and recrystallized from the 2-butanol. The solids obtained were then dried overnight in an oven at a temperature of 60 ^{o}C. A mass of 20 mg of the recrystallized D-phenylalanine solid was dissolved in 2 ml of deuterated water. Proton and carbon-13 NMR spectra of the solution were recorded to verify the formation of the esters. The recrystallized solid obtained for L-phenylalanine and the rest of the recrystallized D-phenylalanine solid sample were then used to prepare separate 3.511 mM stock solutions. A set of thirty sample solutions, varied at a regular interval of 0.03 mole fraction units were prepared for analysis. The thirty samples for this second analysis are referred to here as the '*recrystallized ester samples*' (RE samples).

Preparing β-Cyclodextrin Samples of Phenylalanine

In order to compare our new non-separative, covalent, chiral discrimination strategy (NSCCDS) with the non-covalent, inclusion complex forming, chiral discrimination of β-cyclodextrin at the same concentration level, a third set of samples,'*β-CD samples,*' were prepared for analysis. To prepare these samples for the third analysis of phenylalanine, a 10 mM stock solution of β-cyclodextrin was firstly prepared: 2.8375

g of enantiopure β-cyclodextrin hydrate was dissolved in a limited amount of deionized water by warming. The solution was allowed to cool and transferred quantitatively into a 250-mL volumetric flask. It was then made up to the mark using deionized water to obtain the 10 mM β-CD stock solution. A 5 mM stock solution of D- or L-phenylalanine in β-cyclodextrin was prepared by dissolving 0.0413 g of D- or L-phenylalanine in a limited amount of the 10 mM β-cyclodextrin stock solution, which was transferred quantitatively into a 50-mL volumetric flask and diluted to the mark with the same 10 mM β-cyclodextrin stock solution. The D- and L-Phenylalanine-β-CD stock solutions were mixed in different compositions to prepare thirty β-CD sample solutions varied at a regular mole fraction interval of 0.03.

Preparation of Real-Life Situation Samples of Phenylalanine using the Racemate of 2-Butanol

Phenylalanine samples prepared in this fourth analysis were done so in a manner that is synonymous with a real-life analysis situation. Firstly, different amounts of D- and L-phenylalanine were weighed into different glass sample vials (24 mL), that is, each glass vial contained a given composition of a solid mixture of D- and L-phenylalanine. The total mass of the samples varied between 0.0300 and 0.0305 g. Identical amounts (1 mL) of a reagent solution, 9:1 2-butanol/HCl, were added to the solid samples in the glass vials. The samples were then heated together in a water bath for one hour at 75 ^{o}C. At the end of the heating, the samples were allowed to cool and then transferred quantitatively with deionized water into volumetric flasks of identical volume. The solutions were then diluted to the marks. The spectra of these sample solutions were then recorded for analysis.

Spectral Data Collection, Treatment, and Analysis

The spectra of all the samples for the first, second, and third analyses were collected using the Jobin Yvon-SPEX Fluoro Max-2 spectrofluorometer schematically shown in Chapter 1. The instrument emission slit width was set at 5 nm. Each sample (not more than 25 μL) was excited through our custom-designed capillary micro-cell at an excitation wavelength of 257 nm. The spectrum for each sample was recorded as a single scan spectrum from 274 nm to 450 nm. The 257 nm excitation wavelength used is the wavelength of maximum UV absorption for phenylalanine. The spectra for the real-life samples, on the other hand, were recorded using the Agilent 8453, photodiode array, UV-vis spectrophotometer described in Chapter 1.

The original spectral data of all the samples were subjected to PLS-1 regression analysis using the Unscrambler statistical package (The Unscrambler™ version 9.7; CAMO, Inc., Oslo, Norway) according to the procedure outlined in Chapter 1. In addition, the spectral data of the samples prepared for the first and second analyses were converted to $\log_{10}$ spectral data and subjected to PLS-1 regression analysis. This was done to determine whether $\log_{10}$ pre-treatment of spectral data in analyses of this kind has any benefit.

Results and Discussion

Figure 4.1A shows the original D-phenylalanine crystal sample, 4.1B the gelatinous precipitate of the Fischer esterification reaction of the D-phenylalanine enantiomer with the racemate of 2-butanol, and 4.1C the recrystallized solid sample. Unlike the original D-phenylalanine crystals, which are shiny and flaky, the recrystallized solid is dull and fluffy. This indicates that the two compounds are physically different.

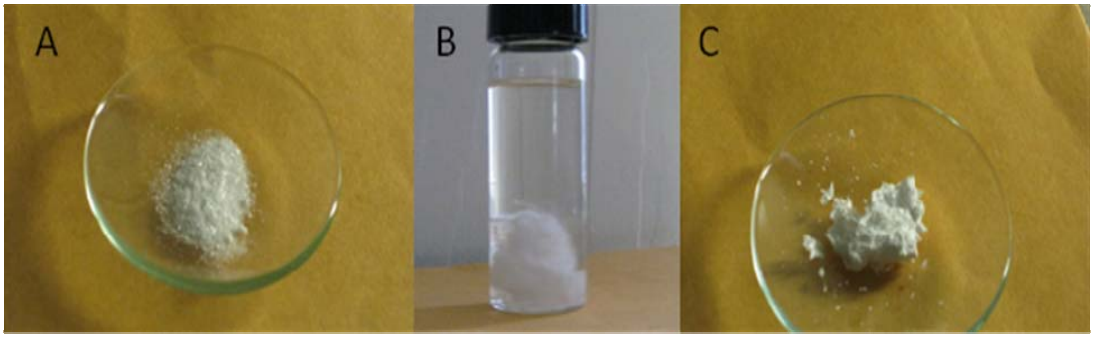

Figure 4.1. A: Original crystal sample of D-phenylalanine. B: White gelatinous precipitate product formed by HCl catalyzed Fischer esterification of D-phenylalanine with the racemate of 2-butanol. C: Recrystallized product of the gelatinous precipitate shown in B. Note the difference in appearance between original D-Phe crystals and the recrystallized esterification product.

Figure 4.2 shows the experimentally measured proton NMR spectrum of the recrystallized gelatinous precipitate obtained from the esterification of D-phenylalanine with the racemate of 2-butanol. The top-left corner insert of Figure 4.2 is the structure of the expected 2-butyl ester of D-phenylalanine. The structure shows numberings from 1 to13, which are used later to match protons or carbons with chemical shifts. The top right corner of Figure 4.2 shows the ChemDraw structure of the 2-butyl ester of D-phenylalanine with proton chemical shifts estimates in addition to the H1 NMR spectrum.

Figure 4.3 shows the experimentally measured C-13 NMR spectrum of the recrystallized gelatinous precipitate obtained from the esterification of D-phenylalanine with the racemate of 2-butanol. Similar to Figure 4.2, the top left corner of Figure 4.3 shows the structure of the ester with numberings to match chemical shifts with nuclei. The top right corner of the same figure shows the ChemDraw structure of the same ester with C-13 chemical shift estimates together with the ChemDraw C-13 NMR spectrum. ChemDraw estimates are used here for reference purposes because empirical references on the NMR of 2-butyl esters of phenylalanine are not available in the literature.

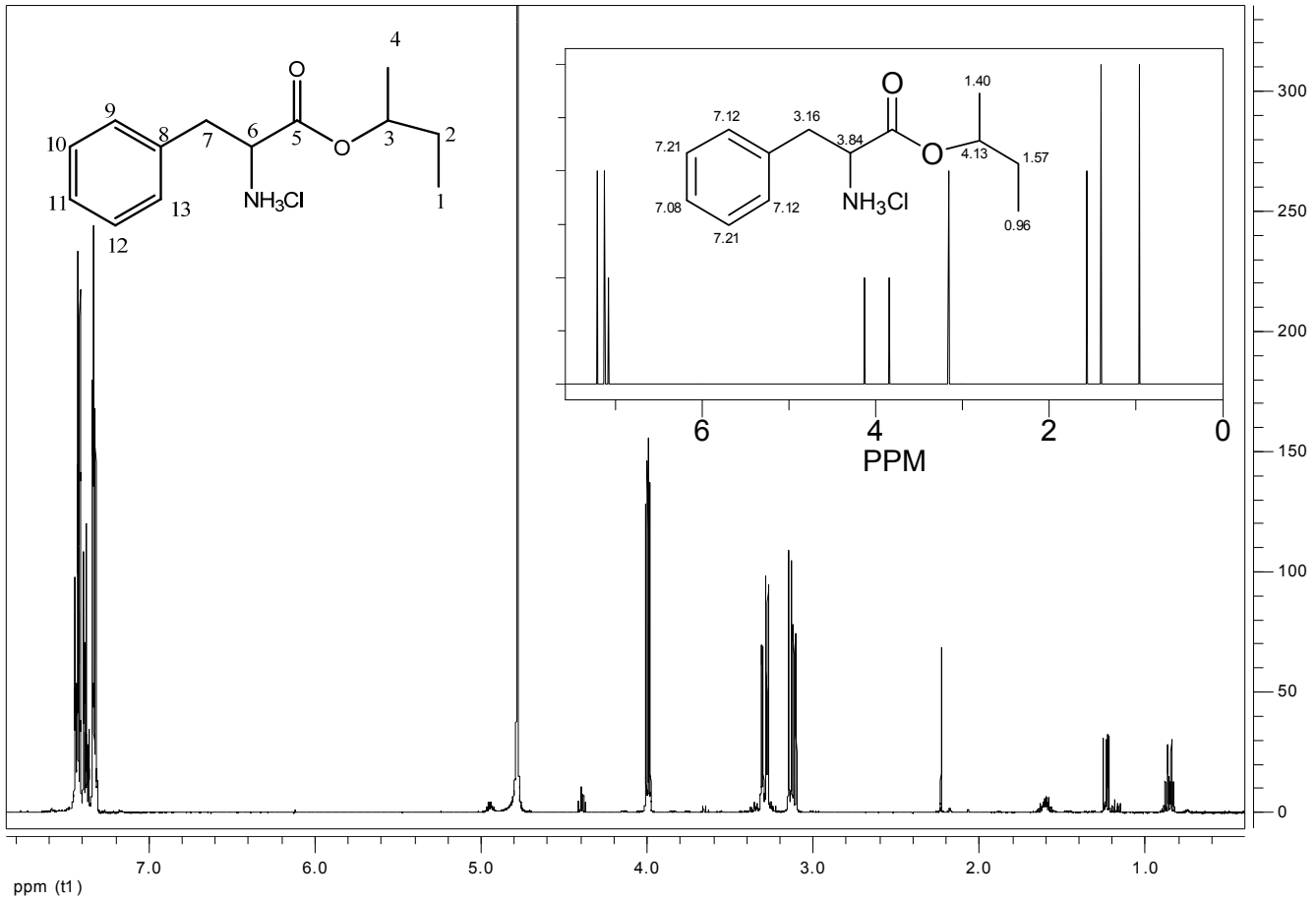

Figure 4.2 H1 NMR spectrum of the solid product formed by reacting the racemate of 2-butanol with D-phenylalanine. The top left insert is the structure of the expected sec-butyl ester of D-phenylalanine. The top right insert is the ChemDraw H1 NMR spectrum showing estimated H1 chemical shifts of the ester.

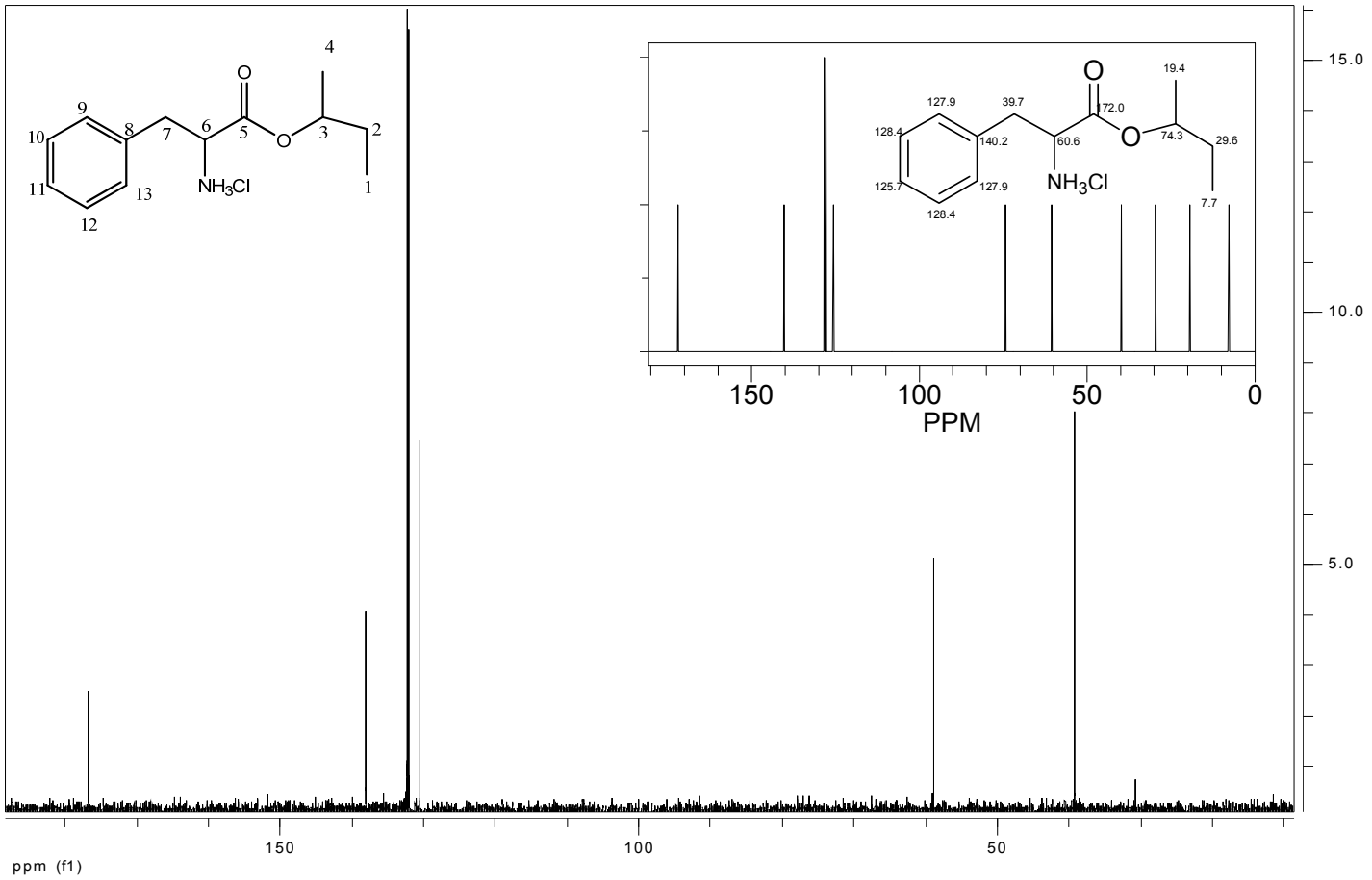

Figure 4.3 C-13 NMR spectrum of the solid product formed by reacting the racemate of 2-butanol with D-phenylalanine. The top left insert is the structure of the expected sec-butyl ester of D-phenylalanine. The top right insert is the ChemDraw C-13 NMR spectrum showing estimated C-13 chemical shifts of the ester

Table 4.1 compares the values of the experimentally measured H1 and C-13 chemical shifts with the ChemDraw estimates according to the number assignments shown in the inserts of the H1 and C-13 NMR spectra in Figure 4.2 and 4.3. The experimental proton chemical shifts in Table 4.1 are reported in a format comparable to the ChemDraw estimates where an average chemical shift position is used to represent the signal of a nucleus or a group of nuclei showing signal splitting. In Table 4.1, proton and C-13 chemical shifts that are contributed by 2-butanol to the structure of the ester are denoted as B and those contributed by D-phenylalanine as Phe.

The chemical shifts reported in Table 4.1 show that the experimentally determined H1 shifts compare favorably with the chemical shifts assigned by the ChemDraw software. The proton shifts at 0.89, 1.60, 3.99, 1.24 ppm agree with the ChemDraw H1 estimates for the 2-butyl alkyl group portion of the D-phenylalanine ester numbered correspondingly as 1, 2, 3, and 4 in Figure 4.2. Experimentally measured proton chemical shifts at 4.39, 3.12, 7.38, 7.43, and 7.32 ppm agree with the ChemDraw H1 protons shift estimates numbered in the structure of the ester shown in Figure 4.2 as 6, 7, 9 and 13, 10 and 12, and 11. Except for the C-13 signals of carbons numbered in the ester structure as 1, 3, and 4, all other carbons shown in the ChemDraw structure and C-13 spectrum in Figure 4.3 are accounted for by the experimentally measured C-13 NMR spectrum. The C-13 chemical shift at 30.8 ppm, which agrees with the ChemDraw estimate for the carbon numbered 2, is contributed by the 2-butyl alky group of 2-butanol to the ester structure. Table 4.1clearly shows that, the experimentally determined C-13 chemical shifts for the carbons numbered from 5 to 13 in the structure of the phenylalanine ester, closely much the ChemDraw estimates. In addition, it is clear from

Table 4.1. Comparison of experimentally measured proton and C-13 chemical shifts of the recrystallized solid product obtained from the HCl catalyzed reaction of D-phenylalanine with the racemate of 2-butanol with the ChemDraw software estimates.

Nucleus or nuclei	ChemDraw H1 shift (ppm)	Experimental H1 shift (ppm)	Nucleus or nuclei	ChemDraw C13 shift (ppm)	Experimental C13 shift (ppm)
1	0.96	0.89: B	1	7.7	No signal
2	1.57	1.60: B	2	29.6	30.8: B
3	4.13	3.99: B	3	74.3	No signal
4	1.40	1.24: B	4	19.4	No signal
5	No proton	No proton	5	172.0	176.8: Phe
6	3.84	4.39: Phe	6	60.6	58.9: Phe
7	3.16	3.12: Phe	7	39.7	39.2: Phe
8	No proton	No proton	8	140.2	137.9: Phe
9 and 13	7.12	7.38: Phe	9, and 13	127.9	131.9: Phe
10 and 12	7.21	7.43: Phe	10 and 12	128.4	132.2: Phe
11	7.08	7.32: Phe	11	125.7	130.5: Phe

Figure 4.2 that no carboxyl proton signal, which usually appears around 10 ppm, was detected in the recrystallized product for the D-phenylalanine ester of 2-butanol. This indicates that the recrystallized solid product is either 100 % the 2-butanol ester of D-phenylalanine or contains undetectable amounts of unreacted D-phenylalanine if any. These NMR results, coupled with the different physical appearance of the recrystallized solid product compared with the original crystals of D-phenylalanine (see Figure 4.1), are compelling evidence that 2-butanol ester of D-phenylalanine was formed. This indicates that the Fischer esterification procedure adapted for our new non-separative, covalent, chiral discrimination strategy (NSCCDS), resulted in the formation of ester diastereomers of the enantiomers of phenylalanine. By extension, the NMR results in this study

strongly suggests that the reaction of phenylalanine and tyrosine with (*S*)-(+)-1,2-propanediol (PD) in the study described in Chapter 2, resulted in the formation PD ester derivatives of phenylalanine and tyrosine.

Figure 4.4A, B, respectively, show the fluorescence emission spectra from 274 to 450 nm recorded for the 5 mM D- and L-phenylalanine ester stock solutions prepared for the first analysis and the 3.511 mM D- and L-phenylalanine ester stock solutions prepared from the recrystallized ester solids. Figure 4.4C shows the 5 mM D- and L-Phenylalanine-β-CD stock solutions prepared by dissolving appropriate amounts D- and L-phenylalanine in the 10 mM β-cyclodextrin stock solution. The spectra shown in Figure 4.4A, B, and C reveal both the phenylalanine emission band at 282 nm (л*← л phenyl group transition) and the characteristic 397 nm peak associated with the capillary cell. These spectral features are similar to the non-blank-corrected spectra recorded with the capillary cell for the 3 mM phenylalanine solution mentioned in Chapter 3. Figure4.4A, B, and C show that the emission intensities of the solutions for the D enantiomer (ester derivative and β-CD associated) are higher in the spectral region from 297 to 264 nm than solutions for the L enantiomer. While the differences between the ester derivatives in Figure 4.4A and B are due to the formation of diastereomeric esters, the spectral difference in Figure 4.4C, between the β-CD associated D- and L-phenylalanine, is reported to be associated with the formation of transient, non-covalent, diastereomeric inclusion complexes [4, 21, 34]. Our research group in a previous fluorescence study of phenylalanine using β-CD as a chiral selector reported a similar spectral difference [67]. Spectra in the previous study were collected using the same commercial (10 mm pathlength) fluorometer cell, which was used in evaluating the

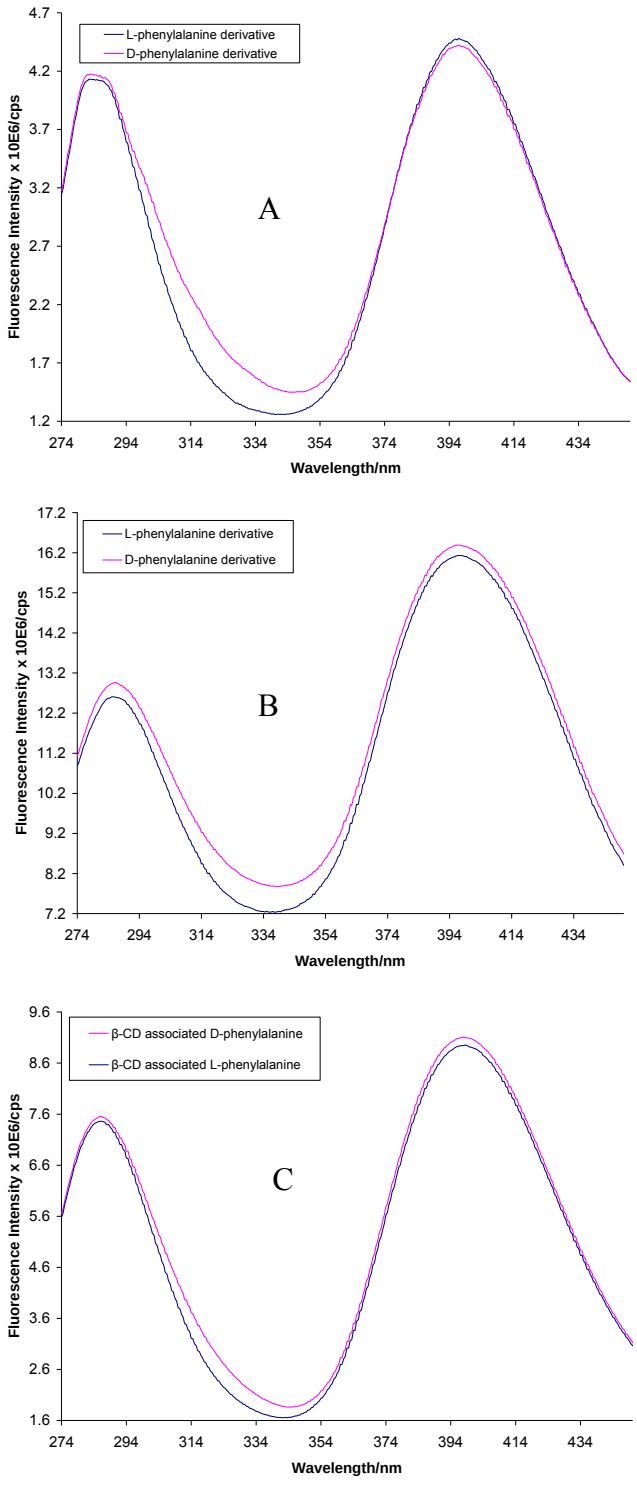

Figure 4.4. A: Fluorescence emission spectra of 5 mM stock solutions of racemate 2-butanol esters of D- and L-phenylalanine prepared by the NSCCDS procedure. B: Fluorescence emission spectra of 3.511 mM stock solutions of racemate 2-butanol esters of D- and L-phenylalanine prepared from the recrystallized ester solid samples. C: Fluorescence emission spectra of 5 mM stock solutions of D- and L-phenylalanine prepared by dissolving D- and L-phenylalanine in 10 mM stock solution of β-cyclodextrin.

performance of our custom-designed capillary cell. This similarity in spectral information is a further indication that the capillary cell is comparable to the commercial fluorometer cell. Comparison of Figure 4.4A, B, and C shows that the difference in intensity between the D and L-phenylalanine esters are about twice the difference recorded between the β-CD associated D- and L-phenylalanine complexes. The smaller difference in spectra recorded for the β-CD solutions could be due to the transient and non-covalent nature of the diastereomeric β-CD-phenylalanine inclusion complex. This is because, unlike the covalent diastereomeric ester pairs, the non-covalent diastereomeric β-CD-phenylalanine complexes could easily undergo conformational changes in solution. These conformational changes could lead to the formation of conformers with closely related spectral properties. In addition, the transient nature of the complexes indicates that with the use of an ordinary steady-state instead of a time resolved fluorescence technique for spectral collection, one is able to capture only an averaged situation: transition between the free enantiomer state and the β-CD complex state– can be captured. This average situation may present a smaller spectral difference between the β-CD-phenylalanine complexes. Zhong et al. reported in a hydrophobic binding study involving a methyl derivative of β-cyclodextrin and 2-(2-hydroxyphenyl)-4-methyloxazole (HPMO) that the bound state of HPMO changes in the cavity of the cyclodextrin molecule within picoseconds [90]. The phenylalanine molecule is smaller and has a lesser number of hydrogen bonding groups than HPMO. It is, therefore, possible that the bound state of phenylalanine could change in the cavity faster than HPMO. Transition between the enantiomeric and diastereomeric states of phenylalanine could, as a result, occur at a rate faster than would allow the individual states to be

captured by the ordinary steady-state fluorescence probe (time scale of 10^{-7}-10^{-9} s) used in this study.

Figure 4.5A, B, C are the fluorescence emission spectra from 274-450 nm recorded for the three sets of thirty sample solutions (NSCCDS, RE and β-CD samples) prepared for the first three analyses. Figure 4.5A shows the fluorescence emission spectra for the NSCCDS samples. Figure 4.5B shows the emission spectra for the thirty RE samples and Figure 4.5C the emission spectra for the thirty β-CD samples. It was shown in the study described in the previous chapter that the inherent spectral properties of our custom-designed capillary cell will not adversely affect quantitative analysis. As such, the spectra for the sample solutions in Figure 3.20 A, B, and C were not blank corrected.

Figure 4.6A shows the mean centered fluorescence emission spectra of the thirty NSCCDS samples, 4.6B the RE samples, and 4.6C the β-CD samples. The three sets of spectra reveal clearly that the sample solutions vary in their fluorescence emission. This is due to the difference in the spectral properties of the diastereomerically discriminated enantiomers of phenylalanine. Unlike the RE and β-CD samples, most of the mean centered spectra for the NSCCDS samples crossed each other at about 379 nm. This behavior is usually observed for a set of solutions containing identical total amounts of two different species having identical molar absorption coefficients at a common wavelength but different at other wavelengths. For a set of solutions containing strictly two of such species, the wavelength at which the absorption of the two species happens to be identical is termed as an isosbestic point. A set of solutions that differ from this ideal situation may show deviations in which case the spectra may not cross perfectly at a

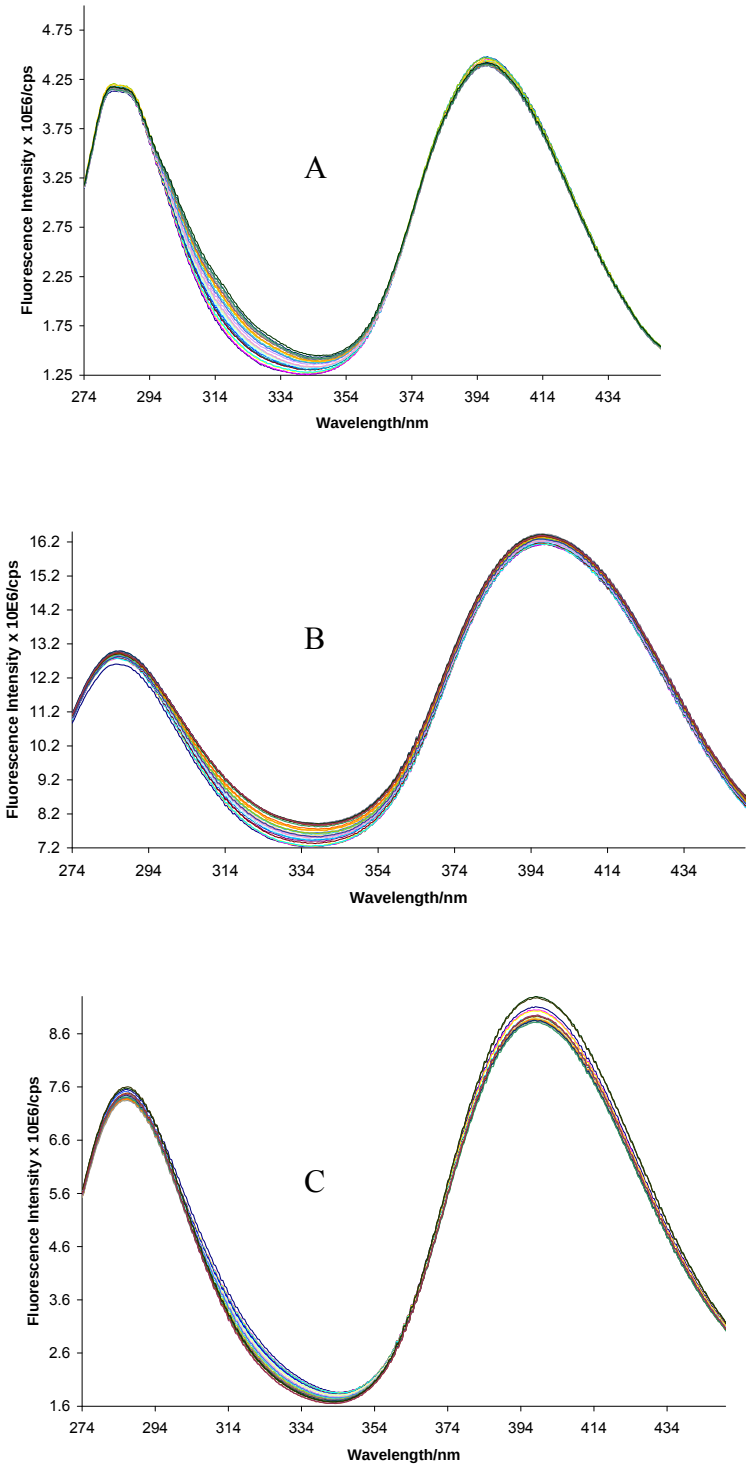

Figure 4.5. A: Fluorescence emission spectra of thirty NSCCDS sample solutions. B: Fluorescence emission spectra of thirty RE samples. C: Fluorescence emission spectra of thirty β-CD samples.

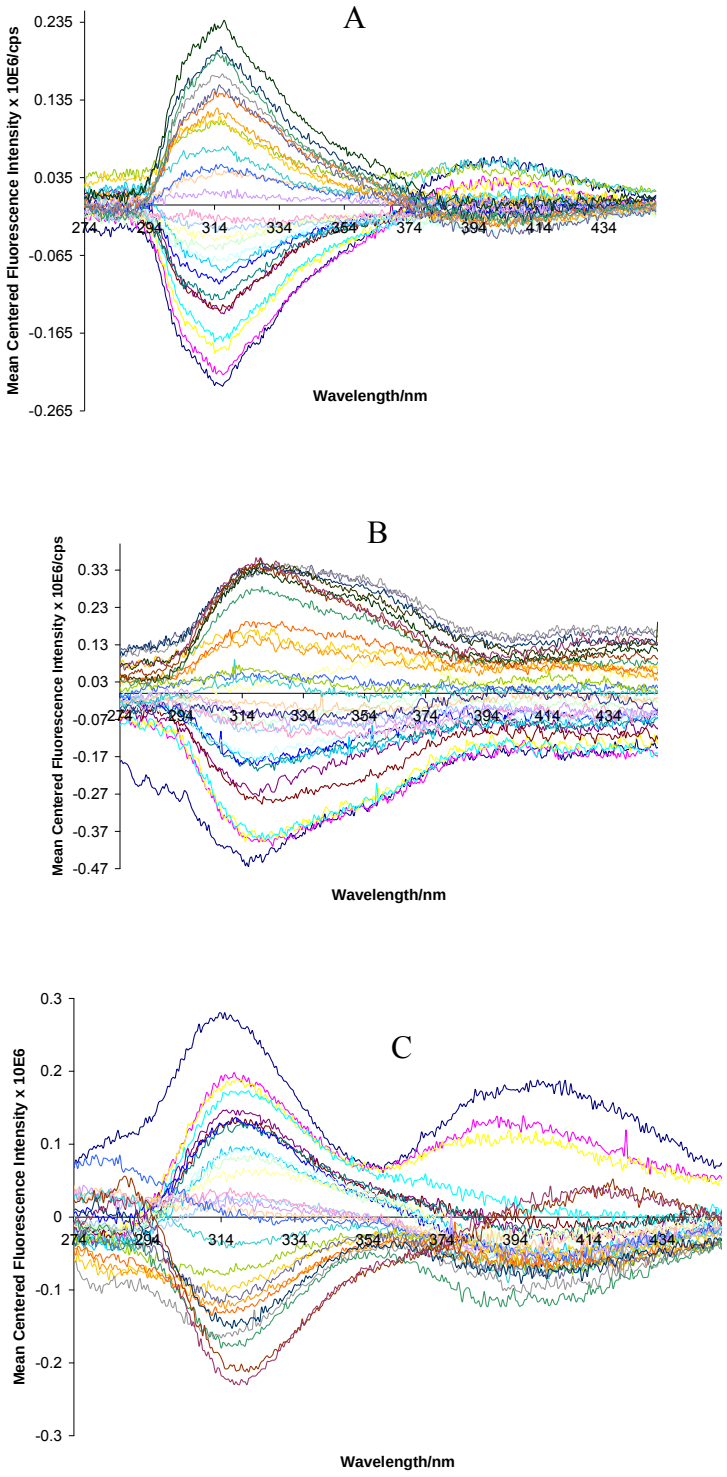

Figure 4.6. A: Mean centered fluorescence emission spectra of the thirty NSCCDS samples. B: Mean centered fluorescence emission spectra of the thirty ester-crystal samples. C: Mean centered fluorescence emission spectra of the thirty β-CD sample.

single wavelength. We term this 'pseudo isosbestic' behavior where the solutions may absorb light identically over a narrow range of wavelengths leading to spectra crossing over a narrow range of wavelengths instead of a single wavelength. Figure 4.6A shows that the NSCCDS samples exhibit a pseudo isosbestic behavior. This 'pseudo isosbestic' behavior rather than a classical isosbestic point is expected for such a set of sample solutions because they contain more than a pair of species. As shown in Figure 4.1 the use of a racemic mixture of 2-butanol in discriminating D- and L-phenylalanine, will result in sample solutions having four pairings of diastereomers and two of enantiomers. As such, the sample solutions deviate from the ideal case where a classical isosbestic point (single wavelength) is expected. Unlike the RE samples with no spectra crossing, the mean centered spectra of some of the β-CD sample cross each other. In addition, the pattern of the mean centered spectra for the β-CD samples bears some resemblance to that of the NSCCDS samples. In contrast, the pattern revealed by the RE samples is completely different even though the sample solutions contain the same 2-butyl D and L-phenylalanine esters as the NSCCDS samples. This difference might be due to the fact that in addition to the phenylalanine esters, the NSCCDS samples, by virtue of the non-separative nature of the sample preparation procedure, contain the unreacted excess of the racemate of 2-butanol and HCl unlike the RE samples. The two sample solutions are therefore not identical. The racemate of 2-butanol, unlike the hydrochloric acid, can undergo non-covalent chiral interactions with the phenylalanine esters. This could enhance the discrimination (Vespalec et al. [34]). Thus, the unreacted excess of the racemate of 2-butanol, could be responsible for the'pseudo isosbestic' behavior recorded.

As usual, the spectral data of a set of calibration samples, which were randomly selected from the total number of NSCCDS, RE and β-CD samples prepared for analysis, were used to develop PLS-1 calibration models for prediction. The D- or L-phenylalanine enantiomer mole fractions of the three sets of calibration samples are listed below.

NSCCDS Samples (D-Phe mole fractions)	Recrystallized Ester Samples (D-Phe mole fractions)	β-CD Samples (L-Phe mole fractions)
0.0606	0.182	0.939
0.242	0.333	0.848
0.303	0.424	0.788
0.364	0.455	0.697
0.394	0.515	0.576
0.515	0.576	0.515
0.697	0.606	0.485
0.727	0.697	0.455
0.758	0.848	0.394
0.788	0.909	0.242
		0.182

Figures 4.7A, B, C, and D show the PLS-1 regression model plots for the NSCCDS calibration samples. Figure 4.7A, is the two-dimensional scores, which reveals a pattern of increasing order of arrangement of the NSCCDS samples from left to right. Figure 4.7B, which is the regression coefficient as a function of a wavelength plot, shows a positive regression coefficient curve for the modeled wavelength region, 297-355 nm. This indicates that the spectral data (x-variable) in this wavelength region and the enantiomeric composition (y-variable) change in the same direction. The curve shows that the highest regression coefficient or rate of change of the enantiomeric compositions with the spectral data is at 316 nm. The smooth nature of the curve indicates that for the

PC used for the model, the enantiomeric compositions change uniformly with the spectral data in the modeled wavelength region. The explained variance plot in Figure 4.7C shows that eight principal components were computed. However, only one principal component, the first PC, was needed for the development of the model. This PC explained 100 % of the variation in both the spectral data and the sample composition. This situation arises when the spectra of the samples are well separated in a given wavelength region as revealed by the mean-centered spectra for the NSCCDS samples (see Figure 4.6A). Figure 4.7D shows the regression line for the predicted (by cross-validation) versus known mole fractions of the 2-butanol ester of Phe calibration samples (NSCCDS samples). The line shows a good fit between the predicted and known enantiomeric compositions of the calibration samples. This is an indication of a strong correlation between the spectral data and the enantiomeric compositions.

Figure 4.8A, B, C, and D show the PLS-1 regression model plots for the recrystallized ester (RE) calibration samples. Figure 4.8A is the scores plot, 4.8B the regression coefficient plot, 4.8C the explained variance plot, and 4.8D the cross-validation regression line plot. Similar to the NSCCDS calibration samples of Phe in the first analysis, the scores plot for the RE calibration samples (Figure 4.8A) shows a pattern of increasing D-phenylalanine mole fractions from left to right. The regression coefficient plot in Figure 4.8B shows a curve that has both positive and negative regions for the modeled wavelength range, 274-450 nm. This is different from the situation observed for the NSCCDS calibration samples. The positive part of the curve indicates that the enantiomeric compositions of the calibration samples change in the same direction with spectral data while the negative part of the curve indicates change in

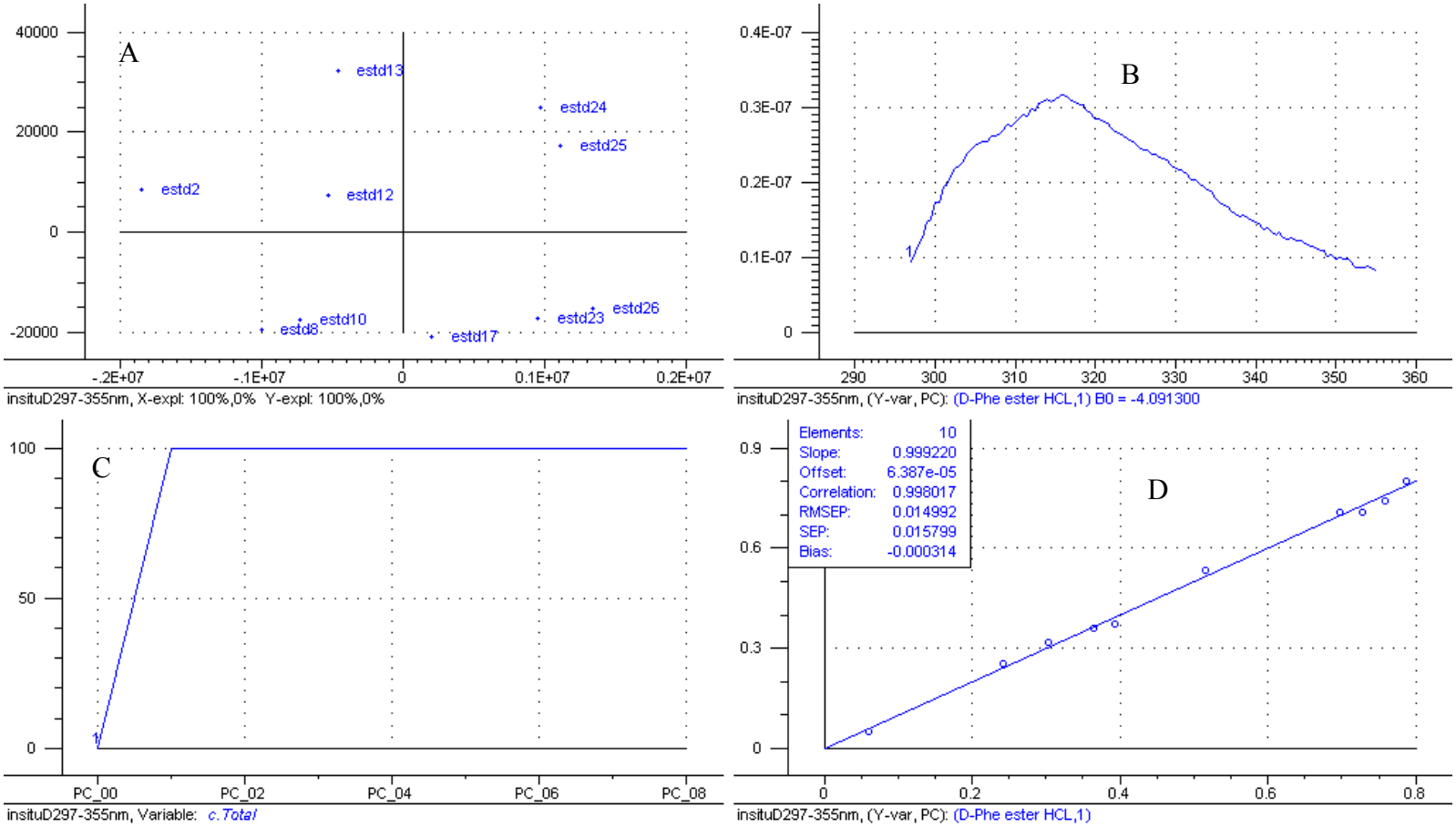

Figure 4.7. Plots of PLS-1 regression calibration model developed using the fluorescence emission spectral data and known enantiomeric compositions of NSCCDS calibration samples of phenylalanine (2-butanol esters of Phe) listed on page 192. A: scores plot, B: regression coefficient as a function of wavelength plot, C: percent explained variance as a function of principal component plot, and D: regression line for the predicted (by cross-validation) mole fractions versus the known mole fractions of calibration samples. The model required only one PC (see below plot B or D).

opposite directions. The highest positive regression coefficient for the RE calibration samples is recorded at 320 nm; a shift of 4 nm from the wavelength at which the highest regression coefficient for the NSCCDS samples in the first analysis of Phe was recorded. The curve shows that the highest negative regression coefficient is associated with the 360 nm wavelength. Unlike the NSCCDS calibration samples of Phe in the first analysis, the regression coefficient curve for the RE calibration samples is noisy. The explained variance plot shown in Figure 4.8C for the RE samples reveal that seven PCs were computed. However, only the first and second PCs were required in developing the model. The first PC explained 99 and 97 % of the variation in the spectral data and the enantiomeric compositions of the samples, respectively. Correspondingly, the second PC explained 1 and 3 %. An attempt to use only the first PC degraded the model. This implies the 3 % variation in enantiomeric composition explained by the second PC is important. Figure 4.8D shows the regression line for the predicted versus actual mole fractions of the RE calibration samples. In spite of the noisy regression coefficient curve, the regression line indicates a strong correlation between the spectral data and the enantiomeric compositions of the RE calibration samples.

The plots shown in Figure 4.9A, B, C, and D are correspondingly the scores, regression coefficient, explained variance, and the predicted (by cross-validation) versus actual mole fraction regression line plots for the β-CD calibration samples. Unlike the models for the first two analyses, the model for the β-CD calibration samples was developed in terms of the L- and not the D-phenylalanine mole fractions. Thus, the scores plot (Figure 4.9A) for the β-CD calibration samples shows a pattern of variation for the β-CD calibration samples that is opposite to the pattern observed for the first two

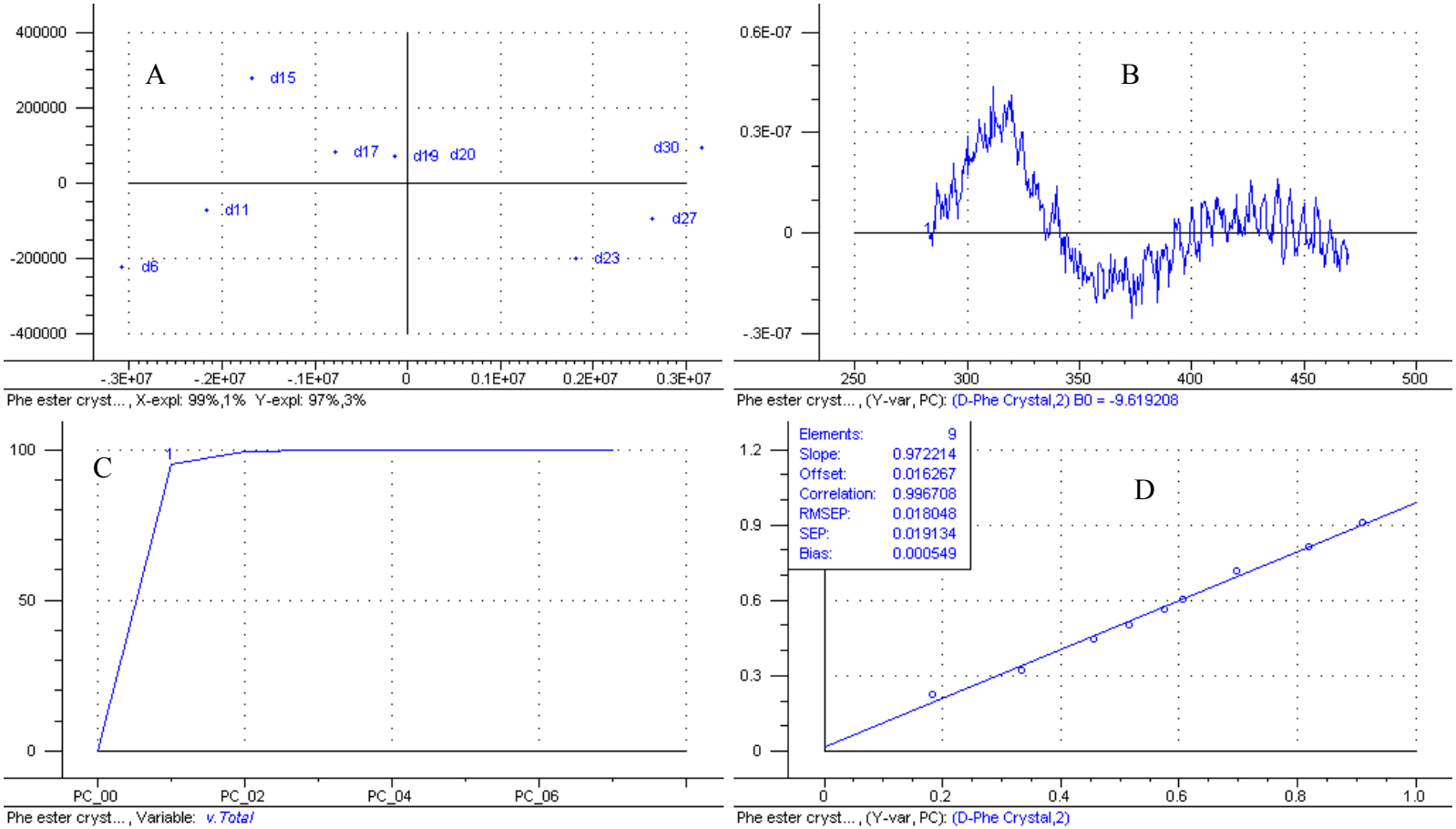

Figure 4.8. Plots of PLS-1 regression calibration model developed using the fluorescence emission spectral data and known enantiomeric compositions of the recrystallized phenylalanine ester calibration samples listed on page 192. A: scores plot, B: regression coefficient as a function of wavelength plot, C: percent explained variance versus principal component plot, and D: regression line for the predicted (by cross-validation) mole fractions versus the known mole fractions of calibration samples. The model required only two PC (see below plot B or D).

analyses. This is an indication of the sensitivity of the PLS-1 regression technique to the spectral difference between the D- and L-phenylalanine diastereomers. The regression coefficient curve for the β-CD samples in Figure 4.9B is less noisy compared to the curve for the RE samples (Figure 4.8B). The regression coefficient curve for the β-CD samples, similar to the RE samples, has both positive and negative regions for the best modeled wavelength range, 300-357 nm. The highest positive regression coefficient for the β-CD samples is associated with the326 nm wavelength while highest negative regression coefficient is associated with the 300 nm wavelength. The explained variance plot in Figure 4.9C for the β-CD samples shows nine PCs were computed with explained variances above 95 %. However, similar to the RE samples, only the first two PCs were required for the model. Though different spectral regions were modeled, these PCs explained the same percentages of variation in spectral data and enantiomeric composition as the first two PCs computed for the RE calibration samples. As noted for the RE model, exclusion of the second PC from the β-CD model degraded the model. The cross-validation regression line shown in Figure 4.9D for the β-CD samples, as usual, indicates strong correlation between the spectral data and the eantiomeric compositions of calibration samples.

Table 4.2 compares the plot characteristics of the cross-validated PLS-1 regression plots for the NSCCDS, RE, and β-CD calibration samples. It is clear from the table that relevant spectral information is contained in similar wavelength regions for the NSCCDS and β-CD calibration samples. This is different from the recrystallized ester (RE) samples, for which the entire emission wavelength scanned was required to extract relevant spectral information. In spite of this difference, the plot statistics– slope,

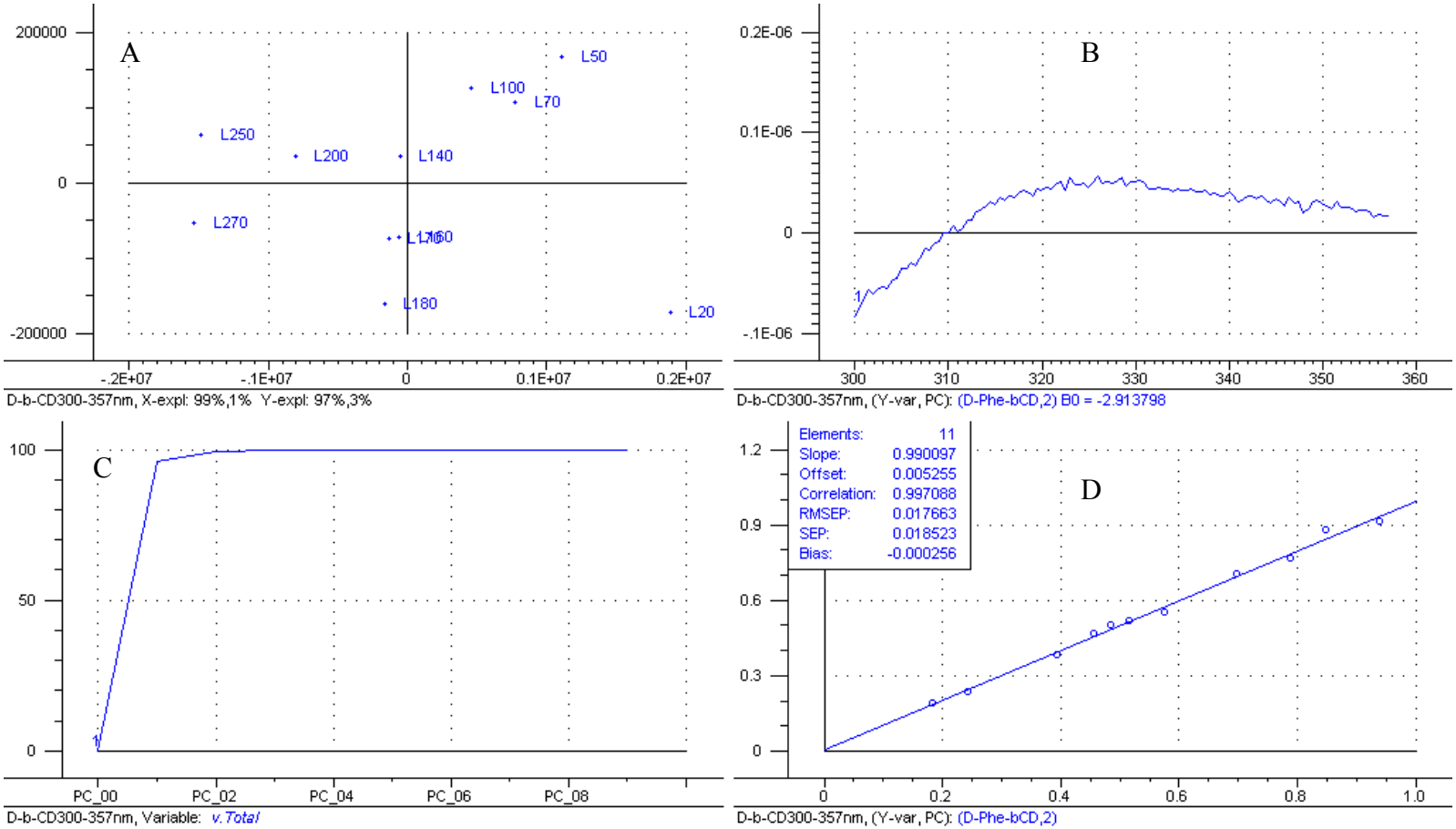

Figure 4.9. Plots of PLS-1 regression calibration model developed using the fluorescence emission spectral data and known enantiomeric compositions of the phenylalanine-β-CD calibration samples listed on page 192. A: scores plot, B: regression coefficient as a function of wavelength plot, C: percent explained variance versus principal component plot, and D: regression line for the predicted (by cross-validation) mole fractions versus the known mole fractions of calibration samples. The model required only two PC (see below plot B or D).

correlation coefficient, and root-mean-square error of prediction computed for cross-validating the three sets of calibration samples, are not significantly different.

Table 4.2. Plot characteristics of the cross-validated PLS-1 regression plots for the NSCCDS, RE, and β-CD calibration samples listed on page 191. The cross-validated PLS-1 regression plots are shown in Figure 4.7 for the NSCCDS samples, Figure 4.8 for the RE samples, and Figure 4.9 for the β-CD samples

Sample type	Modeled wavelength range (nm)	Number of principal components	Slope of regression line	Correlation coefficient of regression line	RMSEP[a]
NSCCDS[b]	297-355	10	0.999	0.998	0.015
Recrystallized ester	274-450	9	0.972	0.997	0.018
β-CD[c]	299-357	11	0.990	0.997	0.018

[a] Root-mean-squares error of prediction, [b] Non-separative, covalent, chiral discrimination strategy, [c] β-cyclodextrin

To show that the strong correlations portrayed by the NSCCDS, RE, and β-CD calibration samples apply to the rest of the corresponding samples not used in developing the calibration models, predictions were made of the samples not used for the calibration. Thus, samples not included in the calibration sets were used as sets of validation samples to validate the calibration models. The validation samples that were identified by the model as outliers were excluded from the analyses.

Table 4.3 shows the predicted D-phenylalanine mole fractions of the NSCCDS, RE, and β-CD validation samples, compared with the actual D-phenylalanine mole fractions. Clearly, the prediction results in Table 4.3 reveal a high level of prediction accuracy– the predicted mole fractions favorably agree with the actual mole fractions. The root-mean-square error of prediction (RMSEP), which is a measure of the average deviation of the predicted sample from the actual sample, is 0.011 for the NSCCDS analysis, 0.023 for the recrystallized ester (RE) analysis, and 0.021 for the β-CD analysis.

Table 4.3 Comparison of predicted D-phenylalanine mole fractions of the NSCCDS, recrystallized ester (RE), and β-CD validation samples with the corresponding actual D-phenylalanine mole fractions.

Actual D-Phe ø for NSCCDSS[a]	Predicted D-Phe ø for NSCCDSS	Actual D-Phe ø for RE[b] sample	Predicted D-Phe ø for RE sample	Actual D-Phe ø for β-CD[c]	Predicted D-Phe ø for β-CD
0.0909	0.0753	0.212	0.220	0.909	0.889
0.121	0.133	0.273	0.297	0.879	0.872
0.152	0.157	0.303	0.331	0.818	0.789
0.212	0.229	0.364	0.406	0.758	0.773
0.273	0.292	0.485	0.501	0.727	0.751
0.333	0.329	0.545	0.576	0.636	0.679
0.485	0.482	0.667	0.684	0.545	0.541
0.545	0.539	0.818	0.811	0.424	0.423
0.576	0.580	0.879	0.854	0.364	0.352
0.636	0.642	0.939	0.932	0.303	0.284
0.667	0.659	-	-	0.212	0.227
0.848	0.863	-	-	0.152	0.123
RMSEP[d]	0.011		0.023		0.021

ø: mole fraction, [a] Non-separative, covalent, chiral discrimination strategy sample, [b] Recrystallized ester, [c] β-cyclodextrin, [d] Root-Mean-Squares Error of Perdiction

β -cyclodextrin is known from our previous studies to be particularly effective for the analysis of phenylalanine [11, 55]. The magnitudes of the root-mean-square errors of prediction for our covalent discrimination strategy, NSCCDS, using the racemate of 2-butanol and the non-covalent discrimination strategy using β-CD indicate that both strategies are effective for the analysis phenylalanine. The predictions for the recrystallized sample (RE) analysis undoubtedly show that the ester pairs that were formed in the present study, and the study described in Chapter 2, are diastereomeric. The results for the NSCCDS analysis in the present study is of a particular interest

because it confirms the effectiveness, robustness, and consistency or reproducibility of our newly developed non-separative, covalent, chiral discrimination strategy (NSCCDS)– the 0.011 RMSEP computed for the present analysis of phenylalanine is consistent with the 0.014 RMSEP computed for the analysis of the same phenylalanine in the study discussed in Chapter 2. This is regardless of the use of different chiral selectors used for the analyses. The strategy, thus, appears to holds a lot of promise for analyses such as this.

As mentioned earlier, the effect of analyzing the $\log_{10}$-converted instead of the original spectral data in analyses such as this may be beneficial. To verify whether PLS-1 regression analysis of log-converted spectral data is beneficial in analyses such as this, the emission intensities of the samples for the first two analyses (NSCCDS and RE analyses) were converted to the $\log_{10}$-emission intensities ($\log_{10}$ spectral data).

Figure 4.10A and C show the $\log_{10}$-converted fluorescence emission spectra from 274 to 450 nm for the NSCCDS and RE samples. The $\log_{10}$ spectra are compared with the corresponding original spectra in Figure 4.10B and D. Figure 4.10A and C compared with Figure 4.10B and D show that the $\log_{10}$ spectral conversion increased the originally small separations recorded among the spectra. This is due to the effect of logarithmic function on small numerical values.

Figure 4.11A, B, C, and D, correspondingly, represents the PLS-1 model scores plot, regression coefficient plot, explained variance plot, and regression line plot for the $\log_{10}$-converted spectral data of the NSCCDS calibration samples (previous samples). These PLS-1 calibration model plots for the log-converted spectral data of the NSCCDS

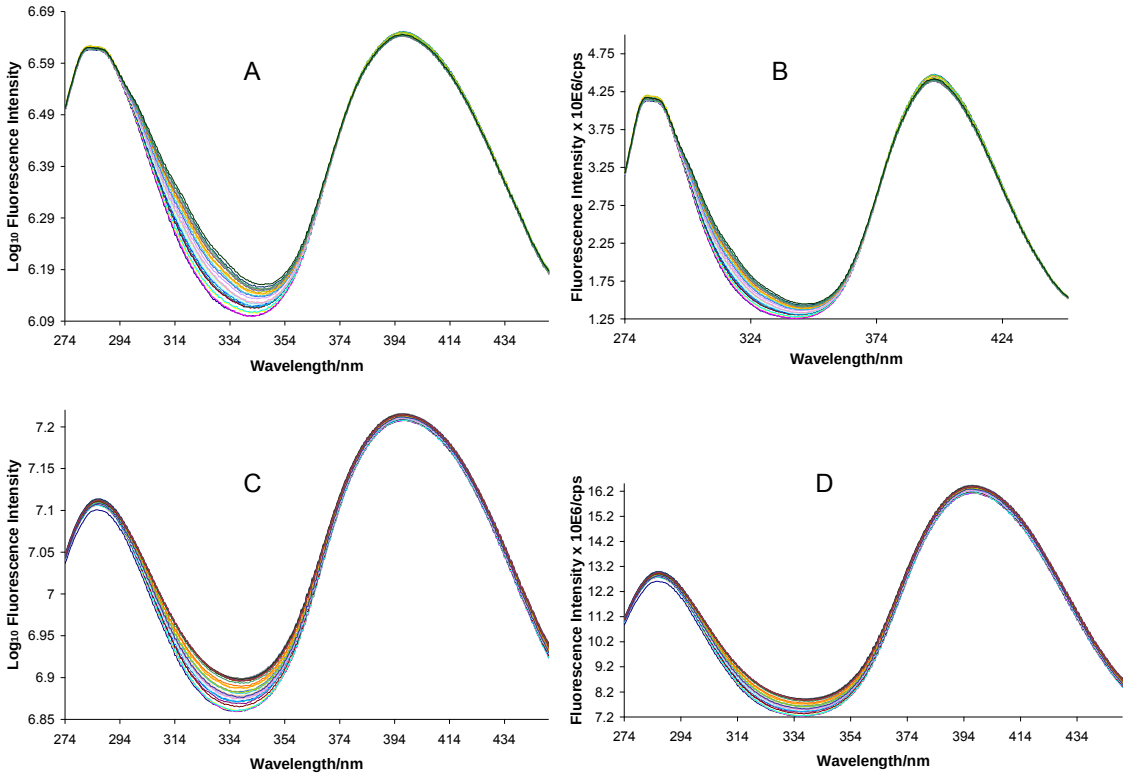

Figure 4.10. A: Log_{10} converted fluorescence emission spectra for the thirty NSCCDS samples compared with the original emission spectra shown in B. C: Log_{10} converted emission spectra for the thirty recrystallized samples compared with the original emission spectra shown in D. E: Log_{10} converted fluorescence emission spectra for the thirty β-CD samples compared with the original fluorescence emission spectra shown in F.

calibration samples reveal features that are identical to the PLS-1 model plots computed using the original spectral data of the samples.

Figure 4.12A, B, C, and D show the PLS-1 regression model scores, regression coefficient, percent variance, and cross-validation regression line plots for the log_{10}-converted spectral data of the recrystallized ester (RE) calibration samples. Similar to the log_{10} model developed for the NSCCDS calibration samples, the log_{10} model plots in Figure 4.12A, B, C, and D for the RE samples reveal features that are identical to the

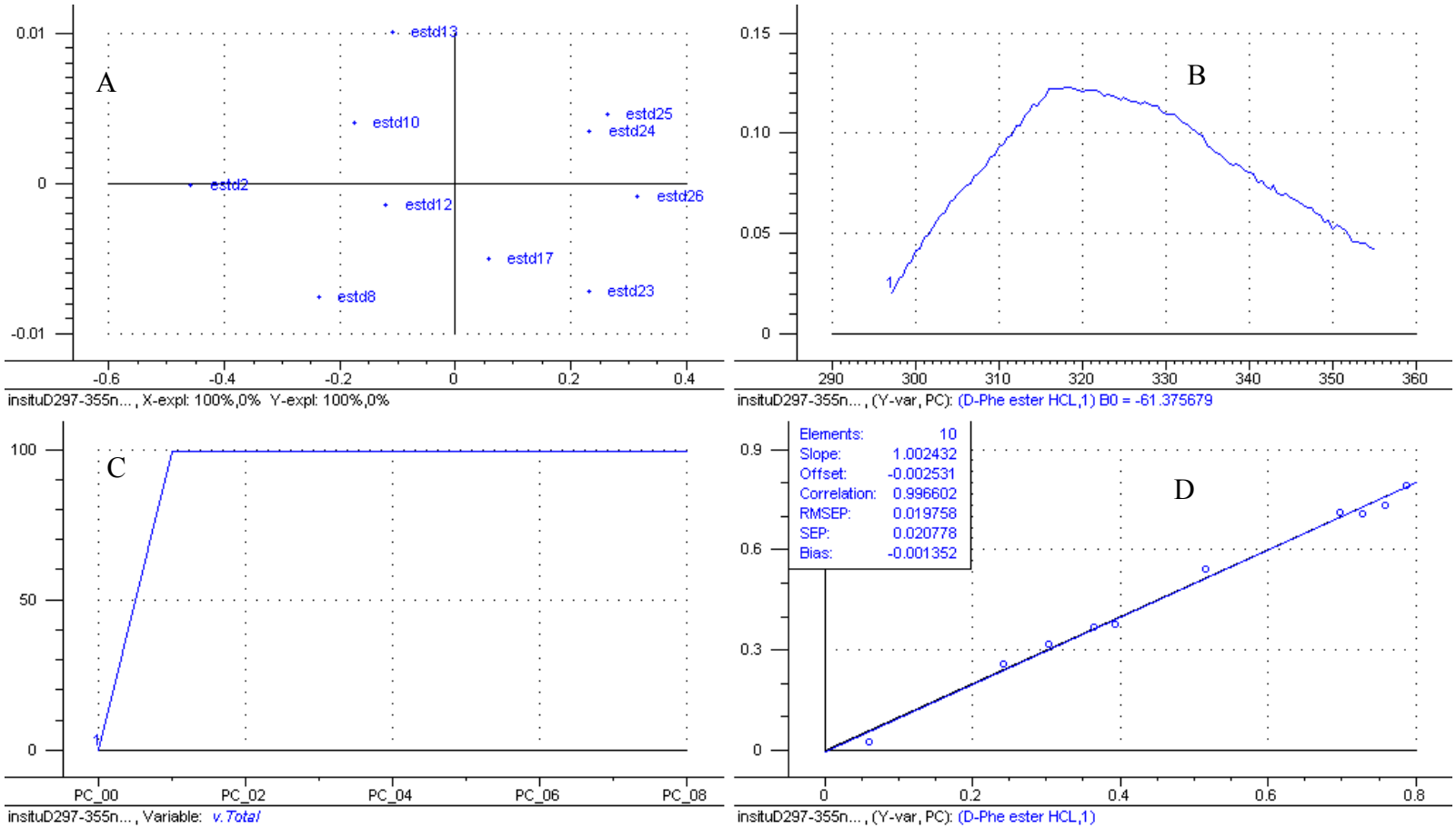

Figure 4.11 Plots of PLS-1 regression calibration model developed using the $\log_{10}$-converted fluorescence emission spectral data and known enantiomeric compositions of NSCCDS calibration samples of phenylalanine (2-butanol esters of Phe) listed on page 191. A: scores plot, B: regression coefficient as a function of wavelength plot, C: percent explained variance as a function of principal component plot, and D: regression line for the predicted (by cross-validation) mole fractions versus the known mole fractions of calibration samples. The model required only one PC (see below plot B or D).

model plots developed using the original spectral data (see Figure 4.8A, B, C, and D) of the RE calibration samples.

Table 4.4 compares the cross-validation PLS-1 regression plot statistics for the original and $\log_{10}$ PLS-1 calibration models developed for the two sets of samples. The table shows that unlike the NSCCDS samples, the cross-validation regression plot statistics for the original spectral data for the RE samples are significantly identical to the cross-validation regression plot statistics computed for the log spectral data. For the NSCCDS samples, the RMSEP, 0.015, and standard error (SE), 0.016 , of cross-validation, computed for the original spectral data of the calibration samples, increased to 0.02 and 0.021, respectively, for the $\log_{10}$-converted spectral data. The increases in these errors signify the weakening of the strength of correlation between the spectral data and enantiomeric composition of the samples.

The predicted and actual D-phenylalanine mole fractions for the NSCCDS validation samples are reported in Table 4.5. In addition, the mole fractions predicted using the original spectral data are reported in the same table for comparison. In order to have the same basis for comparison, the same validation samples, which were predicted for the original spectral data analysis, were predicted for for the $\log_{10}$ spectral data analysis as well. It is clear from Table 4.5 that compared to the actual D-phenylalanine mole fractions, the $\log_{10}$ spectral data predictions for most of the samples are associated with higher absolute errors than the original spectral data predictions. The root-mean-square error of prediction computed for the $\log_{10}$ spectral data predictions is 0.027. The error is more than two times the root-mean-square error of computed for the prediction of the validation samples using the original spectral data. It is clear from these results that

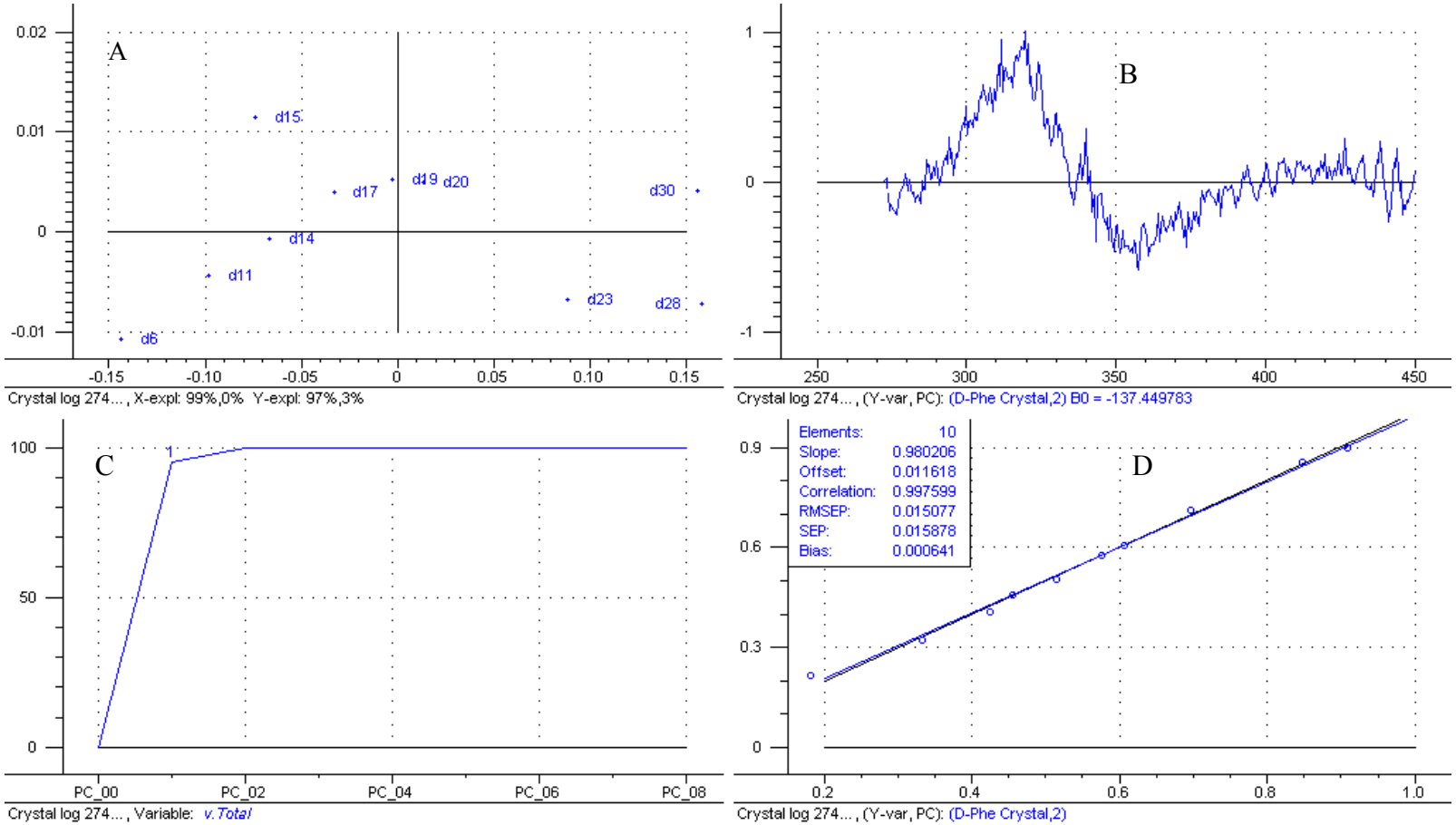

Figure 4.12. Plots of PLS-1 regression calibration model developed using the $\log_{10}$-converted fluorescence emission spectral data and known enantiomeric compositions of the recrystallized phenylalanine ester calibration samples listed on page 191. A: scores plot, B: regression coefficient as a function of wavelength plot, C: percent explained variance versus principal component plot, and D: regression line for the predicted (by cross-validation) mole fractions versus the known mole fractions of calibration samples. The model required only two PC (see below plot B or D).

Table 4.4. Comparison of the cross-validation PLS-1 regression plot statistics computed for the original and $\log_{10}$ spectral data of the NSCCDS and recrystallized ester calibration samples.

Plot Statistic	Plot Statistic Value for Cross-Validated NCCDS and RE Calibration Samples			
	NSCCDS[a] original spectral data	NSCCDS $\log_{10}$ spectral data	RE[b] original spectral data	RE $\log_{10}$ spectral data
Slope	0.999	1.00	0.972	0.980
Offset	6.59×10^{-5}	0.00253	0.0163	0.0116
Correlation coefficient.	0.998	0.997	0.997	0.998
RMSEP[c]	0.015	0.020	0.018	0.015
SEP[d]	0.016	0.021	0.019	0.016

[a] Non-separative, covalent, chiral discrimination strategy, [b] Recrystallized ester,[c] Root-mean-squares error of prediction, [d] Standard error

modeling the $\log_{10}$ converted spectral data of the NSCCDS samples did not improve but negatively affected the information in the spectral data, hence the higher RMSEP value.

Table 4.6 compares the $\log_{10}$ and original spectral data predictions for the D-phenylalanine mole fractions of the recrystallized ester (RE) validation samples with the actual D-phenylalanine mole fractions. Unlike the NSCCDS samples, the absolute errors computed for the $\log_{10}$ spectral data predictions are significantly identical to the absolute errors computed for the original spectral data predictions. The root-mean-square errors for the $\log_{10}$ and original spectral data analysis are, respectively, 0.022 and 0.023. Consequently, the $\log_{10}$ conversion of the spectral data of the recrystallized ester samples resulted in no significant effect on the analysis.

Generally, the PLS-1 regression analysis of the two sets of $\log_{10}$-converted spectral data did not show any improve in the results of the analysis. As noted earlier, the $\log_{10}$ spectral data analyses resulted in an increase in RMSEP for the NSCCDS samples while the RMSEP computed for the RE samples significantly unchanged.

Table 4.5 Prediction results for $\log_{10}$ and original spectral data analyses of NSCCDS validation samples of phenylalanine. Samples were predicted in terms of D-phenylalanine mole fractions.

Actual D-Phe ø [a] of NSCCDS sample	Log_{10} spectral data prediction	Absolute error	Original spectral data prediction	Absolute error
0.0909	0.0634	0.0275	0.0753	0.0156
0.121	0.127	-0.006	0.133	-0.012
0.152	0.151	0.001	0.157	-0.005
0.212	0.232	-0.02	0.229	-0.017
0.273	0.297	-0.024	0.292	-0.019
0.333	0.333	0	0.329	0.004
0.485	0.487	-0.002	0.482	0.003
0.545	0.544	0.001	0.539	0.006
0.576	0.579	-0.003	0.58	-0.004
0.636	0.635	0.001	0.642	-0.006
0.667	0.656	0.011	0.659	0.008
0.848	0.764	0.084	0.863	-0.015
Root-mean-square error of prediction		0.027		0.011

[a] Mole fraction, [b] Non-separative, covalent, chiral discrimination strategy

Figure 4.13 shows the UV absorption spectra from 227-268 nm for ten samples prepared to illustrate the application of the new covalent discrimination strategy in a real-life analysis. The spectra are labeled in terms of the weight compositions, D/L, in mg of the enantiomers of phenylalanine. The weight compositions of the samples were not varied at a regular interval. However, the total weight of each sample is about 0.0300 g. Figure 4.13 clearly shows that the absorbances of the real-life situation samples vary significantly from each other. To determine whether the differences in absorbance shown by the real-life (RL) samples correlate with their enantiomeric compositions, all of the ten

samples were cross-validated, that is, each sample was excluded once from the calibration model and predicted as a validation sample. As such, each sample was tested both as a calibration and a validation sample.

Table 4.6. Prediction results for $\log_{10}$ and original spectral data analyses for recrystalized phenylalanine ester (RE) validation samples. Samples were predicted in terms of D-phenylalanine mole fractions.

Actual D-Phe Ø [a] of RE sample	Log_{10} spectral data prediction	Absolute error	Original spectral data prediction	Absolute error
0.212	0.214	-0.002	0.22	-0.008
0.273	0.293	-0.02	0.297	-0.024
0.303	0.331	-0.028	0.331	-0.028
0.364	0.408	-0.044	0.406	-0.042
0.485	0.5	-0.015	0.501	-0.016
0.545	0.575	-0.03	0.576	-0.031
0.667	0.68	-0.013	0.684	-0.017
0.818	0.811	0.007	0.811	0.007
0.879	0.861	0.018	0.854	0.025
0.939	0.927	0.012	0.932	0.007
Root-mean-square error of prediction		0.022		0.023

[a] Mole fraction, [b] Recrystallized

Figure 4.14A and B, respectively, show the calibration (fitted) and cross-validation regression (predicted versus known weights) plots for the samples. Similar to the previous NSCCDS analyses of phenylalanine, the calibration plot shown in Figure 4.14A reveal strong correlation between spectral data and enantiomeric composition. This is indicated by the plot statistics shown in the plot (see top-left corner of plot). The calibration line in Figure 4.14A, which is repeated (black line) in the cross-validation plot, shows graphically the deviation in the prediction results for the RL samples. The

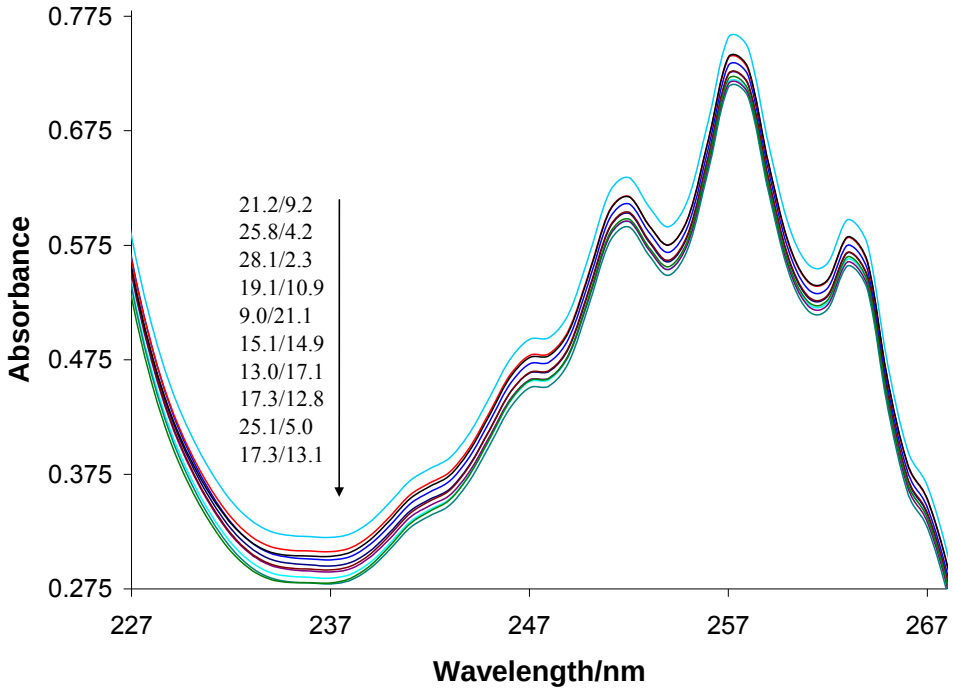

Figure 4.13. UV absorption spectra of ten real-life (RL) samples made up of different compositions of the enantiomers of phenylalanine. The samples were prepared by esterifying known weight compositions of the enantiomers weighed out together using a racemic mixture of 2-butanol in the presence of HCl. The arrow shows the order of the spectra from top to bottom according to the weight compositions, D/L, in mg of the enantiomers of phenylalanine making up the samples.

specific value for the predicted weight of D-phenylalanine in each sample, compared to the actual weight is shown in Table 4.7. It is obvious from the table that the absolute errors computed for the predicted weights are quite small. This is an indication of the effectiveness of the covalent discrimination. The root- mean-square error of prediction computed for the analysis is 0.0012. This error is significantly low compared to errors computed for the other analysis described earlier in this chapter. The low error values computed for this analysis suggest that the covalent discrimination strategy could be even more sensitive or effective for real-life situations. One reason that could possibly account for the high sensitivity or effectiveness of the real-life situation analysis is kinetically

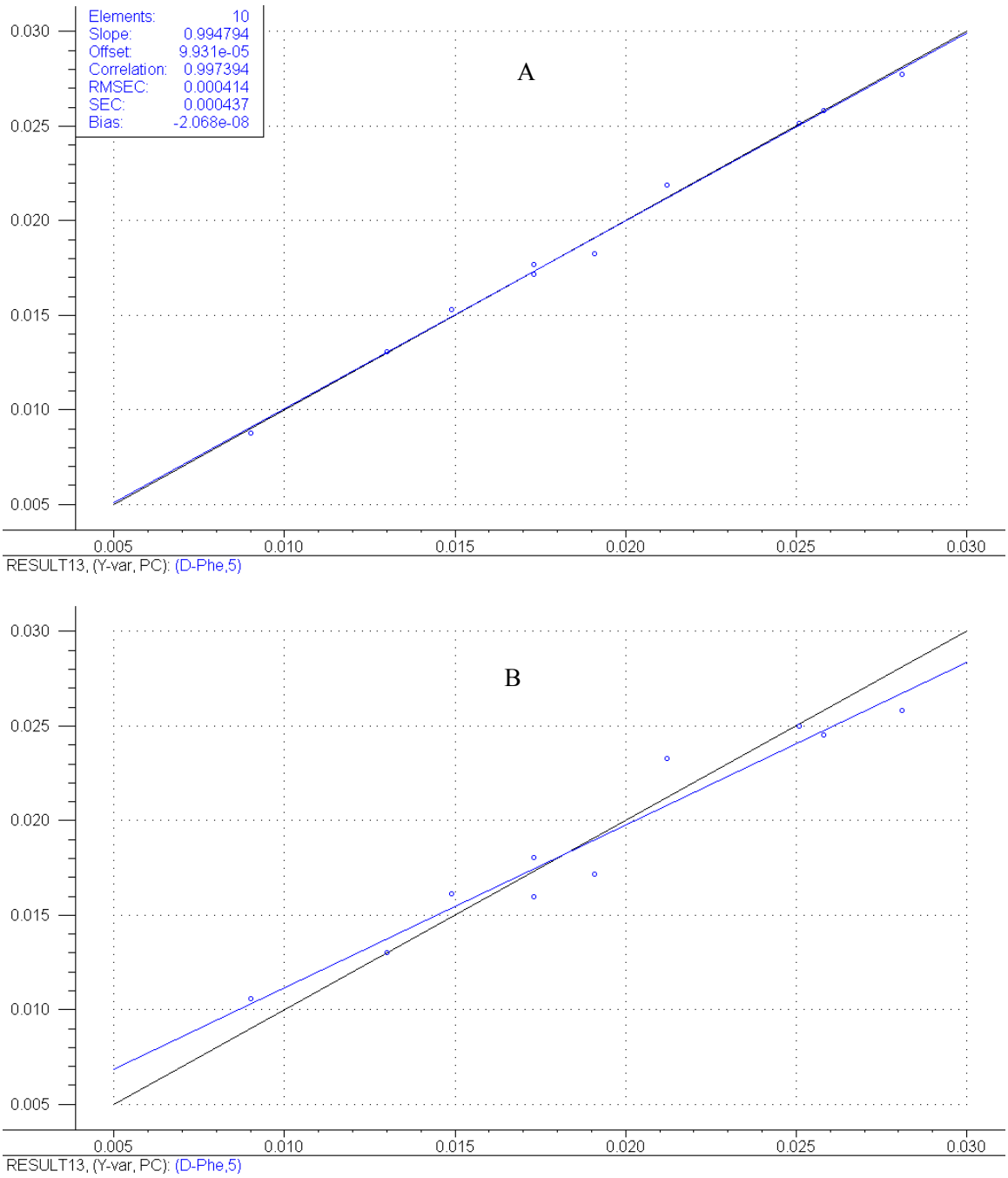

Figure 4.14. A: PLS-1 regression calibration plot developed from the spectral data of the ten phenylalanine samples prepared for real life situation analysis. B: PLS-1 cross-validated plot for the same samples in A.

and/or thermodynamically controlled competition between the enantiomers in their reaction with the chiral selector. Kinetic and /or thermodynamic control in reactions of

Table 4.7. Summary of the prediction results for the analysis of real-life situation samples of phenylalanine

Total weight (g)	Weight of L-Phe (g)	Weight of D-Phe (g)	Predicted weight of D-Phe (g)	Absolute error
0.0301	0.0211	0.009	0.0103	-0.0013
0.0301	0.0128	0.0173	0.0188	-0.0015
0.0301	0.0171	0.0130	0.0120	0.001
0.0300	0.0151	0.0149	0.0158	-0.0009
0.0304	0.0131	0.0173	0.0159	0.0014
0.0300	0.0109	0.0191	0.0182	0.0009
0.0304	0.0092	0.0212	0.0224	-0.0012
0.0300	0.0042	0.0258	0.0244	0.0014
0.0301	0.005	0.0251	0.0232	0.0019
0.0304	0.0023	0.0281	0.0271	0.001
Root-mean-square error of prediction				0.0012

this kind will lead to the preferential formation of the derivative of one of the enantiomers over the other. This could enhance quantitation of the enantiomers.

The Custom-Designed Capillary Micro Cell Compared with the Commercial Cell and the Capillary Flow-Cell

The root-mean-square error of prediction (RMSEP), as noted in the previous chapters can be used as a figure of merit to compare different techniques in analyses such as this because it is a measure of accuracy. In this section, the effects of the different fluorescence cells (the custom-designed capillary, commercial cell, and the capillary flow-cell) on the analysis of phenylalanine using β-CD as a chiral selector are compared. It should be noted that this comparison can be made because the cell used in a particular analysis is an integral part of the analytical technique and its spectral properties or mode

of application will directly impact the spectral data for the study in question. The studies compared in this section differ only in the type of cell used for the fluorescence measurement: the fluorescence instrument (The Jobin Yvon-SPEX Fluoro Max-2 spectrofluorometer), chiral analyte (phenylalanine), and chiral selector (β-CD strategy) are the same.

Table 4.8 compares the RMSEP figure of merit for the analysis of phenylalanine-β-CD samples excited through the custom-designed capillary micro cell to the RMSEP figures of merit computed for the analyses of phenylalanine-β-CD samples excited through the commercial and capillary flow cells. A summary of the results for the NSCCDS studies and analysis of the recrystallized esters are also reported in Table 4.8. Data on studies involving the use of the commercial cell and the capillary flow-cell were taken from previous analyses reported by our research group [55].

From Table 4.8, the RMSEP values for previous analyses of phenylalanine involving the use of the commercial fluorometer cell (10 mm pathlength) range from 0.007 to 0.019. These errors are comparable with RMSEP, 0.021, computed for the analysis of the fluorescence emission spectral data for the phenylalanine collected using the capillary micro cell. The differences between these error values should be due most probably to random errors rather than cell defects because the differences are small. Similar to the β-CD analysis of Phe in the present study, the RMSEP values computed for the analyses of the emission spectral data collected using the capillary cell, for the NSCCDS and RE samples, are comparable to the RMSEP values for studies in which the commercial cell was used. It is obvious from Table 4.8 that neither the concentration of phenylalanine nor the number of principal components appears to influence the RMSEP.

Table 4.8. Comparison of the root-mean-square error of prediction (RMSEP) figures of merit for the analysis of phenylalanine using the custom-designed capillary micro-cell, the commercial micro cell and the capillary flow-cell.

Cell Type	RMSEP[a]	Discrimination Strategy	BMWR[b] (nm)	Number of PC[c]	Concentration (mM)
Capillary micro cell	0.021	β-CD[d]	300-357	2	5
Commercial micro cell	0.013	β-CD	310-375	5	3.75
	0.019		310-360	5	1.875
	0.014		320-375	5	0.9375
	0.007		315-375	5	0.4688
Capillary flow-Cell	0.34	β-CD	275-450	-	3.75
Capillary micro cell	0.011	NSCCDS[e]	297-355	1	5
	0.023	NSCCDS, (Recrystallized ester sample)	274-450	2	5

[a] Root-mean-squares error of prediction, [b] Best modeled wavelength region, [c] Principal component
[d] β-cyclodextrin, [e] Non-separative, covalent chiral discrimination

Unlike the RMSEP values for the capillary and commercial cells, it can be seen from Table 4.8 that an unusually high RMSEP, 0.34, was computed for the study in which the emission spectral data of phenylalanine was collected using the capillary flow-cell. The unusually high error for the flow-cell analysis should be due to the flow system. This is because, except for the use of the flow-cell for emission spectra collection, the study was perform under conditions identical to those for the study reported in Table 4.8 in which the commercial cell was employed in the analysis of Phe at a concentration of 3.75 mM. In addition, the unusually high error should be due to the flow system because the capillary tube used for the flow-cell is similar to the capillary tube used for the

present study, which resulted in RMSEP values comparable to those for the commercial cell. It is noted in the reference [55] for the flow-cell study that the flow injection system needs optimization.

Based on the RMSEP values computed for the analyses involving the use of the custom-designed capillary cell compared to the commercial cell, it is undoubtedly clear that the capillary cell is comparable to the 10-mm pathlength commercial cell for steady-state fluorescence emission measurement.

Conclusion

The use of the racemic mixture of 2-butanol in place of (*S*)-(+)-1,2-propanediol in our newly developed covalent discrimination strategy, NSCCDS, for the successful analysis phenylalanine, indicates that the strategy will possibly lend itself to the use of a variety of chiral selectors. Thus, the strategy has the potential for being a general strategy for enantiomeric composition analysis. The successful application of the racemic mixture of 2-butanol in the present study shows that the use of isotropic spectroscopic (non-chiroptical) techniques, as employed by us, for chiral analyses will allow the use of racemate forms of chiral selectors for the assessment of enantiomeric purity. This is beneficial in view of the high cost of enantiopure chiral selectors as opposed to their racemates or racemic mixtures. Furthermore the use of the racemate of 2-butanol as a chiral selector in this study suggests it might be worthwhile investigating the possibility of using racemates as chiral selectors for quantitative chiral analysis, involving other techniques, particularly in chromatography. This should be possible because, as mentioned earlier, enantiomeric pairs are known not to react equally with any

given enantiomer. Thus, there is always the possibility of the preferential formation of one diastereomer of a pair of enantiomers over the other. However, the viability of using racemic mixtures for enantiomeric purity assessment in chromatographic can only be proven experimentally.

The small sample volume (25 μL) required by our custom-designed capillary cell is certainly a significant advantage over the use of the commercial cell, which requires not less than 1400 μL of sample volume. In addition, the use of our custom-designed capillary cell is less cumbersome and faster for spectral collection than the commercial cell. Thus, analysis involving fluorescence measurements can be performed more rapidly using the capillary cell than the commercial cell. There is, however, the need to improve on the quality of the cell by using a capillary tube made of high quality quartz material. With such a high quality quartz material, spectra collected using the capillary cell may not need to be blank corrected for qualitative purposes. The Jobin Yvon-SPEX Fluoro Max-2 spectrofluorometer used in this study is designed with an excitation beam for exciting a flat and wider surface area than presented by our custom-designed capillary cell. It is, therefore, possible that a spectrofluorometer whose optical configuration is modified to suit the geometry and size of the capillary cell might improve spectra collection with the capillary cell.

CHAPTER FIVE

(*S*)-(-)-1-phenylethylamine As a Chiral Selector for Non-Covalent Enantiomeric Composition Analysis

Introduction

In chapter two, (*S*)-(+)-1,2-propanediol (PD) was employed both as a covalent and a non-covalent chiral selector or discriminator for the enantiomeric composition analysis of selected chiral analytes including tyrosine and phenylalanine. The non-covalent chiral discrimination of tyrosine was particularly effective resulting in a root-mean-squares error of prediction of 0.019 (1.9 %) compared to 0.047 (4.7 %) for phenylalanine. This error difference in the analyses was noted could be most probably due to the difference in the chemical structure of the two analytes. Unlike phenylalanine, tyrosine has a phenolic group, which is a good hydrogen bonding donor capable of forming strong hydrogen bonds with the hydroxyl groups of (*S*)-(+)-1,2-propanediol. (*S*)-(+)-1,2-propanediol, on the other hand, is a weak base with a pKa of 14.9. Consequently, (*S*)-(+)-1,2-propanediol is capable of acting as a good hydrogen bonding acceptor for tyrosine to form strong hydrogen bonds. The non-covalent (*S*)-(+)-1,2-propanediol discrimination analysis of tyrosine is noteworthy. This is because it revealed that a non-inclusion complex forming chiral compound, capable of strong non-covalent interactions with a chiral analyte, can be used for effective non-covalent chiral discrimination in our CARMSD technique. This is important because such non-covalent discrimination strategy alternatives could be equally sensitive and/or more cost effective. For the amino acids analyzed in Chapter 2 and allied chiral compounds, non-covalent quaternary salt

formation could be an alternative discrimination strategy to the covalent esterification strategy described in Chapter 2. The non-covalent quaternary salt formation could be achieved through the use of a chiral amine whose pKa is higher than that of the chiral organic acid (amino acid or other) in question. On the other hand, a chiral selector, capable of protonating the amino group, for example, of amino acids can be used as a non-covalent chiral selector for the analysis of amino acids and allied chiral compounds. Generally, the classically non-covalent protonation reaction between an organic acid and an amine can be represented as shown in reaction equation 5.1 below. Such coordinate

$$RCOOH + NHR_2 = RCOO^{-}\,{}^{+}NH_2R_2 \qquad 5.1$$

bond forming interaction between the enantiomeric pair of an organic acid and a chiral amine will lead to the formation of a pair of diastereomeric salts. As a pair of diastereomeric compounds, the solution spectral properties, among others, of the pair of diastereomeric salts, should be different. This should allow for spectral discrimination of the enantiomeric pair of the organic acid in question for enantiomeric composition analysis.

For environmentally friendly strategies, it is desirable that these non-covalent interactions take place in environmentally friendly solvents like water. In addition, it was noted that chromatographic, electrophoretic, NMR and chiroptical analytical techniques employed in analyses such as this, are limited by one or more of the following: (1) long analysis time, (2) large sample amount requirement, (3) high sample concentration, and (4) high cost of analysis [4, 21, 91, 92-95]. As such, the chromatographic, electrophoretic, NMR and chiroptical techniques, even though effective, are less attractive for routine and high-throughput application in analyses such as this. As noted

earlier, these limitations have created the need for the development of effective alternative methods that are simpler, fast, robust, and less expensive [56, 96].

This chapter describes the determination of the enantiomeric composition of selected chiral analytes using (*S*)-(-)-1-phenylethylamine (S-PEA) as a non-covalent chiral selector. Similar to our previous strategies, S-PEA is used as a chiral discriminating agent for the formation of non-covalent diastereomeric pairs *in situ* from enantiomeric pairs of chiral analytes

(*S*)-(-)-1-phenylethylamine (S-PEA) or alpha-methylbenzylamine is a chiral amine with an optical activity of – 30 ± 1° ($[\alpha]_D^{20}$, 10% ethanol) and can be obtained in high purity (≥ 99 %). S-PEA is soluble in a large number of organic solvents including ethanol, benzene, toluene, acetonitrile, chloroform, and tetrahydrofuran (THF). Its solubility in water is 0.04 mg/mL. The non-covalent interactions possible with S-PEA include: (1) classically non-covalent Bronsted-Lowry or Lewis base reactions with appropriate acids and metal complex formation [97], (2) hydrogen bonding, and (3) aromatic π-system interactions [98, 99] .

The procedure for the application of (*S*)-(-)-1-phenylethylamine as a chiral selector is quite simple: calibration stock solutions are prepared by dissolving identical amounts of the pure enantiomers of the chiral analyte in separate but identical volumes of a stock solution of S-PEA. Calibration sample solutions are then prepared for spectral analysis by mixing known amounts of the stock solutions of the enantiomers dissolved in the S-PEA solution. The spectral data collected are then subjected to PLS-1 regression modeling to develop a calibration model. The calibration model is then used as usual for the determination of the enantiomeric composition of unknowns. This mode of

application of S-PEA for chiral analysis is novel. This is because though several reports are in the literature on the application of S-PEA in stereochemistry, [100-108] none indicates the use of 1-phenylethylamine for the determination of enantiomeric composition according to the simple procedure outlined for this study. (*R*/*S*)-(+/-)-1-phenylethylamine is an attractive chiral selector for our approach of chiral analysis because: (1) it can be dissolved in water, (2) it can be obtained in high purity (≥ 99 %), (3) it is capable of associating with a broad spectrum of other molecules through different intermolecular interactions– ionic, hydrogen bonding, and aromatic pi interactions, (4) it is inexpensive, and (5) it can be analyzed using several spectroscopic techniques including ordinary UV spectroscopy. Unlike the 1,2-propanediol covalent discrimination analysis described in chapter two, the present S-PEA strategy does not require any heating thus making the analysis simpler.

In this study, three amino acids (alanine, phenylalanine, and tyrosine) and a sugar/carbohydrate (arabinose) were analyzed. The structures of these chiral analytes are shown in Figure 5.1. Based on the functional groups of these chiral compounds, S-PEA could interact non-covalently with alanine, phenylalanine, and tyrosine through: (1) ion pair formation (quaternary salt formation) and (2) hydrogen bonding. Aromatic pi system interactions could also occur between S-PEA and tyrosine or phenylalanine [100, 101]. The obvious mode of interaction of arabinose with S-PEA will be hydrogen bond formation. This is because it has hydroxyl groups, which could be used in forming hydrogen bonds with the amine group of S-PEA. Ion pair formation could be possible with arabinose provided its hydroxyl groups are acidic enough. In addition to the above-mentioned modes of interactions, van der Waals and dipole moment interactions are

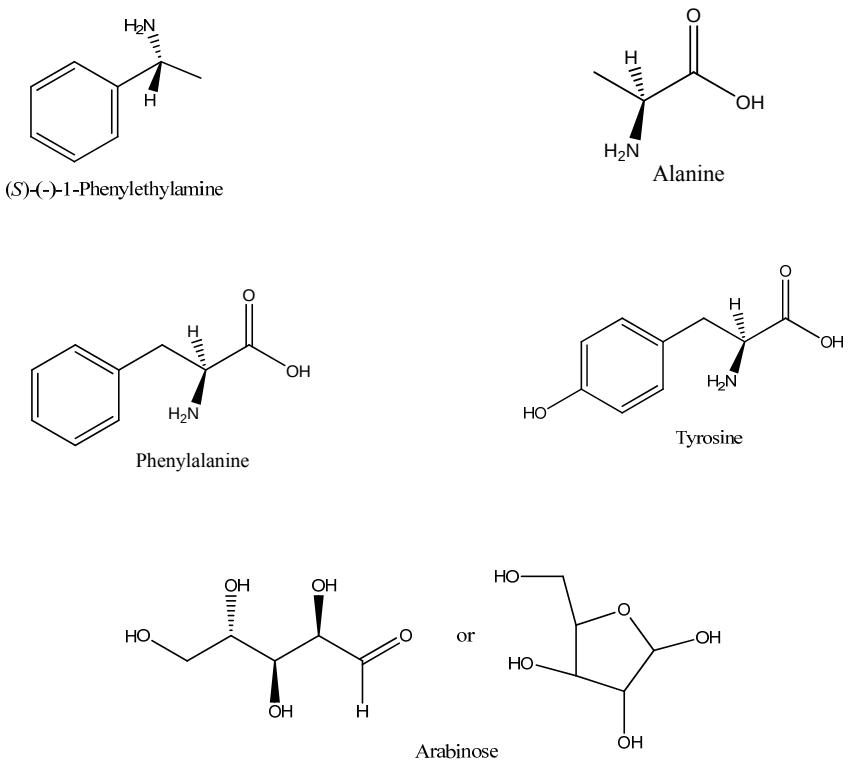

Figure 5.1. Chemical structures of (*S*)-(-)-1-Phenylethylamine (S-PEA), Alanine (Ala), Phenylalanine (Phe), Tyrosine (Tyr), and Arabinose.

also possible. These latter interactions could be useful if they differ for a given pair of enantiomers.

Methodology

Materials

Enantiopure Alanine (D and L, 99 %), Phenylalanine (D and L, ≥ 99 %), Tyrosine (D and L, 99 %), and arabinose (D and L, 99 %) were purchased from Aldrich Chemical Company, Inc. Enantiopure (*S*)-(-)-1-Phenylethylamine (98 %) was purchased from Alfa Aesar. All chemicals were used as received.

Instrumentation, Spectra Collection, and Spectral Data Analysis

The spectra of samples analyzed in this study were collected using the same Agilent 8453, photodiode array, UV-vis spectrophotometer and the black-wall, 10-mm pathlength, quartz sample cell used in the study described in Chapter 2. The original spectral data of samples in this study were subjected to multivariate, PLS-1 regresion analysis as usual using the same Unscrambler statistical package employed in the studies described in the previous chapters.

Analysis of the Amino Acids: Preparation of Stock and Sample Solutions

Tyrosine. Approximately 2.5 mM stock solution of S-1-PEA was prepared by quantitatively transfering 0.0758 g of S-PEA into a 250-mL volumetric flask using deionized water. The solution was then diluted to the 250 mL mark using the same deionized water A 2.5 mM D- or L-tyrosine-S-PEA solution was prepared by dissolving 0.0453 g of D- or L-tyrosine in some amount of the S-PEA stock solution, which was then transferred quantitatively into a 100-mL volumetric flask and diluted to the mark using the same 2.5 mM S-PEA stock solution. Seventeen sample solutions were prepared for analysis by mixing pre-determined volumes of the D- and L-tyrosine-S-PEA stock solutions, using a 1000 μL eppendorf pipet. The mole fractions of D- or L-Tyr were computed using the volume compositions of the samples. The mole fractions of the sample solution were varied at a regular interval of 0.05 mole fraction units.

Phenylalanine. The molar absorption coefficient of phenylalanine is lower than that of tyrosine. As such, 4 mM instead of 2.5 mM solutions of phenylalanine were prepared. To do this, 0.4851 g of S-PEA was quantitatively transferred into a one liter

volumetric flask with deionized water. The solution was then diluted to the 1 L mark using deionized water to prepare approximately a 4mM S-PEA stock solution. A 4 mM stock solution of D- or L-Phenylalanine dissolved in the S-PEA stock solution was prepared by dissolving 0.0661 g of D- or L-Phenylalanine in a minimum amount of the S-PEA stock solution. This was then transferred quantitatively into 100mL volumetric flask and made up to the 100 mL mark using the same S-1-PEA stock solution. Sixteen sample solutions made up of varying enantiomeric compositions of phenylalanine were prepared for analysis by mixing pre-determined amounts of the D- and L-phenylalanine in S-PEA stock solutions.

Alanine. Similar to phenylanine, alanine solutions were prepared at a concentration of 4 mM. Part of the approximately 4 mM stock solution of S-PEA, prepared during the analysis of phenylalanine, was used in this experiment to prepare stock solutions of D- and L-alanine disolved in S-PEA solution according to the procedure described above for phenylalanine. For the 4 mM D or L-alanine-S-PEA stock solution, a mass of 0.0356 g of D- or L-alanine was required. Fourteen sample solutions, made up of varying enantiomeric compositions, were prepared for analysis as usual by mixing pre-determined amounts of the D- and L-alanine-S-PEA stock solutions.

Analysis of Arabinose

Arabinose is an aldopentose monosaccharide that is known to be more abundant in nature in the L than the D form. Arabinose is a significant component in corn and green soybean fiber and can be found in biopolymers like hemicellulose, pectin, and other cellulosic biomass [109-111]. The L-arabinose operon of *Escherichia coli* (*E. coli*),

which has been studied for over forty years, is still an active area of research in recombinant gene studies and ethanol fuel production [112-114]. Generally, carbohydrates serve as energy reservoirs and metabolic intermediates, several of which are linked to proteins and lipids of great biological importance. In addition, the vital biomolecules, DNA and RNA, which are responsible for the storage of genetic information and gene expression, contain the pentose sugars, deoxyribose and ribose, as part of their structural framework. In a recent publication, Augusti et al. noted that studies have revealed that carbohydrate groups on cell surfaces play key roles in cell-cell recognition [115]. Similar to other biological molecules, the biological functions of carbohydrates or sugars are closely related to their chiral stereochemistry. As such, carbohydrates or sugars constitute an important class of molecules studied in the field of chiral analysis. Usually, chiral analysis of carbohydrate or sugars involves the use of chromatographic techniques [115, 116]. However, the significant progress made in the past few years in mass spectrometric techniques, has made possible the use of mass spectrometry for chiral identification and quantification [115]. Several studies including a recent publication by Augusti et al. in which modified amino acids and divalent cations of transition metals were used as chiral selectors for enantiomeric composition analysis of simple sugars are reported [115-119]. As part of the extension of our research in chiral analysis, our research group recently developed a UV spectrophotometer-based spectropolarimetric technique for the determination of sucrose and other optically active compounds [120]. Unlike the previous spectropolarimetric study, the present study on arabinose, similar to our previous chiral analysis studies, used a chiral selector, (S)-(-)-1-phenylethylamine, instead of a polarized light source in combination with an ordinary

UV spectrophotometer for the analysis. Compared to the traditional chromatographic and recent mass spectrometric techniques, our present technique involving S-PEA as a chiral selector is simpler, faster, less expensive, and can be used for routine and high throughput analysis. In addition, the present S-PEA approach will afford determination of enantiomeric excess/composition of carbohydrates or sugars at lower concentration levels than some of the currently used methods [121-122].

The analysis of arabinose in this study was performed at two concentration levels. The first analysis was performed at a concentration of 3 mM and the second at 12 mM. The second analysis at a higher concentration was necessitated by the unsatisfactory results of the analysis at the 3 mM concentration level. This was suspected to be due to ineffective chiral discrimination, which in turn was suspected to be due to weak intermolecular interactions at the 3 mM concentration level; the possibility of this was explained in Chapter 2.

Preparation of Stock and Sample Solutions of Arabinose. The stock and sample solutions for arabinose were prepared following the procedure used in preparing the stock and sample solutions for tyrosine, phenylalanine and alanine. For the a 3 mM analysis, 0.0450 g of D- or L-arabinose was dissolved in an appropriate volume of 3 mM S-PEA solution. Twelve arabinose-S-PEA sample solutions were prepared using the 3 mM D- and L-arabinose-S-PEA stock solution for spectral analysis. In case of the 12 mM analysis, a mass of 0.1802 g of D- or L-arabinose was dissolved in 6 mM S-1-PEA solution giving arabinose/S-PEA ratio of 2:1. This ratio of arabinose to S-PEA was used to create competition for the purpose of enhancing discrimination of the enantiomers.

Thirteen sample solutions made up of varying enantiomeric compositions of the 12 mM D- and L-arabinose-S-1-PEA stock solutions were prepared for spectral analysis similar to the other analytes.

Results and Discussion

Analysis of Tyrosine

Figure 5.2A shows the UV absorption spectra from 205 to 356 nm for 2.5 mM aqueous solutions of enantiopure L-tyrosine and S-PEA. The tyrosine spectrum reveals the usual absorption peak of tyrosine in water with an absorption maximum at 274 nm. The spectrum for the S-PEA reveals the usual absorption peak of the phenyl group, which has an absorption maximum at 257 nm. The absorption peaks recorded for tyrosine and S-PEA are due to the $^1A_{g1} \leftarrow {}^1B_{2u}$ forbidden л*←л transitions of the phenolic group in tyrosine and the phenyl group in S-PEA respectively. Figure 5.2B shows the spectra from 250 to 340 nm for the eighteen tyrosine-S-PEA sample solutions prepared for analysis. The solutions are made up of different enantiomeric compositions but identical total amount of tyrosine and S-PEA. Similar to the pure tyrosine solution, the tyrosine-S-PEA samples solutions reveal the usual absorption maximum of tyrosine at 274 nm. In addition, the spectra of the tyrosine-S-PEA sample solutions, compared to the spectrum for the enantiopure L-tyrosine or S-PEA, show dramatic hyperchromic and bathochromic effects in the spectral regions from 250 to 260 nm and about 290 to 313 nm. These changes in spectral signature, undoubtedly, should be due to the interaction of S-PEA with tyrosine. This is because such features are not revealed by the spectrum of pure tyrosine (see Figure 5.2A) in those spectral band regions.

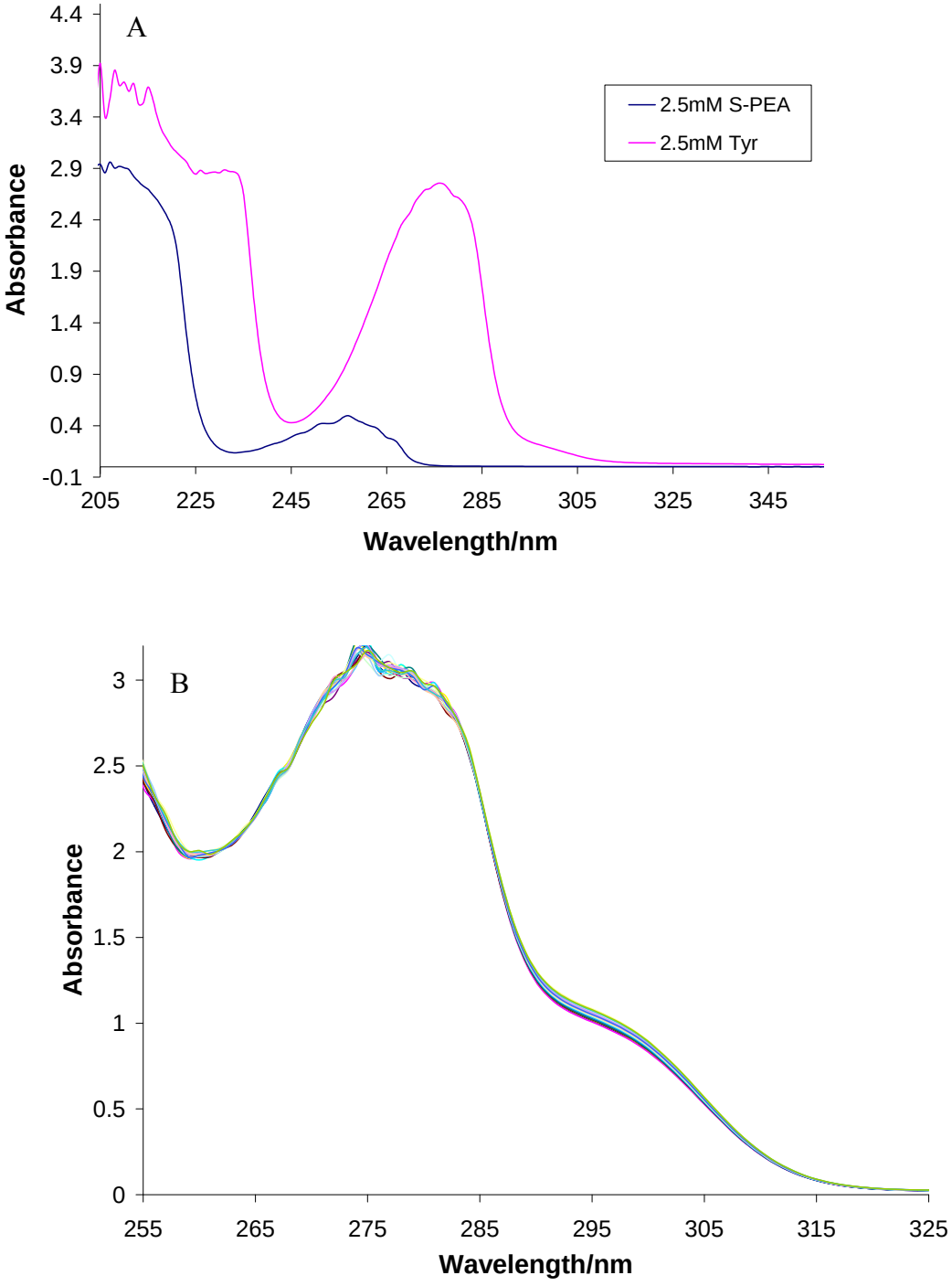

Figure 5.2. A: UV absorption spectra of 2.5 mM aqueous solutions of tyrosine (pink spectrum) and (S)-(-)-1-phenylethylamine (blue spectrum). B: UV absorption spectra of eighteen tyrosine-S-PEA sample solutions made up of varying enantiomeric compositions of tyrosine but identical total amounts of tyrosine and S-PEA

Figure 5.3 shows from 285 to 405 nm the mean-centered spectra of the original UV absorption spectra shown in Figure 5.2B for the eighteen tyrosine-S-PEA sample solutions. Like all other spectra labeled in this chapter using mole fractions, the mole fractions shown in Figure 5.2B are corrected to two decimal places (2 dp). The figure clearly shows differences in absorption of the sample solutions and an isosbestic point at 340 nm. These features indicate that two different UV absorbing species were formed by the interaction of tyrosine with S-PEA in solution. Thus, tyrosine-S-PEA diastereomeric pair complexes were formed in solution.

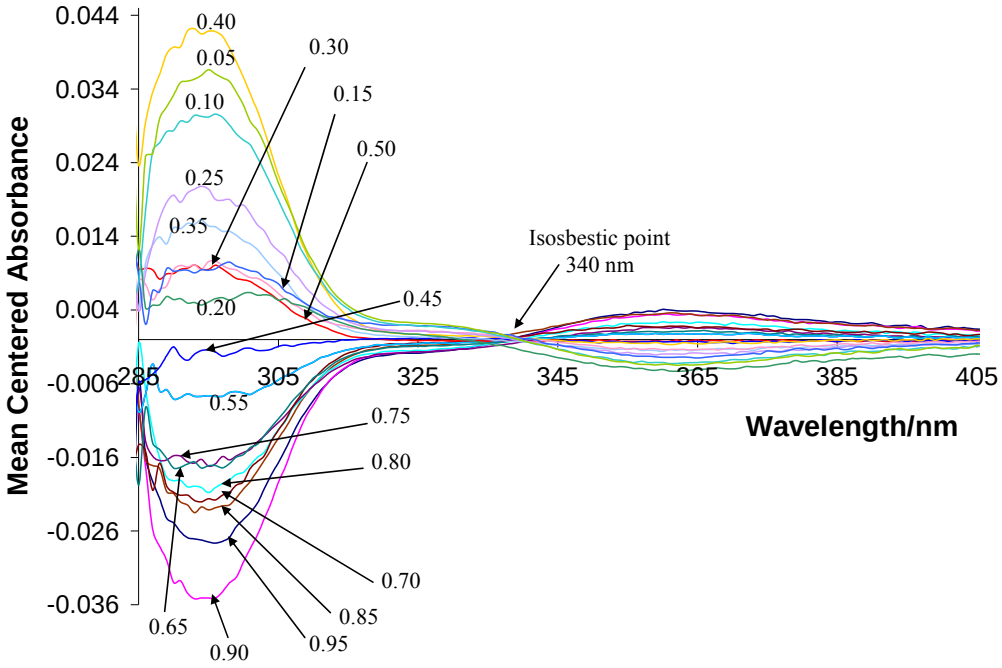

Figure 5.3. Mean-centered UV absorption spectra of eighteen tyrosine-S-PEA sample solutions made up of varying compositions of D- and L-tyrosine but identical total amounts of tyrosine and S-PEA. The spectra are labeled in terms of the mole fractions (to two decimal places) of the D-tyrosine enantiomer.

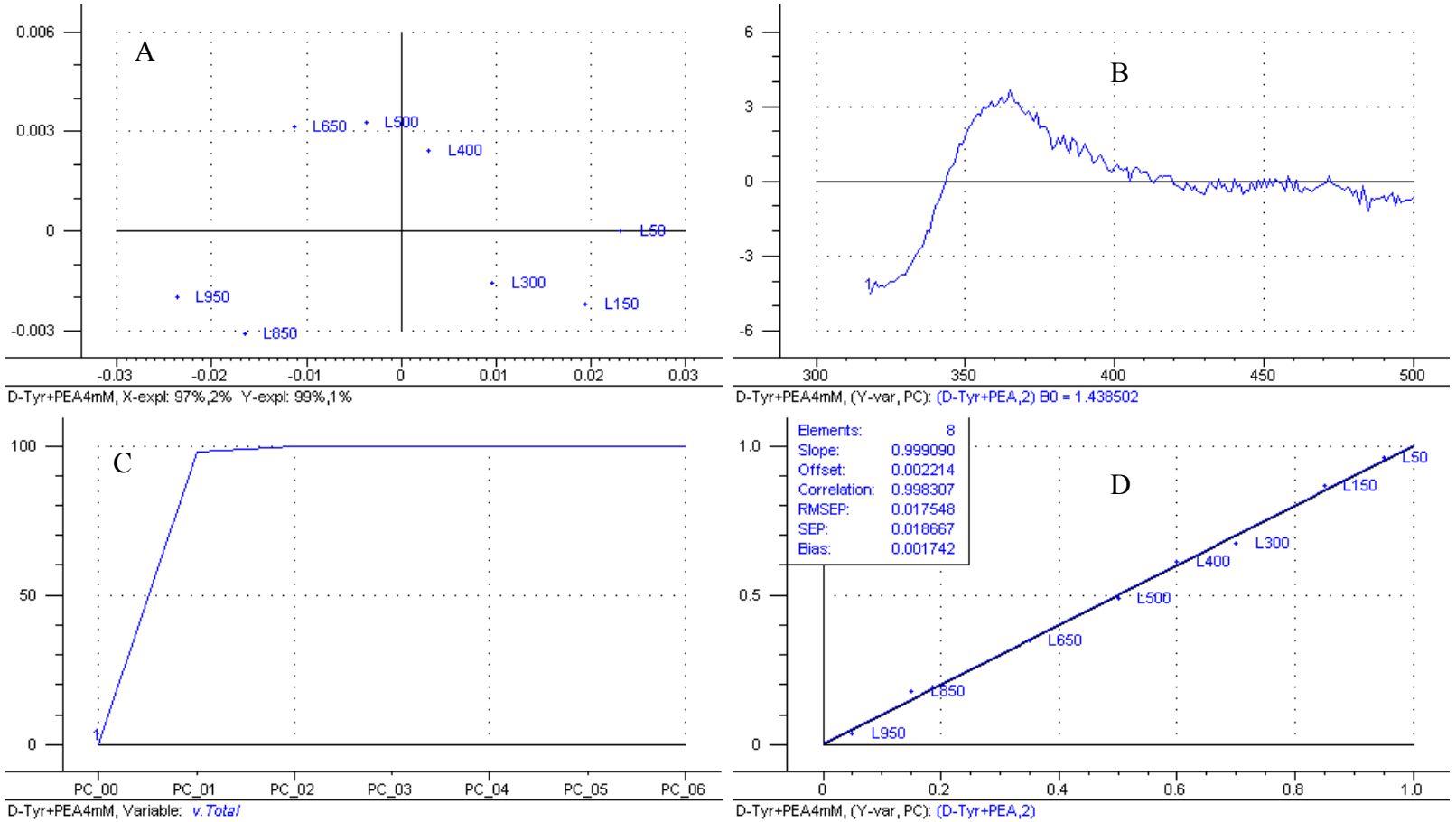

Figure 5.4. Plots of PLS-1 regression calibration model developed using the UV absorption spectral data and known enantiomeric compositions of tyrosine-S-PEA calibration samples. A: scores plot, B: regression coefficient as a function of wavelength plot, C: percent explained variance as a function of principal component plot, and D: calibration and cross-validation regression lines for the fitted (black) and predicted (blue) mole fractions, respectively, versus the known mole fractions of calibration samples. The model required two PCs (see below plot B or D).

Figure 5.4A, B, C, and D show the multivariate, PLS-1 plots of the tyrosine-S-PEA calibration model. Figure 5.4A is the scores plot, which reveals the pattern of variation in sample composition of the calibration samples. Figure 5.4B represents the regression coefficient plot. The regression coefficient curve has both positive (above zero) and negative (below zero) parts. The negative part shows that enantiomeric composition changes in an opposite direction with spectra in that wavelength region while the positive part indicates enantiomeric composition changes in the same direction with spectra in that wavelength region. The regression coefficient with the highest positive value is associated with the 365 nm wavelength and the regression coefficient with the highest negative value is recorded at 319 nm. Figure 5.4C shows that six PCswere computed. However, only the first two PCs were needed for the model. The first PC explained 97 and 99 % of the variation in the spectral data and enantiomeric composition. The second PC explained 2 and 1 % of the variation in the spectral data and enantiomeric composition. Though the variations explained by the second PC were small they were found to be useful. Figure 5.4D, shows the regression line for the predicted (by cross-validation) versus known enantiomeric compositions of the calibration samples plot. The plot statistics computed for the regression line are: 0.999 for the slope, 0.00221 for the offset, 0.998 for the correlation coefficient, 0.018 for the root-mean-square error of prediction and 0.019 for the standard error. These values indicate a strong correlation between the predicted and known sample compositions of the calibration samples as shown by the plot in Figure 5.4D. This in turn signifies that the spectral data of the calibration samples are well correlated with the corresponding enantiomeric compositions.

Table 5.1 shows the mole fractions predicted for eight tyrosine-S-PEA validation samples using the tyrosine-S-PEA calibration model whose plots are shown in Figure 5.4A, B, C, and D. The actual mole fractions of the tyrosine-S-PEA validation samples are also reported in the table. In addition, the mole fractions predicted in Chapter 2 for the analysis of tyrosine, using (*S*)-(+)-1,2-propanediol both as a covalent and non-covalent chiral selector, are reported in the same table together with the corresponding

Table 5.1. Comparison of the actual and predicted D-tyrosine mole fractions of 2.5 mM tyrosine validation samples containing varying compositions of D- and L-Tyr. All samples contain identical amounts of total tyrosine and a fixed concentration of S-PEA.

Actual D ø[a] for S-PEA NCA[b]	Predicted D ø for S-PEA NCA	Actual D ø for PD[c] NCA	Predicted D ø for PD NCA	Actual D ø for PD CA[d]	Predicted D ø for PD CA
0.250	0.250	0.100	0.109	0.800	0.794
0.300	0.303	0.150	0.153	0.750	0.737
0.400	0.401	0.344	0.357	0.550	0.581
0.450	0.462	0.400	0.427	0.300	0.248
0.650	0.659	0.599	0.568	0.200	0.166
0.750	0.758	0.898	0.884	0.100	0.0766
0.800	0.802				
0.900	0.901				
RMSEP[e]	0.006		0.019		0.03

[a] Mole fraction, [b] Non-covalent analysis, [c] (*S*)-(+)-1,2-propanediol [d] Covalent analysis, [e] Root-mean-squares error of prediction

actual mole fractions for comparison. The predicted mole fractions (second column) for the tyrosine-S-PEA analysis, compared with the actual mole fractions (first column), clearly reveal a high level of accuracy of the analysis. The root-mean-square error of

prediction (RMSEP) computed for the analysis is 0.006. This low magnitude of the RMSEP is an indication of the effective chiral discriminatory effect of (*S*)-(-)-1-phenylethylamine. The 0.006 RMSEP computed for the tyrosine-S-PEA analysis, compared to the prediction errors computed for the (*S*)-(+)-1,2-propanediol analyses, indicates that the non-covalent S-PEA discrimination is the most effective strategy for the analysis of tyrosine. In addition, the prediction errors appear to suggest that generally, the non-covalent discrimination analyses are more effective for the analysis of tyrosine. This is because the results for the non-covalent (*S*)-(+)-1,2-propanediol discrimination analysis are also better than the results for the covalent analysis. This reinforces the point made earlier for the need for alternative strategies in these analyses. The effectiveness of the non-covalent discrimination by S-PEA might be related to the extent to which the effect of discrimination is reflected in the spectral property of the analyte. This is because unlike (*S*)-(+)-1,2-propanediol, S-PEA significantly changed in the spectral signature of tyrosine (compare Figure 5.2A to 5.2B).

Analysis of Phenylalanine

Figure 5.5 shows the UV absorption spectrum (pink) for a 4 mM solution made up of 1:9 mole fraction ratio of D- and L-phenylalanine dissolved in S-PEA solution (~ 4mM) and the spectrum (blue) of a 4 mM solution of enantiopure D-phenylalanine. It is clear from Figure 5.5 that the absorbance of the phenylalanine-S-PEA solution at the wavelength of maximum absorption, 257 nm, for the phenyl group present in both molecules, is about twice the absorbance recorded for the enantiopure D-phenylalanine solution. This is expected because the phenylalanine-S-PEA solution contains twice as much phenyl groups as the enantiopure D-phenylalanine solution. In addition, the

spectrum for the phenylalanine-S-PEA solution reveals a bathochromic shift in the spectral region between224 and 244 nm. Furthermore, the vibrational structures revealed by the spectrum for the enantiopure D-phenylalanine solution, in the spectral region 249-264 nm, are partially smoothed out in the spectrum recorded for the phenylalanine-S-PEA solution. The above-noted changes in spectral signature for the phenylalanine-S-PEA solution (see Figure 5.5) are significantly different from those revealed in Figure5.2B by the tyrosine-S-PEA sample solutions. This could possibly mean that the modes of interaction of S-PEA with tyrosine and phenylalanine are different.

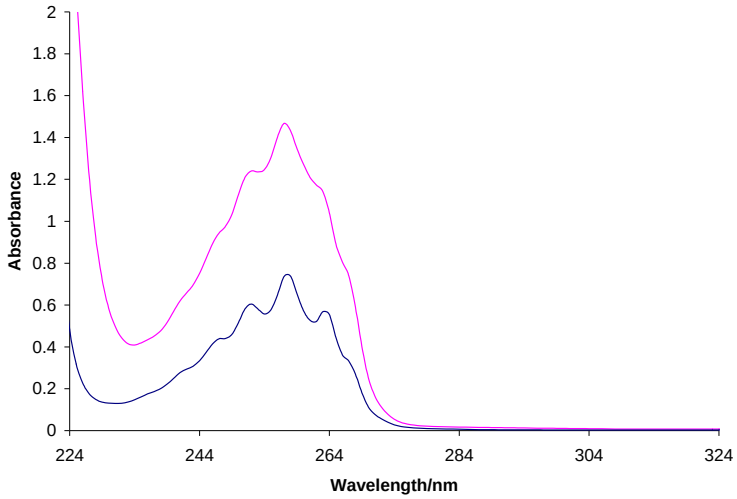

Figure 5.5. UV absorption spectrum (pink) of a 4 mM solution made up of 1:9 mole fraction ratio of D- and L- phenylalanine dissolved in ~ 4 mM S-PEA solution and the UV absorption spectrum (pink) of the ~ 4 mM S-PEA solution.

Figure 5.6A and B, respectively, show the original and mean-centered UV absorption spectra (227-272 and 232-253 nm respectively) for the seventeen phenylalanine-S-PEA sample solutions prepared for analysis. The sample solutions are made up of different enantiomeric compositions of D- and L- phenylalanine but identical

total concentrations of phenylalanine and S-PEA. Similar to the tyrosine samples, the mean centered spectra in Figure 5.6, which are labeled in terms of the mole fractions (to 2 dp) of the D-phenylalanine enantiomer, clearly show that the phenylalanine-S-PEA sample solutions differ in their absorbances. This is an indication that diastereomers of phenylalanine were formed by the interaction of the S-PEA chiral selector with the enantiomers of phenylalanine in solution. The phenyalalnine-S-PEA samples, as shown by their mean-centered spectra in Figure 5.6, reveal no spectra-crossing unlike the tyrosine samples. Consequently, the interaction of the S-PEA chiral selector with phenylalanine did not lead to the formation diastereomers that absorb UV identically at any wavelength recorded as observed for tyrosine.

As usual, a multivariate, PLS-1 regression calibration model was developed using the original spectral data of eight randomly selected phenylalanine-S-PEA calibration samples made up of D-phenylalanine mole fractions of 0.0500, 0.100, 0.200, 0.392, 0.500, 0.527, 0.700, and 0.950. The cross-validated regression plot statistics of the phenylalanine-S-PEA calibration samples (second column) are compared with the cross-validated regression plot statistics reported in Chapter 2 for the analyses of phenylalanine using (*S*)-(+)-1,2-propanediol both as a covalent and a non-covalent chiral selector (column 2 and 3). Table 5.2 also shows the regression plot statistics computed for the S-PEA-tyrosine calibration samples (fifth column) for comparison. Table 5.2 shows that the values of the cross-validated PLS-1 regression plot statistics for the phenylalanine-S-PEA calibration samples differ from those computed for the phenylalanine calibration samples discriminated using (*S*)-(+)-1,2-propanediol as a non-covalent chiral selector (Table 5.2, column 2). On the other hand, they compare favorably with the plot statistics

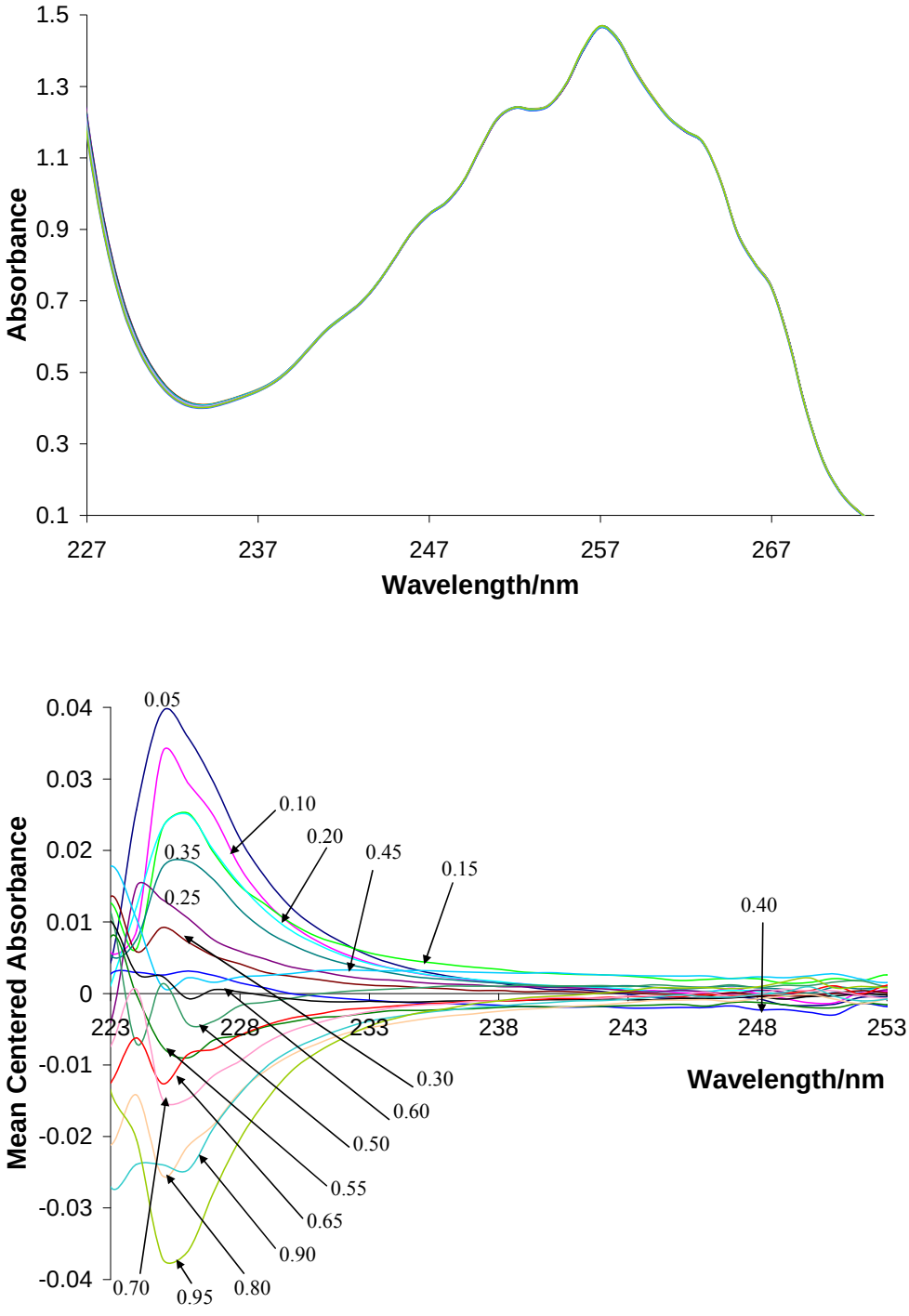

Figure 5.6. Mean-centered UV absorption spectra of seventeen phenylalanine-S-PEA sample solutions (4 mM) made up of varying compositions of D- and L-phenylalanine but identical total amount phenylalanine and S-PEA. The mean centered spectra are labeled in terms of the mole fractions (to two decimal places) of the D-phenylalanine enantiomer.

Table 5.2. Comparison of the cross-validated PLS-1 regression plot statistics computed for the calibration samples of phenylalanine and tyrosine analyzed using (S)-(-)-1-phenylethylamine (S-PEA) or (S)-(+)-1,2-propanediol (PD) used for covalent or a non-covalent chiral discrimination of phenylalanine.

PLS-1 Regression Plot Statistic	Cross-Validated PLS-1 Regression Plot Statistic Value			
	S-PEA NCA[a] of Phenylalanine	PD[b] NCA of Phenylalanine	PD CA[c] of Phenylalanine	S-PEA NCA of Tyrosine
Slope	0.988	0.881	0.967	0.999
Offset	0.00643	0.0908	0.00828	0.00221
Correlation coefficient	0.996	0.992	0.998	0.998
RMSEP[d]	0.025	0.0500	0.023	0.018
SEP[e]	0.027	0.0501	0.024	0.019
Modeled wavelength range	223-360 nm	225-450 nm	235-567 nm	318-500 nm

[a] Non-covalent analysis, [b] (*S*)-(+)-1,2-propanediol, [c] Covalent analysis, [d] Root-mean-squares error of prediction, [e] Standard error

computed for the phenylalanine calibration sample discriminated using (*S*)-(+)-1,2-propanediol as a covalent chiral selector (Table 5.2, column 4). Compared to the plot statistic values for tyrosine discriminated using S-PEA as a non-covalent chiral selector, the plot statistics values computed for tyrosine are of slightly higher merit than those for the phenylalanine-S-PEA calibration samples.

The PLS-1 regression calibration model of the phenylalanine-S-PEA calibration sample, whose cross-validated regression plot statistics are shown in Table 5.2, was used in predicting eight of the phenylalanine-S-PEA samples. The results of the prediction are reported in Table 5.3. Also included in Table 5.3 are the prediction results reported in Chapter 2 for the analysis of phenylalanine using (*S*)-(+)-1,2-propanediol. It is clear from the table that the mole fractions of the phenylalanine-S-PEA samples are predicted quite accurately. The root-mean square errors of prediction (RMSEP) computed for the analysis is 0.013. This is comparable to the RMSEP of 0.014 computed for the

Table 5.3. Comparison of the actual and predicted D-Phe mole fractions of 4 mM phenylalanine validation samples containing varying compositions of D- and L-Phe. All samples contain identical amounts of total phenylalanine.

Actual D ø[a] for S-PEA NCA[b]	Predicted D ø for S-PEA NCA	Actual D ø for PD[c] CA[d]	Predicted D ø for PD CA	Actual D ø for PD NCA	Predicted D ø for PD NCA
0.150	0.185	0.103	0.0848	0.0499	0.0160
0.267	0.264	0.400	0.407	0.102	0.124
0.352	0.348	0.451	0.425	0.200	0.227
0.468	0.464	0.597	0.596	0.299	0.259
0.486	0.483	0.801	0.801	0.601	0.576
0.527	0.524	0.851	0.859	0.700	0.701
0.600	0.597			0.855	0.846
0.650	0.640				
RMSEP[e]	0.013		0.014		0.026

[a] Mole fraction, [b] Non-covalent analysis, [c] (S)-(+)-1,2-propanediol, [d] Covalent analysis

(*S*)-(+)-1,2-propanediol covalent discrimination analysis of phenylalanine reported in Chapter 2. The prediction error, 0.026, computed for the non-covalent discrimination analysis of phenylalanine using (*S*)-(+)-1,2-propanediol for non-covalent chiral discrimination of phenylalanine is quite good. The differences between these errors, most probably, could be due to random errors; not necessarily one strategy being better than the other. Compared to tyrosine, the RMSEP values reported in Table 5.3 for the three approaches used in analyzing phenylalanine suggest that unlike tyrosine, both the S-PEA non-covalent and (*S*)-(+)-1,2-propanediol covalent discrimination strategies are effective for the analysis of phenylalanine.

Analysis of Alanine

Figure 5.7 shows four UV absorption spectra from 190 to 310 nm recorded for four different solutions: the ~ 4 mM S-PEA stock solution, (blue spectrum), a 4 mM solution of enantiopure D-alanine (pink spectrum), the 4 mM D-alanine dissolved in ~4 mM S-PEA solution (green spectrum), and the 4 mM L-alanine dissolved in ~4 mM S-PEA solution (brown spectrum). Alanine (Ala) has a weak chromophore and shows an end-absorption. However, the spectral effect of the interaction of Ala with S-PEA is reflected in the spectrum for the D- or L-alanine-S-PEA solution as a shift to lower

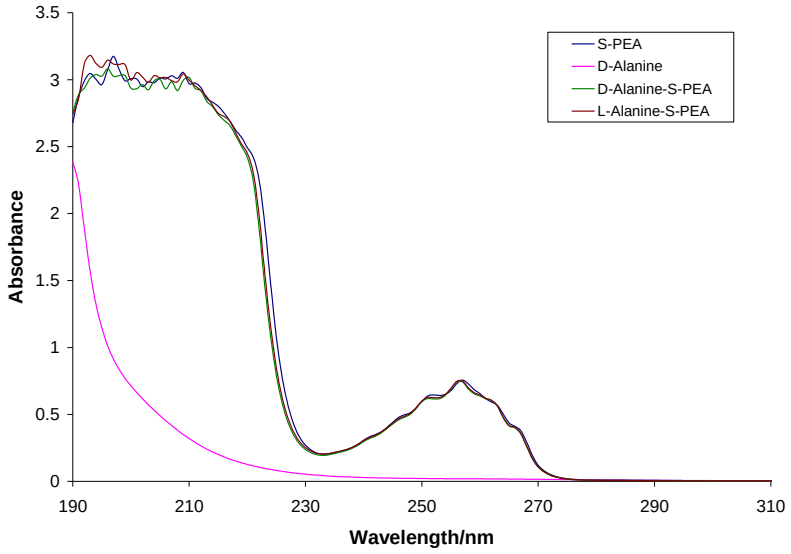

Figure 5.7. UV absorption spectra for four different solutions: S-PEA (blue spectrum), enantiopure D-almandine (pink spectrum), D-phenylalanine dissolved in S-PEA solution (green spectrum), and L-phenylalanine dissolved in S-PEA solution (brown spectrum).

wavelength relative to the spectrum recorded for the S-PEA solution. This hypsochromic shift is recorded in the spectral region from 210 to 230 nm. Though this change is small in magnitude, it has been consistently observed. The change in spectral signature of the

Ala-S-PEA solution relative to spectral signature of the S-PEA solution indicates a non-passive intermolecular interaction between Ala and S-PEA in solution.

Figure 5.8A and B, respectively, show the original and mean-centered UV absorption spectra (227-297 and 220-250 nm respectively) for the seventeen Ala-SPEA sample solutions prepared for analysis. Similar to the tyrosine- and phenylalanine-S-PEA samples, the mean-centered UV absorption spectra of the Ala-S-PEA sample, which are labeled in terms of the mole fractions (to 2 dp) of D-Ala, reveal quite clear differences in absorbance. This indicates that diastereomeric pairs of Ala (D-alanine-S-PEA and L-alanine-S-PEA) were formed in solution by the interaction of the S-PEA chiral selector with Ala. Unlike tyrosine but similar to phenylalanine, no spectral crossing is revealed by the mean-centered spectra shown in Figure 5.8B for the Ala-S-PEA samples. This indicates that the non-covalent S-PEA diastereomers of Ala do not have the same molar absorptivity coefficient at any of the wavelengths recorded.

For the PLS-1 regression analysis, eight randomly selected samples (0.0500, 0.150, 0.250, 0.350, 0.500, 0.650, 0.750, 0.900, and 0.950) were used to develop a PLS-1 calibration model. The calibration model, as usual, was employed in predicting the rest of the seventeen Ala-S-PEA samples, which were used as validation samples. Contained in Table 5.4 are the plot statistic values computed for the regression of the predicted (by cross-validation) mole fraction on the actual mole fractions of the calibration samples. The regression plot statistic values shown in Table 5.2 for tyrosine and phenylalanine are lso reported in Table 5.4 for comparison. It is obvious from Table 5.4 that except for the slope and offset, the regression plot statistics for the Ala-S-PEA calibration samples are significantly identical to those for the phenylalanine-S-PEA calibration samples. Though

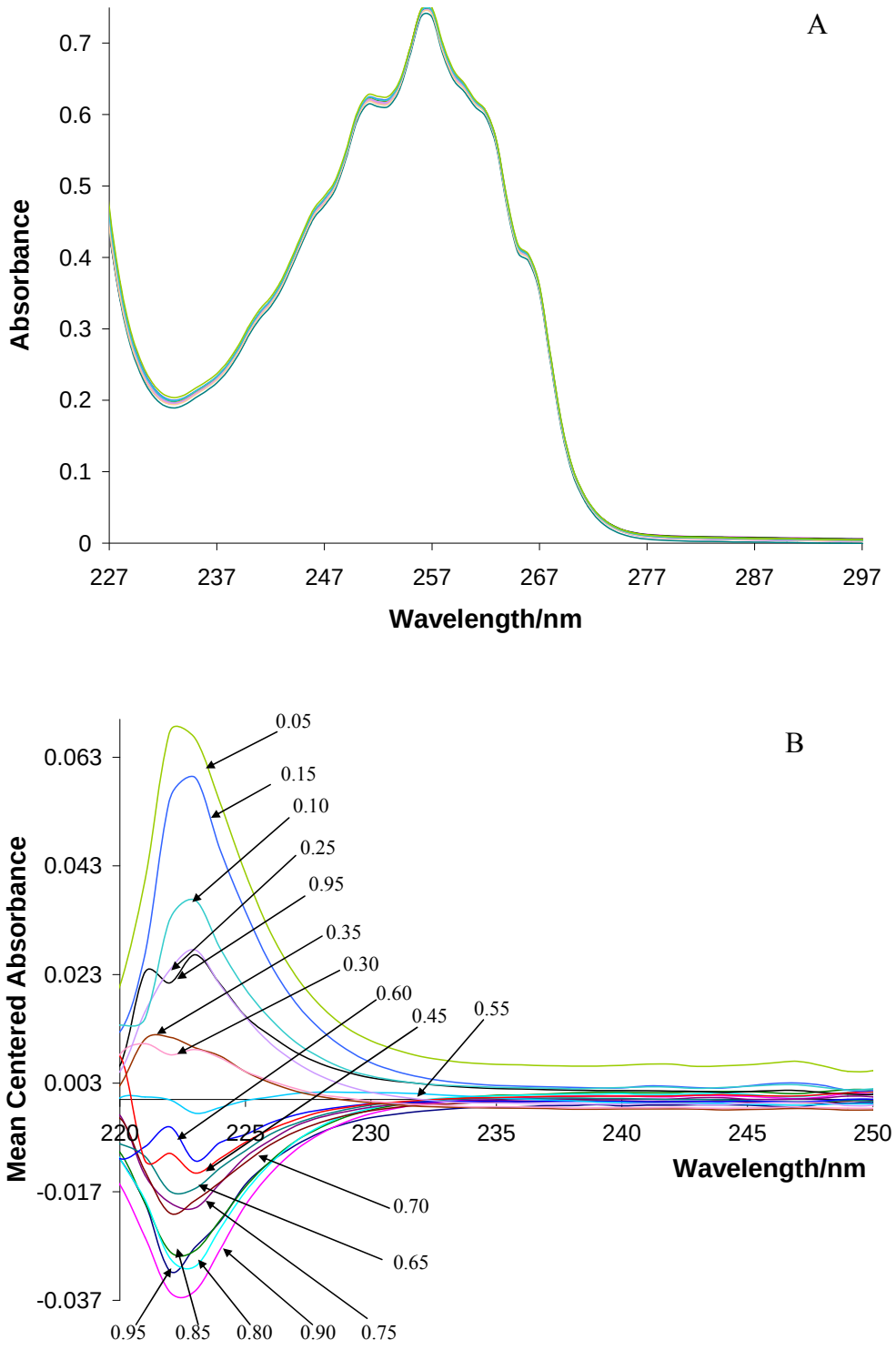

Figure 5.8. A: UV absorption spectra of seventeen 4 mM alanie-S-PEA sample solutions made up of varying enantiomeric compositions of alanine but identical total amounts of alanine and S-PEA. B: Mean-centered form of the UV absorption spectra shown in A for the seventeen 4 mM alanie-S-PEA samples. The mean centered spectra are labeled in terms of the mole fractions (to 2 dp) of the D-Ala enantiomer.

a most of the regression plot statistics values computed for the Ala-S-PEA calibration samples are of lower merit compared to the values computed for the tyrosine calibration samples, the correlation coefficient for both samples are the same. It is possible that the difference in the values of the other statistics might be due to random errors. It is clear in Table 5.4 that the modeled wavelength ranges reported for the three sets of calibration samples differ significantly from one set of calibration samples to the other. This is a reflection of the different effects of the S-PEA chiral selector on the spectral properties of the three amino acids. The PLS-1 regression model for the Ala-S-PEA calibration samples, whose regression plot statistics are reported in Table 5.4, were used in predicting the rest of the seventeen Ala-S-PEA samples used as validation samples

Table 5.4 Comparison of the cross-validated PLS-1 regression plot statistics computed for the calibration samples of alanine, phenylalanine, and tyrosine analyzed using (S)-(-)-1-phenylethylamine (S-PEA) as a non-covalent chiral selector

PLS-1 Regression Plot Statistic	Cross-Validated PLS-1 Regression Plot Statistic Value		
	S-PEA NCA[a] of Alanine	S-PEA NCA of Phenylalanine	S-PEA NCA of Tyrosine
Slope	0.940	0.988	0.999
Offset	0.0398	0.00643	0.00221
Correlation coefficient	0.998	0.996	0.998
RMSEP[d]	0.029	0.025	0.018
SEP[e]	0.029	0.027	0.019
Modeled wavelength range	229-989 nm	223-360 nm	318-500 nm

[a]. Non-covalent analysis

Out of the remaining eight Ala-S-PEA samples used as validation samples, three were identified as outliers and were excluded from the analysis.

Table 5.5 compares the predicted mole fractions of the Ala-S-PEA validation samples with the actual mole fractions. Similar to the tyrosine and phenylalanine samples, the Ala-S-PEA validation samples are predicted with quite a high level of accuracy. The highest absolute error computed is only 0.031 and the root-mean-square error of prediction computed for the entire analysis is 0.016. These error values clearly indicate the chiral discriminatory efficiency of S-PEA as a non-covalent chiral selector.

Table 5.5. Comparison of the actual and predicted D-alanine mole fractions of alanine-S-PEA validation samples containing varying compositions of D- and L-Ala but identical total concentrations of Ala and S-PEA

Actual mole fraction of D-Ala	Predicted mole fraction of D-Ala	Absolute Error for D-Ala Prediction
0.800	0.789	-0.011
0.700	0.721	0.021
0.600	0.596	-0.004
0.400	0.369	-0.031
0.300	0.308	0.008
Root-Mean-Squares Error of Prediction		0.016

Analysis of Arabinose

As note earlier, arabinose was initially analyzed at a concentration of 3 mM and later repeated at 12 mM as a result of unsatisfactory analysis results obtained at the 3 mM concentration level. Figure 5.9A shows the UV absorption spectra from 226 to 306 nm for the 3 mM stock solutions of D-and L-arabinose dissolved in 3 mM S-PEA solution, and the spectrum of the 3 mM S-PEA solution. The spectra in pink and blue colors are respectively the spectra for D- and L-arabinose dissolved in S-PEA solution and the spectrum in brown is the spectrum for the S-PEA solution. The UV absorption spectra

for the for the 12 mM stock solutions of D- and L-arabinose dissolved in 6 mM S-PEA solution and the spectrum for the 6 mM S-PEA solution are in Figure 5.9B. Unlike the 3 mM solutions in Figure 5.9A, the spectra for the 12 mM solutions of D- and L-arabinose dissolved in 6 mM S-PEA solution differ significantly both in absorbance and shape (peak region) from the spectrum recorded for the 6 mM S-PEA solution. In addition, a

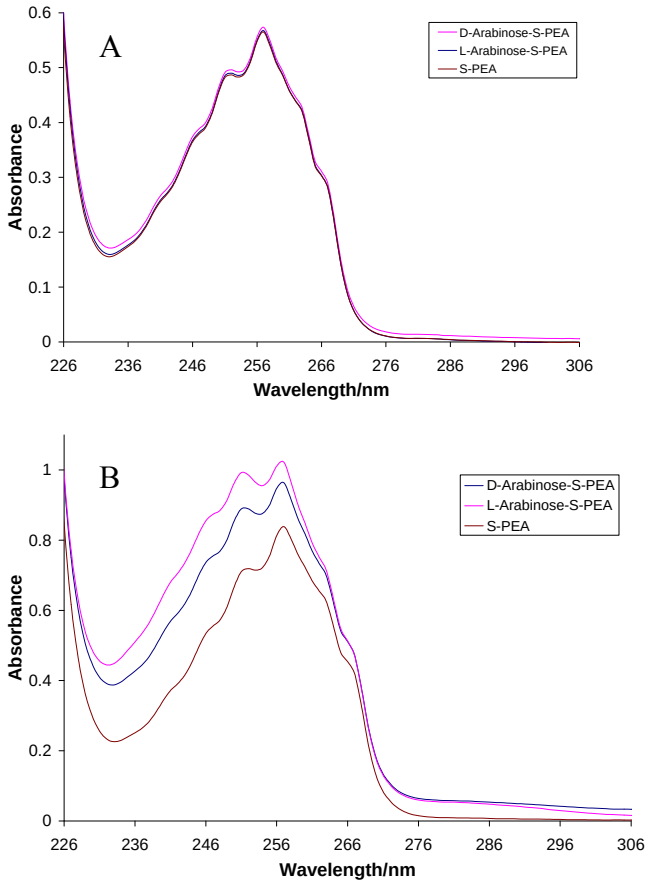

Figure 5.9. UV absorption spectra recorded for solutions of D-and L-arabinose dissolved in S-PEA solution (pink and blue colors respectively), and S-PEA (brown color spectrum). A: spectra for solutions prepared at a 3 mM concentration level. B: spectra for 12 mM solutions of D-and L-arabinose dissolved in 6 mM S-PEA solution and the spectrum for the 6 mM S-PEA solution

significant difference in absorbance is recorded between the 12 mM D- and L-arabinose solutions from 231 to 257 nm. These differences between the 3 and 12 mM arabinose-S-

PEA solutions should be due either to the difference in concentration or the ratio of arabinose to S-PEA of the solutions or a combination of both. As explained in Chapter 2, non-covalent chiral discriminations that may depend on weak intermolecular interactions could be made more effective by increasing the concentrations of both analyte and chiral selector. This is because it will increase the proximity of the molecules in solution. The effect of increasing concentration should be particularly useful in cases where the solvent is capable of interacting with either the analyte or chiral selector in a way similar to the interaction between the analyte and chiral selector. For the effect of using a 2:1 instead of 1:1 arabinose/S-PEA ratio, it is presumed that chiral discrimination could be enhanced through competitive interaction of the enantiomers with the S-PEA chiral selector. In this way the most favorable interaction may predominate leading to better chiral selectivity in the 2:1 arabinose/S-PEA ratio samples than the 1:1 ratio samples.

Figure 5.10A and B, respectively, show the spectra recorded for the twelve 3 mM and thirteen 12 mM arabinose-S-PEA sample solutions prepared by mixing varying compositions of the corresponding D- and L-arabinose-S-PEA stock solutions. These two sets of spectra reveal clearly the effect of differences between the 3 and 12 mM solutions discussed above; the spectra for the 12 mM sample solutions are better separated from each other than the spectra for 3 mM samples. The mean-centered form of the UV absorption spectra for the 3 and 12 mM sets of samples are shown in Figure 5.11A and B respectively. The mean-centered spectra, which are labeled in terms of the mole fractions (to 2 dp) of the D-arabinose enantiomer, reveal in much detail the difference between the two sets of samples. For example unlike the 3 mM samples, the 12 mM samples reveal two distinct wavelength regions (227-260 nm and 282-352 nm) of spectral variation. In

addition, the 12 mM samples reveal clearly a pseudo isosbestic behavior centered on 265 nm. Compared to the mean-centered UV spectra of the amino acids discussed above, the shape or form of the mean-centered UV spectra for the 3 mM arabinose-S-PEA samples is similar to those described by the phenylalanine and alanine (see Figure 5.6 and 5.8B) samples while the mean-centered spectra for the 12 mM arabinose-S-PEA samples describe a shape or form that is similar to that for tyrosine. As explained for the amino

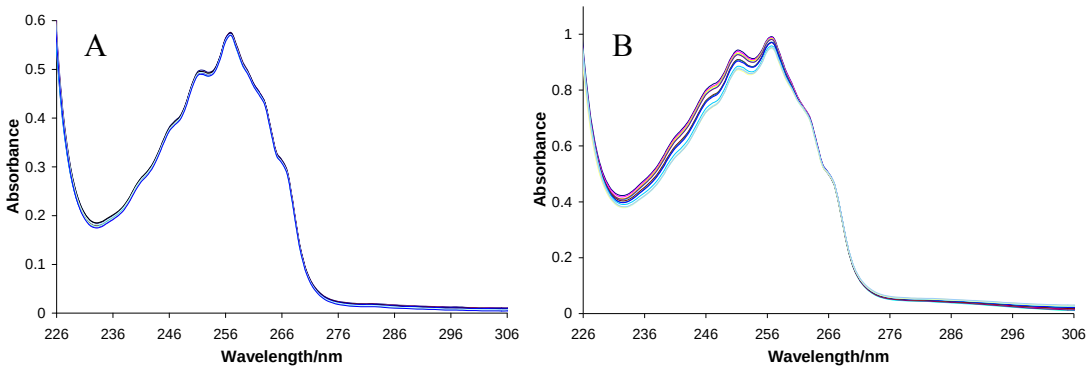

Figure 5.10. UV absorption spectra of sample solutions made up of varying enantiomeric compositions of D- and L-arabinose dissolved in S-PEA solution. A: samples prepared at 3 mM concentration level of arabinose and S-PEA. B: sample solutions prepared at 12 mM concentration level of arabinose and 6 mM of S-PEA.

acids, the difference in shape or form of the mean-centered spectra for the 3 and 12 mM arabinose-S-PEA samples indicate either the presence of two different forms of interaction or the formation of two types of non-covalent diastereomer. While the present study is limited in providing information on the possible interactions, the mean-centered spectra for the 12 mM arabinose samples signify that the non-covalent diastereomers formed absorb UV light nearly equally around 265 nm (pseudo isosbestic behavior) and significantly differently in the regions 227-260 nm and 282-352 nm. This spectral

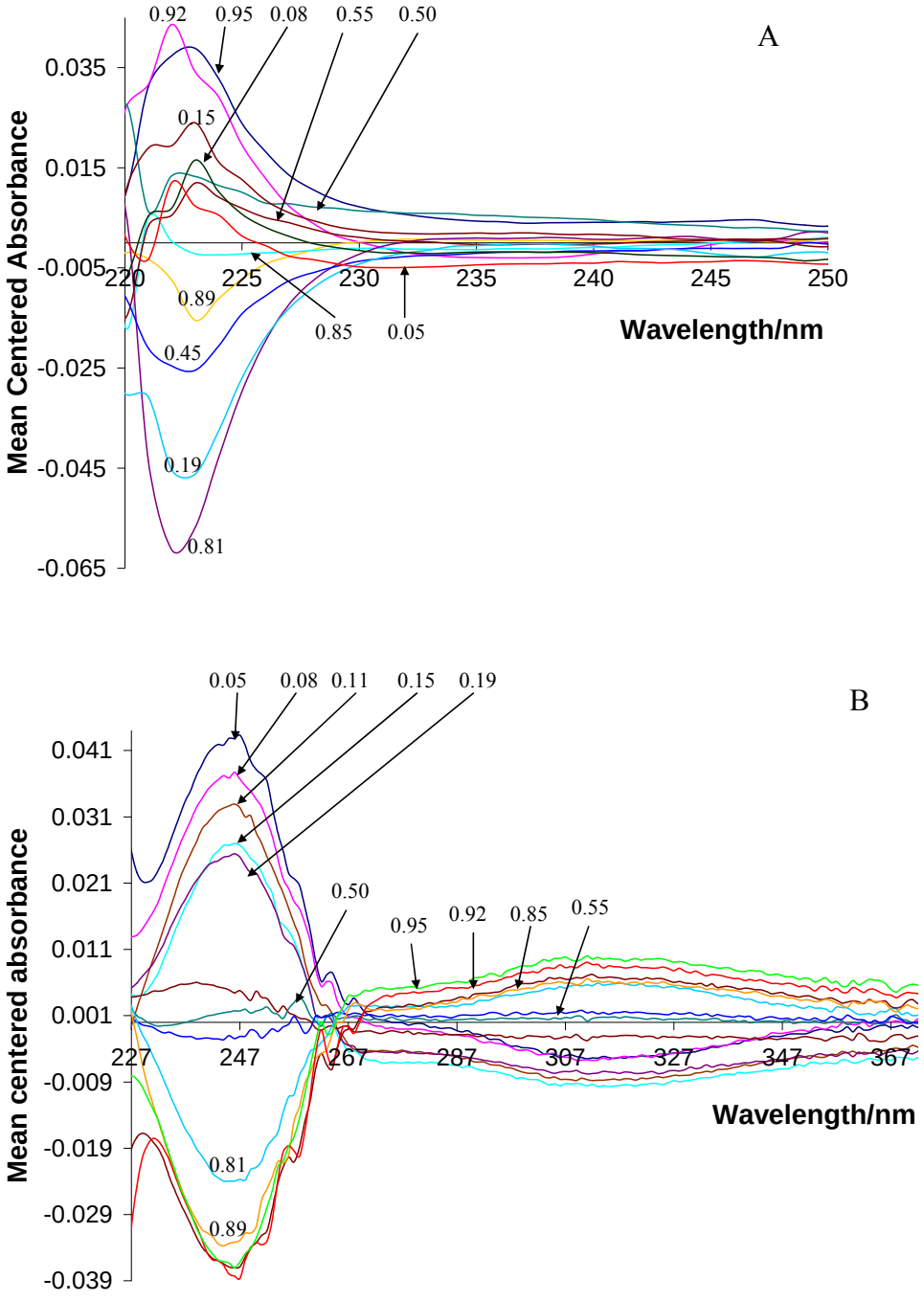

Figure 5.11. Mean-centered UV absorption spectra of sample solutions made up of varying enantiomeric compositions of D- and L-arabinose dissolved in S-PEA solution. A: samples prepared at 3 mM concentration level of arabinose and S-PEA. B: sample solutions prepared at 12 mM concentration level of arabinose and 6 mM of S-PEA. The spectra are labeled in terms of the mole fractions (to 2 dp) of the D-arabinose enantiomer.

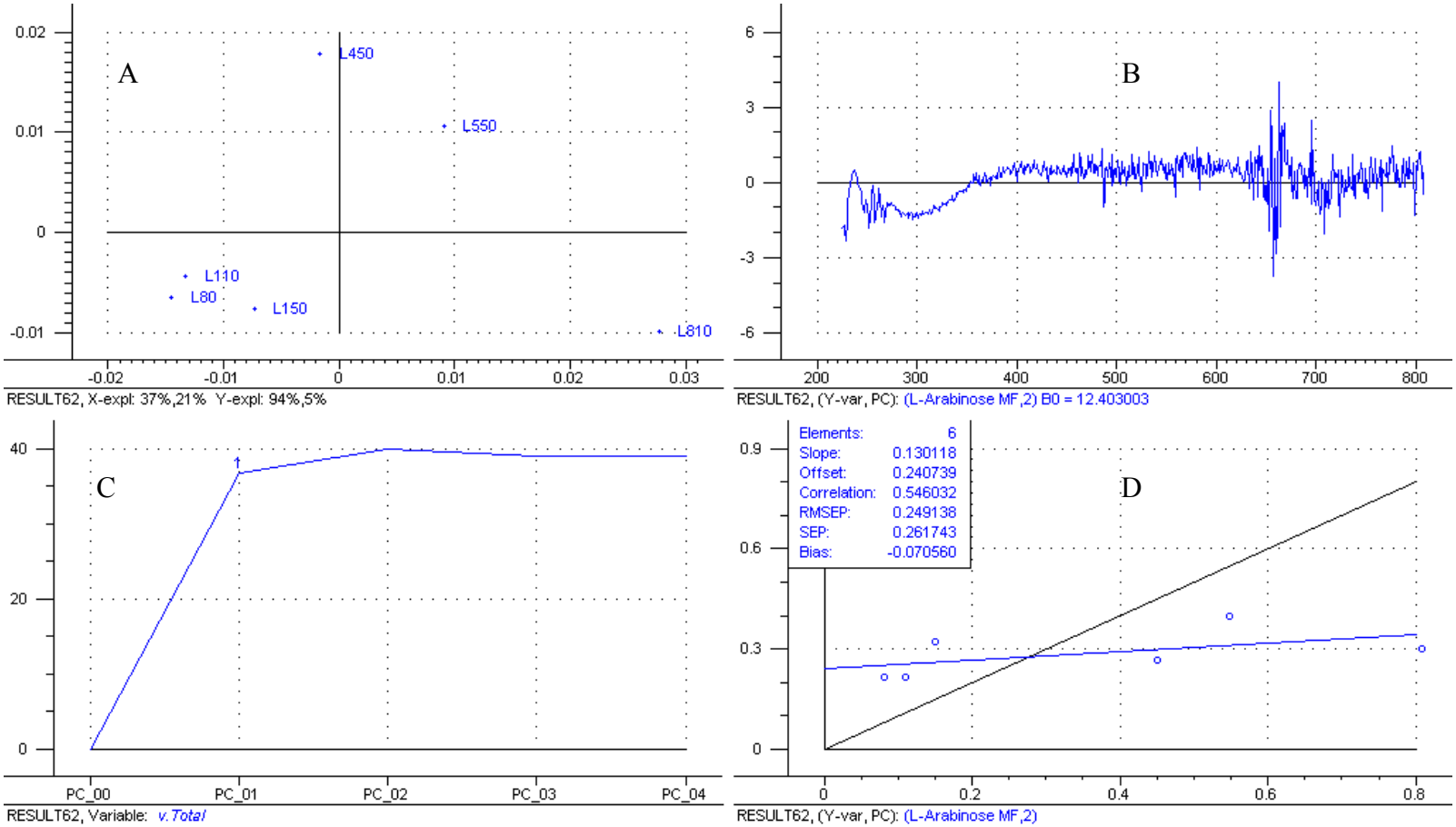

Figure 5.12. Plots of PLS-1 regression calibration model developed using the UV absorption spectral data and known enantiomeric compositions of 3 mM arabinose-S-PEA calibration samples. A: scores plot, B: regression coefficient as a function of wavelength plot, C: percent explained variance as a function of principal component plot, and D: calibration and cross-validation regression lines for the fitted (black) and predicted (blue) mole fractions, respectively, versus the known mole fractions of calibration samples. The model required two PCs (see below plot B or D).

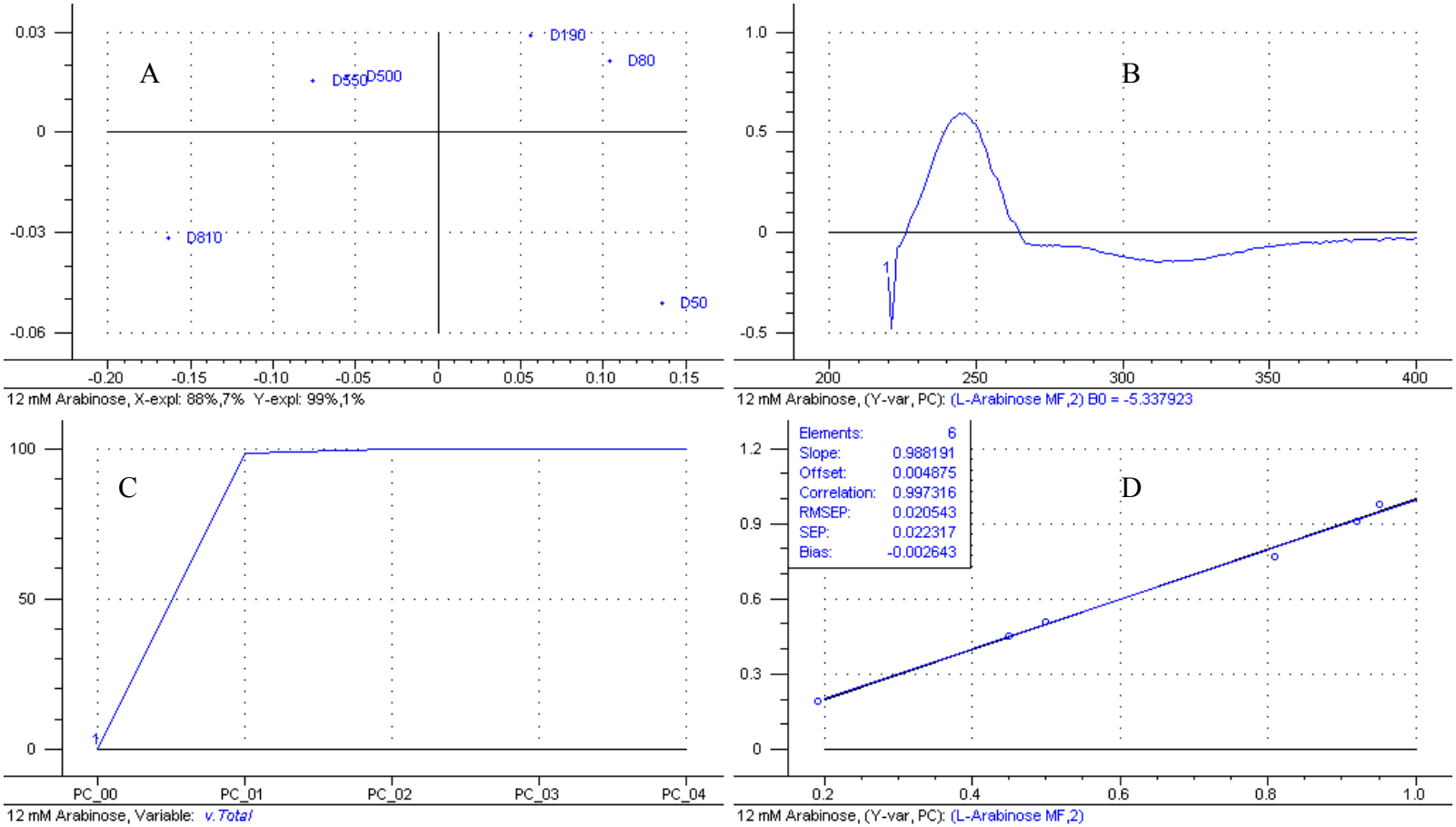

Figure 5.13. Plots of PLS-1 regression calibration model developed using the UV absorption spectral data and known enantiomeric compositions of 12 mM arabinose-S-PEA calibration samples. A: scores plot, B: regression coefficient as a function of wavelength plot, C: percent explained variance as a function of principal component plot, and D: calibration and cross-validation regression lines for the fitted (black) and predicted (blue) mole fractions, respectively, versus the known mole fractions of calibration samples. The model required two PCs (see below plot B or D).

behavior is different from that revealed by the mean-centered spectra of the 3 mM samples. This indicates differences in the effectiveness of the discrimination at the two concentration levels (3 and 12 mM).

As usual, the original spectral data of the two sets of arabinose-S-PEA samples solutions were subjected to PLS-1 regression modeling in order to verify the correlation of the spectral differences shown by the samples with enantiomeric composition.

Figures 5.12A to 5.12D and 5.13A to 5.13D show the PLS-1 calibration model plots developed using the spectral data and enantiomeric compositions for the 3 and 12 mM arabinose-S-PEA calibration samples. Each calibration model was developed using six calibration samples, which were randomly selected from the total samples prepared for analysis. The calibration samples for the 3 mM solutions are made up of L-arabinose mole fractions of 0.0800, 0.110, 0.150, 0.450, 0.550, and 0.810. Those for the 12 mM calibration samples are 0.0500, 0.0800, 0.190, 0.500, 0.550, and 0.810. Figure 5.12A and 5.13A are the respective scores plots for the 3 and 12 mM calibration samples. Figure 5.12B and 5.13B are theregression coefficient as a function of wavelength plots for the 3 and 12 mM calibration samples, respectively. The plots in Figure 5.12C and 5.13C are respectively the percent explained variance versus principal component plots for the 3 and 12 mM calibration samples and Figure 5.12D and 5.13D, respectively, show the cross-validated regression line plots for the 3 and 12 mM arabinose-S-PEA calibration samples.

Generally, the scores plots in Figure 5.12A and 5.13A for both sets of calibration samples reveal patterns describing the variation in enantiomeric compositions of the calibration samples. The scores plot for the 3 mM samples show increasing order from

left to right of the mole fraction of the L enantiomer. This is opposite to the order portrayed by the 12 mM samples: increase from right to left. Compared to the 12 mM samples, the regression coefficient curve (Figure 5.12B) for the 3 mM samples is noisy, unlike the 12 mM regression coefficient curve (Figure 5.13B), which is smooth. The explained variance plots (Figure 5.12C and Figure 5.13C) for the two sets of samples reveal for each a total of four PCs. However, only the first two PCs were required in each case in developing the separate models. For the 3 mM samples, less than 70 % of the variation in the spectral data is explained by both PCs: both PCs explained only 58 % of the variation. Thus less than significant information is explained in the spectral data. However, the two PCs explained 99 % of the variation in enantiomeric composition. On the other hand, the two PCs for the 12 mM model explained 95 % of the variation in the spectral data and 100 % of the variation in enantiomeric composition. As such, a high percentage of information in the data on the 12 mM samples is accounted for by the model. This is as a result of the increase in the effectiveness of the chiral discrimination reflected in the spectra of the samples due to the increase in concentration, which enhanced the effectiveness of the interaction in solution. The less than enough information explained in the spectral data for the 3 mM calibration samples is clearly revealed by the cross-validation regression line plot shown in Figure 5.12D for the 3 mM calibration samples. The cross-validated regression line, shown in blue, deviates significantly from the fitted calibration line shown in black. This indicates poor correlation between enantiomeric composition and the spectral data. This situation is completely different for the 12 mM samples, which reveal a strong correlation between enantiomeric composition and spectral data as shown in Figure 5.13D. The cross-

validation regression plot statistics for the two sets arabinose-S-PEA calibration samples are reported together with those computed for the amino acids in Table 5.6. The values in the table clearly show that the cross-validation plot statistics for the 3 mM arabinose samples are extremely poor compared to the values computed for the other samples. The values computed for the 12 mM samples, on the other hand, compare favorably with those for the amino acids. The correlation coefficient computed for the 12 mM samples, for example, is 0.997. This is significantly identical to the correlation coefficients computed for the amino acids, which vary from 0.996 to 0.998.

As mentioned earlier, the calibration models for the two sets of arabinose samples were developed to predict in each case part of the samples (samples remaining after random selection of calibration samples) prepared for analysis. Table 5.7 shows the mole

Table 5.6 Comparison of the cross-validated PLS-1 regression plot statistics computed for the calibration samples of arabinose, alanine, phenylalanine, and tyrosine analyzed using (S)-(-)-1-phenylethylamine as a non-covalent chiral selector

PLS-1 Regression Plot Statistic	Cross-Validated PLS-1 Regression Plot Statistic Value				
	S-PEA NCA[a] of 3 mM Ara[b]	S-PEA NCA of 12 mM Ara	S-PEA NCA of Alanine	S-PEA NCA of Phenylalanine	S-PEA NCA of Tyrosine
Slope	0.130	0.988	0.940	0.988	0.999
Offset	0.241	0.00488	0.0398	0.00643	0.00221
Correlation coefficient	0.546	0.997	0.998	0.996	0.998
RMSEP[d]	0.250	0.021	0.029	0.025	0.018
SEP[e]	0.262	0.022	0.029	0.027	0.019
Modeled wavelength range	229-808 nm	220-400 nm	229-989 nm	223-360 nm	318-500 nm

[a]. Non-covalent analysis, [b] Arabinose

fractions of L-arabinose predicted for the 3 and 12 mM arabinose-S-PEA samples used as validation samples in comparison with the actual mole fractions. It is clear from Table 5.7 that the prediction results for the 3 mM arabinose analysis are poor. Except for one sample predicted with an absolute error of 0.0422, the absolute errors computed for all other samples are above 0.14. The root-mean-squares error of prediction computed for the entire analysis is 0.18. This error value is quite high for analyses such as this, which requires quite a high level of accuracy. On the other hand, the predicted L-arabinose mole fractions for the 12 mM analysis reveal quite a high level of accuracy. For this analysis, only one sample was predicted with an absolute error as high as 0.0457. The root-mean-squares error of prediction computed for the entire analysis at the 12 mM concentration level is 0.025. This error value compared to that for the 3 mM analysis shows that by increasing the concentration of arabinose from 3 to 12 mM and doubling

Table 5.7. Comparison of the mole fractions of L-arabinose predicted for 3 and 12 mM arabinose-S-PEA validation samples containing varying compositions of D- and L-arabinose but identical amounts of total arabinose. The 3 mM samples were dissolved in 3 mM S-PEA and the 12 mM samples in 6 mM S-PEA

Actual ø of 3 mM L-Ara	Predicted ø for 3 mM L-Ara	Absolute Error	Actual ø of 12 mM L-Ara	Predicted ø for 12 mM L-Ara	Absolute Error
0.0499	0.00767	-0.0422	0.890	0.905	-0.015
0.191	0.332	0.141	0.851	0.823	-0.028
0.500	0.347	-0.153	0.549	0.554	0.005
0.849	0.656	-0.193	0.151	0.118	0.033
0.920	0.674	-0.246	0.110	0.107	0.003
0.950	0.731	-0.219	0.0808	0.0802	0.0006
			0.0500	0.0957	0.0457
RMSEP		0.18			0.025

the concentration of the S-PEA chiral selector, the efficiency of the discrimination increased by a factor of 7.2. Compared to the analysis of the amino acids, analysis of arabinose at the 12 mM concentration level is significantly equally as accurate as the analysis of the amino acids. This indicates that S-PEA is capable of discriminating enantiomeric pairs of non-carboxyl hydroxyl functional group containing chiral compounds. S-PEA, therefore, is capable of molecular interactions other than the supposed ion pair formation interaction with carboxyl functional groups.

Table 5.8 contains the results reported by Augusti et al. [115] for the enantiomeric composition analysis of selected sugars/carbohydrates using electrospray ionization tandem mass spectrometry technique. The figures shown in the table are averages of five analyses in which combinations of divalent transition metal cations, coupled with modified amino acids, were used as chiral selectors. The samples were reported to be

Table 5.8. Results for the enantiomeric composition analysis of selected sugars using metal-modified amino acid chiral selectors combined with electrospray ionization tandem mass spectrometry (results were compiled from reference 115)

Carbohydrate/Sugar	Chiral Selector	CC[a] for Calibration Plot	Enantiomeric Excess of D-Sugar (% ee)	
			Actual	Experimental
Mannose	Cu^{2+}/N-Fmoc[b]-L-Pro	0.9985	-52	-51.6 ± 0.5
Mannose	Cu^{2+}/N-Fmoc-L-Pro	0.9985	-92	-94 ± 3
Glucose	Cu^{2+}/N-Fmoc-L-Pro	0.9974	66	68 ± 2
Galactose	Ni^{2+}/O-Me[c]-L-Tyr	0.9990	70	75 ± 6
Galactose	Ni^{2+}/O-Me-L-Tyr	0.9990	40	40 ± 5
Ribose	Cu^{2+}/N-Ac[d]-L-Phe	0.9994	76	76 ± 3

[a] Correlation coefficient, [b] N-(9-Fluorenylmethoxycarbonyl)-, [c] O-Methyl, [d] N-Acetyl

analyzed at a concentration of 0.2 mM. This concentration is significantly lower than the concentration at which arabinose was successfully analyzed in this present study. That not withstanding, the correlation coefficients reported by Augusti et al. [115] are significantly identical to that obtained in our present study for the analysis of arabinose at a concentration of 12 mM using S-PEA as a non-covalent chiral selector combined with ordinary UV spectroscopy. Compared to our error results for the 12 mM arabinose samples, Table 5.8 reveals that results obtained by Augusti et al. are within a slightly higher error margin than ours. Generally, however, our non-covalent S-PEA discrimination strategy, combined with ordinary UV spectroscopy for chiral analysis by regression modeling of spectral data, is comparable in terms of accuracy with the mass spectrometric technique used by Augusti et al. Regarding sensitivity, our technique can be improved through the use of fluorescence spectroscopy and/or a chiral amine with a more sensitive chromophore, and capable of interacting more strongly with sugars than S-PEA. A study involving the testing of several potential chiral amines is underway by our research group. In addition, the design and synthesis of a chiral amine with the appropriate properties for the above-mentioned purpose is being considered.

Conclusion

This study clearly shows that S-PEA is a potentially powerful and efficient chiral selector that can be used for the determination of the enantiomeric composition of amino acids, carbohydrates/sugars, and other chiral compounds containing similar functional groups. The study also shows that while some chiral compounds can be analyzed effectively at low concentrations, for example, at 2.5 mM (analysis of tyrosine), analysis of others may require higher concentrations to be effective. S-PEA, based on this study,

has shown consistency in terms of its effectiveness as a non-covalent chiral selector for various chiral analytes than any of our previously used non-covalent chiral selectors including: (1) native cyclodextrins, (2) derivatized cyclodextrins, and (3) mixed surfactant-cyclodextrin systems [55]. This is obvious from the prediction errors computed for the S-PEA analyses, which are consistently below 0.03 or 3 %. In addition, S-PEA is more effective at relatively lower analyte concentrations than the above-mentioned chiral selectors for UV studies. In terms of RMSEP figure of merit, the non-covalent, non-inclusion complex forming, S-PEA discrimination strategy compares favorably with the non-separative, covalent, chiral discrimination strategy (NSCCDS) described in Chapter 2. However, both methods may have their limitations. For example, the time required for the covalent reaction in the application of the NSCCDS may prolong the analysis. The non-covalent S-PEA strategy on the other hand, may not work for certain analytes or may require higher concentrations than would be required for the NSCCDS strategy. It should be noted, however, that S-PEA, similar to PD, can be used as a covalent chiral selector as well because its amine functional group can undergo several covalent reactions with a variety of functional groups. Examples of these covalent reactions include amide and Schiff base formation with the carboxyl and carbonyl functional groups respectively. As such, (*R/S*)-(+/-)-1-phenylethylamine is capable of being a versatile chiral selector for chiral analysis by regression modeling of spectral data (CARMSD) and promising for both industrial and research applications.

REFERENCES

1. Gal, J. *Chirality*, **2007**, *19*, 89-98

2. Cintas, *P. Angew. Chem. Int. Ed*. **2007**, *46*, 4016-4024

3. Hicks, J. M. *Chirality: Physical Chemistry, ACS Symposium Series 810*; American Chemical Society: Washington DC, 2002, pp 1-16

4. Eliel, E. L.; Wilen, S. H.; Doyle, M. P. *Basic Organic Stereochemistry*; John Wiley and Sons: New York, 2001

5. Graham Solomons, T. W. *Organic Chemistry, 6th ed;* John Wiley and Sons: New York, 1996; 178-218

6. Manus, C. *Right and Left Hand: The Origins of Asymmetry in Brains, Bodies, Atoms, and Cultures*; London, 2002, 51-58

7. Van Cleve, J.; Fredrick R. E. *The Philosophy of Right and Left: Incongruent Counterparts and the Nature of Space*; Kluwer Academic, Dordrecht, 1991, 31

8. Ramberg, P. J. *Chemical Structure, Spatial Arrangement: The Early History of Stereochemistry, 1874-1914*; Ashgate: Burlington, 2003

9. Reggelin, M. *Angew Chem. Int. Ed.* **2005**, *44*, 669-671

10. Eliel, E. L.;Kofron, J. T. *J. Am. Chem. Soc*. **1953**, *75*, 4585

11. Ingle, J. R. Studies on Regression Modeling of Spectral Data as a Means of Chiral Analysis. Ph.D. Dissertation, Baylor University, TX, August 2006

12. Rabbe, D. H. Practical Developments in Analytical Spectroscopy. Ph.D. Dissertation, Baylor University, TX, August 2003

13. Lahav, M.; Laub, F.; Gati, E.; Leiserowitz, L.; Ludmer, Z. *J. Am. Chem. Soc*. **1976**, *98* (6), 1620-1622

14. Sokolov, V. I. *Russian. Chemical. Bulletin Int. Ed*. **2001**, *50*(8), 1339-1355

15. Huang, W.; McKevitt, M.; Palzkill, T. *Gene* **2000**, *251*, 187-197

16. Bruton, J.; Hoorner, W. H.; Russ, G. A. *J. Biol. Chem*. 1**967**, *242*, 813

17. Barreiro, E. J.; Ferreira, V. F.; Costa, P. R. R.; *Chem. Abstr. (Engl. Trans.)* **1997**, *20*(6)

18. Quan, Z.; Xiao-Feng, Y.; Weng-Sheng, P.; Su, Z. *World J. Gastroenterol* **2008**, *14*(16), 2617-2619

19. Stinson, S. C. *Chem. Eng. News* **2000**, *78*(43), 55-78

20. Shimazawa, R.; Nagai, N.; Toyoshima, S.; Okuda, H. *Journal of Health Science* **2008**, *54*(1), 23-29

21. *Chiral Analysis*; Busch, K. W.; Busch, M. A., Ed; Elsevier: Amsterdam, 2006

22. Blanco, M.; Coello, J.; Iturriaga, H. Maspoch, S.; Perez-Maseda, C. *Anal. Chim. Acta* **2000**, *407*, 233-245

23. Geng, L.; McGown, L. B. *Anal. Chem.* **1994**, *66*, 3243-3246

24. Vollmer, F. *Opt. Lett*. **2006**, *31*(4), 453-455

25. Costante, J.; Hecht, L.; Polavarapu, P. L.; Collet, A.; Barron, L. D. *Angew. Chem. Int. Ed*. **1997**, *36*, 885-887

26. Barron, L. D.; Hecht, L.; McColl, I. H.; Blanch, E. W. Mol. Phys. **2004**, *102*(8), 731-744

27. Guo, C.; Shah, R. D.; Dukor, R. K.; Cao, X.; Freedman, T. B.; Nafie, L. A. *Appl. Spectrosc*. **2005**, *59*(9), 200A-220A

28. Finn. M. G. *Chirality* **2002**, *14*, 534-540

29. Liu, X.; Ilankumaran, P.; Guzei, I. A.; Verkade, J. G. *J. Org. Chem*. **2000**, *65*, 701-706

30. McCreary, M. D.; Lewis, D. W.; Wernick, D. L.; Whiteside, G. M. *J. Am. Chem. Soc*. **1974**, *96*, 1038-1054

31. Ilisz, I.; Berkecz, R.; Peter, A. *J. Pharm. Biomed Anal*. **2008**, *47*, 1-15

32. Ladanyi, L.; Sztruhar, I.; Slegel, P.; Vereczekey-Donath, G. *Chromatographia* **1987**, *24*, 477-481

33. Moscow University. Discovery of Electrokinetic Phenomena. http://www.icc2008.ru/en/conference/plenary_en.pdf (accessed February 7, 2009)

34. Vespalec, R.; Bocek, P. *Chem. Rev*. **2000**, *100*, 3715-3753

35. Capillary Electrophoresis: A Simple Technique. http://www.beckman.com/resourcecenter/labresources/ce/cedefinitionmodes.asp

36. Fales, H. M.; Wright, G. J. *J Am. Chem. Soc*. **1977**, *99*(7), 2339-2340

37. Zahorsky, U-I.; Musso, H. *Chem. Ber*. **1973**, *106*, 3608

38. Laidler, K.; Meiser, S.; Santuary, B. *Physical Chemistry; 4th ed*; Houghton Mifflin: New York, 2003, Chapter 13

39. Skoog, D. A.; Holler, F. J.; Nieman, T. J. *Principles of Instrumental Analysis*; Thomson Learning: USA, Chapter 15

40. Harris, D. C. *Quantitative Chemical Analysis; 3rd ed*;W. H. Freeman: New York, 1991, pp 377-378

41. Brown, S. D. *Chemom. Intell. Lab. Syst*. **1995**, *30*, 49-58

42. Wold. S. *Chemom. Intell. Lab. Syst*. **1995**, *30*, 109-115

43. What is Chemometrics? http://www.wiley-vch.de/templates/pdf/3527314180_c01.pdf (accessed February 2009)

44. Eigenvector. Homepage. http://www.eigenvector.com/About/definition.html (accessed February 2009)

45. Beebe, K. R.; Pell, R. J.; Seasholtz, M. B. *Chemometrics: A Practical Guide*; John Wiley and Sons: New York, 1998

46. Adams, M. J. *Chemometrics in Analytical Spectroscopy*; The Royal Society of Chemistry: Cambridge, 1995

47. Brereton, R. G. *Chemometrics: Data Analysis for Laboratory and Chemical Plant*; John Wiley and Sons: West Sussex, 2002

48. Martens, H.; Naes, T. *Multivariate calibration*; John Wiley and Sons: Chichester, 1989

49. Water structure and science. http://www.lsbu.ac.uk/water/cyclodextrin.html (accessed December 2008)

50. Han. S. M. *Biomed. Chromatogr*. **1997**, *11*, 259-271

51. Avakyan, V. G.; Nazarov, V. B.; Alfimov, M. V.; Bagatur´yants, A. A. *Russian Chemical Bulletin*, ***1999***, *48*(10), 1833-1844

52. Schneiderman, E.; Stalcup, A. *J. Chromatogr* B, **2000**, *745*, 83-102

53. Li, S.; Purdy, W. *Chem. Rev*. **1992**, *92*, 1457-1470

54. Armstrong, D. W.; Ward, T. J.; Armstrong, R. W.; Beesley, T. E. *Science* **1986**, *232*, 1132

55. Fakayode, S. O. Chiral Analysis by Multivariate Regression Modeling of Spectral Data of Cyclodextrin Guest-Host Complexes. Ph.D. Dissertation, Baylor University, TX, August 2006

56. Ingle, J. R.; Busch, K. W.; Busch, M. A. *Talanta* **2008**, *75*, 572-584

57. Fakayode, S. O.; Busch, M. A.; Busch, K. W. *Talanta* **2006**, *68*, 1574-1583

58. Fakayode, S. O.; Swamidoss, A. M.; Busch, M. A.; Busch, K. W. *Talanta* **2005**, *65*, 838-845

59. Fakayode, S. O.; A. M.; Busch, M. A.;Bellert, D. J.; Busch, K. W. *Analyst* **2005**, *130*, 233-241

60. Busch, K. W.; Swamidoss, A. M.; Fakayode, S. O.; Busch, M. A. *Anal. Chim. Acta* **2004**, *525*, 53-62

61. Busch, K. W.; Swamidoss, A. M.; Fakayode, S. O.; Busch, M. A. *J. Am. Chem. Soc*. **2003**, *125*, 1690-1691

62. Williams, A. A.; Fakayode, S. O.; Lowry, M.; Warner, I. M. *Chirality* **2009**, *21*(2), 305-315

63. Tran, C. D.; Oliveira, D.; Grishko, V. I. *Anal Biochem*. **2004**, *325*, 206-214

64. Lovely. A. E.; Wenzel, J. T. *Chirality* 2008, *20*, 370-378

65. Welch, C. J.; Hyun, M. H.; Kubota, T.; Schafer, W.; Bernardoni F. Choi, J. H.; Wu, N.; Gong, X.; Lipshutz, B. Chirality **2008**, *20*, 815-819

66. Carey, F. A.; Sundberg, R. J. *Advanced Organic Chemistry. Part B: Reactions and Synthesis;* Springer: 2007, pp 252

67. Bhushan, R.; Tanwar, S. *Chromatographia* **2008**, *68*(9&10), 849-853

68. Santoro, M, I .R .M.; Cho, H. S.; Kedor-Hackmann, E. R. M. *Drug Dev. Ind. Pharm*.**2000**, *26*, 1107-1110

69. Smith, M B.; March, J. *March's Advanced Organic Chemistry: Reactions, Mechanisms and Structure*; John Wiley and Sons: 2007, pp 1407-1421

70. Flavahan, N. *J. Pharmacol. Exp. Ther*. **2004**, *313*(1), 432-439

71. Fujita, K.; Li, Z.; Ozeki, N.; Yamaguchi, R. *Tetrahedron Lett*. **2003**, *44*, 2687-2690

72. Watanabe, Y.; Ohta, T.; Tsuji, Y. *Bull. Chem. Jpn*. **1983**, *56*, 2647-2651

73. Gunanathan, C.; Ben-David, Y.; Milstein, D. *Science* **2007**, *317*, 790-792

74. Campins-Falco, P.; Meseguer-Lloret, S.; Climent-Santamaria, T.; Molins-Legua, C. *Talanta* **2008**, *75*, 1123-1126

75. Singh, M. M.; McGowan, C. B.; Pike, R. M.; Szafran, Z. *J. Chem. Edu*. **2000**, 77, 625-626

76. Richardson, J. N.; Stauffer, M. T.; Henry, J. L. *J. Chem. Edu*. **2003**, *80*, 65-67

77. Pluskal, M. G. *Nat. Biotechnol*. **2000**, *18*, 104-105

78. Pluskal, M. G.; Bogdanova, A.; Lopez, M.; Gutierrez, S.; Pitt, A. M. *Proteomics* **2002**, *2*, 145-150

79. Moliner-Martinez, Y.; Herraez-Hernandez, R.; Campins-Falco, P. *J. Chromatogr* A **2007**, *1164*, 329-333

80. Lu, C-Y.; Feng, C-H.; *J. Chromatogr* A **2007**, *1156*, 249-253

81. Li, Y.; George, J. E.; McCarty, C. L. *J. Chromatogr* A **2007**, *1176*, 223-230

82. Ballesteros-Gomez, A.; Rubio, S.; Perez-Bendito, D. *J. Chromatogr* A **2008**, *1203*, 168-176

83. Caner, H.; Grona, E.; Levy, L.; Agranat, I. *DDT* **2004**, *9*(3), 105-110

84. Hutt, A. J.; Valentova, J. Acta Pharmaceuticae Universitatis Comenianae: Tomus 2003

85. Tsukamoto, M.; Kagan, H. B. *Adv. Synth. Catal*. **2002**, *344*(5), 453-463

86. Abato, P.; Seto, C. T. *J. Am. Chem. Soc*. **2001**, *123*, 9206-9207

87. Korbel, G. A.; Lalic, G.; Shair, M. D. *J. Am. Chem. Soc*. **2001**, *123*, 361-362

88. Rouhi, A. M. *Chem. Eng. News* **2004**, *82*, 47-62

89. Robbitt, D. R.; Yeung, E. S. *Anal. Chem.* **1984**, *56*, 1577-1581

90. Zong, D.; Douhal, A.; Zewail, A. H. *PNAS* **2000**, *97*(26), 14056-14061

91. Wenge, W.; Fengnian, M.; Xiumin, S.; Zhang, C. *Tetrahedron: Asymmetry*,**2007** *18*, 832-837

92. Garcia-Ruiz, C.; Mariana, M. L. *Electrophoresis*, **2006**, *27*, 195

93. Guebitz, G.; Schmid, M. G. *Mol. Biotechnol*, **2006**, *32*, 159

94. Eeckhsut, A. V.; Michotte, Y. *Electrophoresis*, **2006**, *27*, 2880

95. Erny, G. L.; Cifuentes, A. *J. Pharm. Biol. Anal*. **2006**, *40*, 509

96. Wang, Y.; Zhang, F.; Liang, J.; Li, H.; Kong, *J. Spectrochemica Acta* Part A, **2007**, 68, 279-283

97. Orisaku, K. K.; Hagiwara, M.; Ohgo, Y.; Arai, Y.; Ohgo, Y. *Acta Cryst*. **2005**, C*61*, m190-m193

98. Balint, J,; Egri, G.; Czugler, M.; Schindler, J.; Kiss, V.; Juvancz, Z.; Fogassy, E. *Tetrahedron: Asymmetry*, **2001**, *12*, 1511-1518

99. Fischer, A. T.; Pagni, R. M.; Campton, R. N. *J. Phys. Chem*. **2007**, *111*, 8187-8196

100. Camps, P.; Munoz-Torrero, D.; Rull, J.; Font-Bardia, M.; Solans, X. *Tetrahedron: Asymmetry*, **2007**, *18*, 2947-2958

101. Gimazetdinov, A. M.; Vostrikov, N. S.; Miftakov, M. S. *Tetrahedron: Asymmetry*, **2008**, *19*, 1094-1099

102. Federsel, H-J.; Hedberg, M.; Qvarnstrom, F. R.; Sjogren, M. P. T.; Tian, W. *Acc. Chem. Res*. **2007**, *40*, 1377-1384

103. Jabin, I.; Revial, G.; Pfau, M.; Netchitailo, P. *Tetrahedron: Asymmetry*, **2002**, *13*, 563-567

104. Kontrec, Darko.; Vinkovic, V.; Lesac, A.; Sunjic, V.; Hollosi, M. *Tetrahedron: Asymmetry*, **1999**, *10*, 1935-1945

105. Ashraf, S. A.; Pornputtkul, Y.; Kane-Maguire, L. A. P.; Wallace, G. G. *Aust. J. Chem*. **2007**, *60*, 64-67

106. Martin, A.; Cocero, M. J. *J. Supercritical Fluids*, **2007**, *40*, 67-73

107. West, K. N.; McCarney, J. P.; Griffith, K. N.; Liotta, C. L.; Eckert, C. A. Co_2 as an anti-solvent for chiral separations, in: Proceedings of the AIChE Annual Meeting, Dallas, 1999

108. Kaboudin, B.; Haghighat, H.; Yokomatsu, T. *Tetrahedron: Asymmetry*, **2008**, *19*, 862-866

109. Chaikumpollert, O.; Methacanon, P.; Suchiva, K. Carbo. *Polymers*, **2004**, *57*, 191-196

110. Bedouet, L.; Denys, E.; Courtois, B.; Courtois, *J. Carb. Polymers* **2006**, *65*, 165-173

111. Redondo-Ciuenca, A.; Villanueva-Suarez, M. J.; Rodriguez-Sevilla, M. D.; Mateos-Aparicio, I. *Food Chemistry*, **2006**, *101*, 1216-1222

112. Schleif, R. *TIG* **2000**, *16*(12), 559-565

113. Sedlak, M.; Ho, N. W. Y. *Enzyme Mic. Technol*. **2001**, *28*, 16-24

114. Huang, W.; McKevitt, M.; Palzkill, T. *Gene* **2000**, *251*, 187-197

115. Augusti, D. V.; Lago, R. M.; Augusti, R. *J. Braz. Chem. Soc*. **2004**, *15*(5), 786-790

116. Lopes, J. F.; Gaspar, E. M. S. M. *J. Chromatogr*. A, **2008**, *1188*, 34-42

117. Gomis, D.; Tamayo, D.; Alonso, *J. Anal. Chim. Acta* **2001**, *436*, 173

118. Muynck, C. D.; Soetaert, B. W.; Vandamme, E. *J. Chromatogr*. A **2006**, *1101*, 115

119. Little, M. *J. Biochem. Biophys. Methods* **1985**, *11*, 195

120. Lamari, F.; Kuhn, R. *J. Chromatogr*. B **2003**, *793*, 15

121. Tran, C. D.; Oliveria, D.; Grishko, V. I. *Anal. Bichem*. **2004**, *325*, 206-214

122. Wei, Y.; Lin, X.; Zhu, C. Canadian *J. Analytic. Sci. and Spectrosc*. **2005**, *50*(3), 135-140